



**Developing a label-free microfluidic strategy for downstream processing of stem cell-derived red blood cells**

**Ewa Guzniczak**

Submitted for the degree of Doctor of Philosophy

**Heriot-Watt University**

School of Engineering and Physical Sciences

Institute of Biological Chemistry, Biophysics and Bioengineering

May 2019

The copyright in this thesis is owned by the author. Any quotation from the thesis or use of any of the information contained in it must acknowledge this thesis as the source of the quotation or information.

## **Abstract**

Stem cell-originated therapeutic products, such as *in vitro* manufactured red blood cells (mRBC), offer a novel route to treating disease by administration of a viable somatic cells that have been selected and manipulated outside the body. Cell-based therapeutics are different to traditional biopharmaceutical products and that presents a challenge of developing robust and economically feasible manufacturing processes, especially in sample purification. To address this challenge, I investigated label-free separation methods based on cell endogenous properties such as size and deformability as sorting parameters. In this study the mechanical properties of umbilical cord blood CD34+ cells undergoing *in vitro* erythropoiesis were characterised to identifying the best route for mRBC purification. For the first time it has been demonstrated how deformability-induced lift force affects and contributes to particles separation in spiral microchannels. These findings were translated and incorporated into a new route for high-throughput (processing millions of cells /min and mls of medium/ min) continuous purification strategy for separating mRBC from contaminant by-products (purity >99%). This work is anticipated to bring the benefits of mRBC to a wide range of patients by enabling their manufacture as a reliable, safe and controlled supply of red blood cells for transfusion.

To Paul de Sousa  
&  
all scientists following their personal research path

## **Acknowledgements**

Undertaking this PhD has been a truly wonderful adventure for me and it would not be as fantastic as it was without the support, guidance and companionship of many people.

I would like to first say a very big thank you to all my supervisors and mentors: Helen Bridle and Nick Willoughby- thank you for being such fantastic partners in crime, for staying openminded, patient and supportive. Melanie Jimenez- thank you for being my academic everything- my mentor, my friend and my greatest collaborator. Graeme Whyte- thank you for welcoming me in your group, all the top-notch science discussions we had and your extremely valuable input into my work. Oliver Otto- thank you for having me in your group, for creating such a wonderful safe space for me and the rest of your academic family and for inventing my favourite RT-DC. Fiona Dempsey- thank you for looking after me and kindly teaching me all your best tricks and tips.

I gratefully acknowledge the funding received towards my PhD from the Industrial Biotechnology Innovative Centre (IBioIC) and support I received from Tim Ryan and his team at Epigem. I am also grateful for the Royal Society of Edinburgh John Moyes Lessells Travel Scholarships, which allowed me to work at the Greifswald University in Germany.

I am also very grateful to all those who were always so helpful and provided me with their assistance: Mary Pratt- for being a champion in sorting out all the seemingly impossible tasks, Martin Waterfall- for FACS sorting my cells and sharing your knowledge and wisdom, Doreen Biedenweg- for sharing your expertise and all your help with the facility at Greifswald University, Fabian Czerwinski- for sharing your knowledge in microscopy and fluid dynamics and all the discussions we had, Bob Fregin- for using your natural engineering talent to fix and improve my equipment, Ali Dun- for all your help and assistance with microscopy at ESRIC, Tamir Chandar and Neil Robertson for your help and assistance with the gene expression profiling, David Brown- for letting me use your camera, booking microscopy rooms and bringing a bright smile on every occasion, Krysia Maciaszek- for being my RNA extraction guru, Helen Wise- for your valuable guidance with the mysteries of molecular biology, Katarzyna Cialowicz- for welcoming me in IB3 and making me feel like home and helping me with findings my ways in our facility at Heriot-Watt University and Miguel Hermida- without you and your reagents I would not have that much fun in the lab.



I am indebted to all my friends who opened their hearts and homes to me: Adam Sobor, Filip Sobieszek and Elisenda Raga Gil- simply but greatly thank you for being. Dorota, Julia and Lili Markowskie- thank you for your support and all the beautiful adventures we had together.

Olga Szerryyy Okruszek Chwilowicz, my twin sister Aleksandra Gajewska and my friend-brother Jakub Ruminkiewicz- for your unconditional friendships, Paul Turner- for boosting my morale with delicious cakes, strong coffee, intriguing art and wonderful conversations, Ricardo Pires and Melinda Fekete- thank you for your kindness, friendly and generous reception in Greifswald and for trusting me with Kitty, all my German kids: Nithya Shree, Yesaswini Komaragiri, Venkata Aditya Saimadhukiran Dabbiru, Patrick Bohn (Mr Bond) and Felix Nagel- thank you for feeding me best Indian food, chocolate cakes and being wonderful company.

And finally, I would also like to say a heartfelt thank you to my family, my mum Maria Guzniczak- thank you Kuczakowa Mamo for your wonderful love and support, conditioning me to love science and always crave for knowledge. My Peter Szustakowski- thank you for being by my side and distracting me with the most amazing laughter- without you I would complete this work so much faster :\*, my sister Anna Guzniczak and my brother Dawid Guzniczak- for being the best siblings and friends I could ever wish for. My grandparents Genowefa and Eugeniusz Kluczynscy and my family Katarzyna, Stanislaw, Lukasz, Wiktor, Barbara Kluczynscy and Teresa and Patrycja Paluszynskie- thank you for creating my favourite place on Earth- Skulsk- where is my base camp. My acquired family: Bogumila Szustakowska, Pan Dziadzio Jerzy Grzeszczak, Ewunia Szustakowska and Iza Piatek- thank you for your support and for always making me feel so welcome.

My father Eugeniusz Andrzej Guzniczak and my grandparents Irena and Eugeniusz Guzniczak- I wish you could see this.

## Research Thesis Submission

Please note this form should be bound into the submitted thesis.

---

Name:	Ewa Guzniczak		
School:	EPS		
Version: <i>(i.e. First, Resubmission, Final)</i>	First	Degree Sought:	PhD

---

### Declaration

In accordance with the appropriate regulations I hereby submit my thesis and I declare that:

1. The thesis embodies the results of my own work and has been composed by myself
2. Where appropriate, I have made acknowledgement of the work of others
3. Where the thesis contains published outputs under Regulation 6 (9.1.2) these are accompanied by a critical review which accurately describes my contribution to the research and, for multi-author outputs, a signed declaration indicating the contribution of each author (complete Inclusion of Published Works Form – see below)
4. The thesis is the correct version for submission and is the same version as any electronic versions submitted\*.
5. My thesis for the award referred to, deposited in the Heriot-Watt University Library, should be made available for loan or photocopying and be available via the Institutional Repository, subject to such conditions as the Librarian may require
6. I understand that as a student of the University I am required to abide by the Regulations of the University and to conform to its discipline.
7. Inclusion of published outputs under Regulation 6 (9.1.2) shall not constitute plagiarism.
8. I confirm that the thesis has been verified against plagiarism via an approved plagiarism detection application e.g. Turnitin.

\* *Please note that it is the responsibility of the candidate to ensure that the correct version of the thesis is submitted.*

Signature of Candidate:		Date:	
-------------------------	--	-------	--

---

### Submission

Submitted By <i>(name in capitals)</i> :	Ewa Guuzniczak
Signature of Individual Submitting:	

Date Submitted:	

**For Completion in the Student Service Centre (SSC)**

Received in the SSC by ( <i>name in capitals</i> ):				
Method of Submission ( <i>Handed in to SSC; posted through internal/external mail</i> ):				
E-thesis Submitted ( <b>mandatory for final theses</b> )				
Signature:	<table border="1" style="width: 100%;"> <tr> <td style="width: 60%;"></td> <td style="width: 20%; text-align: center;">Date:</td> <td style="width: 20%;"></td> </tr> </table>		Date:	
	Date:			

**Inclusion of Published Works**

---

**Declaration**

This thesis contains one or more multi-author published works. In accordance with Regulation 6 (9.1.2) I hereby declare that the contributions of each author to these publications is as follows:

Citation details	<u>Ewa Guzniczak</u> , Maryam Mohammad Zadeh, Fiona Dempsey, Melanie Jimenez, Henry Bock, Graeme Whyte, Nicholas Willoughby and Helen Bridle, <b>High-throughput assessment of mechanical properties of stem cell derived red blood cells, toward cellular downstream processing</b> . <i>Sci. Rep.</i> <b>7</b> , 14457 (2017)
Ewa Guziczak	Designed and performed the RT-DC, widefield microscopy, cytospin, flow cytometry and FACS experiments, performed CB CD43+ differentiation and wrote all parts of the manuscript relevant to this work
Maryam Mohammad Zadeh	Performed AFM work and wrote a relevant part of the manuscript (not presented in this thesis) and widefiled microscopy
Fiona Dempsey	Provided cells for the research and trained EG in the differentiation protocol and cytospin assay
Melanie Jimenez	Provided ROC curves for FigS.3 (not presented in this thesis) and contributed to the writing of the manuscript
Henry Bock	Help with AFM data analysis- not presented in this thesis
Graeme Whyte	Contributed to the writing of the manuscript
Nicholas Willoughby	Provided cells for the research, helped with AFM work (not presented in this thesis) and contributed to the writing of the manuscript
Helen Bridle	Contributed to the experiments design and writing of the manuscript
Signature:	

Date:	

Citation details	<u>Ewa Guzniczak</u> , Melanie Jimenez, Matthew Irwin, Oliver Otto, Nicholas Willoughby, and Helen Bridle, <b>Impact of Poloxamer 188 (Pluronic F-68) Additive on Cell Mechanical Properties, Quantification by Real-Time Deformability Cytometry.</b> <i>Biomicrofluidics</i> 12 (4), 44118 (2018)
Ewa Guziczak	Design and performed all presented experimental work and wrote the manuscript
Melanie Jimenez	Contributed to the writing of the manuscript
Matthew Irwin	Provided preliminary data (not presented in this work)
Oliver Otto	Contributed to the experiments design and writing of the manuscript
Nicholas Willoughby	Contributed to the writing of the manuscript
Helen Bridle	Contributed to the experiments design and writing of the manuscript
Signature:	
Date:	

Citation details	Ewa Guzniczak, Melanie Jimenez, Oliver Otto, Nicholas Willoughby, and Helen Bridle, “Deformability-induced lift force in curvilinear microchannels for stem cell-derived product purification.,” in <i>22nd International Conference on Miniaturized Systems for Chemistry and Life Sciences</i> , 2018, pp. 2049–2052.
Ewa Guziczak	Designed and performed all presented experimental work and wrote the conference paper
Melanie Jimenez	Contributed to the experimental design and writing of the paper
Oliver Otto	Contributed to the experimental design and writing of the paper
Nicholas Willoughby	Contributed to the experimental design and writing of the paper
Helen Bridle	Contributed to the experimental design and writing of the paper
Signature:	
Date:	

# Table of Contents

Method of Submission .....	7
E-thesis Submitted (mandatory for final theses) .....	7
Chapter 1. Introduction.....	1
1.1. Project motivation .....	1
1.2. Label-free markers .....	3
1.3. Traditional cell separation.....	7
1.4. Microfluidic label-free separation.....	8
1.5. Inertial microfluidics .....	9
1.6. Thesis structure .....	18
Chapter 2. Materials and methods .....	20
2.1. Cell culture .....	20
2.1.1. Cord CD34+ stem cell culture .....	20
2.1.2. Jurkat cells .....	20
2.1.3. HEK cells .....	21
2.2. Real-time deformability cytometry .....	21
2.3. Real-time fluorescent and deformability cytometry.....	22
2.4. Cell morphology- cytopsin.....	23
2.5. Flow cytometry and FACS-staining protocol .....	24
2.6. Microfluidic system.....	25
2.7. Receiver Operating Characteristic (ROC) curves .....	26
Chapter 3. Assessment of mechanical properties of stem cell-derived red blood cells.....	28
3.1. Introduction .....	28
3.2. Results and discussion.....	30
3.3.1. High-throughput size and deformability assessment .....	30
3.3.2. Correlation between mechanotype and biology.....	36
3.4. Conclusion.....	39
3.5. Materials and methods .....	40
3.5.1. Flow Cytometry .....	40
3.5.2. Mechanotype Characterisation- Real-Time Deformability Cytometry .....	40
3.5.3. Widefield Microscopy .....	41
Appendix A .....	42
Chapter 4. Understanding contribution of deformability-induced lift force to cells focusing in spiral microchannels .....	43
4.1. Introduction .....	43
4.2. Theoretical background.....	44

4.3.	Results .....	46
4.3.1.	Cellular deformability model .....	46
4.3.2.	Lateral equilibrium position as a function of cell deformability .....	51
4.3.3.	Deformability difference for sorting cells in spiral microchannel.....	55
4.3.4.	Impact on cell viability .....	58
4.4.	Discussion .....	59
4.5.	Conclusion.....	64
4.6.	Materials and methods .....	64
4.6.1.	Deriving the cellular deformability model.....	64
4.6.2.	Cell characterisation RT-FDC .....	65
4.6.3.	Cells separation in spiral channels .....	66
4.6.4.	Viability flow cytometric assay .....	66
Chapter 5.	Purifying stem cell-derived red blood cells: Translating cell mechanical properties into complete high-throughput label-free downstream processing strategy. ....	75
5.1.	Introduction .....	75
5.2.	Results and Discussion.....	76
5.2.1.	Sample characterisation .....	76
5.2.2.	Size measurements.....	76
5.2.3.	Deformability measurements .....	79
5.2.4.	Sorting- principles and optimisation.....	81
5.2.5.	mRBC purification process.....	84
5.2.6.	Filtration justifications .....	86
5.2.7.	Donor-to-donor variability and reproducibility .....	91
5.2.8.	Processing impact on cells .....	95
5.3.	Conclusion and future outlook .....	100
5.4.	Materials and methods .....	101
5.4.1.	Flow cytometry .....	101
5.4.2.	Real-time fluorescence and deformability cytometry (RT-FDC).....	101
5.4.3.	Cytospin analysis .....	102
5.4.4.	Cell processing.....	102
5.4.5.	Trypan blue exclusion assay .....	104
5.4.6.	Global gene expression .....	104
Appendix E.....		105
Appendix F.....		106
Appendix G .....		108
Appendix H.....		109

Appendix I.....	111
Appendix J.....	112
Appendix K.....	113
Appendix L.....	114
Appendix M.....	115
Appendix N.....	116
Appendix O.....	117
Chapter 6. Bioprocess considerations Part I- predicted versus experimental results .....	120
6.1. Introduction .....	120
6.2. Results .....	122
6.3. Discussion .....	128
6.4. Conclusion.....	130
6.5. Materials and methods .....	130
6.5.1. Sample preparation .....	130
6.5.2. Hydrodynamic behaviour in spiral microchannel.....	131
Chapter 7. Bioprocessing considerations Part II- medium choice- impact of Poloxamer 188 (Pluronic F-68) additive on cell mechanical properties.....	133
7.1. Introduction .....	133
7.2. Results .....	135
7.2.1. Effect of Pluronic on Jurkat cells size and deformability- time-dependency ..	135
7.2.2. Effect of Pluronic on Jurkat cell size and deformability- concentration dependency .....	137
7.2.3. Effect of Pluronic F-68 on RBCs size and deformability .....	139
7.2.4. Effect of Pluronic F-68 on adherent HEK cells.....	140
7.2.5. Hydrodynamic behaviour in spiral microchannel.....	142
7.3. Discussion and conclusion .....	147
7.4. Materials and methods .....	150
7.4.1. Real-time deformability cytometry.....	150
7.4.2. Viability study.....	150
7.4.3. Sample preparation- Jurkat cells.....	150
7.4.4. Sample preparation- red blood cells .....	152
7.4.5. Sample preparation- HEK cells .....	152
7.4.6. Microscopy .....	152
7.4.7. Assessing hydrodynamic behaviour of Pluronic-treated Jurkat cells and RBC in spiral microchannel.....	153
Appendix P.....	154
Appendix R .....	159

Appendix S.....	164
Chapter 8. Summary and future outlook .....	169
Bibliography .....	172



## Glossary

a	Particle diameter
AFM	Atomic Force Microscopy
AUC	Area Under the Curve
BEL-A	Bristol Erythroid Line Adult
c	Circularity
CB CD34+	Umbilical Cord Blood CD34 positive cells
CD	Cluster of differentiation
$C_L$	Lift coefficient
CytoD	Cytochalasin D
D	Deformation
DD	Differential Deformation
De	Dean number
$D_h$	Hydraulic diameter
$EC_{50}$	Half maximal effective concentration
EDTA	Ethylenediaminetetraacetic acid
FACS	Fluorescent Activated Cell Sorting
FBP	Fetal bovine serum
$F_D$	Deformability-induced lift force
$F_{DD}$	Dean Drag
$F_L$	Shear-gradient lift force
$F_N$	Net-inertial lift force
FSC-A	Forward Light Scatter
$F_W$	Wall-induced lift force
$F_\Omega$	Rotation-induced lift force
G	Shear rate
GFP	Green Fluorescent Protein
GMP	Good Manufacturing Practice
H	Height
HEK	Human Embryonic Kidney cells

hESC	Human Embryonic Stem Cells
hiPSC	Human induced Pluripotent Stem Cells
IF	Inertial Focusing
MACS	Magnetic Activated Cell Sorting
mRBC	Manufactured Red Blood Cells
MTC	Magnetic Twisting Cytometry
PB	Peripheral Blood
PBS -/-	Phosphate-buffered saline without calcium and magnesium
PDMS	Polydimethylsiloxane
PI	Propidium Iodide
PMMA	Poly(methyl methacrylate)
PTFE	Polytetrafluoroethylene
RBC	Red Blood Cells
R	Radius
Re	Reynolds number
Re <sub>p</sub>	Particle Reynolds number
ROC	Receiver Operating Characteristic
ROI	Region Of Interest
RT-DC	Real-Time Deformability Cytometry
RT-FDC	Real-Time Fluorescent and Deformability Cytometry
SD	Standard Deviation
U	Medium velocity
W	Width
V <sub>F</sub>	Volume fraction
$\alpha$	Length fraction
$\lambda$	Particle confinement ratio
$\mu$	Dynamic viscosity
$\rho$	Medium density

# Chapter 1. Introduction

## 1.1. Project motivation

Rapid development in the field of stem cell research has led to the development of new treatments and highly innovative cellular therapeutic products. These new cell-based medicinal products have a high potential where there is a previously unmet medical need [1].

Despite an annual 112.5 million blood donations collected across 176 countries in over 13000 blood centres, increased demand for safe blood for transfusion might not be satisfied by donated blood [2], hence there is a niche for unconventional solutions such as manufacturing red blood cells (RBC) from stem cells. Stem cells- derived red blood cells could constitute an attractive pathogen- free and sustainable alternative for donated blood for rare blood groups and patients requiring systematic transfusions[3]. In many cases, such as sickle cell anaemia, myelodysplasias and leukaemia, multiple blood transfusions are regarded the only available symptomatic treatment and that can lead to immunization against the allogenic red blood cells and transfusion impasses [4].

The efficient production of manufactured red blood cells (mRBC) is an ambitious goal for blood services around the world, and production of a single therapeutic dose ( $\sim 2 \times 10^{12}$  cells) still remains a significant bioprocessing challenge [5][6]. The main challenge for future clinical applications of mRBC is to identify and develop technological solutions that would allow production of mRBC at a satisfactory scale and quality in compliance with good manufacture practice (GMP) regulations within the realms of economic feasibility [7][8][9][10][11]. New strategies for the large-scale automated expansion [10] [12], purification and formulation will have to be implemented [13] and the choice of adequate methods is strongly motivated by cost considerations [14][3].

To date, numerous customised differentiation protocols have been developed to produce mRBC from several sources of starting material: CD34+ hematopoietic stem cells from peripheral blood (PB) [15] and umbilical cord blood (CB) [16][17][18], peripheral blood mononuclear cells (PBMC) [19], embryonic [20][21] and induced pluripotent stem cells [22] and recently immortalised adult human erythroid line (Bristol Erythroid Line Adult BEL-A) [23]. In the last fifteen years, considerable progress has been achieved in terms of optimising the biological processes underpinning erythroid cells' expansion and maturation [24]. The selection of starting cell material has been expanded of iPSC and BEL-A cell line, providing a potentially unlimited source for *in vitro* erythroid differentiation with the flexibility to mitigate

blood-compatibility challenges. Moreover, all xenogeneic culture compounds, like serum, transferrin, insulin and growth factors have been replaced, resolving the associated risks of virus, prions and immunological complications [25][26][27][28][28]. In 2011 a mini-transfusion ( $10^{11}$  cells) of autologous CB CD34+ derived under GMP conditions mRBC was given to a volunteer [29][30] providing data and the proof of principle of mRBC feasibility for clinical use.

Despite the considerable progress in improving the expansion rate and yield of mRBC, all of these approaches lack a sufficient enucleation rate (**Table 1.1**). In other words, the efficiency of the current differentiation protocols is lower than 100% which means that the end-product is a heterogeneous mixture containing enucleated mRBC, nucleated cells that remain at earlier developmental stages as well as free-floating nuclei expelled during the enucleation process, which in *in vivo* situation would be removed by macrophages [31]. In 2008 Fujimi *et al.* reported CB CD34+ differentiation strategy providing an almost complete enucleation (99.4%) [17], however that was achieved by co-culture with macrophages, making the protocol impossible to scale-up [32].

Source	Culture period	Enucleation rate	Ref
<b>CB CD34+</b>	21 days	4%	[18]
	20 days	75-80%	[25]
	21 days	44-84%	[33]
	-	>90%	[26]
	38	99.4%	[17]
<b>PB CD34+</b>	18 days	68%	[29]
	18 days	55-95%	[34]
	21 days	63%	[35]
<b>PBMC</b>	20 days	80-90%	[19]
<b>hESC</b>	59 days	1.5-16%	[36]
	42 days	10-65%	[21]
	60-125 days	2-10%	[37]
<b>hiPSC</b>	26 days	4-10%	[22]
	60/125 days	2-10%	[37]
	52 days	20-26%	[38]
<b>BEL-A</b>	18 days	30%	[23]

**Table 1.1**

*Examples of published in vitro erythroid differentiation protocols and reported enucleation rates.*

Presence of free-floating nuclei in large quantities may prove particularly problematic in large-scale culture systems by fouling surfaces and entangling the desired cell product in DNA [39]. Most importantly, the presence of residual nucleated cells and the expelled nuclei constitute potentially harmful by-products if transfused into patients [40][41]. Undifferentiated nucleated cells can give rise to teratomas (benign tumours of differentiating cells) and teratocarcinomas (malignant metastatic tumours composed of highly proliferative cells). Thus they have to be removed from the sample and require adequate purification approaches [13][42].

As stem cell-originated mRBC progress into clinical trials and commercialisation [43], that creates new issues for bio-production and processing, requiring a re-think of the current manufacturing strategy [44]. To meet the demand for high-quality mRBC, development of bioprocesses compliant with current GMP standards and operating at satisfactory scale (ml of medium/min and millions of cells/ min) is required. To address the need for efficient and safe manufacturing processes, this project aims to develop a label-free continuous and scalable separation protocol, suitable for industrial-scale cell purification.

**1.2. Label-free markers**

The label-free description implies purification processes that do not require cell modification for detection and discrimination. The indigenous properties such as cell size and deformability (defined as the ability of a cell to change shape under applied load without cell lysis) have been recognised as promising label-free markers [45]. In many cases, alterations in cell mechanical properties are correlated with their molecular activity, such as cell cycle regulation [46], differentiation [41], immune-cell activation [47], malignant transformation [48] and disease (e.g. osteoarthritis [49] and malaria [50]). The mechanical properties of cells have been shown to be useful label-free markers of cell state. Since there is no need to add costly antibodies to reveal the label-free markers and the number of processing steps (washing and centrifugation) is reduced, they are seen as a potential route for developing industrially-viable cell enrichment approaches [51].

Cell mechanical phenotype is determined by their intracellular components and the way they interact with each other, with a particular importance given to the cytoskeleton. The cytoskeleton is a dynamic protein scaffold supporting the cell membrane and organelles,

providing spatiotemporal flexibility of cells, required to respond and adapt to their physical environment and maintain their integrity [52]. There are three main cytoskeletal building blocks: microfilaments (helical protein structures providing cell motility and governing movements of the organelles within the cell due to high speed of polymerization/depolymerisation), intermediate filaments (provide mechanical support for of cell membrane for cell-cell and cell-microenvironment interactions) and microtubules (provide resistance to external stimulus) [53]. Overall the cytoskeletal mechanical characteristic is a consequence of relative content of each cytoskeletal protein as well as filament network organisation [54].

The cell membrane has a significant mechanical characteristic at the nanoscale (deformation is not deep enough to be applicable to underlying cytoskeleton). However, in an holistic mechanical approach its function is dependent on its interaction with cytoskeleton. Additionally the cell-nucleus ratio significantly influences whole-cell mechanical properties. A large nucleus undermines the cell membrane overall stiffness, and when this is the case, cell deformability is dominated by nuclear mechanical traits [55]. A popular example are human pluripotent stem cells, where nucleus occupies most of the cell volume, and it is the defining feature of cell mechanics [56]. The nuclear mechanical properties are determined by content of lamins, proteins found in nuclear envelope, as well as chromatin architecture and compaction [57]. Lamins are an extended part of the LINC (Linker of Nucleoskeleton and Cytoskeleton) complex, which is believed to be the ultimate mechanosensory unit in cell by which transmission of forces between the nucleus and cytoskeleton are enabled, resulting in altered gene expression [58]. Studying the LINC complex led to identification of the correlation between content of the nucleoskeletal protein lamin-A, which stabilizes the nucleus, with cells stiffness [59].

Because of the increased interest in cell mechanics as separation parameter, a range of approaches have been applied to measure the viscoelastic properties of individual cells (as outlined in **Table 1.2**).

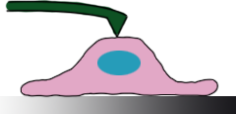
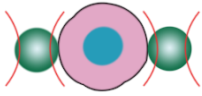
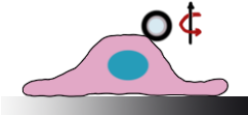
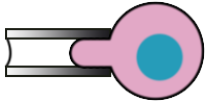
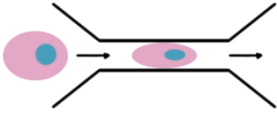
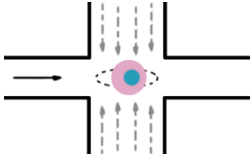
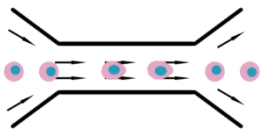
There is a variety of tools available for assessing cell deformability at a single cell level. Most of those methods (Atomic Force Microscopy (AFM), optical stretching, Magnetic Twisting Cytometry (MTC) and micropipette aspiration) operate at very low throughputs (<100 cells/min) as they rely on time-consuming, manual protocols. These approaches, developed for basic biophysics research on tens of cells, are not expected to be directly translatable to bioprocessing of heterogeneous samples. AFM, MTC and micropipette aspiration techniques probe locally on cell surface, thus the position of the probe can yield different measurements even among a single cell population. Optical stretching throughput is

limited by intense manual operation as well as limitations to the maximum applied optical force- its increase leads to significant heating of the measured sample.

The accurate characterisation of complex samples, in a statistically relevant manner, is possible by overcoming the throughput limitation with introduction of microfluidic platforms (microconstrictions, hydrodynamic cytometry, real-time deformability cytometry (RT-DC)) for high-throughput (tens-thousands of cell/ min) mechanotyping. A short processing time is valuable to minimise the physical changes introduced by prolonged incubation in processing buffers or exposure to suboptimal environment (e.g. humidity, temperature and CO<sub>2</sub> and O<sub>2</sub> content). In contrast to AFM, MTC and micropipette aspiration microfluidic platforms deform the entire cell, providing a holistic insight into cells mechanical behaviour.

Cell transit through microconstrictions is sensitive to changes in cell size and adhesiveness (softer, smaller and non-sticky cells travel faster through the constrictions). The size of constriction has to be well-matched to measured cells because small cells will pass through the constriction without deformation and too large cells will clog the channel.

Hydrodynamic approaches measure cell deformability by using fluid-dynamic stresses generated by the design of the microfluidic channel. Due to throughput reaching those of standard flow cytometers (thousands of cells / min) and contactless measurement mode, in this study, the end-product of CB CD34+ *in vitro* erythropoiesis, was thoroughly characterised by RT-DC, described further in detail in **Chapter 2**.

	Methodology	Throughput	Ref.
Atomic Force Microscopy	 <p>Using scanning probe (cantilever with a sharp tip) for poking/ touching surface of the sample with a resolution of fractions of nanometres for viscoelasticity measurement</p>	< 100 cells/ hr	[60] [61] [62] [49] [63] [64] [65] [66]
Optical stretcher	 <p>Optical stretcher is a dual-beam optical trap where a particle/ cell is trapped by optical forces generated by two opposite laser beams.</p>	< 100 cells/ hr	[67] [68]
Magnetic twisting cytometry/ tweezers	 <p>Magnetic bead is strongly attached to cell surface and by applying and manipulating magnetic field a portion of cell is twisted.</p>	< 100 cells/ hr	[69] [70] [71]
Micropipette aspiration	 <p>Applying suction pressure on a cell membrane and measuring extension into the bore of glass micropipette.</p>	< 100 cells/ hr	[72] [73] [74]
Transit through constrictions	 <p>Cells are pushed through custom-made constrictions smaller than cell size , it can be aspiration-, fluid- and electrically induced process</p>	1-100 cells/ s	[75][76] [77]
Hydrodynamic cytometry	 <p><b>Deforming cell at high strains in a stretching extensional flow filed within microfluidic device</b></p>	Thousands cells/ min	[78]
Real-time deformability cytometry	 <p>Cells are deformed by pressure gradient and shear stress in a constriction in a contact-less manner</p>	Thousands cells/ min	[79] [80] [81]



**Table 1.2**

*Summary of commonly used currently available methodologies for cell meachanotyping. The table contain the name of a technique, a graphical representation of the method accompanied by a description, throughput (a number of cell that could be assessed in a given time) as well as a selection of references, where a given method was used for assessing cell mechanical properties.*

**1.3. Traditional cell separation**

Traditionally, cell purification is performed using Fluorescent and Magnetic Activated cell sorting (FASC and MACS) and density gradient centrifugation [82] Both, FACS and MACS are well-established, commonly-used and very precise (cells are purified based on their molecular features), however, they have limited throughput (only millions of cells per hours are purified), and they are not cost-effective due to the addition of fluorescence-conjugated antibodies (immuno-labelling). Immuno-labelling is a laborious multi-step process consisting of numerous centrifugation, washing and incubation steps often resulting in a significant (reported up to 70%) cell loss [82] and post-isolation cell quality impairment [83]. Additionally, currently a limited number of fluorophore-conjugated antibody reagents suitable for clinical processing[84]. The effects of introducing these probes into patients are unknown, but it is generally recognised that they could potentially trigger immune and toxic responses, thus they have to be removed prior clinical application [85]. FACS and MACS generate highly-defined, purified cell populations with a low number of unwanted cells in the final product, however the requirement for cell-specific ligands constrains adaptation of these methods to industrial-scale processing due to the high cost of antibodies.

The most commonly used large-scale separation approach- density gradient centrifugation- makes use of the cells' physical properties such as density and size. It is a rapid process (processing time ~1 hour) with a low technical hurdle suitable for a crude debulking of large number of cells (e.g.  $1-3 \times 10^{10}$  input cells). However it is a heavily manual process, operating in batch mode, proving it challenging for automation, maintaining sterility and scaling-up. Scale-up requires a transition from batch to continuous operation, which is not easily compatible with density gradient [86].

Another golden standard in cell separation is filtration. This process removes solid particles of desired size from a liquid-solid mixture. The mixture is passed either through a filter medium or a porous membrane of defined pore size. Filters are rated based on cut-off point, which represents the size of the largest spherical glass particle (expressed in mm) that

can pass through the filter under laboratory conditions [87]. There are two approaches, dead-end filtration (where feed is passed through the filter, particles larger than cut-off point are captured on the surface of the filter creating “filter cake”) and tangential-flow filtration (considered as advanced and improved filtration, as this operates in a continuous fashion, the feed travels tangentially across the surface of the filter subsequently “filter cake” is washed away by the flowing media) [88].

Centrifugation and filtration are traditionally used methods in laboratory setting and for industrial applications. They are well-established and they serve the purpose however with a development of the biological field more sophisticated and cost-effective technologies are of interest.

#### **1.4. Microfluidic label-free separation**

Cell sorting and isolation from a heterogeneous mixture is a crucial task in many aspects of cell biology, biotechnology and medicine. Recently, there has been interest in methods allowing cell separation upon their intrinsic properties (label-free) without the need of use of biochemical labels [86][51]. In order to satisfy the increased demand for label-free sorting, as shown in **Fig. 1.1** numerous microfluidic platforms have been developed.

Label-free sorting operates based on differences in an intrinsic property of the cell to be separated including size, density, shape, hydrophobicity, net charge, sedimentation density, intrinsic hydrodynamic forces, differential magnetic susceptibility, refractive index, polarisability, membrane properties such as surface charge, cytosol conductivity, and cell deformability/stiffness [89]. Label-free sorting approaches can be further classified as (1) active- externally applied forces are used for cell manipulation and (2) passive- rely on flow characteristics determined by channel geometry.

Recently, due to their operating simplicity, accuracy, high-throughput (ml/min) and low cost, inertial focusing (IF) microfluidic platforms have gained recognition for label-free continuous passive cell separations [90]. IF devices do not use any external forces (except a pump, for injecting fluid into the device) for cell ordering and separation, as the process is determined by the channel geometry.

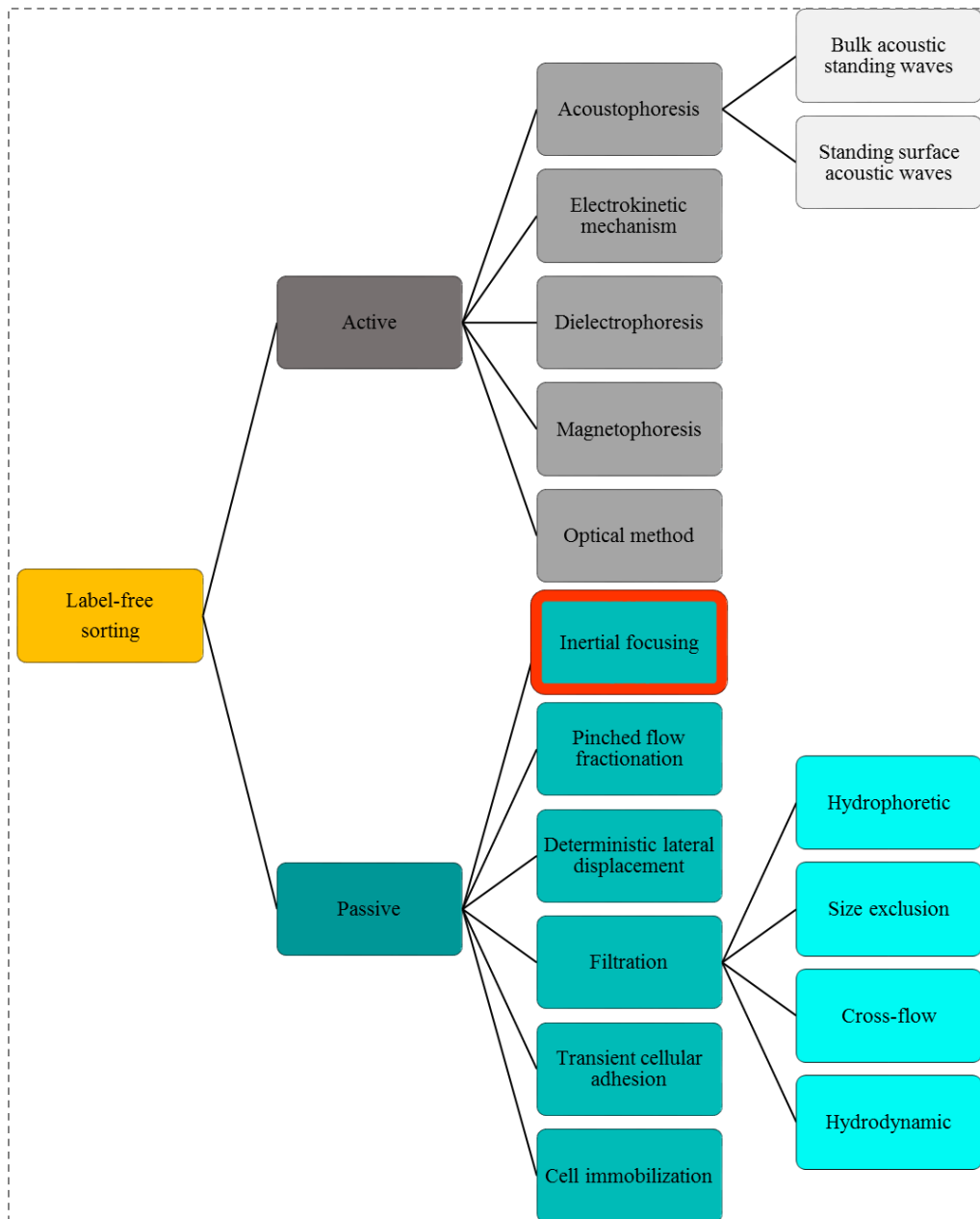


**Fig. 1.1**  
*Classification of currently available microfluidics platforms for label-free cell separation.*

## 1.5. Inertial microfluidics

Inertial focusing (IF) and ordering happen in confined channels at intermediate Reynolds number ( $1 < Re < 1000$ ), where inertia and viscous forces are finite and inertial migration and secondary flow are generated, although they remain within the laminar flow realm [91].

The channel  $Re$  is a dimensionless parameter which describes the unperturbed channel flow

$$Re = \frac{\text{Inertial forces}}{\text{Viscous forces}} = \frac{\rho U D_h}{\mu} \quad (1)$$

where  $\rho$ - is medium density,  $U$ - medium velocity,  $\mu$ - dynamic viscosity and  $D_h$  is hydraulic diameter defined as

$$D_h = \frac{2 \times H \times W}{H + W} \quad (2)$$

where  $H$ - channel height and  $W$ - channel width.

An additional dimensionless parameter- particle Reynolds number ( $Re_p$ ), which includes parameters describing both the particle and the channel, describes particle flow in a closed channel system and allows determination of a minimum particle size in relation to the channel geometry for IF to occur,

$$Re_p = Re \times \lambda^2 \quad (3)$$

where the particle confinement ratio is  $\lambda$  and

$$\lambda = a/D_h \quad (4)$$

where  $a$  is a particle diameter.

The first evidence of inertial focusing was reported in 1961 by Segre et al. [92] examining particle behaviour in a 1cm circular cross-section pipe. They noted that at sufficiently high flow rates particles are focused around the centreline (**Fig. 1.2 a**). Back then, the main postulate preached that since microfluidics systems operate at very low  $Re \ll 1$ , inertial effects are irrelevant and negligible [93].

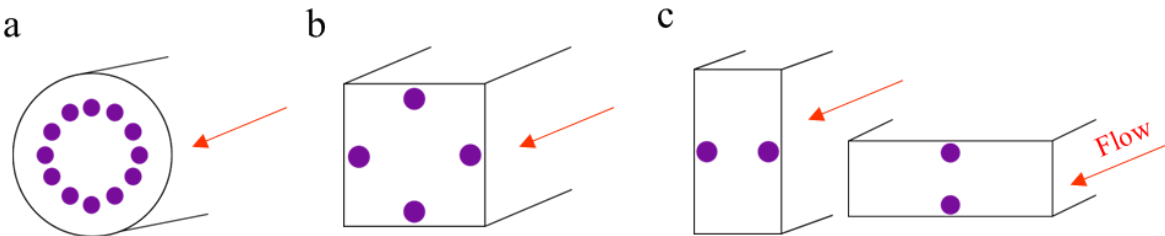


**Fig. 1.2**

*Randomly dispersed particles at given equilibrium position, following different patterns depending on the cross-section geometry. In circular channels particles equilibrate as presented in (a). In a square cross-section (b) particles are focused at four preferential symmetrical positions near the centre of each wall. When the cross-section is narrowed to rectangular shape (c), number of equilibrium positions decreases to two in the middle of the*

longest wall. It is believed that it occurs because of changes in the velocity gradient that is stronger along the shorter dimension. Red arrows indicate the direction of the flow.

In 2007, Di Carlo *et al.* for the first time demonstrated the counterintuitive contribution of inertial effects to particles ordering in a micrometre scale [94]. They studied behaviour of 2-17  $\mu\text{m}$  particles in a straight microchannel with square cross-section at  $Re_p$  ranging between 0.075 and 225. Based on their observation they tried to explain key forces contributing to the focusing mechanism in straight microchannels. As shown in **Fig. 1.3**, particles flowing through a straight channel at intermediate  $Re$ , experience asymmetric shear gradient lift force ( $F_L$ ) from the Poiseuille flow profile, which pushes the particles toward the channel walls, and a competing wall induced lift force ( $F_W$ ) repulsing particles back toward the centre of the channel.

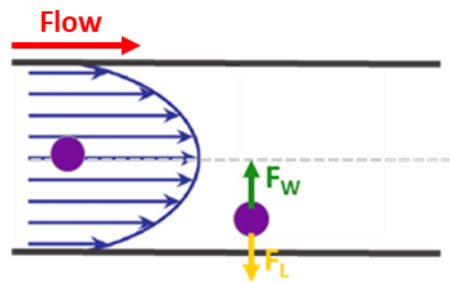


**Fig. 1.3**

*Schematic showing particle migration in a straight microchannel as an effect of balance of shear gradient lift force ( $F_L$ ) and wall-induced lift force ( $F_W$ )*

When a particle travels a distance long enough, the balance of these two forces defines particles equilibrium positions within the channel symmetric cross-section [95] (in a straight channel with a circular cross-section (**Fig. 1.2 a**)- a ring of equilibrium positions at a fixed distance from the wall, with a square cross-section (**Fig. 1.2 b**) - four preferential equilibrium positions near the centre of each wall and a rectangular cross-section (**Fig. 1.2 c**) reduces the number of equilibrium positions to two in the middle of the longest wall).

The current understanding of inertial focusing in straight microchannels with rectangular cross-section was proposed and verified experimentally by Zhou and Papautsky in 2013 [96]. As shown in **Fig. 1.4**, in this model the inertial migration process is dissected into two steps.

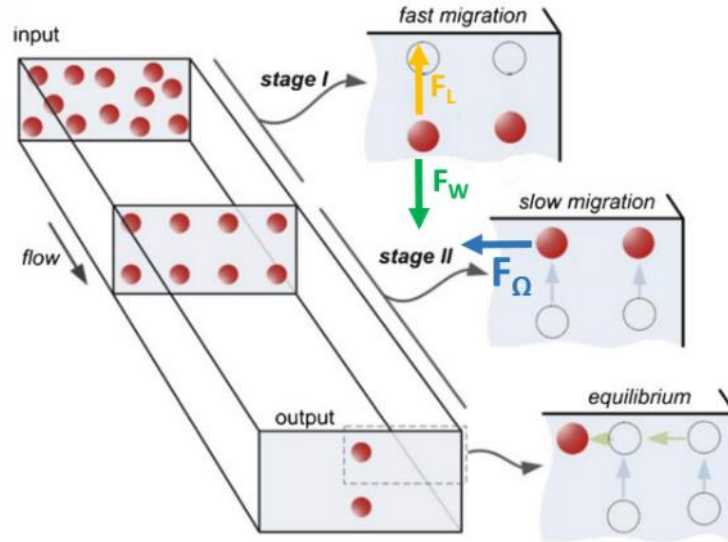


**Fig. 1.4**

Two stages inertial focusing mechanism in a low aspect ratio microchannel at intermediate  $Re$ , reproduced from Zhou, J. and I. Papautsky “Fundamentals of inertial focusing in microchannels”, *Lab Chip*, 2013. 13(6): p. 1121-32.[96], with permission from the Royal Society of Chemistry (license: 4563030210617). During stage I chaotically dispersed particles at the inlet assemble equilibrium positions near wall under the influence of shear-induced lift force ( $F_L$ ) and wall-induced lift force ( $F_W$ ). In stage II, particles migrate into wall centred equilibrium positions due to the action of rotation-induced lift force ( $F_\Omega$ )

In stage I- fast migration- particles are influenced by  $F_L$  and  $F_W$  as proposed by Di Carlo *et al.* 2007. During the stage II-slow migration- particles migrate to the centre of the channel as their motion is dominated by the rotation-induced lift force  $F_\Omega$  (due to particle rotation dictates particle motion near sidewalls). The combination of  $F_L$  and  $F_W$  is collectively called the net lift force ( $F_N$ ). Asmolov *et al.*1999 introduced a dimensionless lift coefficient ( $C_L$ ) to relate  $F_N$  to its dependent variables [97].

$$F_N = C_L \times G^2 \times \rho \times a^4 \quad (5)$$

where  $G$  is shear rate defined as

$$G = \frac{2U}{D_h} \quad (6)$$

Despite the fact that inertial focusing was observed in straight microchannels, multiple equilibrium positions hindered the application of the design. To overcome this limitation it has been proposed to add curvature to the channel [98][99][100]. The enhanced channel geometry

results in a centrifugal effect that shifts the fluid toward the inner wall, where more pressure is applied and to satisfy the mass conservation law and release the pressure, the liquid bounces off the wall in the centre and is shifted toward the outer wall, consequently a secondary flow is generated manifested in a form of two counter-rotating Dean vortices- perpendicular to the liquid main flow (**Fig. 1.5**).

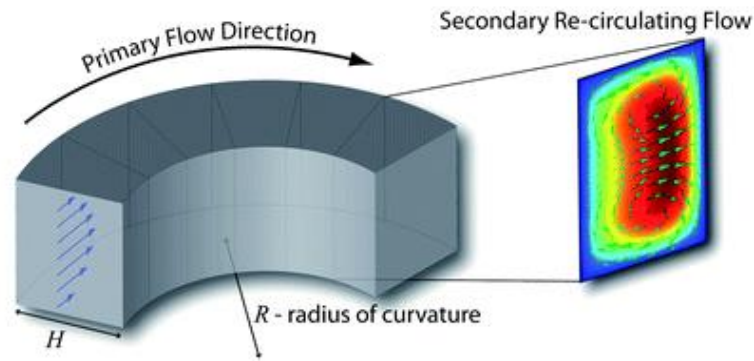


**Fig. 1.5**

*Characteristic secondary re-circulating flow (Dean flow) profile generated due to curvature of the channel. Graphic reproduced from Dino di Carlo “Inertial Microfluidics”, Lab Chip, 2009. (9): p.3038-3046 [91], with permission from the Royal Society of Chemistry (license: 4563040055452).*

Consequently, the maximum velocity at the centreline of the symmetric Poiseuille flow shifts from centre to the boundaries of the system. Particles travelling through the spiral microchannel follow the direction of Dean vortices in addition to the main stream since they experience a supplementary fluid force- the Dean drag ( $F_{DD}$ )- proportional to the net fluid velocity distributed on the particle [101]. The secondary flow can be quantified by Dean number

$$De = Re \sqrt{\frac{D_h}{R}} \quad (7)$$

Particles of different size interact with different sections of this characteristic velocity profile, moving the same direction as the velocity. As shown in **Fig. 1.6** small particles interact with the section of the Dean vortices pushing them towards inner wall, while sufficiently larger particles experience more outward velocity directing them toward outer wall [102].

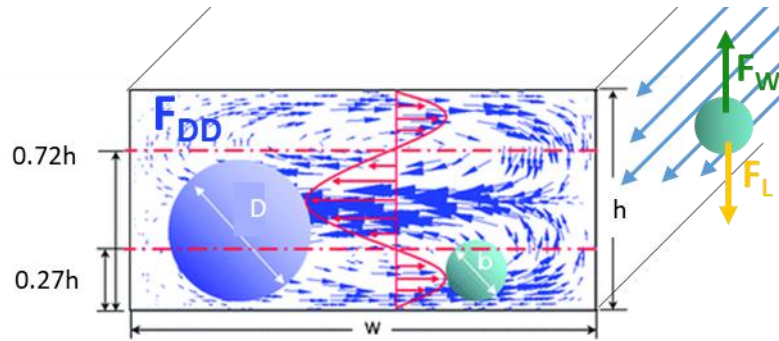


**Fig. 1.6**

*Fig. 1.6 Mechanism of size-selective separation in curved microchannels. Graphic reproduced from adapted from Yoon et.al 2009 “Size-selective separation of micro beads by utilizing secondary flow in a curved rectangular microchannel.,” Lab Chip, (9)1, p. 87–90 [102] with permission from the Royal Society of Chemistry (license: 4563050175771) . Inertial focusing within spiral microchannels occur due to balance of shear gradient lift force ( $F_L$ ), wall-induced lift force ( $F_W$ ) as well as Dean drag ( $F_{DD}$ ). Particles of different sizes (indicates as diameter  $D$ ) interact with different section of the characteristic cross-sectional velocity profile (Dean vortices).*

Both  $F_N$  and  $F_{DD}$  are a function of the fluid velocity and consequently strongly depend on the applied flowrate. Inertial focusing within spiral channels is determined by balance of  $F_N$  and  $F_{DD}$ , which in turn are influenced by a relation of channel dimensions and particle size ( $\lambda$ ). In previous research, minimum thresholds for inertial focusing in spiral microchannels with rectangular cross-section, have been empirically determined and found to be  $\lambda > 0.07$  and the  $Re_p \geq 1$  [91][103]. All forces involved in particles gathering at their cross-sectional equilibrium positions are function of particles’ size ( $\frac{F_L}{F_{DD}} \propto a^3$ ) [101] meaning that the equilibrium position predominantly depends on their size and this principle has been successfully translated for multiple applications in biological particles separation. **Table 1.3** below outlines examples of spiral channel application translated into medicine and research purpose protocols. Label-free separation in spiral microchannels, utilizing size becomes popular since it is a gentle (cell viability maintained >90%) and precise method (recover >80-85%) and is in most cases efficient (purity of target cells >80%).

Cell type/ process	Channel specifications	Process specifications	Ref.
Cell cycle synchronisation of several cell lines (HeLa, KKU-100, CHO-CD36 and hMSCs)	Spiral channel (9 loops, 40cm long, single inlet, 8 outlets) 500 $\mu$ m wide Height was fine tuned for each cell type to satisfy $a/D_h > 0.07$	Throughput: $15 \times 10^6$ cells/h Flow rate: 2.5ml/min Enrichments of cells at G0/G1: >85%	[104]



	Made of PDMS	Viability: 95%	
Focusing and ordering of HL-60 and K562 cells to facilitate deterministic single cell encapsulation in droplets	Spiral channel (5 loops, 7.2cm long), 50µm wide, 29µm high, initial radius of 1500µm Made of PDMS	Flow rate: 15µl/min	[105]
Separation of tumour cells (MCF-7 and HeLa) from spiked blood sample	Double spiral channel (12 loops: 6 loops counter-clockwise & 6 loops clockwise, one inlet, three outlets), 300µm wide, 50µm deep Made of PDMS	Throughput: $3.33 \times 10^7$ cells/min Flow rate: 350µl/min Recovery: 88.5%	[106]
Isolation of CTC from whole diluted blood (20-25% hematocrit) from cancer patients.	Spiral channel (2 loops, 10cm long, 2 inlets, 2 outlets), 500µm wide, 160µm deep Made of PDMS	Flow rate: 3ml/hr Efficiency: 88% Detection rate: 100% (cells detected in all cancer patients' blood samples, n=20)	[107]
Separation of single cells from cell clumps for murine neurosphere assay	Spiral channel (5 loops, one inlet, 8 outlets), 500µm wide, 150µm deep, initial radius of curvature 1cm. Made of PDMS	Efficiency: 75% Flow rate: 3ml/min Viability: >97%	[108]
Separation of plasma from whole blood sample ×20 diluted	Spiral channel (5 loops, 16cm long, one inlet, two outlets), 150µm wide, 50µm deep, the initial radius was 3500µm. Made of PDMS	Throughput: 700µl/min Efficiency: 38.5% Plasma purity: 99.9%	[109]
Separation of non-motile sperm cells from RBC in TESE/mTESE samples	Spiral channel (4 loops, 1 inlet, 4 outlets), 150µm wide, 50µm deep, the initial radius was 700µm Made of PDMS	Throughput: 520µl/min Efficiency: 81% for sperm cells, 99% for RBC	[110]
Separation of higher quality sperm from lower quality sperm without using sperm motility	Spiral channel (4 loops, 1 inlet, 4 outlets), 150µm wide, 50µm deep, initial radius 853µm. Made of PDMS	Throughput: 550µl/min Cell concentration: $2 \times 10^7$ cells/ml Higher quality sperm was 4 times enriched in comparison to the input	[111]
Separation and concentration of <i>Phytophthora ramorum</i> sporangia (fungal plant pathogen, Ø30µm)	Spiral channel (3 loops, 1 inlet, 2 outlets), 600µm wide, 200µm deep, the radius of curvature was 2cm on average Made of thermoplastic polymer	Throughput: 2ml/min 5.3-fold increase in pathogen content with 95% recovery	[112]

Separation of algae (sub-millimetre phytoplankton) of two specimens: <i>Monoraphium griffithii</i> from <i>Cyanothece aeruginosa</i> .	Spiral channel (3 loops, 1 inlet, 2 outlets), 350µm wide and 100µm deep, initial radius 5mm, total length ~14cm  Made of PDMS	Flow rate: 3.2ml/min  Efficiency: 77%	[113]
Isolation of blood plasma, blood sample diluted 1:20	A cascade of two spiral channels, each with 1 inlet, 3 outlets and 5 loops:  1 <sup>st</sup> : 500µm wide, 60µm deep 2 <sup>nd</sup> : 250µm wide, 60µm deep  Made of PDMS	Flow rate: f 1.25ml/min  Efficiency:  1 <sup>st</sup> : 55% of blood cells removed  2 <sup>nd</sup> : 99% of blood cells removed	[114]
Concentration of <i>E.coli</i> and 1µm beads	Spiral channels (3 loops, 1 inlet and 2 outlets):  1 <sup>st</sup> part: 10 × 24µm <sup>2</sup> cross-section 2 <sup>nd</sup> part: 10 × 60µm <sup>2</sup> cross-section  Made of glass to withstand high pressure (up to 200 bar)	Flow rate:  50µl/min (generated 70 bars)  100µl/min (generated 150 bars)	[115]
Separation of neural stem cells derived from induced pluripotent stem cells from spontaneously differentiated non-neural cells	Spiral channel (1 inlet, 8 outlets and 10 loops), 500µm wide and 160µm deep, total length ~ 50cm  Made of PDMS	Flow rate: 3ml/min  Efficiency: 2.5× enrichment of neural stem cells with 38% recovery	[116]
Enrichment of mesenchymal stem cells from bone marrow	Spiral channel (1 inlet, 8 outlets, 10 loops), 500µm wide and 160µm deep, total length ~50cm	Flow rate: up to 3 ml/min  Efficiency: the best performance at 1.6ml/min, 6× enriched, 73% recovery rate	[83]

**Table 1.3**

*Examples of published data using IF in spiral channels with a symmetrical cross-section for separating a wide range of biological samples.*

One commonly overlooked factor in IF research is the fact that biological particles, such as mammalian cells, are deformable in contrast to rigid polymer beads used in the basic studies. The first evidence of appreciating the cells' dynamic response to experienced hydrodynamic force within IF microsystems was reported by Hur *et al.* 2011 [117]. They described the joint action of  $F_N$  and deformability-induced lift force ( $F_D$ ) in straight microchannels and adapted the observation to classify and enrich cells based on deformability. In 2018, I [118] described the contribution of  $F_D$  to the focusing mechanism in spiral microchannels, demonstrating for the first time, that cells can be sorted within spiral microchannels based solely on deformability.

Year	Contribution	Ref
1960	Demonstrating IF of spherical particles at high flow rates in a circular cross-section pipe at cm scale	[92]
2007	Demonstrating inertial effect in microscale channels (straight and serpentine) for focusing, ordering, and separation of particles	[94]
2007	Proposing spiral geometry of microchannel for enhanced particles focusing and concentration	[119] [120]
2008	Demonstrating applicability of the effect of Dean vortices in spiral microchannels to differential particle focusing based on size differences	[99]
2011	Adapting straight microchannels to deformability-based particles separation	[117]
2013	Introducing two stage model explaining mechanism of inertial focusing within straight microchannel with square and rectangular cross-section	[96]
2018	Demonstrating contribution of $F_D$ to the focusing mechanism within spiral microchannels with high aspect ratio rectangular cross-sections.	[118]

**Table 1.4**

*Chronological summary of research contributions to understating and advancing IF microfluidics.*

As described above and summarised in **Table 1.4**, since the introduction of the IF in microfluidic devices for particles manipulation, substantial progress has been achieved towards understanding the governing forces and underpinning mechanisms and enhancing design of IF microfluidics. The advanced knowledge has been adapted and translated into practical applications for particles ordering and separation based on size and deformability.

## 1.6. Thesis structure

Stem cell-derived RBC are a potential supplementary source to donated blood for transfusion. However they will not become an economically viable therapeutic product unless bioprocess limitations (discussed in **Project Motivation** section) are addressed. This thesis focuses on challenges associated with formulation step of the cell therapy manufacturing process as indicated in pink dashed line in **Fig. 1.7**. In order to develop a novel, label-free purification strategy for mRBC it was first necessary to thoroughly characterise- by means of mechanical phenotyping- the therapeutic cells, to ensure most optimal solutions.

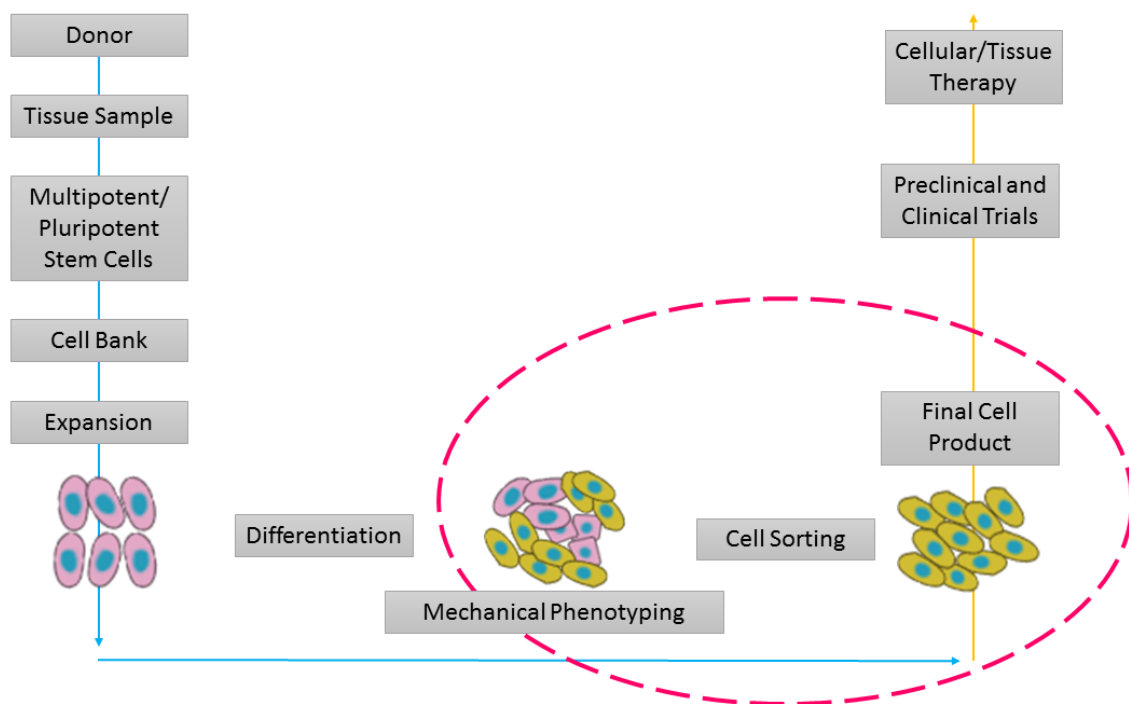


**Fig. 1.7**

*An outline of the cellular product derivation process. The dashed pink circle indicates stages of the workflow that will be addressed by this project.*

**Chapter 2** focuses on the detailed methodology used for the experimental studies. It presents the detailed procedures used universally throughout the studies, like RT-DC, microfluidic set-up and morphological and flow cytometric assays. Procedures specific for individual chapters are described accordingly in the end of each chapter.

Cost-effectiveness was one of the main assumptions for the process development. Currently, target cell purification requires addition of costly protein labels to distinguish desired cells from contaminant cellular by-products. Hence, the first step focused on finding the correlation of molecular identity biomarkers and cell mechanical properties. **Chapter 3**

describes mechanical properties of the end-product of CB CD34+ cells undergoing *in vitro* erythropoiesis and relates them to the underlying molecular and architectural changes.

Due to numerous advantages offered by IF microfluidic devices, a spiral microchannel was the method of choice for the core purification unit. **Chapter 4** investigates the contribution of deformability-induced lift force ( $F_D$ ) to the focusing mechanism within spiral microchannels, which is further translated and incorporated into a complete purification strategy for mRBC, as described in **Chapter 5**.

Throughout the course of the study some bioprocessing challenges have been identified regarding the nature of processed sample, used technology as well as processing conditions. Understanding of such issues will enable future improvements to the purification process and therefore key challenges were discussed in detail in **Chapter 6** and **Chapter 7**. **Chapter 8** offers a general summary of the presented work and indicates future directions.

## **Chapter 2. Materials and methods**

### **2.1. Cell culture**

#### **2.1.1. Cord CD34+ stem cell culture**

All methods were carried out in accordance with relevant guidelines and regulations and were approved by the Heriot-Watt Engineering and Physical Sciences Ethics Committee as well as the Heriot-Watt Engineering and Physical Sciences Biosafety Review. The cells used in this work were commercially obtained from donated cord blood and therefore consented to the research use. The CD34+ hematopoietic stem cells were primarily purchased from Stem Cell Technologies, expanded and cryopreserved after 6 days in culture using a variation of the method previously described [34]. A master cell bank from one healthy donor was created with D6 cells cryopreserved in fresh medium supplemented with 30% Knockout Serum Replacement and 10% DMSO. Cells at day 6 were resuscitated, washed and re-cultured in fresh pre-warmed growth medium: Iscove's basal medium (VWR, cat. BCHRFG0465), 5% human AB+ Serum (Sigma Aldrich, cat. H4522), 3 U/ml heparin (Sigma Aldrich, cat. H5515), 10 µg/ml insulin (Sigma Aldrich, cat. 19278) and 200 µg/ml human holotransferrin (VWR, cat. 616397-500) supplemented with 60 ng/ml recombinant human stem cell factor (SCF) (PeproTech, cat. 300-07), 5 ng/ml recombinant human IL-3 (PeproTech, cat. 200-03), 3 U/ml Erythropoietin (EPO) (clinical grade material, Roche) and 1 µM hydrocortisone (Sigma Aldrich, cat. H0888) until day 8. At day 8 cell culture medium was replaced with fresh ISHIT cell culture medium supplemented with 10 ng/ml SCF, 3U/ml Erythropoietin, 1 µM Hydrocortisone and 300 µg/ml Transferrin and cultured until day 14. At day 14, a cell count was performed using the trypan blue exclusion technique, cells centrifuged at 300g for 5 min and re-seeded in fresh culture medium containing 3 U/ml erythropoietin and 300 µg/ml holotransferrin. After a further four days of culture (day 18) cells were re-seeded in fresh medium (the same composition as day 14). Each time cells were harvested, they were transferred into a centrifuge tube (Corning, UK) and centrifuged at 300g for 5 min. All cell culture manipulations were carried under aseptic conditions in a cabinet with a laminar air flow.

#### **2.1.2. Jurkat cells**

Jurkat cells were cultured in Roswell Park Memorial Institute (RPMI) medium (ThermoFisher Scientific) supplemented with 10% (v/v) fetal bovine serum (FBS, Gibco) in a humidified incubator at 37°C in 5% CO<sub>2</sub>. Cells from the same batch were collected when at

their exponential growth phase, split into fresh cell culture flask to maintained researched conditions.

### 2.1.3. HEK cells

HEK cells were cultured in basal Dulbecco's Modified Eagle's medium (DMEM, ThermoFisher Scientific) supplemented with 10% (v/v) FBS (Gibco) and 1% (v/v) GlutaMAX™ (ThermoFisher Scientific) in a humidified incubator at 37°C in 5% CO<sub>2</sub>.

## 2.2. Real-time deformability cytometry

While there are many available well-established technologies for assessing cell mechanotype such as Atomic Force Microscopy (AFM) [121], micropipette aspiration [64], magnetic tweezers and optical stretchers [68], these methods suffer from low-throughput [122]. To assess a high number of cells (thousands of events per minute), we used a microfluidic-based Real-Time Deformability Cytometer (RT-DC) [46]. RT-DC is a contactless technique, allowing gain of thousands of events per minute, which is convenient for the global characterisation of complex samples [79]. As shown in **Fig. 2.1**, in the RT-DC set-up, a PDMS (Polydimethylsiloxane) channel consisting of three sections, two reservoir sections and one constriction channel ( $20\ \mu\text{m} \times 20\ \mu\text{m}$  or  $30\ \mu\text{m} \times 30\ \mu\text{m}$  cross section), where cells undergo deformation and measurements are undertaken.

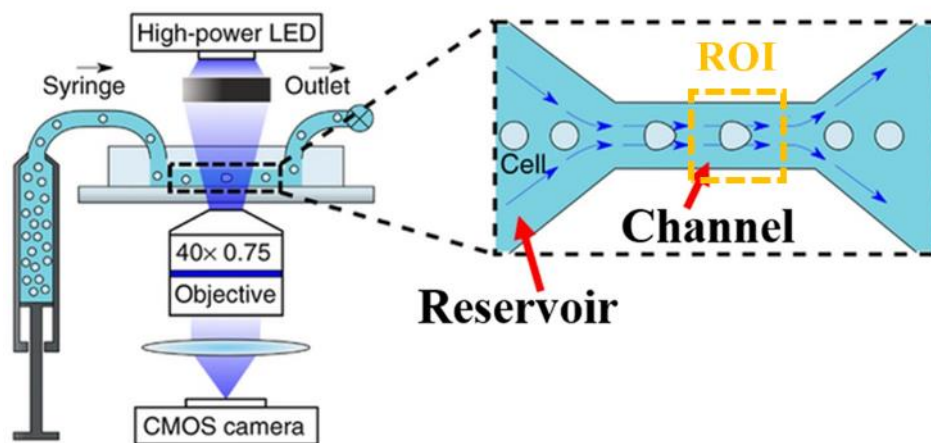


**Fig. 2.1**

*A schematic adapted from Otto, Oliver, et al. 2015 "Real-time deformability cytometry: on-the-fly cell mechanical phenotyping." Nature methods 12.3, p. 199-202 with permission from Springer Nature (license: 4563220521969). RT-DC consist of syringe pump that pumps cell suspension into a PDMS chip mounted on a microscope. Cells enter the chip through the reservoir section, next they are concentrated into a single stream by sheath fluid and enter the measurement channel where they experience deformation due to applied shear stress and*

*pressure. The degree of deformation is measured in ROI based on high-throughput real-time image analysis.*

The microfluidic chip is mounted on a microscope. A syringe pump is used to pump cells suspension in the chip, pulsing LED light enables high-speed image acquisition (4000 fps), for a standard measurements, the images are acquired at  $\times 40$  magnification. Cells are introduced in the chip through central reservoir channel and they are directed into the measurement channel by sheath flow (both flow liquid and cell carrier are viscous solution of methylcellulose). Measurement channel has a cross-section slightly bigger than the cell diameter, thus cells entering the channel experiences shear stress that causes cell deformation. The images are captured in the Region of Interest (ROI) at the end of the measurement channel and processed in real time.

The RT-DC system employs image processing algorithms which enable the measurement of cell area and deformation. Deformation ( $D$ ) is expressed as a deviation from a perfect circle

$$D = 1 - c \quad (8)$$

where  $c$  is the circularity defined as

$$c = 2\sqrt{\pi A}/l \quad (9)$$

$A$  being the projected cell area and  $l$  the cell perimeter

Deformation ( $D$ ) in the channel is independently measured from the initial cell shape and therefore any treatment-induced morphological changes to shape. Consequently, when possible, a differential deformation ( $DD$ ) parameter has been introduced [123].  $DD$  includes morphological information acquired in the reservoir section of the RT-DC chip (where applied shear is negligible) by subtracting this value from the deformation measured in the channel. Subtraction is done by statistical representations of channel and reservoir measurements and using a bootstrapping approach [123] [124].

### **2.3. Real-time fluorescent and deformability cytometry**

RT-FDC is an enhanced high-throughput (thousands of events per minute) microfluidic platform that enables mechanotype analysis of cells within a heterogeneous sample with no necessity of pre-sorting into pure populations, due to the integration of fluorescent signal for confirmation of cell identity [125]. As in the conventional real-time deformability cytometry



(RT-DC) [46], cells are deformed in a contactless manner by experiencing shear stress generated by flowing in a viscous buffer through the measurement channel which is only slightly larger than the actual cell dimensions. As shown in **Fig. 2.2**, in RT-FDC, when cells pass through the region of interest an image is acquired for the size and deformability information and in addition to the image acquisition cell is illuminated by lasers and detectors collect emitted fluorescence.

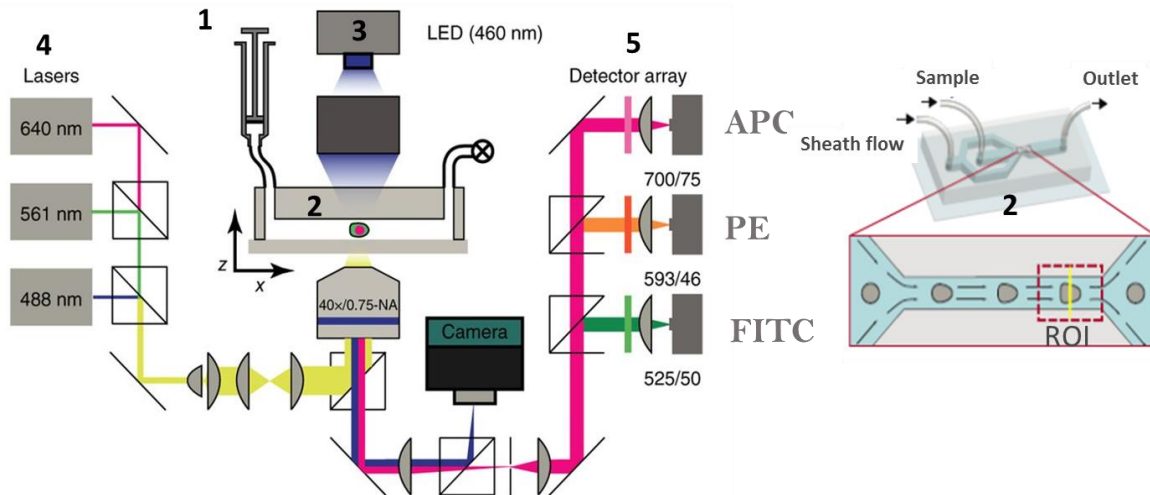


**Fig. 2.2**

*Real-time fluorescence and deformability cytometry setup (graphic adapted from P. Rosendahl et al. 2018, “Real-time fluorescence and deformability cytometry,” Nat. Methods, vol. 15, no. 5, p. 355–358 [125] with permission from Springer Nature (license: 4563220817805)). (1) Immuno-labelled cells are introduced into the microfluidic chip mounted on a microscope and while passing through the measurement channel (2) in the ROI they are imaged by bright-field microscopy (3). Information about cells size (expressed as projected cell area [ $\mu\text{m}^2$ ]) and induced by applied shear stress deformability (understood as 1- circularity) is generated by image processing in real time for each captured event and reported as a scatter plot. Additionally, cells passing through the ROI are illuminated by focused lasers (4) which excite signal detected and measured in the detector array. (5) The fluorescent signal is correlated with the acquired image, which allows cell identity confirmation.*

## 2.4. Cell morphology- cytopsin

To visualise cells’ morphology and structure, cells were transferred onto microscope slides using a cytocentrifuge then fixed and stained using Giemsa-Wright staining (Rapid Romanowsky Stain Pack, TCS Bioscience, cat. SW167/500). Cells at selected time points (D11, D14, D18 and D21) were harvested by centrifugation at 300 g for 5 min and re-suspended at  $2 \times 10^6$  cells/ml in PBS-/- (Dulbecco’s Phosphate-Buffered Saline buffer without calcium and magnesium, Gibco). 100 $\mu\text{l}$  of cell suspension was transferred into a cytocentrifuge cell

funnel and centrifuged at 450 rpm for 4 min in a cyto centrifuge (Cellspin I Tharmac, Germany) to transfer the cells onto the slide. Slides were then air-dried for 15 min, fixed and stained according to the manufacturer's instructions. After staining, slides were air-dried then fixed with DePeX mounting medium (Sigma Aldrich, cat. 06522). Slides were photographed for further image analysis either using an EOS 60D Canon camera (Canon, UK) mounted on an AXIO Scope.A1 Zeiss microscope (Zeiss, Germany) at  $\times 100$  magnification. Images were analysed in Matlab R2016b using a custom-made script or using a Canon 650d camera (Canon, UK) mounted on a Motic AE31 microscope (Motic, UK) at  $\times 40$  magnification. Images were analysed using bespoke LabView software (kindly provided by Dr Graeme Whyte, Heriot-Watt University) which detected the outline of the cells and nuclei by thresholding. The detected objects were classified into nucleated cells, enucleated cells and free floating nuclei, and the measurements of the morphological features extracted for further processing

## **2.5. Flow cytometry and FACS-staining protocol**

The end-product of the CB CD34+ differentiation protocol is a heterogeneous mixture of enucleated cell, nucleated cells (cells that did not differentiate fully, still contain a nucleus) and free-floating nuclei expelled during the enucleation process. Each population is characterised by a combination of molecular markers such as presence/absence of DNA (DNA+/ DNA-) and expression/lack of expression of Glycophorin A (CD235a+/ CD235a-). Enucleated cells are DNA- and CD235a+, nucleated cells are DNA+ and CD235a+, free-floating nuclei are DNA+ and CD235a+, however, they express lower levels of CD235a than nucleated cells. To reveal those markers cells were stained with fluorescent probes. To each 100  $\mu$ l aliquot of cells at concentration around  $1 \times 10^7$  cell/ml in PBS-/- (Gibco) supplemented with 0.5% bovine serum albumin (BSA, Sigma-Aldrich), 0.625  $\mu$ l of FITC-conjugated Mouse Anti-Human CD235a (BD, cat. 559943) and 0.5  $\mu$ l of 5 mM DRAQ5™ DNA Fluorescent Probe (BD, cat. 564902) was added to obtain a final concentration of 5  $\mu$ M. Cells were incubated for at least 20 min at room temperature in darkness. The excess fluorescent stain was not removed to prevent cell damage.

The same staining strategy was used for cell sorting by FACS (FACSAria IIu flow cytometer, Beckton Dickinson Immunocytometry Systems (BD, UK) running BD FACSDiva v6 Software. FACS sorting was performed in University of Edinburgh FACS Facility by Dr Martin Waterfall (the facility manager).

## 2.6. Microfluidic system

Throughout the course of this work, two configurations of an Archimedean spiral with six loops and rectangular cross-sections (design I:  $360 \times 60 \mu\text{m}$ , design II:  $170 \times 30 \mu\text{m}$ ), one inlet and four outlets, were used (**Fig. 2.3**). A single inlet was located at the centre of each spiral channel. The radius of the curvature (measured as the distance from a centre of the channel to the inner wall of a loop) varies between design I: 0.515 mm (loop I)- 3.805 mm (loopIV) and design II: 0.325 mm (loop I)- 1.95 mm (loop VI). The microfluidic devices were fabricated by lithography in Poly(methyl methacrylate (PMMA, Epigem, UK).

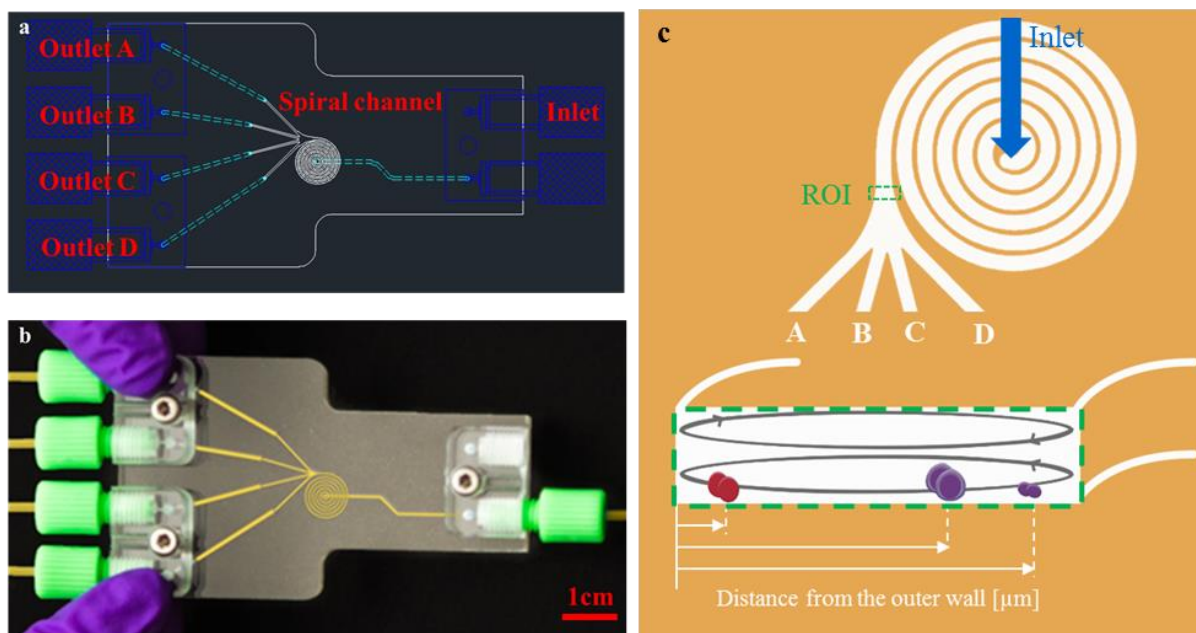


**Fig. 2.3**

(a) Schematic of the spiral channel with six loops, one inlet and four outlets for size and deformability-based separation. (b) Picture of the microfluidic chip manufactured in PMMA. (c) Cells are introduced into the system via inlet. Hydrodynamic behaviour of cells is assessed in the end of the spiral channel in the ROI and it is expressed as lateral position within the cross-section of the channel, measured as a distance from the outer wall of the channel [ $\mu\text{m}$ ].

Cell suspensions were introduced into the device with a mid-pressure syringe pump (neMESYS 1000N, Cetoni, Germany) through 1/1600 PTFE tubing of 0.5 mm internal diameter (Thames Restek, UK). Hydrodynamic behaviour of cells was assessed in terms of lateral equilibrium position (measured as a distance from the particle centre to the outer wall [ $\mu\text{m}$ ]) obtained at the end of the spiral channel by monitoring the ROI, by high-speed microscopic imaging. Images of cells inside the spiral channels were recorded either at  $\times 20$  magnification using objective with 4.9 mm free working distance (421251-9911-000 LD A-

Plan 20x Ph1, Zeiss) facilitating access to observe the channels through 2 mm thick PMMA layer. Images of cells were recorded by a high-speed CMOS camera (MC1362, Mikrotron, Germany), mounted on a microscope (Zeiss Axio Observer 3, Zeiss, Germany), at a speed of 2000 frames per second. Lateral position within the channel was recorded for more than 10000 events at three independent occasions, for each researched condition, using a custom-written program ShapeIn and quantified using ShapeOut version 0.8.4 (available at www.zellmechanik.com)

Sorting performance was assessed using the following three parameters:

$$Recovery [C]_{outlet_i} = \frac{[C_{type}]_{outlet_i}}{\sum_{i=1}^4 [C_{type}]_{outlet_i}} \quad (10)$$

of each cell type in each outlet, where  $[C_{type}]$  is the concentration of given cell type cells in a given outlet  $i$  ( $i=A, B, C$  or  $D$ ).

$$Purity[C]_{outlet_i} = \frac{[C_{type}]_{outlet_i}}{[C_{all}]_{outlet_i}} \times 100\% \quad (11)$$

indicating a fraction of each subset in a sample collected after processing, where  $[C_{all}]$  is concentration of all cell types found in the sample and

$$Enrichment\ ratio = \frac{[C_{all}]_{outlet_i}}{[C_{all}]_{inlet}} \quad (12)$$

## 2.7. Receiver Operating Characteristic (ROC) curves

Receiver Operating Characteristic (ROC) curves and Area Under the Curve (AUC) were generated using Prism GraphPad 7, to discriminate the degree of overlap in terms of properties (such as sizes, deformability, lateral positions) of events from different samples, where AUC=1 means total separation and AUC=0 means total overlap. As shown in **Fig. 2.4 a**, a ROC curve, is a graphical plot that illustrates the relationship between True Positive Rate (y-axis) and False Positive Rate (x-axis), for a given cut-off point (indicated as green ellipse and blue vertical line in **Fig. 2.4 b**). True positive rate is defined as fraction of true positives divided by total number of control events and True Negative Rate is defined as fraction of true negatives divided by all test events [126].

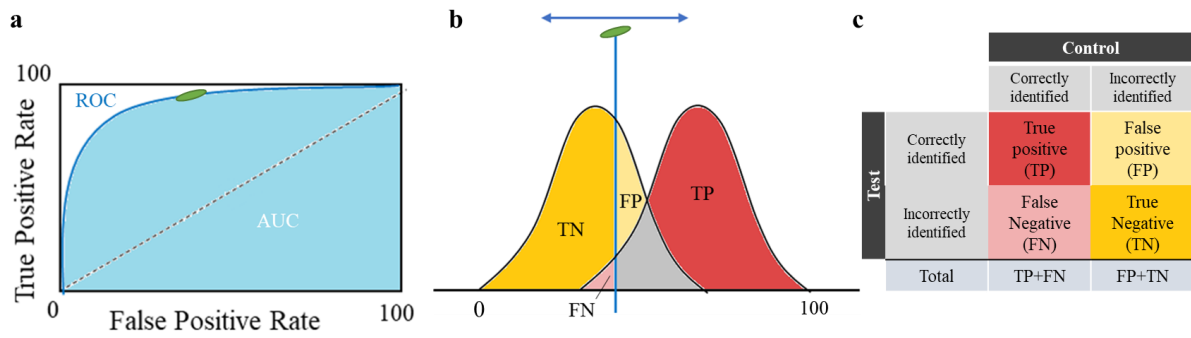


**Fig. 2.4**

*Illustration explaining Receiver Operating Characteristic (ROC) curves. (a) ROC curve is a graphical plot showing the relationship between True Positive Rate and False Negative Rate, for a different cut-off points (indicated as a green ellipse on the ROC curve) The area under the ROC curve ( AUC ) is a measure of how well a parameter can distinguish between two diagnostic groups (b) ROC curve is generated by plotting the True Positive Rate against the false Positive Rate at various threshold settings (indicated as a blue vertical line) (c) True positive rate is defined as fraction of true positives divided by total number of control events and True Negative Rate is defined as fraction of true negatives divided by all test events.*

## Chapter 3. Assessment of mechanical properties of stem cell-derived red blood cells

### Highlights

- The changing mechanical properties of umbilical cord blood CD34+ cells undergoing *in vitro* erythropoiesis were quantified in a high-throughput manner by real-time deformability cytometry for the first time.
- For each subpopulation present in the end-product of the CD34+ differentiation into mRBC (enucleated and nucleated cells as well as nuclei) a unique combination of size and deformability has been identified that could serve as label-free markers to distinguish between them.
- Distinct mechanotypes are correlated with specific morphological features, such as content of cytoskeletal protein F-actin and nucleus-to-cytoplasm ratio.

### Published work:

Ewa Guzniczak, Maryam Mohammad Zadeh, Fiona Dempsey, Melanie Jimenez, Henry Bock, Graeme Whyte, Nicholas Willoughby and Helen Bridle, **High-throughput assessment of mechanical properties of stem cell derived red blood cells, toward cellular downstream processing.**

*Sci. Rep.* **7**, 14457 (2017).

licensed under a Creative Commons Attribution 4.0 International License (<http://creativecommons.org/licenses/by/4.0/>)- please consult Research Thesis Submission form for authors contribution.

### 3.1. Introduction

Stem cell products, such as manufactured red blood cells (mRBC), require efficient sorting and purification methods to remove components potentially harmful for clinical application. However, standard approaches for cellular downstream processing rely on the use of specific and expensive labels (*e.g.* FACS or MACS). Techniques relying on inherent mechanical and physical properties of cells offer high-throughput scalable alternatives but knowledge of the mechanical phenotype is required. Deformability is emerging as a novel homogeneity marker that could serve to identify subpopulations within complex cell samples such as mRBC [127]. However, while qualitative observations have noted changes in phenotype throughout the differentiation protocol of CD34+ cells, little is known about their mechanical phenotype changes.

The *in vitro* manufacture of RBC from hematopoietic stem cells (CD34+) follows an *in vitro* protocol which is a recapitulation of *in vivo* erythropoiesis through distinct developmental stages [128][129] (for details of the protocol and the different stages involved

consult **Fig. 3.1**). Initially, the culture is expanded for the first ten days (D0 to D10) before differentiation is induced at D11, resulting in drastic cell phenotype changes during the final 11 days of differentiation.

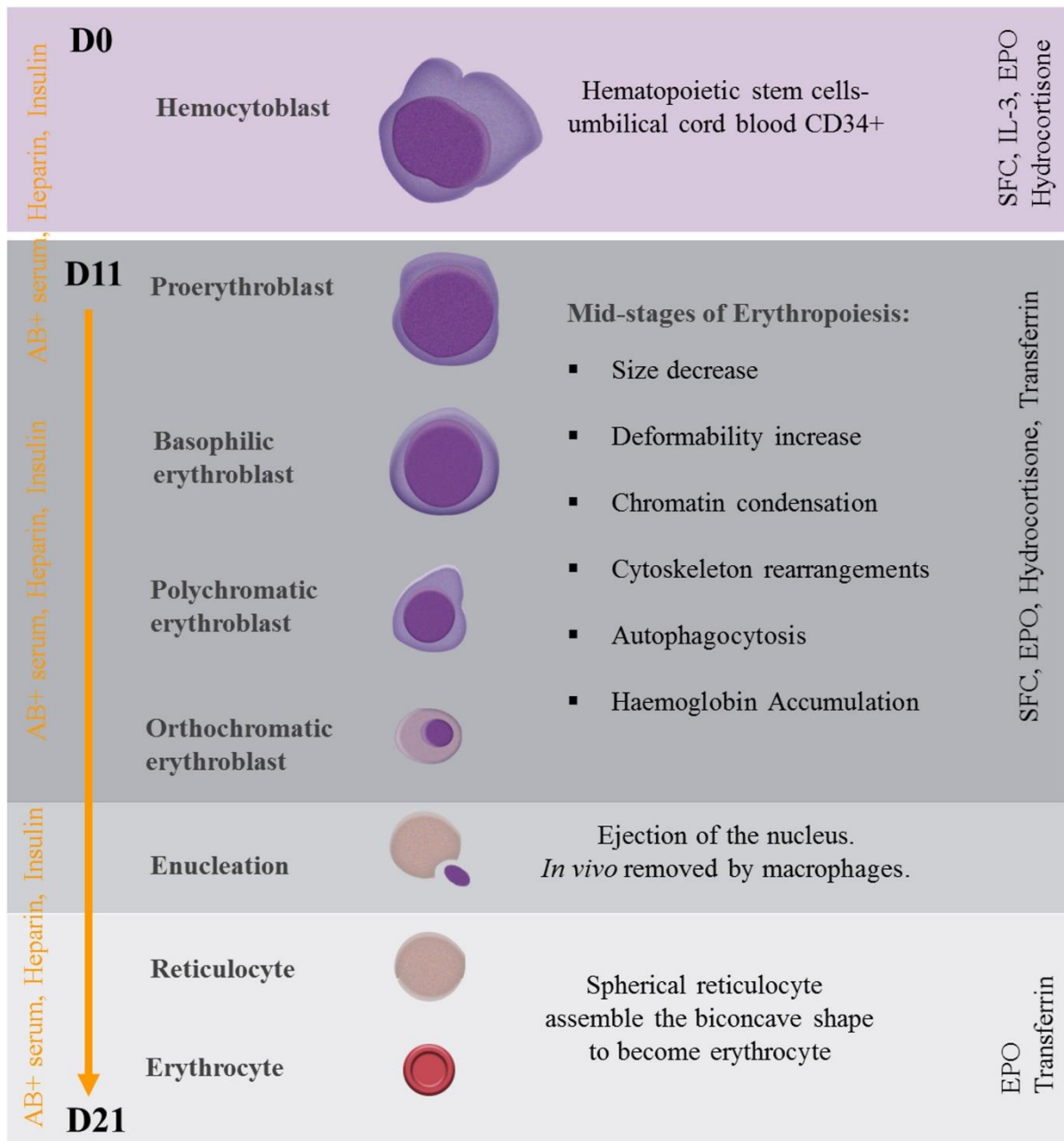


**Fig. 3.1**

*Schematic showing stem cells differentiation into red blood cells. The process starts (day 0) with hematopoietic stem cells, CD34+ subpopulation obtained from umbilical cord blood. Basal medium always contains 5% AB+ human serum, Heparin and Insulin. Over the course of the differentiation protocol cell culture medium is supplemented with different cytokines and growth factors. Those changes in medium composition push stem cell through distinct developmental stages (in vitro recapitulation of in vivo erythropoiesis). By day 18 cells lose their nuclei to become reticulocytes, which mature into erythrocytes by day 21.*

Observed changes are induced stage-wise, by adjusting cell culture medium components. The presence of biological markers at different points in the differentiation has been studied [130][37][17], underpinning the label-based separation approaches, and it is known that between D0 and D11, CD34+ cells extensively proliferate without changing their identity. Around D14 cells start producing haemoglobin and reduce their intracellular structures (the cytoplasm becomes simplified) and size. By D18, chromatin becomes compacted, cellular division slows and in the final stages, the nucleus is expelled. Based upon this, four distinct time points (at D11, D14, D18 and D21) were selected to assess the changing mechanotype of CD34+ during *in vitro* erythropoiesis to determine the potential for mechanical properties to act as a homogeneity marker upon which passive cell separation methods can be developed.

Here, I characterized, for the first time, deformability and size changes in CD34+ cells, and expelled nuclei, during their differentiation process into red blood cells at four key stages (days 11, 14, 18 and 21). This chapter provides extensive quantitative analysis of these changes, combining both high-throughput microfluidics as well as traditional biophysical characterisation. Data was collected determining the size and deformability of enucleated cells, nucleated cells and free-floating nuclei using real-time deformability cytometry (RT-DC) and bright field/fluorescent imaging. Furthermore, staining of the nucleus and cytoskeletal proteins was undertaken to investigate the potential contribution of these factors to the observed mechanotypical changes.

## **3.2. Results and discussion**

### **3.3.1. High-throughput size and deformability assessment**

CD34+ cells size and deformability at D11, D14, D18 and D21 were assessed using RT-DC for both individual and mixed populations of nucleated and enucleated cells as well as expelled nuclei. Free-floating nuclei and undifferentiated cells constitute the two main contaminants that must be removed from the sample, prior to clinical application, to leave purified mRBCs. A global view of mechanical changes using mixed populations, directly from the cell culture, is presented in **Fig. 3.2**, plotting deformation against cell area.



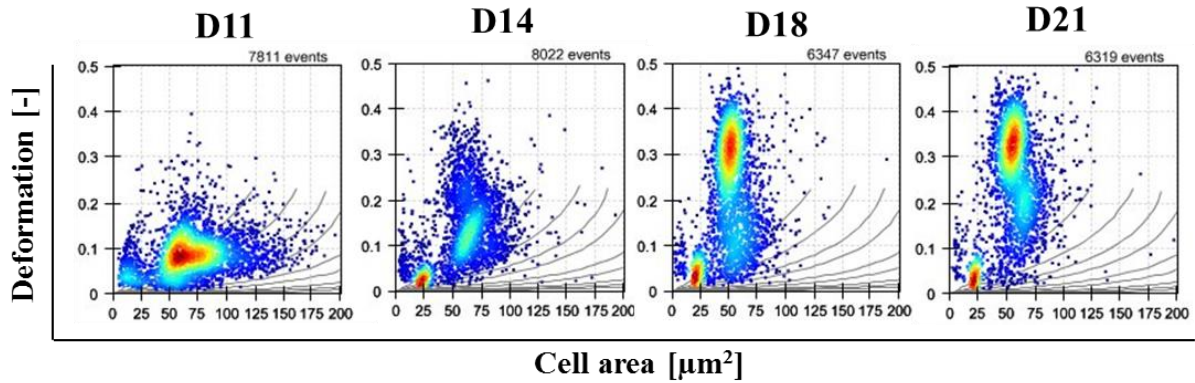


**Fig. 3.2**

Scattered plots obtained from RT-DC for CD34+ undergoing *in vitro* haematopoiesis corresponding to four time points: D11, D14, D18 and D21. Cells are flowing at 0.12  $\mu\text{l}/\text{min}$  through a 20  $\mu\text{m} \times 20 \mu\text{m}$  channel. Each dot represents a single event (the total number of collected events is displayed on the top of each diagram). Colours indicate a density scale. Grey isoelasticity lines on the scatter plots represent a predicted cell deformability for cells of the same elasticity and different size

The results indicate that as the differentiation process progresses, deformability increases while size decreases and the emergence of a greater number of different cell populations can be observed. At D11 cells are strongly heterogeneous in size (cell areas ranging between 25 and 175  $\mu\text{m}^2$ ) while deformability is low ( $< 0.2$ ). At D14 the first spontaneous enucleation events are observed characterized by a new emerging subpopulation on the deformation axis (events with deformation  $> 0.2$ ) and the reduction in cell size (very few cell areas above 100  $\mu\text{m}^2$ ). Closer to the end of the differentiation process (D18 and D21), the enucleated cell subpopulation becomes dominant (deformability  $> 0.25$ ) and another population corresponding to expelled nuclei appears (deformability  $< 0.03$ ). In *in vivo* differentiation, nuclei would be removed by macrophages [31][131].

Utilising the above data, I compared the size and deformability of enucleated and nucleated cells and nuclei at each of the time points. Firstly, I confirmed the identity of the three subpopulations by collecting data from a mixed sample as well as from samples which were sorted into pure populations by FACS and assessed using the RT-DC separately (**Fig. 3.3**). Regions corresponding to each subpopulation were therefore identified and used for analysis (using the polygon tool in the ShapeOut software) (**Fig. S2**).

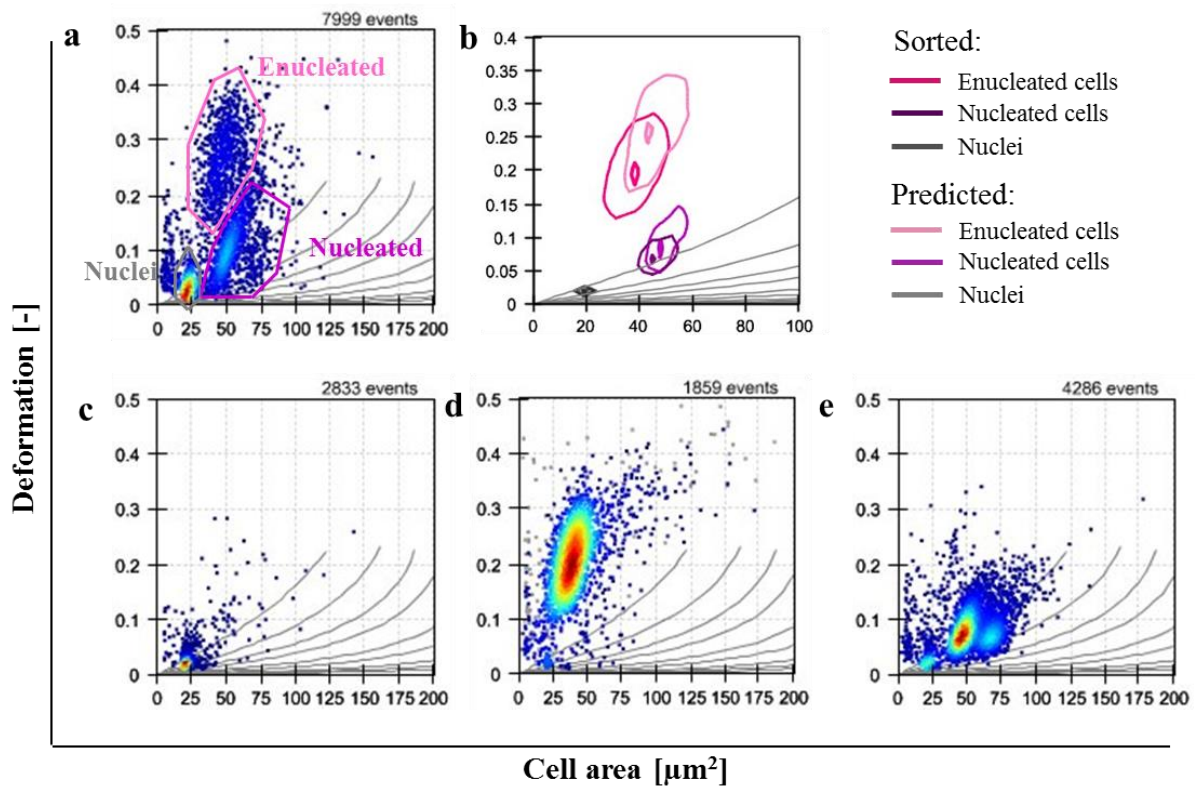


**Fig. 3.3**

*Gating strategy. Presented data was generated using RT-DC with a  $20\ \mu\text{m} \times 20\ \mu\text{m}$  cross-section channel and a flowrate of  $0.12\ \mu\text{l}/\text{min}$ . Each dot represents the measurement for one cell at D14, with the total number of events indicated on the top of each diagram. Grey isoelasticity lines on the scatter plots represent a predicted cell deformability for cells of the same elasticity and different size. On the first dot plot (a) three subpopulations can easily be distinguished, corresponding to enucleated and nucleated cells as well as nuclei. Properties for nuclei (c), enucleated cells (d) nucleated cells (e) were assessed separately on the RT-DC after being sorted into pure subpopulations by FACS. Predicted populations from (a) were gated using the polygon tool in the ShapeOut software and their contour were compared with the contour plots (b) generated for the pure subpopulations (c, d, e). The contour for each population consist of a smaller inner contour representing 50% density and a larger outer contour corresponding to 90% density.*

The populations identified from the mixed sample (**Fig.3.3 a**) correspond to the individual gated enucleated (**Fig. 3.3 d**) and nucleated (**Fig. 3.3 e**) cells and nuclei (**Fig. 3.3 c**) populations. In general, the individual populations of cells are slightly stiffer than those from the mixed population, due to the extra processing undertaken [132]. However, **Fig. 3.3 b** shows that the three different subpopulations plot in different regions suggesting that there is potential to utilise size and deformability changes as a basis for separation and sorting. Secondly, to confirm that software could utilise size and deformability differences to classify cells, events from the scatter plot of a mixed sample were analysed using a Gaussian mixture model also

identifying three subpopulations (**Fig. 3.4**), as expected from the previous gating analysis (**Fig. 3.3**).

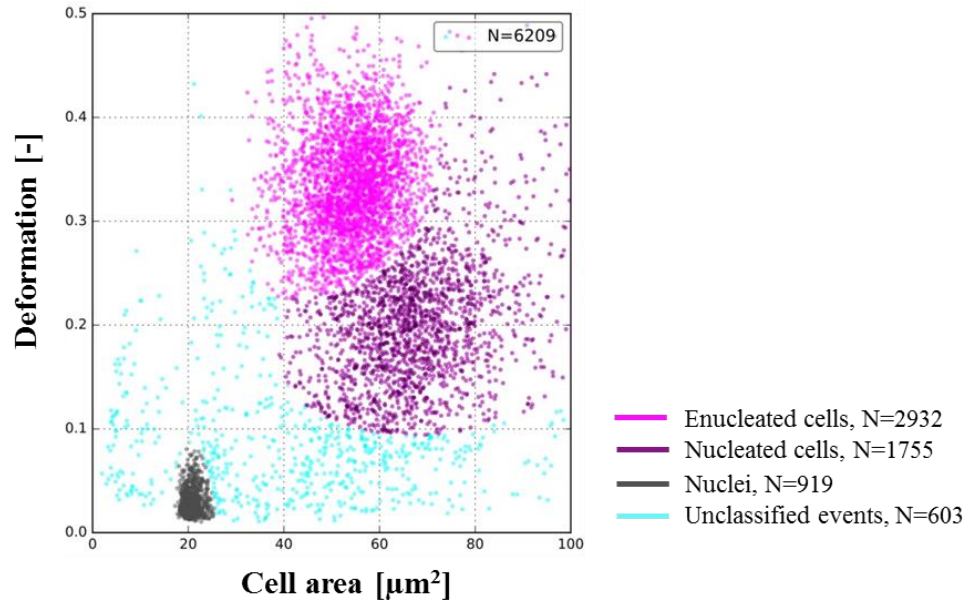


**Fig. 3.4**

By analysing raw data with a Gaussian mixture model at least three subpopulations within sample from D18 were detected and colour-coded, corresponding to nucleated (purple), enucleated cells (pink) and nuclei (grey). Remaining events (blue) are considered unclassified events, artefacts and cell debris.

To further analyse the data, box plots were generated showing the average and range of the size and deformability characteristics for each of the subpopulations. **Fig. 3.5 a** illustrates the size variation of the three populations at the selected time points (D11 only appears for nucleated cells as this is before the enucleation step). Nuclei are much smaller (with area  $22.8 \pm 3.8 \mu\text{m}^2$  mean  $\pm$  SD) than the nucleated cells (D11  $72.9 \pm 25.8$ , D14  $71.6 \pm 12.8$ , D18  $54.7 \pm 7.2$  and D21  $52.2 \pm 7.5 \mu\text{m}^2$ ) and enucleated cells (D14  $57.6 \pm 8.6$ , D18  $50.9 \pm 9$  and D21  $47.9 \pm 7.5 \mu\text{m}^2$ ) with little size overlap ( $p < 0.0001$ ). In terms of the size of cells, there is a statistically significant difference between enucleated and nucleated cells ( $p < 0.0001$ ). However, there is an overlap between events from both subpopulations.

**Fig. 3.5 b** considers the deformability differences between the three populations and demonstrates greater discrimination potential. Nuclei deformability is  $0.03 \pm 0.01$  whereas that of nucleated cells is greater than 0.1 (D14  $0.13 \pm 0.04$ , D18  $0.18 \pm 0.05$  and D21  $0.12 \pm 0.05$ ) and enucleated cells greater than 0.25 (D14  $0.26 \pm 0.05$ , D18  $0.34 \pm 0.05$  and D21  $0.33 \pm 0.05$ ) and the difference is statistically significant ( $p < 0.0001$ ). Additionally, a significant difference

in deformability ( $p < 0.0001$ ) is observed for nucleated (deformability 0.1-0.25) and enucleated (deformability  $> 0.25$ ) cells.

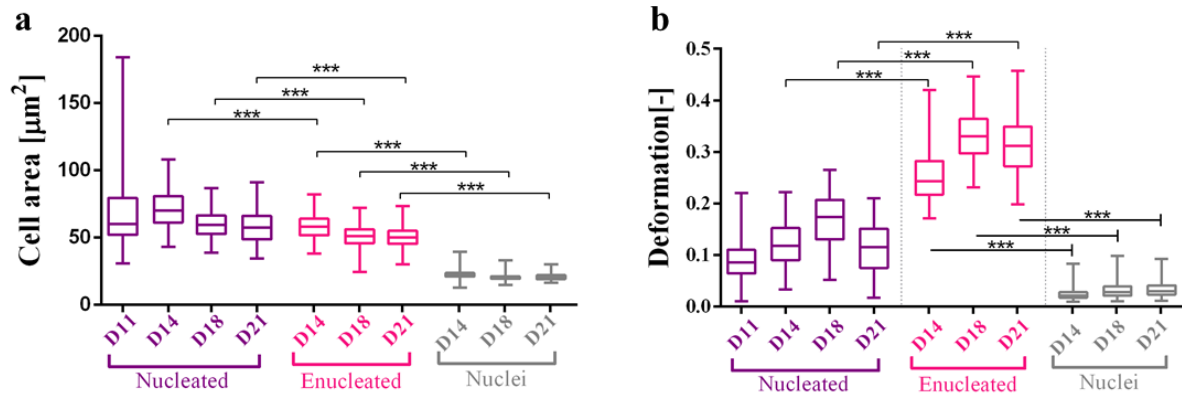


**Fig. 3.5**

Box plots summarizing (a) cell area and (b) deformation respectively. Values for each subpopulation are extracted from raw data by gating enucleated, nucleated cells and nuclei as justified in Fig. 3.3.  $P$ -values were calculated using a generalized mixed model (\*\*\*)  $p < 0.0001$ ). The line in the box represents the median and the box itself represents data from lower and upper quartile while the whiskers correspond to the lowest and highest extreme values. For summary of triplicate results please consult Appendix A.

To quantify the degree of the size and deformability overlap, receiver operating characteristic (ROC) curves were plotted and the corresponding area under the curve (AUC) calculated (Fig. 3.6). Using this approach we determined that enucleated cells are 100% separated (AUC=1) from the nuclei population in terms of size (Fig. 3.6 a) and deformability (Fig. 3.6 b). Microfluidic systems have been designed to separate particles in the same range of sizes (diameter) as nuclei (6 µm) and enucleated cells (7-10 µm) [89][51] and the data supports the potential for a size-based separation as a route for nuclei removal. Fig.3.6 a shows that within a population classified in terms of size as enucleated cells, ~20% of those cells belong to the nucleated cell population (AUC= 0.82, 0.83 and 0.75). Therefore size-based separation between nucleated and enucleated cells would be possible but would result in a significant contamination. The deformability difference between enucleated and nucleated cells (Fig. 3.6 b) is close to 100% (AUC=0.99) suggesting the feasibility of deformability to separate these populations.

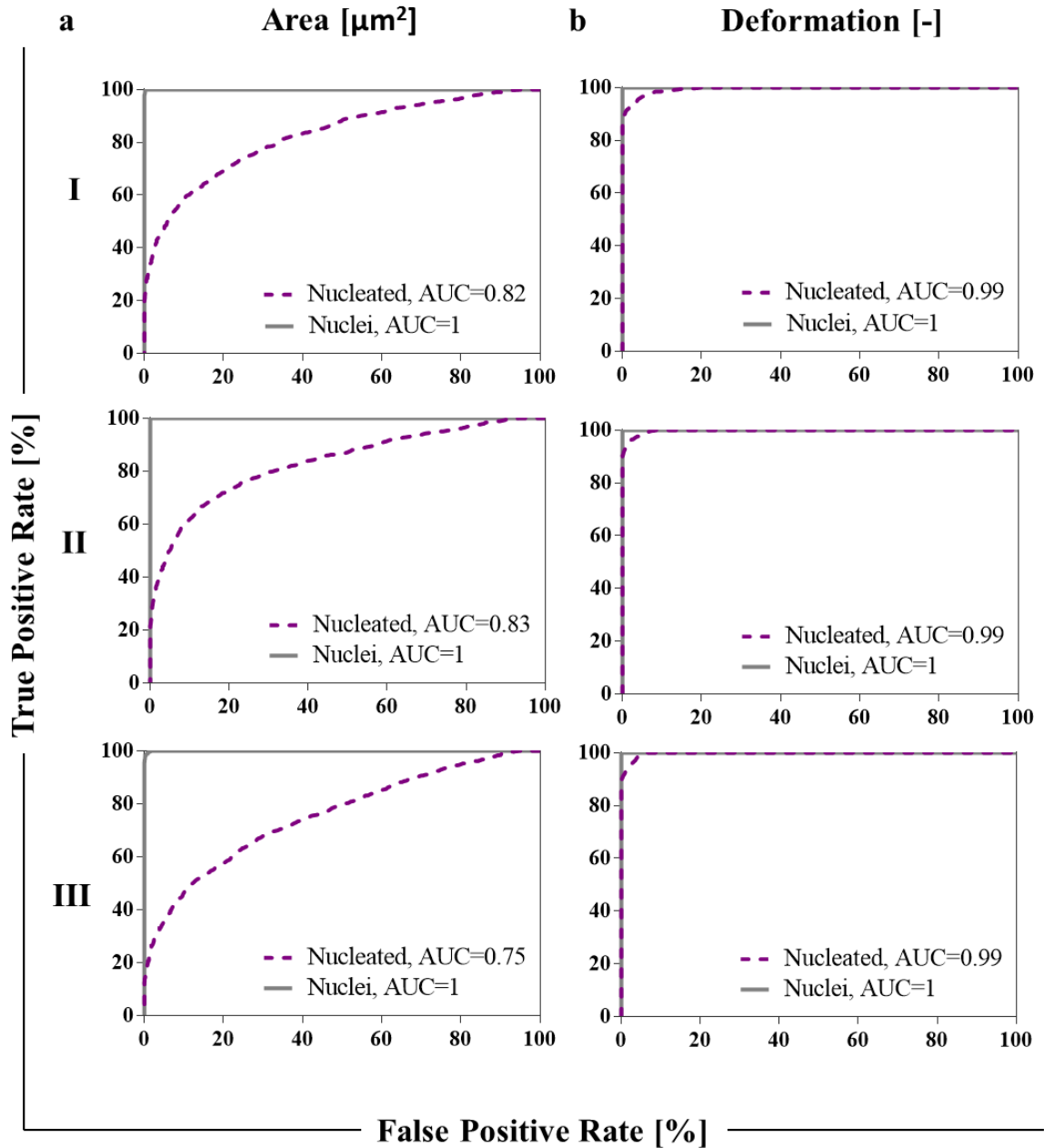


**Fig. 3.6**

Receiver Operating Characteristic (ROC) curves were plotted for (a) size (expressed as area [ $\mu\text{m}^2$ ]) and (b) deformation [-] for enucleated versus nucleated cells (purple) and nuclei (grey) at D18. The True Positive Rate is defined as the number of enucleated cells measured for a certain cut-off point (size or deformability) and divided by the total number of enucleated cells. The False Positive Rate is the corresponding number of nucleated cells (resp. nuclei) divided by the total number of enucleated cells (resp. nuclei) for the same cut-off. The Area Under the Curve (AUC) was calculated to quantify the size overlap between enucleated and nucleated cells population, enucleated cells and nuclei as well as deformation overlap between enucleated and nucleated cells and enucleated cells and nuclei populations.



### 3.3.2. Correlation between mechanotype and biology

Cell deformability is determined by the structural components of the cell, particularly the cytoskeleton [52]. The cytoskeleton is a protein network (mostly actin and spectrin in RBCs [133]) supporting the cell structure and providing mechanical integrity to the cells. This network underlies the cell membrane and connects with the nucleus by extending through the cytoplasm and plays a crucial role in the enucleation, which is a dynamic process lasting approximately 10 min [134]. During the process, F-actin and myosin filaments undergo rearrangements to facilitate the act of enucleation. Paraformaldehyde fixed cell samples were stained at D11, D14, D18 and D21 for F-actin (**Fig. 3.7 a**), one of the most abundant cytoskeletal protein, and imaged. At D11 and D14 F-actin assembles into a uniform shell surrounding the cell interior. By the end of the differentiation protocol, at D18 and D21, the shell becomes thinner and less visible with small aggregates visible, which support the observed softening of nucleated cells between those days.

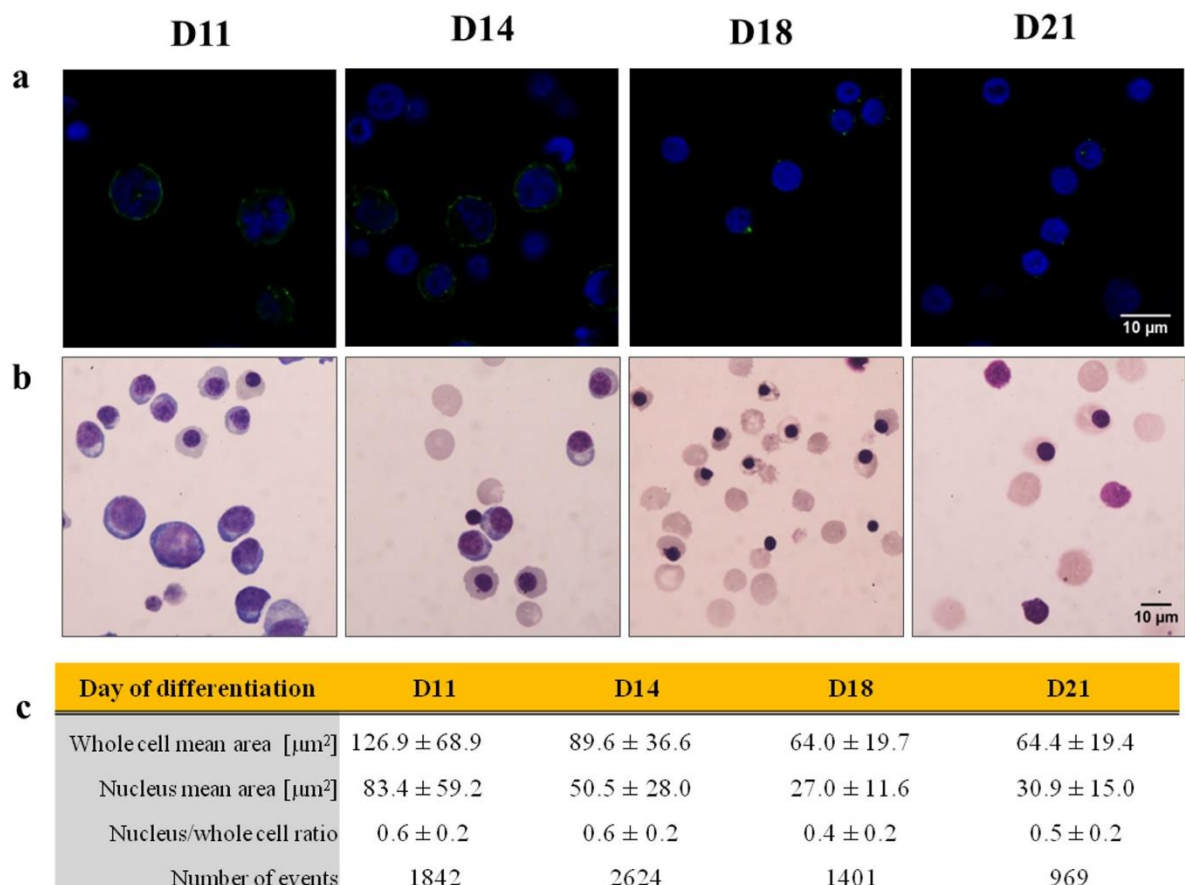


**Fig. 3.7**

*To visualise changes in cell morphology over the course of the differentiation procedure (Day 11, 14, 18 and 21) (a) cytoskeletal protein F-actin (green) and nuclei (blue) were stained with fluorophores and (b) cytoplasm and nuclei were stained with Romanowsky stain. Scale bars represent 10  $\mu\text{m}$ ; (c) cytospin images of Romanowsky's stained cells were analysed using*

*Matlab for cell and nucleus area (mean  $\pm$  SD) and nucleus/ whole cell ratio were calculated (mean  $\pm$  SD).*

Observed thinning is in agreement with literature evidence, where cytoskeletal protein levels were quantified by Western Blot [128]. It was reported that actin is downregulated during erythropoiesis with  $\alpha$ -spectrin and  $\beta$ -spectrin expressed in higher quantities. Together, those rearrangements are believed to be an adaptation of RBCs to change their shape under the applied stress they experience during the vascular circulation, without haemolysis. The lack of a nucleus is the main feature providing optimal cell deformability for oxygen transfer in tissues [135]. The presence of a nucleus, its changing characteristics and eventual expulsion throughout differentiation, could contribute substantially to the overall cell mechanical behaviour [56].

The contribution of the nucleus to the mechanotype is determined by its relative size [136]. To assess the nucleus/whole cell ratio, cytopsin cell slides prepared at D11, D14, D18 and D21 were stained with rapid Romanowsky stain and visualised using a bright field microscope (**Fig. 3.7 b**). Approximately 1000 events per condition were analysed and results are presented in **Fig. 3.7 c**. Nuclei become smaller over time and at D11, on average, they constitute around 60% of the cell. The cytoplasm becomes simplified at later days and the nucleus is more compacted and smaller (50% for D14 and 40% for D18).

We further explored the contribution of nuclei to the mechanical behaviour of cells by looking at cell elongation within the RT-DC microfluidic device under shear stress (**Fig. 3.8 a and b**). In the RT-DC system, cells first pass through a reservoir section before being forced through a smaller channel where a sheath flow induces a shear stress on the cells (**Fig. 2.1**). As presented in **Fig. 3.8**, the y-axis for enucleated and nucleated cells is larger than nuclei in the reservoir. When cells enter the main channel, the nuclei y-axis remains unchanged while the enucleated y-axis is shortened and the nucleated y-axis remains above the length of the nucleus. The presence of the nucleus seems therefore to constitute a barrier to the capability of a cell to deform under shear stress.

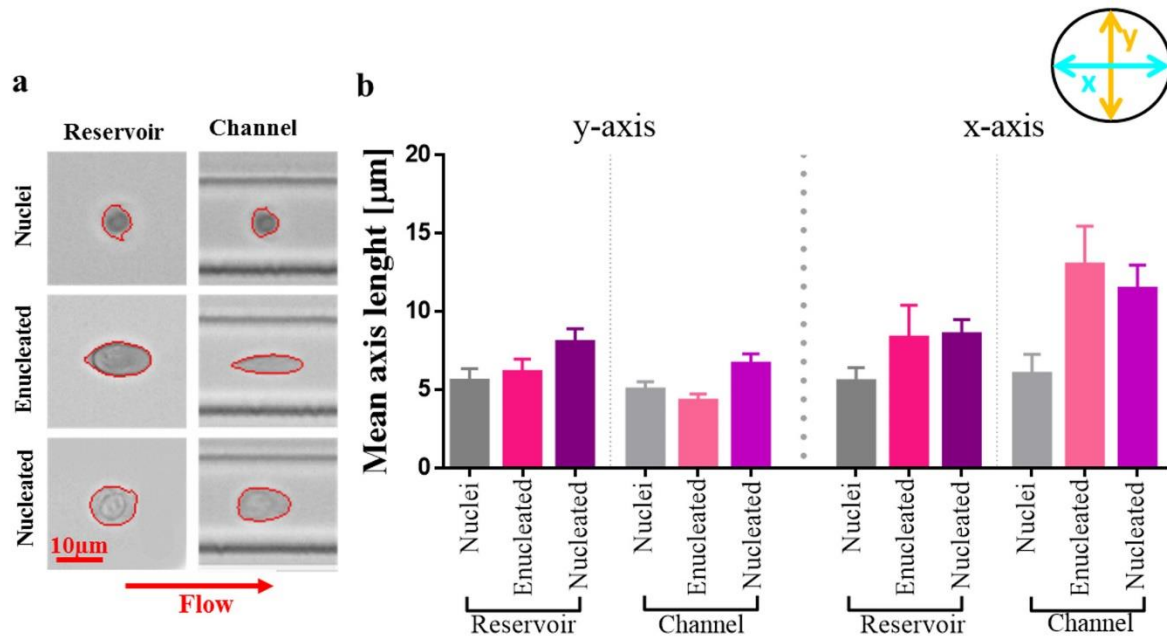


**Fig. 3.8**

Cells at D14 were sorted on FACS into enucleated, nucleated cells and nuclei populations. Their minor and major axis ( $y$  and  $x$  respectively) were assessed by RT-DC image analysis. (a) Measurements were captured in both the reservoir (with negligible degree of shear stress) and in the channel ( $20\ \mu\text{m}$  width) where shear stress exerted on cells causes them to deform from their original shape. (b) Changing  $x$ - and  $y$ -axis length for pure populations, in the reservoir and in the channel, were captured. Bar graph represents mean axis length with error bars showing SD from the mean.

To verify if it would be possible to separate enucleated and nucleated cells based on the degree of deformation they undergo under hydrodynamic stress, the length of the  $y$ -axis of enucleated and nucleated was compared. The measurement was obtained in the reservoir section of the device where cells experience shear stress and by creating a ROC curve and calculating the  $\text{AUC} = 1$  (Fig. 3.9) we see that there is no overlap in the  $y$ -axis length. Deformability and size are coupled and the cell size, revealed by their original shape change under applied stress, could constitute a basis for cell separation (e.g. by passing through a filter with a cut-off size smaller than the length of  $y$ -axis for nucleated cells).



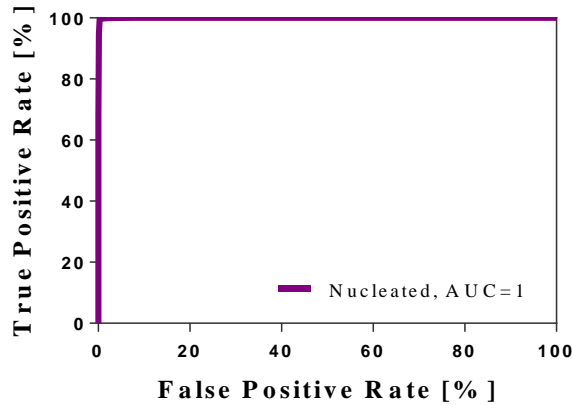


**Fig. 3.9**

Receiver Operating Characteristic (ROC) curves were plotted to compare enucleated and nucleated cells y-axis overlap (Fig. 3.8). The True Positive Rate is defined as length of y-axis for number of enucleated cells measured for a certain elasticity cut-off point and divided by the total number of enucleated cells. The False Positive Rate is the y-axis of corresponding number of nucleated cells divided by the total number of enucleated cells for the same cut-off. The Area Under the Curve (AUC) was calculated to quantify the overlap between the measured length of the y-axis for enucleated and nucleated cells.

### 3.4. Conclusion

Regenerative medicine, and cell therapy, in particular, are seen as a potential route to revolutionize medicine and to improve healthcare for patients who currently have either limited or no treatment options. The *in vitro* produced RBC are seen to address needs in transfusion medicine.

For the wide-spread adoption of mRBC, and indeed other cell therapies, challenges related to cell source, maturation and viability need to be addressed by biologists, while advancements in cell processing technologies will be required to manufacture those cells in meaningful quantities and achieve satisfactory purity. Label-free separation techniques based on mechanical phenotype differences offer a promising route to large-scale purification. However, to design optimal downstream processing protocols we first need to understand the mechanical characteristics of subpopulations within the samples, how these relate to molecular and architectural changes and how those changes evolve with cell-state and progressing differentiation protocols. Thus, here I characterised the mechanical properties (size and deformability) of CD34+ cells from cord blood as they undergo *in vitro* erythropoiesis. Cell size and deformability are highly dynamic features, significantly changing during the differentiation process. Based on the observations, using novel high-throughput techniques

(RT-DC), cells become smaller and softer between D11 and D18 as different cell subpopulations emerge. The staining results, linked with data from the literature, suggest that this phenomenon is driven by changes in the nucleus properties, which is expelled towards the end of the protocol, coupled to morphological changes in the cytoplasm and cytoskeleton.

Several key findings emerged from our mechanotype analysis. Firstly, there is no overlap between the sizes of the nuclei and the cells (both enucleated and nucleated). Data confirmed a 100% separation for both size and deformability. It could, therefore, be possible to design label-free systems to remove the nuclei exploiting the 2  $\mu\text{m}$  difference in the average diameter of the cells and the nuclei at D18, a size at which there is plenty of evidence in the literature for successful separation approaches targeting different applications [51].

Secondly, since the data showed a significant overlap of the enucleated/ nucleated cell populations in terms of size, the cell mechanotype marker of size might thus not be practical. Thirdly, we demonstrated a significant difference in deformability (from ROC curves AUC=0.99) between the enucleated/ nucleated cell populations. In order to purify enucleated cell from nucleated cells, methods which exploit observed differences in deformation under shear stress could be utilised.

Overall, this study provides the first quantitative information regarding the mechanotype of CD34+ cells undergoing *in vitro* differentiation into mRBC, which could assist in the design of robust label-free purification approaches.

## **3.5. Materials and methods**

### **3.5.1. Flow Cytometry**

Cells were assayed for expression of CD235a (Glycophorin A) and for the presence of a nucleus using flow cytometry during differentiation. At each control time point: day 11, 14, 18 and 21 (D11, D14, D18 and D21), cells were collected and counted, centrifuged at 300 g for 5 min and re-suspended in basal medium supplemented with 0.5% BSA at a concentration of  $1 \times 10^7$  cells/ml and fluorescently stained as per **materials and methods Chapter 2**. Cells were analysed on a BD FACSCalibur within two hours of staining and raw data analysed using FlowJo V10 CL. The same staining strategy was used for cell sorting by FACS (FACS Aria IIu flow cytometer, Beckton Dickinson Immunocytometry Systems (BD, UK) running BD FACSDiva v6 Software.

### **3.5.2. Mechanotype Characterisation- Real-Time Deformability Cytometry**

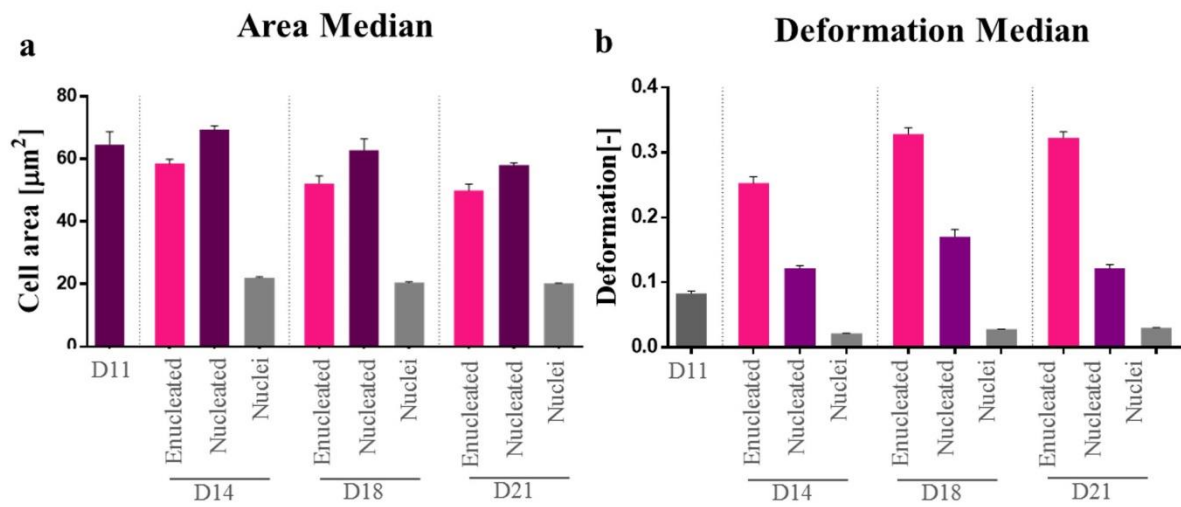
Cells size and deformability changes were assessed using a Real-Time Deformability Cytometer (RT-DC). Measurements were performed as described in Nat. Methods 2015 [46]

and **Chapter 2**. In this work, a PDMS chip with a  $20\ \mu\text{m} \times 20\ \mu\text{m}$  cross-section channel was used. Prior to measurements, cells were harvested by centrifugation at 300g for 5 min and resuspended in a 0.05% methylcellulose solution at  $1\text{-}2 \times 10^6$  cells/ml. Cells were pumped into the channel at 0.12  $\mu\text{l}/\text{min}$ . RT-DC data were analysed using original RT-DC software ShapeOut 0.6.9 (available at [www.zellmechanik.com](http://www.zellmechanik.com)). Using the polygon tool built in the software, area and deformability values were obtained separately for day 11, 14, 18 and 21 as well as for separate subpopulations (enucleated cells, nucleated cells and nuclei). Data were then extracted from the software and further analysed using MatLab R2016b and GraphPad Prism 7. The significance of the results was calculated using a standardized mixed model that assumes non-normal distribution with three replicas of each experiment (**Appendix A**). The receiver operating characteristic curves were generated and the area under the curve was calculated using a customised MatLab script (MatLab R2016b).

### **3.5.3. Widefield Microscopy**

To study the cytoskeletal changes in CD34+ cells undergoing *in vitro* erythropoiesis, cells at day 11, 14, 18 and 21 were fixed in 4 % paraformaldehyde (PFA) (ThermoFisher Scientific, cat. 28906) and imaged using a widefield microscope Olympus IX-81 TIRF+ with a x150 1.4 NA immersion oil lens and EMCCD camera (Hamamatsu, UK). First cells were stained for 30 min at room temperature against F-actin with Actin Green 488 Ready Probes reagents (Life Technologies, cat. R37110) then cells were transferred onto poly-D-lysine hydrobromide (Sigma Aldrich, cat. P6407, UK) coated cover slips to attach. Two minutes before the end of the incubation time, Hoechst 33342 (Sigma Aldrich, cat. 14533) was added to a final 10 ng/ml concentration. After 2 minutes the cover slip was gently washed with PBS -/- to unattached free-floating cells. Twenty stack images per differentiation day (D11, D14, D18 and D21) were collected. Obtained stack images were deconvoluted with the Huygens Professional software.

## Appendix A



Area		D11	D14 enucleated	D14 nucleated	D14 nuclei	D18 enucleated	D18 nucleated	D18 nuclei	D21 enucleated	D21 nucleated	D21 nuclei
Median	Mean	64.63	58.57	69.43	22.10	52.23	62.87	20.43	49.90	58.00	20.27
	Std. Deviation	4.12	1.36	1.16	0.17	2.33	3.56	0.29	2.07	0.78	0.06
25% Percentile	Mean	54.43	52.48	61.07	20.97	47.27	56.17	19.60	45.24	48.97	19.33
	Std. Deviation	2.50	1.43	0.49	0.25	2.28	3.68	0.17	2.04	1.91	0.06
75% Percentile	Mean	83.60	64.55	80.07	23.67	57.27	70.10	21.67	54.73	66.40	22.20
	Std. Deviation	3.68	0.83	0.97	0.15	1.94	3.45	0.42	2.01	1.21	0.20

Deformation		D11	D14 enucleated	D14 nucleated	D14 nuclei	D18 enucleated	D18 nucleated	D18 nuclei	D21 enucleated	D21 nucleated	D21 nuclei
Median	Mean	0.08	0.25	0.12	0.02	0.33	0.17	0.03	0.32	0.12	0.03
	Std. Deviation (%)	0.33	1.00	0.40	0.05	1.02	1.15	0.04	0.93	0.59	0.03
25% Percentile	Mean	0.06	0.22	0.09	0.02	0.29	0.13	0.02	0.28	0.08	0.02
	Std. Deviation (%)	0.34	0.60	0.28	0.03	1.21	0.97	0.01	0.91	0.49	0.03
75% Percentile	Mean	0.11	0.29	0.16	0.03	0.36	0.20	0.04	0.36	0.16	0.04
	Std. Deviation (%)	0.35	1.10	0.56	0.14	0.85	1.33	0.10	0.87	0.67	0.03

Presented bar graphs show mean of area (**a**) and deformations (**b**) medians for three replicas of the RT-DC measurements for cells at D11 and enucleated, nucleated and nuclei populations from D14, D18, D21. Populations were identified from mixed samples by the gating scheme as described in the main body of the text. Error bars represent standard deviation from the mean. All measurements were performed in three replicas for cells at the same days of differentiation protocol. Cells come from three separate batches, from the same master bank created for one donor. Tables (**c**) and (**d**) show averaged medians for cell area and deformability values obtained at three separate occasions. Because deformation values are small, the SD is represented as % for the easiness of reading.

# Chapter 4. Understanding contribution of deformability-induced lift force to cells focusing in spiral microchannels

## Highlights

- A novel additional force, deformability-induced lift force ( $F_D$ ), involved in the cell focusing mechanism within spiral microchannels has been investigated and reported for the first time.
- The effect of  $F_D$  has been studied using a customised cellular deformability model consisting of cells of the same size and five degrees of gradually changing deformability.
- The effect of  $F_D$  is revealed at sufficiently elevated flow rates and it has been successfully applied for efficient deformability-based cells separation in spiral microchannels.

## Published work

Presented data was partially published as referred conference papers:

- (1) E. Guzniczak, M. Jimenez, H. Bridle. **Fluid flow in curvilinear microchannels for stem cell purification- understanding the deformability-induced lift force**, *German Physical Society annual meeting*, 11-15 March 2018, Berlin, Germany- selected as top 10 research posters.
- (2) E.Guzniczak, M.Jimenez, O.Otto, N. Willoughby, H.Bridle. **Deformability-induced lift force in curvilinear microchannels for stem cell-derived product purification**. *Micro Total Analysis Systems ( $\mu$ TAS) Conference* 10-15 Oct 2018, Kaohsiung, Taiwan. [118]

## 4.1. Introduction

Separation of cells based on their indigenous properties, such as size and deformability (cell shape change as a response to applied load), have been recognised as a viable alternative to conventional techniques (e.g. FACS and MACS) [51][89]. This is especially true for novel cellular therapeutics, where the final products are not traditional biological molecules (e.g. monoclonal antibodies), but cells themselves (e.g. stem cell-derived red blood cells) [86]. Label-free biomarkers are cost-effective since there is no need to add costly antibodies to reveal cell identity markers and number of processing steps (staining, washing) is reduced [137]. Cell sorting is often used to enrich or purify cell samples into well-defined populations and recently various microfluidic platforms such as acoustophoresis, magnetophoresis, dielectrophoresis and passive sorting (inertial focusing (IF), pinch flow fractionation, deterministic lateral displacement and filtration) have been used for continuous label-free separation [51]. IF in

spiral microchannels represents one of the passive techniques used to manipulate cells on the microscale without an externally applied force [91]. Due to simplicity in operation, low manufacturing cost and proven scalability by parallelisation (millions of cells per minute) IF is considered as a very attractive approach for developing high-throughput industrially-viable processes for large-scale cell enrichment [138].

Traditionally, fluid flow in microscale confined channels has been associated with a negligible inertia since fluid flow in microchannels occurs at low Reynolds numbers [95]. However previous work has shown useful physical phenomena occurring at commonly neglected intermediate flow regimes within spiral microchannels, namely secondary flow and IF [91]. Both of them are determined by channel geometry, particle size and applied flow rate. The interplay between fluid flow pattern and particles, if fine-tuned, leads to particles ordering, i.e. focussing into particular cross-sectional positions; separation based on size has been demonstrated and the effect has been exploited for myriad applications in point-of-care and clinical diagnostics as discussed in **Chapter 1**. However, biological particles due to their deformable nature add complexity to the focusing mechanism.

This chapter presents an investigation of the contribution of the deformability-induced lift force ( $F_D$ ) to the mechanism of inertial focusing in a high aspect ratio spiral microchannel with rectangular cross-section. In order to study the phenomena of deformability as a migration mechanism, a cellular model of deformability has been derived. Cells of the Jurkat cell line were chemically treated to gradually change their deformability without alterations in the cell size. Treated cells were analysed using a high-throughput phenotyping technique, namely real-time deformability cytometry (RT-DC), and that lead to identification of five optimal conditions within the cellular deformability spectrum (from stiff to soft), which were used to research  $F_D$  in spiral channels. For the first time, it has been demonstrated that biological particles of the same size can be separated in spiral microchannels based on difference in deformability only.

## 4.2. Theoretical background

Inertial focusing and ordering happen in microscale confined channels at intermediate Reynolds numbers ( $Re$ ), as defined in **Equation (1)**, where inertia and viscous forces are finite and inertial migration and secondary flow are generated although they remain within the laminar flow realm [95].

Particles travelling within a spiral microchannel channel experience an asymmetric shear gradient lift force ( $F_L$ ) from the Poiseuille flow profile, which pushes the particles toward the channel walls, and a competing wall induced lift force ( $F_W$ ) repulsing particles back toward the centre of the channel [91][96]. Additionally, due to the curvature of the channel, centrifugal forces create a secondary flow, manifested in a form of two counter-rotating Dean vortices perpendicular to the liquid main flow [99]. The secondary flow can be quantified by Dean number, defined in **Equation (7)**.

When a particle travels a sufficiently long distance, the balance of the net inertial lift force and the De force defines particles equilibrium positions within the channel cross-section [100]. Although the dynamics of internal focusing have been proven to depend significantly on size, it has been demonstrated that solid elastic particles flowing in a straight microchannel in Poiseuille flow, experience additional deformability-induced lift force ( $F_D$ ) that pushes them away from the channel wall [117]. As shown in **Fig. 4.1** softer particles are positioned closer to the channel centre in comparison to their more rigid counterparts.

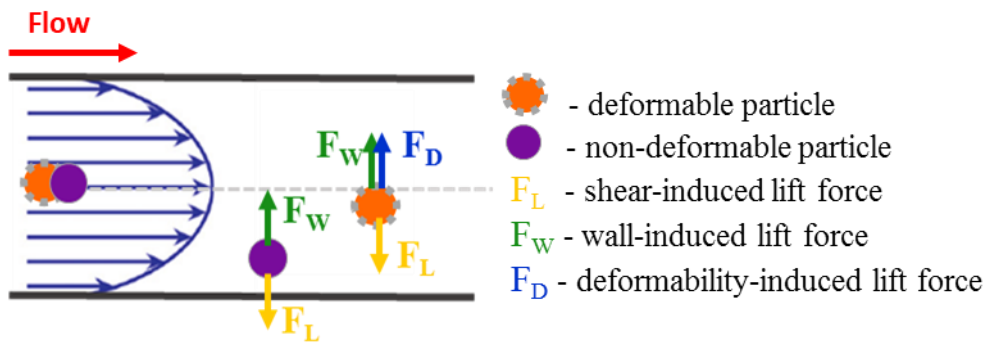


**Fig. 4.1**  
Schematic adapted from [117] illustrating contribution of deformability-induced lift force to inertial focusing in a straight microchannel with rectangular cross-section.

The magnitude of response to  $F_D$  is associated with deformation as well as relative viscosity of fluid inside a cells in respect to the surrounding fluid [139][140]. To capture the degree of deformation, different geometrical measures have been proposed, e.g. (1) reduced volume ( $v$ ) [141] defined as the ratio of actual particle volume to that of a sphere with the same surface area

$$v = \frac{V}{\frac{4}{3}\pi\left(\frac{A_S}{4\pi}\right)^{\frac{3}{2}}} \quad (13)$$

where,  $V$  is deformed particle volume and  $A_S$  is deformed particle surface area, and (2) excess area ( $\Delta$ ) [142] defined as the differences in projected area between the particle and a sphere with equivalent volume

$$\Delta = \frac{A_S}{R^2} \quad (14)$$

where  $R$  is the effective particle radius

$$R = \left(\frac{3V}{4\pi}\right)^{\frac{1}{3}} \quad (15)$$

In this study cell deformability ( $D$ ) was measured with RT-DC (see **Chapter 2**) and it is expressed as  $D = 1 - circularity$ , a deformable object will be characterised by  $c < 1$ .

Deformability-induced particles migration has been explored on numerous occasions for droplets, bubbles, vesicles and viscous capsules in straight channels [143]. To the best of my knowledge there is no literature describing this hydrodynamic mechanism in conjugation with Dean vortices in spiral microchannels. Exploring and understanding the contribution of  $F_D$  to the focusing and ordering mechanism in spiral microchannels opens up a new way to separate cells from complex heterogeneous samples based on their intrinsic mechanical properties.

## 4.3. Results

### 4.3.1. Cellular deformability model

To study  $F_D$  in spiral microchannels, a cellular model of deformability was derived by inducing gradual changes in cell deformability with chemical treatment (**Fig. 4.2**). We used Jurkat cells (round cells,  $\text{Ø}13 \pm 2 \mu\text{m}$ , mean  $\pm$  SD, cultured in suspension) and treated them with CytochalasinD (CytoD), known for softening cell properties by alteration of cytoskeletal protein F-actin, **Fig. 4.2 a**), and Glutaraldehyde (Gluta), making cells stiffer by cross-linking proteins, **Fig. 4.2 b**. Both compounds were tested at gradually increasing concentrations in order to generate dose-response graphs and identify concentrations corresponding to half-maximum and maximum response to the treatment manifested in changing cell deformability.



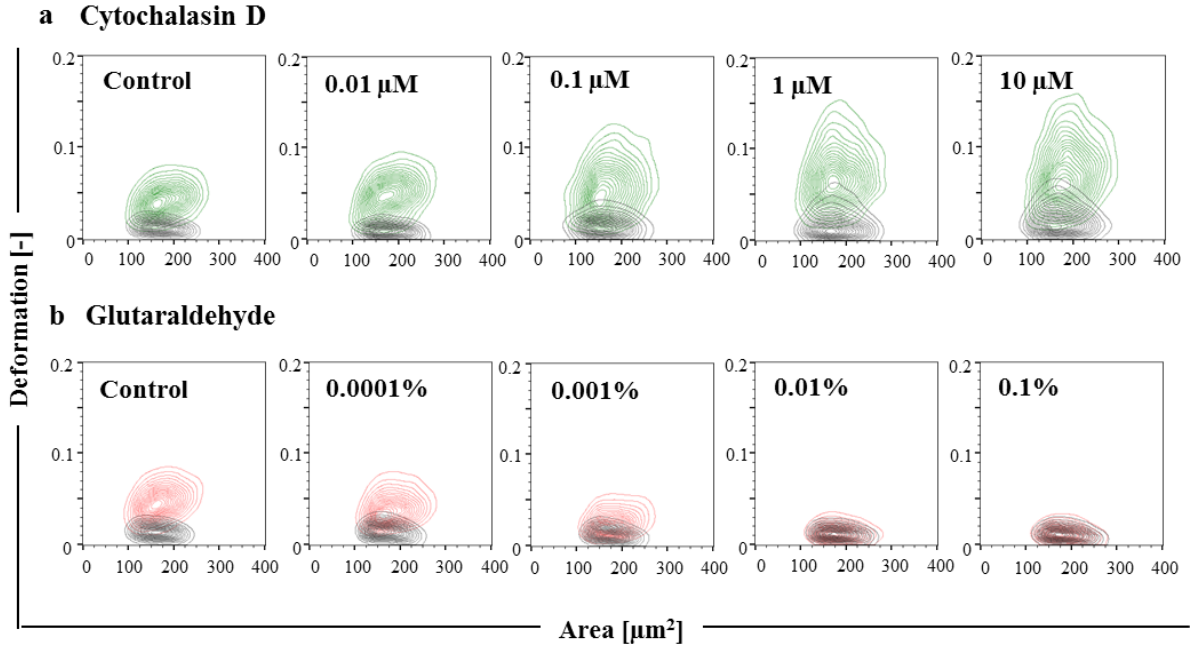


**Fig. 4.2**

*Exemplary contour plots for Jurkat cells treated with (a) Cytochalasin D (CytoD) and (b) Glutaraldehyde showing the controlled change in deformability without affecting size. Size is expressed as the projected cell area [ $\mu\text{m}^2$ ] vs deformation [-], measured in both the high-shear stress channel (green-CytoD and red- Glutaraldehyde) as well as inlet reservoir section (grey for both conditions) of RT-DC chip. All experiments were carried out at a flow rate of  $0.16 \mu\text{l/s}$  in a  $30 \times 30 \mu\text{m}$  cross-section channel for around 10000 events for each replicate.*

Deformability was measured by RT-DC and here it is reported as differential deformation (DD) where deformation in the measurement channel is independently measured from the initial cell shape. Therefore any treatment-induced morphological changes to shape were neglected. DD includes morphological information acquired in the reservoir section of the RT-DC chip (where applied shear is negligible) and subtracts this value from the deformation measured in the channel. Interestingly, as in **Fig. 4.3**, cells treated with 0.1, 1 and 10  $\mu\text{M}$  CytoD appear more deformable ( $D=0.019 \pm 0.017$  and  $D=0.023 \pm 0.017$ , respectively) in in the reservoir of the RT-DC chip, in comparison to control cells ( $D=0.013 \pm 0.006$ ) with increased heterogeneity manifested by increased SD. Since in the reservoir section the amount of shear stress is negligible, the apparent elevated deformability could originate from loss of the typical spherical shape by some of the cells (as shown in **Fig. 4.3**) due to lack of cytoskeletal integrity as a results of the F-actin depolymerisation.

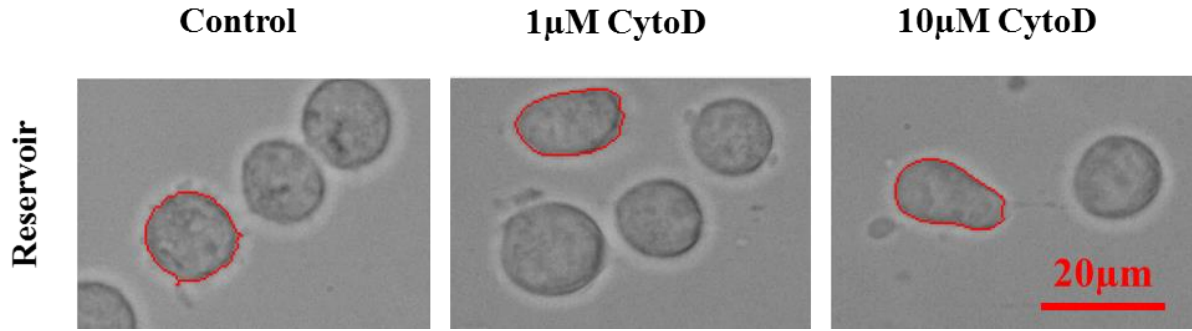


**Fig. 4.3**

*Exemplary images captured in the reservoir section of RT-DC chip for untreated control cells as well as cells treated with 1 and 10  $\mu\text{M}$  CytoD. The red lines indicate a currently detected cell by the RT-Dc software. The scale bar corresponds to 20  $\mu\text{m}$ .*

**Fig. 4.4 a** displays mean  $\pm$  SD DD for Jurkat cells treated with CytoD in relation to untreated control cells (0  $\mu\text{M}$ , DD= 0.031  $\pm$  0.001). Exposure of cells to a concentration of 0.01  $\mu\text{M}$  CytoD triggers a significant (p-value <0.01) change to cell deformability, towards increased DD=0.041  $\pm$  0.001. Cell DD increases gradually with increasing CytoD concentrations to reach a plateau (maximal response) at 1  $\mu\text{M}$  (DD=0.061  $\pm$  0.007, p-value < 0.001), corresponding to a relative change in DD of 96% along with increased heterogeneity as standard deviation increases from SD=0.001 (control) to SD=0.007. The half-maximal concentration ( $\text{EC}_{50}$ ) of 0.09  $\mu\text{M}$  was extracted by using a sigmoidal fit to the data, corresponding to DD=0.046.

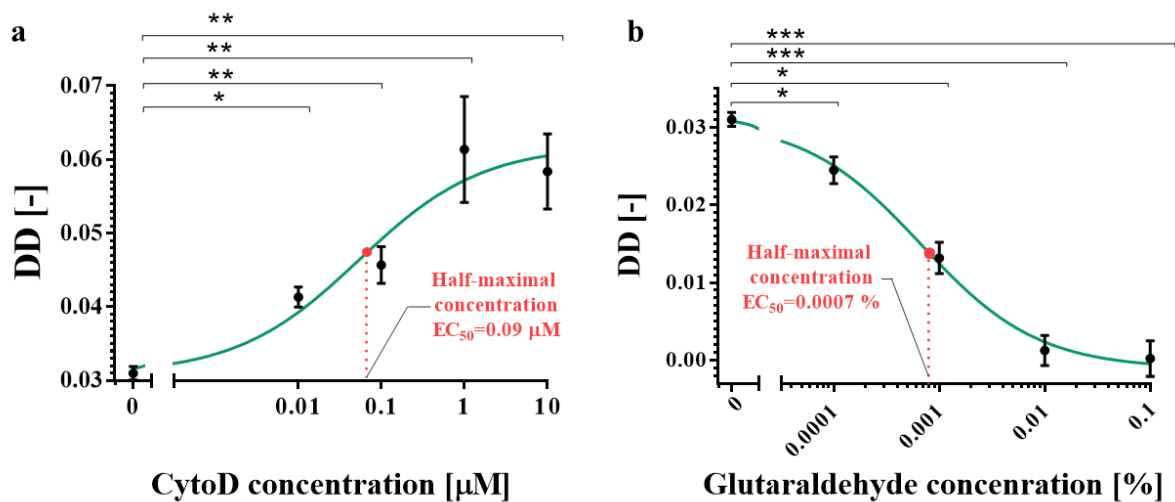


**Fig. 4.4**

*Cellular deformability model was derived, using Jurkat cells, by chemical treatment triggering gradual changes in cell stiffness. Cells of Jurkat cell line (round cells in suspension,  $\varnothing \sim 13 \mu\text{m}$ ) were treated with (a) CytochalasinD (CytoD) and (b) Glutaraldehyde. Both compounds were tested at different concentration to generate dose-response graphs (mean deformation  $\pm$  SEM*

*measured with real-time deformability cytometry RT-DC). Sigmoidal fit to the data allowed identification of the half maximum (EC50) and maximum concentration for the effect of CytoD and Glutaraldehyde on the deformability. P-values were calculated using the linear mixed model (\*p-value <0.01, \*\* p-value<0.001)*

**Fig. 4.4 b** summarises effect of increasing concentrations of the cross-linking Glutaraldehyde on Jurkat cells, which affects cell-surface particles, stress fibres, actin cortex, and inner structures, stabilising the whole cell structure [144]. At concentrations as low as 0.0001% (v/v) cells become 22% stiffer ( $DD=0.031 \pm 0.001$ , p-value<0.01) than control cells. Cells' deformability decreases gradually with elevated Glutaraldehyde concentration, up to 0.01% ( $DD=0.001 \pm 0.002$ , p-value < 0.001) when cells do not deform any further (maximal response), corresponding to 97% drop in deformability. The  $EC_{50}$  for the effect of Glutaraldehyde was identified at 0.0007%, corresponding to  $DD=0.014$ .

In order to verify if the chemically-triggered changes of deformability were decoupled from size alteration we used flow cytometry to quantify forward light scatter (FSC-A) - a measurement of the amount of a laser beam that passes around the cell – corresponding to a relative cell size. Since the RT-DC technique is based on image analysis it allows also size measurement, which is expressed as a projected cell area reported in  $\mu\text{m}^2$ . Typically, cell size is obtained from images acquired in the reservoir section. Although accurate, the technique can at times be sensitive to changes in focus setting. Hence rather than reporting the projected cell area the FSC-A parameter was used instead. Additionally, to quantify the degree of size overlap Receiver Operating Curves (ROC) were generated and the corresponding Area Under the Curve (AUC) was calculated.

As demonstrated in **Fig. 4.5** proposed chemical treatments altering cell deformability have little if any impact on cell size. CytoD treatment (**Fig. 4.5 a & b**) introduced a minute (~10% ) shift in cell size distribution (AUC= 0.60, 0.60, 0.62 and 0.61 for 10, 1, 0.1 and 0.01  $\mu\text{M}$ , respectively). Treatment with Glutaraldehyde (**Fig. 4.5 c & d**) preserved cell size, and that was true for all tested concentrations (AUC=0.53, 0.50, 0.54 and 0.53 for 0.1, 0.01, 0.001 and 0.0001%, respectively).

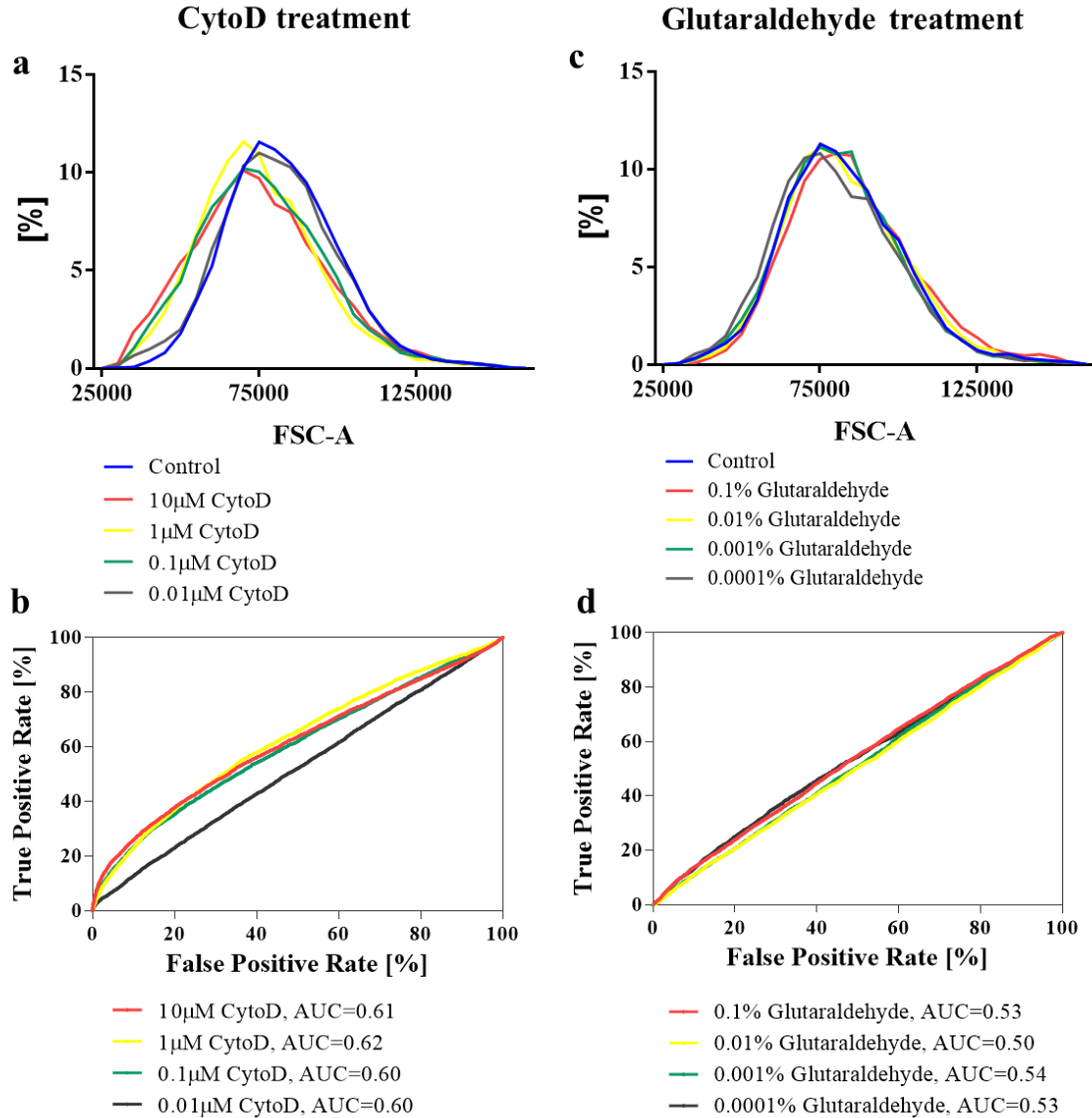


**Fig. 4.5**

Cell size of (a) CytochalasinD (CytoD) and (c) Glutaraldehyde- treated cells was assessed using forward light scatter parameter (FSC-A) measured using flow cytometer for 10000 events per condition. (b & d) Receiver Operating Characteristic (ROC) curves were plotted for (size expressed as FSC-A). The True Positive Rate is defined as the number of control cells measured for a certain size cut-off point and divided by the total number of control cells. The False Positive Rate is the corresponding number of treated cells (with CytoD or Glutaraldehyde) divided by the total number of treated cells (CytoD or Glutaraldehyde, respectively) for the same cut-off. The Area Under the Curve (AUC) was calculated to quantify the size overlap between control and treated cells, where a value of 0.5 represents complete overlap and 1 represents complete separation.

High-throughput investigation of CytoD and Glutaraldehyde impact on cell mechanical properties allowed us to establish the cellular deformability model, consisting of cells of five different degrees of deformability (see **Table 4.1**), but remaining within the same size ranges. We used these model cells for further study of  $F_D$  in spiral microchannels.

Cellular Deformability Model		
Deformability	DD	Treatment
Soft max	0.061	1 $\mu$ M CytoD
Soft half-max	0.046	0.09 $\mu$ M CytoD
Soft	0.031	N/A
Stiff half-max	0.014	0.007% Glutaraldehyde
Stiff max	0.001	0.01% Glutaraldehyde

**Table 4.1**

*Cellular deformability model derived for Jurkat cells, consisting of degrees of differential deformability (DD), induced chemically with CytoD (cells softening) or Glutaraldehyde (cells stiffening).*

#### 4.3.2. Lateral equilibrium position as a function of cell deformability

Cells of the cellular deformability model, were tested as pure populations in two designs of spiral microchannels at five different flow rates. Design I was a spiral channel with  $360 \times 60 \mu\text{m}$  cross-section and it was tested at  $\text{Re} = 79, 119, 158, 197$ . Design II was a spiral channel  $170 \times 30 \mu\text{m}$  cross-section, tested at  $\text{Re} = 33, 66, 97, 132$  and  $168$ . Next, the hydrodynamic behaviour of the cells (described as their lateral equilibrium position at the end of the spiral channel, measured as a distance from the outer wall [ $\mu\text{m}^2$ ]) was compared with reference rigid spherical polystyrene beads of corresponding  $10$  and  $15 \mu\text{m}$  diameters (please note,  $15 \mu\text{m}$  beads could not be tested in the design II since they clogged the device at the inlet).

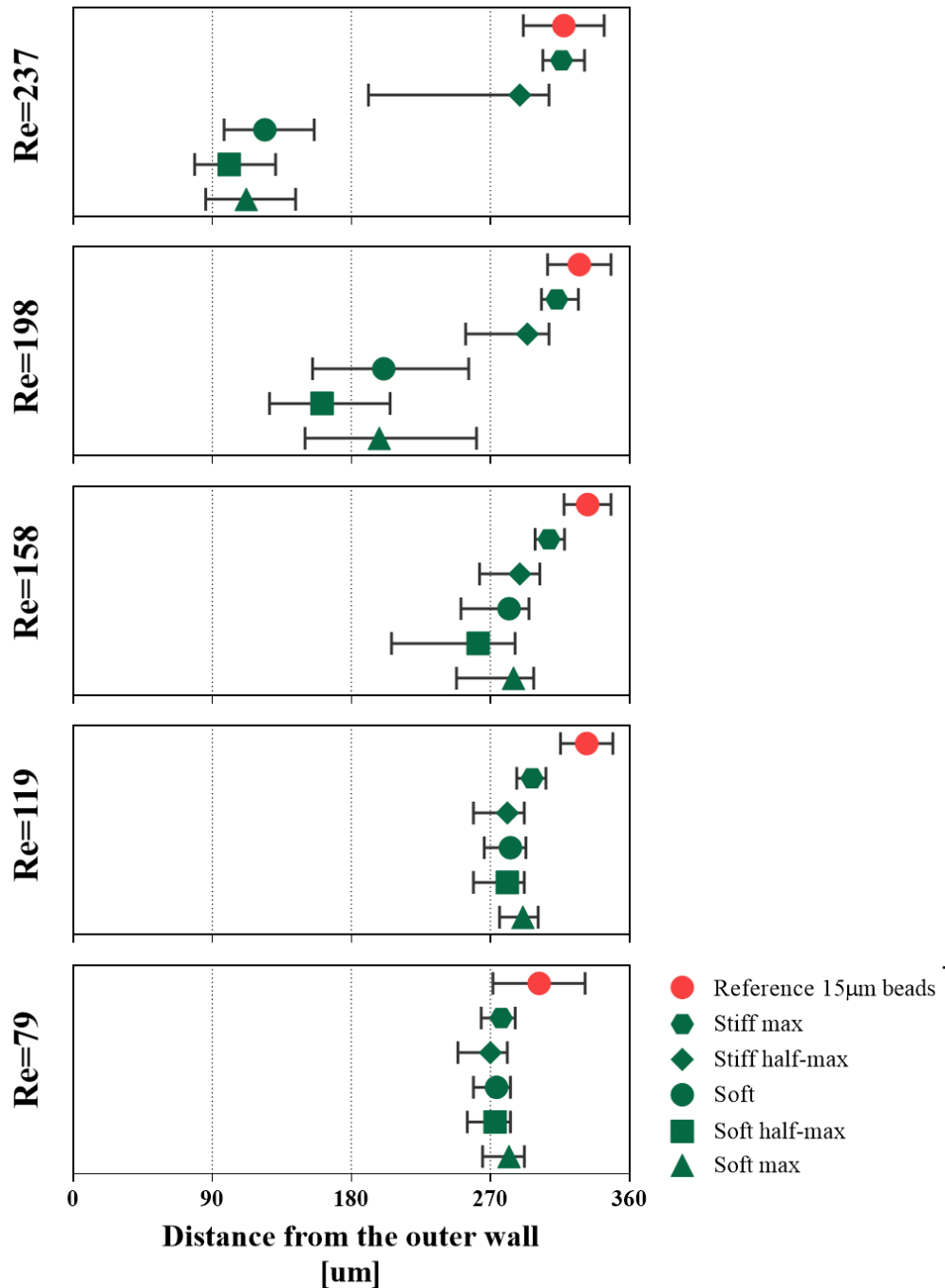


**Fig. 4.6**

*Hydrodynamic behaviour of cells of five different deformabilities (Soft max, soft half-max, soft, stiff half-max and stiff) in comparison to reference 15 µm beads, in design I spiral channel with  $360 \times 60 \mu\text{m}$  cross-section at five different flow rates corresponding to  $Re=79, 119, 158, 198$  and  $237$ . The lateral equilibrium positions were measured as a distance from the outer wall ( $\mu\text{m}$ ) at the end of the spiral channel and there were generated by image analysis. Here, it is reported as median (represented as the symbols) and the interquartile range (indicated by the short vertical lines). Vertical dotted lines indicate four sections of the channel corresponding to four outlets of the channel ( $0-90 \mu\text{m}$ - outlet A,  $90-180 \mu\text{m}$ - outlet B, etc.). Events belonging to a given section have the highest probability of being captured within the corresponding outlet. For summary of triplicate results please consult **Appendix B***

As shown in **Fig. 4.6**, in design I, at lower flow rates ( $Re=79, 119$  and  $158$ ) cells of all five deformability degrees behave in a similar manner, i.e. they remain focussed in the side of the channel, closest to the inner wall of the channel, at around  $270 \mu\text{m}$ . Increased flow rates ( $Re=198$ ) triggered a shift of soft, soft half-max and soft max cells to lateral positions closer to the channel centreline ( $184 \pm 60, 168 \pm 87$  and  $219 \pm 60 \mu\text{m}$ , respectively) accompanied by cells defocusing from the uniform streak of cells, manifested by cells occupying larger space within the channel. Stiff half-max and stiff max cells were not affected in the same way, and they remain focused close to the inner wall, with stiff max cells being focused in a tighter streak closer to the outer inner wall ( $304 \pm 21 \mu\text{m}$ ) in comparison to stiff half-max cells ( $269 \pm 61 \mu\text{m}$ ). Further flow rate increases ( $Re=237$ ) resulted in shift of soft, soft half-max and soft max cells closer to the outer wall of the channel ( $132 \pm 50, 109 \pm 44$  and  $121 \pm 49 \mu\text{m}$ , respectively). The highest applied flow rate did not change hydrodynamic behaviour of stiff max cells, which were still focused closer to the inner wall ( $305 \pm 45 \mu\text{m}$ ), but interestingly stiff half-max cells started shifting towards centreline of the channel, with the characteristic defocusing indicated by wider spread of assembled lateral position ( $251 \pm 77 \mu\text{m}$ ), similarly to softer cells at  $Re=198$ . At all tested flow rates reference  $15 \mu\text{m}$  beads remained tightly focused close to the inner wall.

In design II (**Fig. 4.7**), due to cell diameter approaching height of the channel, Jurkat cells were geometrically forced towards centreline of the channel. At lower  $Re$  numbers ( $Re=33, 66$  and  $97$ ) cells from all five conditions behaved in a similar manner, i.e. they remained focussed near the centre of the channel ( $85 \mu\text{m}$ ). Increased flow rates ( $Re=132$ ) resulted in a noticeable stiff max cells deviation from the centreline ( $101 \pm 25 \mu\text{m}$ ). At the highest applied flow rates ( $Re=168$ ) the difference between soft and stiff cells were revealed; soft cells were pushed closer to the outer wall (soft:  $68 \pm 21 \mu\text{m}$ , soft half-max:  $80 \pm 26$  and soft max:  $113 \pm 21 \mu\text{m}$ ) while stiff cells focussed close to the inner wall (stiff half max:  $100 \pm 27 \mu\text{m}$  and stiff max:  $113 \pm 21 \mu\text{m}$ ). The reference  $10 \mu\text{m}$  beads behaved similarly to stiff max cells, i.e. they remained focused close to the centreline at lower applied flow rates ( $102 \pm 8, 99 \pm 17$  and  $108 \pm 20 \mu\text{m}$  for  $Re=33, 66$  and  $97$ , respectively), and slightly diverged towards the inner wall at higher flow rates ( $128 \pm 11$  and  $119 \pm 23$  and  $Re=132$  and  $168$ , respectively).

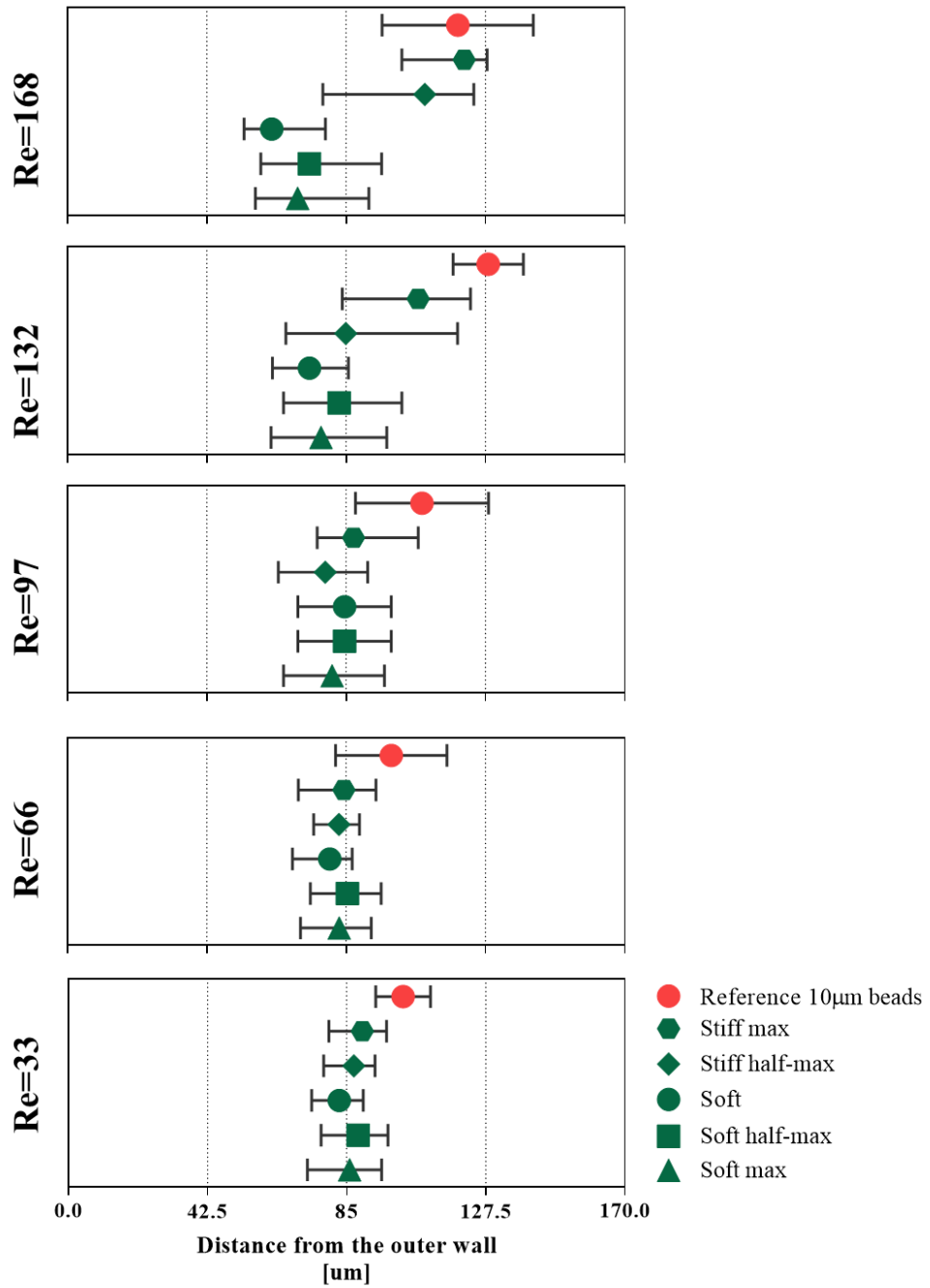


**Fig. 4.7**

Hydrodynamic behaviour of cells of five different degrees of deformability (Soft max, soft half-max, soft, stiff half-max and stiff) in comparison to reference 10 µm beads, in design II spiral channel with  $170 \times 30 \mu\text{m}$  cross-section at five different flow rates corresponding to  $Re=33$ , 66, 97, 132 and 168. The lateral equilibrium positions were measured as a distance from the outer wall ( $\mu\text{m}$ ) at the end of the spiral channel and there were generated by image analysis. Here, it is reported as median (represented as the symbol) and the interquartile range (indicated by the short vertical lines). Vertical dotted lines indicate four sections of the channel corresponding to four outlets of the channel (0-42.  $\mu\text{m}$ - outlet A, 42.5-85  $\mu\text{m}$ - outlet B, etc.). Events belonging to a given section have the highest probability of being captured within the corresponding outlet. For summary of triplicate results please consult **Appendix C**



### 4.3.3. Deformability difference for sorting cells in spiral microchannel

Using the significant differences in lateral equilibrium position adopted by soft and stiff max cells within spiral microchannels, we conducted label-free separation of these cells. The Design I spiral channel is divided into four balanced outlets (A, B, C and D) for cell collection. The spiral channel itself could be divided into four sections: 0-90  $\mu\text{m}$ , 90-180  $\mu\text{m}$ , 180-270  $\mu\text{m}$  and 270-360  $\mu\text{m}$ , measured from the outer wall, corresponding to the four outlets A, B, C and D, respectively. Due to the laminar flow regime, cells equilibrated at the end of the channel within the realm of one of the four sections, will travel to the corresponding outlet. This principle allows for prediction of sorting outcome without labour-intensive outlet quantification, which is a common practice for optimising spiral channels performance. Prior to separation, pre-sorted/ pure populations are run separately at a range of flow rates and their lateral equilibrium positions are compared in order to identify the optimal flow rate. The most distinct difference in equilibrium positions of soft and stiff max cells were observed within the design I channel at  $\text{Re}=237$ , with separation reaching 98% (AUC=0.98, **Fig. 4.8 a**), hence that was the flow rate applied for sorting cells from mixed sample. Additionally, by quantifying number of cells in each section of the channel a mock separation efficiency was generated (**Fig. 4.8. a & b**), showing it would be possible to capture 91% of stiff cells in outlet D with >96% purity, while soft cells should be mainly distributed between outlets A (recovery: 29%, purity: 99%) and B (recovery: 60%, purity: 96%).

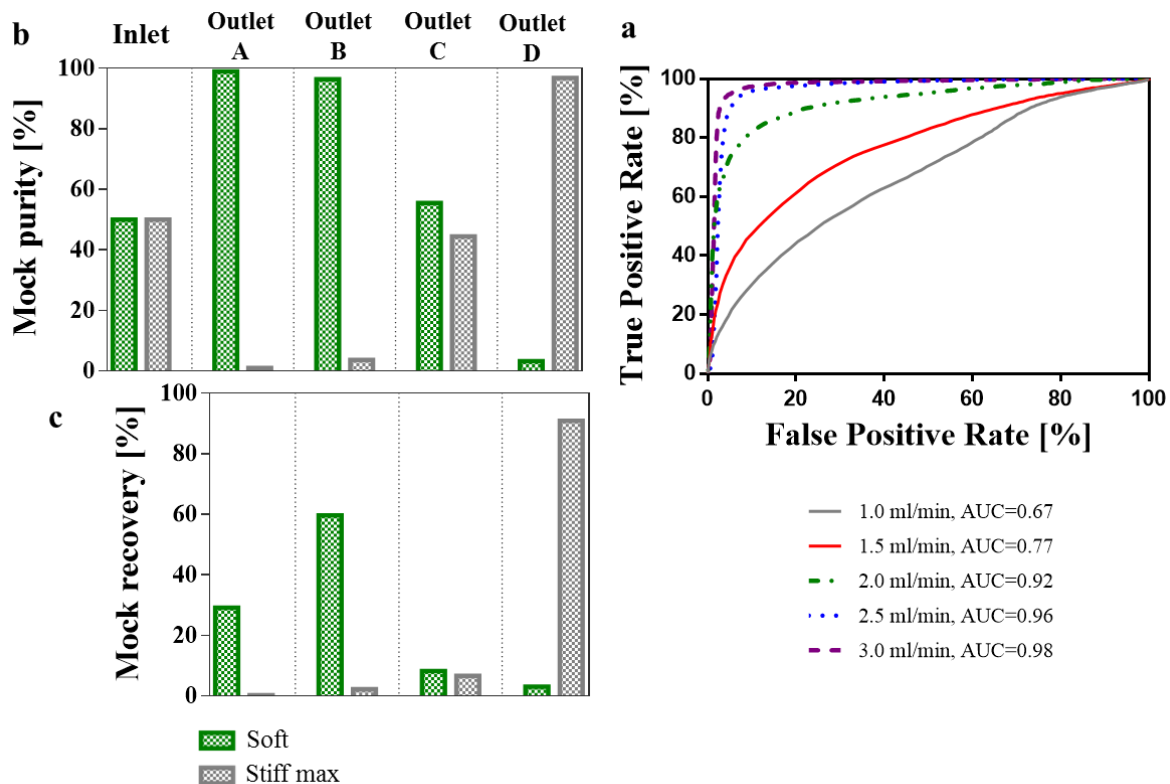


**Fig. 4.8**

*Predicted outcome for sorting soft (untreated) and stiff max (Glutaraldehyde max) cells in design I spiral microchannel with  $360 \times 60 \mu\text{m}$  cross-section. (a) First Receiver Operating Characteristic (ROC) curves were plotted for lateral equilibrium position for soft cells versus stiff max cells, to identify optimal flow rate. The True Positive Rate is defined as the number of soft cells found at a given lateral position and divided by the total number of soft cells. The False Positive Rate is the corresponding number of stiff max cells divided by the total number of soft cells for the same cut-off. To determine which of the applied flow rates ensures the best separation efficiency the Area Under the Curve (AUC) was calculated. By quantifying number of cells in each section of the channel corresponding to one of four outlets, run as pure populations of soft (green) and stiff max (grey), it was possible to generate mock (b) purity and (c) recovery to assess possible sorting outcome for the mixed sample. The bars represent predicted mean values*

For the separation experiment it was necessary to distinguish between soft and stiff cells in order to quantify the process performance (purity and recovery). To achieve that, Jurkat cells were modified to express green fluorescence protein (GFP), without compromising their deformability (**Fig. 4.9**), which would allow for their detection by flow cytometry. To avoid further validation of the impact of Glutaraldehyde on emitted fluorescent signal, transfected with GFP Jurkat cells (GFP+) served as the soft subpopulation, mixed with GFP-negative (GFP-) stiff max cells.

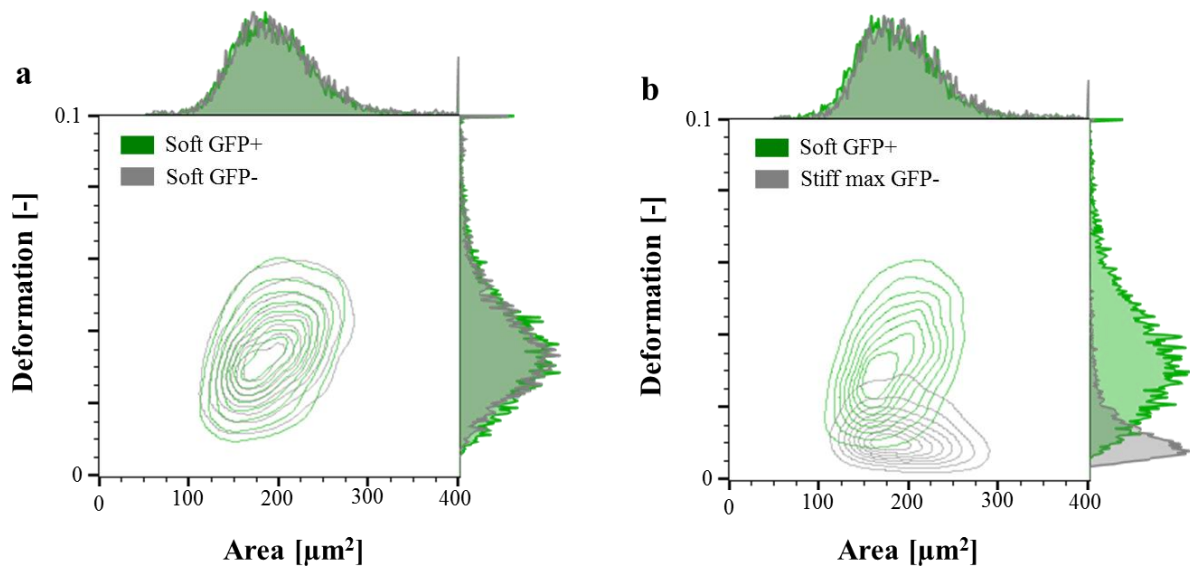


**Fig. 4.9**

*RT-FDC characterisation of GFP+ (green) in comparison to GFP- (grey) cells. Equal probability contour plots (the same number of cells fall between each pair of contour lines) with adjacent histograms of deformation vs cell size (expressed as projected cell area in  $\mu\text{m}^2$ ) for GFP+ and GFP- cells. Measurements were performed at 0.16  $\mu\text{l}/\text{min}$  flow rate in a  $30 \mu\text{m} \times 30 \mu\text{m}$  channel. More than 10000 of total events were acquired and split accordingly between each subset. (a) Comparison of GFP+ versus GFP- untreated cells and (b) comparison of untreated GFP+ cells and GFP- cells fixed with Glutaraldehyde.*

The input cell sample, containing soft GFP+ and stiff max GFP- cells, mixed at around 50:50 ratio (**Fig. 4.10 a**), up to a final  $1 \times 10^6$  cells/ml concentration, were passed through the design I spiral channel at  $\text{Re}=237$  at three independent occasions. As shown in **Fig. 4.10 b**, the majority ( $78.5 \pm 1.6 \%$ ) of the stiff max GFP- cells were hydrodynamically directed to outlet D, reaching 80% purity. Soft GFP+ cells were mainly distributed between outlets A (recovery:33.1%, purity:92%) and B (recovery:38.9%, purity: 79%).

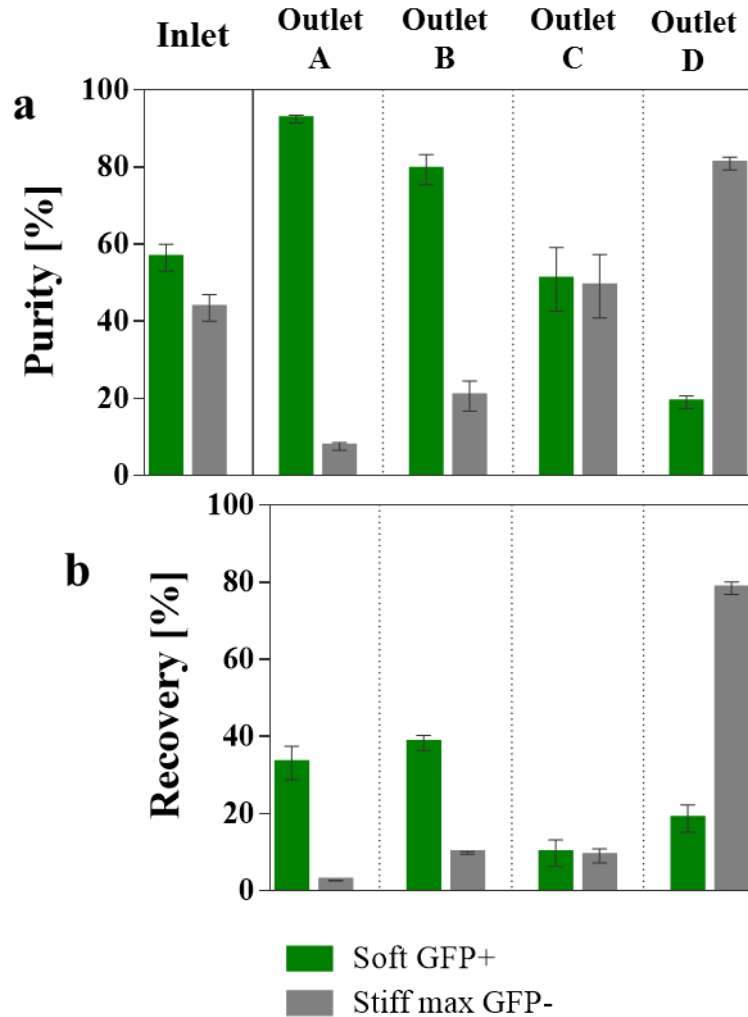


**Fig. 4.10**

Characterisation of the deformability-based purification process in the design I spiral microchannel, with  $360 \times 60 \mu\text{m}$  cross-section. The purification efficiency of untreated soft GFP+ cells (green) from the Glutaraldehyde treated stiff max GFP- (grey) after processing in the spiral channel. (a) Purity and (b) recovery were generated by quantification of cells collected at the outlets (A -closest to the outer wall, B, C and D) at flow rate corresponding to  $Re=237$ . The process validation was performed at three independent occasions, the bars represent mean value and error bars correspond to the standard deviation of the mean.

#### 4.3.4. Impact on cell viability

Processing in spiral microchannels has been recognised as a gentle technique, with little if any impact on cell viability. To take advantage of the  $F_D$  in spiral channels it is necessary to work at elevated flow rates, which result in an elevated degree of shear stress potentially deteriorating cell quality. Cells after processing in design I and design II spiral at highest applied flow rate, were collected from all outlets into one tube and investigated by flow cytometry. The earliest detectable signs of apoptosis are membrane asymmetry. In apoptotic

cells phosphatidyl serine is translocated from inner to the outer layer of the cell membrane and can be identified by its conjugate Annexin V. Necrotic cells are characterised by increased cell permeability, which allows propidium iodide, which is not permeant to live cells, to enter the cell and bind to DNA.

**Fig. 4.11** shows that cells processing at high flow rates in spiral microchannels does not significantly affect cell viability. Viability of control cells, which were not flowed through the system, was around 80% with remaining 20% being split between apoptotic and necrotic cells within the sample. These proportions were not affected after exposure to shear flow in spiral microfluidic.

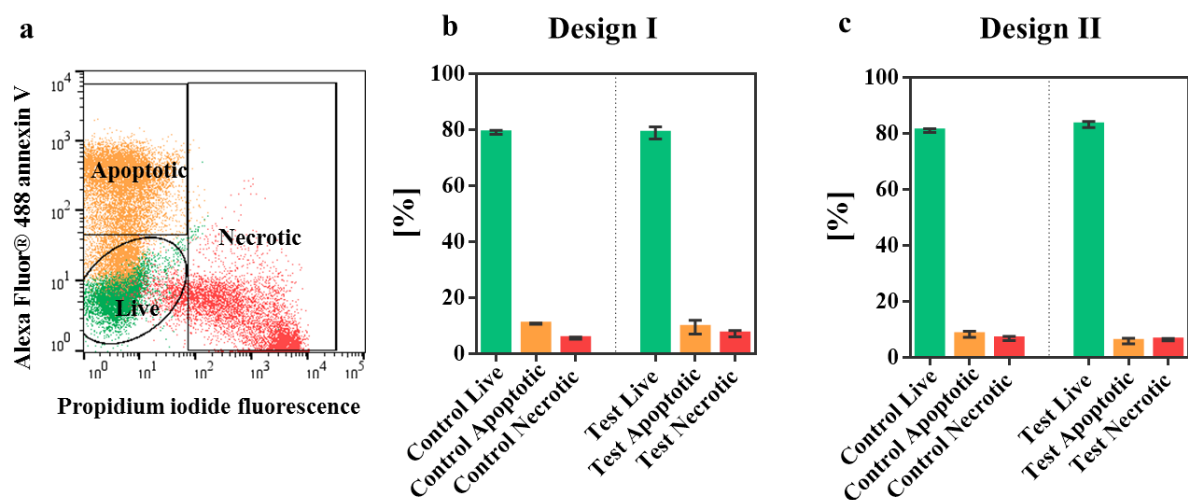


**Fig. 4.11**

*Flow cytometric viability assay. (a) An exemplary scatter plot showing gating strategy for live cell (green, negative for both Alexa Fluor 488-annexin V and propidium iodide (PI) fluorescence), apoptotic cells (yellow, annexin V-positive and PI-negative) and necrotic (red, annexin V-positive and PI-positive). Summary of flow cytometric assessment of the presence of live, apoptotic and necrotic Jurkat cells before (control) and after (test) processing in (b) design I and (c) design II spiral microchannels at highest applied flow rates, corresponding to  $Re=237$  and  $Re=168$ , respectively. The process validation was performed at three independent occasions, the bars represent mean value and error bars correspond to the standard deviation of the mean. For summary of scatter plots for triplicate results please consult **Appendix D***

#### 4.4. Discussion

Exploiting the contribution of  $F_D$  in spiral microchannels offers new ways to separate cells from complex heterogeneous samples based on their intrinsic mechanical properties. In previous reports, the  $F_D$  effect for particles focusing in straight channels has been used either solely or in conjunction with other effects, such as viscoelasticity and inertia. At inertia-less regimes (where Re numbers remain small) in microchannels, deformability-based separation

is possible due to cell-wall interaction, where more deformable cells experience more repulsion from the wall in comparison to their stiffer counterparts. This principle was successfully employed by Geslinger *et al.* to separate red blood cells from platelets, where cells were pushed against wall using sheath flow.

Incorporating the effect of inertia increases separation throughput, since it occurs at intermediate Re numbers. Hur *et al.* demonstrated that the  $F_D$  effect in combination with inertial effects in straight microchannel with high aspect-ratio cross-section, yields throughputs of  $\sim 2.2 \times 10^4$  cells/ min in a single device. Adding curvature to the channel brings two advantages over straight channels. Firstly, the presence of Dean flow reduces number of equilibrium positions and modifies the preferred locations of the particles depending on their size. Secondly, it accelerates particles displacement; particles travel shorter distances to be equilibrated in comparison to straight channels with the same cross-section and operating at equivalent flow rates. Identifying operating regimes for harnessing the effect of  $F_D$  in inertial focussing channels, introduces another important advancement, which could be translated into enhanced passive label-free cell sorting.

In this research, it has been experimentally demonstrated that hydrodynamic effects in spiral microchannels can be used to separate cells of the same size but different deformability. The effect of  $F_D$  in straight channels has been studied using droplets and vesicles. The degree of deformation in droplets depends on viscosity ratio with respect to the surrounding fluid. More viscous droplets undergo less deformation thus the lateral push triggered by  $F_D$  is weaker. Vesicles, composed of lipid bilayers, are commonly used in biophysics studies as a simplified model for cell membrane dynamics and red blood cells. In shear flows vesicles deform, adopting an ellipsoidal shape and flowing in a fixed orientation in regards to the flow direction and channel wall, while the surrounding membrane is circulating around its interior. This internal circular motion is responsible for maintaining their fixed alignment.

Both of these systems have been widely studied, however they do not reflect the real nature of cells and their hydrodynamic behaviour. Cells are surrounded by a lipid bilayer underlined with a dynamic cytoskeleton, which primarily determines cell deformability. Additionally, most cells contain nucleus, which under sufficiently high shear stress constitutes a limiting factor for cell deformability. For all these reasons, the cellular deformability model has been developed. Using cells of five degrees of deformability I studied their behaviour within two designs of spiral microchannels. Based on the experimental observations two conclusions could be drawn.

(1) The effect of  $F_D$  requires sufficiently high Re numbers (design I: Re=237, design II: Re=168). Cells passing through the channel at lower flow rates behave according to their size, and thus no significant differences were observed between soft and stiff cells. At elevated flow rates stiff cells behaved like rigid reference beads while soft cells enter a characteristic defocused state, when they diverge from their previously assembled equilibrium position, near the inner wall of the channel, to occupy a much wider section of the channel around the centreline, and finally, are re-focused closer to the outer wall at sufficiently high flow rates.

(2) The effect of  $F_D$  appears to be sensitive to a certain deformability threshold, above which the experienced drag reaches its maximal magnitude. At sufficiently high flow rates, all soft cells- soft, soft half-max and soft max cells- with insignificant variations between them- were focused closer to the outer wall. Interestingly, in design I at Re= 237, stiff max cells remained focused in a tight streak close to the inner wall, while stiff half-max cells started defocusing into a wider streak in comparison to the positions they occupied at lower flow rates (design I: Re=198), suggesting that if the applied flow rate was high enough, they could possibly travel to the outer wall side of the channel.

It has been experimentally verified, that the unique combination of Dean flow and  $F_D$  can be adapted to separate cells within the microfluidic system, when there is a sufficient difference in deformability between cells of interest. Promisingly, the elevated flow rates had no impact on cell viability. In order to take a full advantage of the hydrodynamic effects within the spiral microchannel, an optimal flow rate has to be identified by experiment. We noted that there were discrepancies between predicted and experimental sorting outcome. The focusing positions followed by capture in a corresponding outlet is altered when cells of different properties are run as a mixture through the system, in comparison to their behaviour when run separately as pure populations. We believe that the aberrations are introduced due to hydrodynamic interaction of particles upon their entry to the channel, resulting in an intriguing effect, creating “trains” of particles (discussed in detail in **Chapter 6**). Briefly, this dynamic self-assembly into trains at the entry of the channel is stabilised by the inertial forces, thus particles which joined the “wrong” train at the entry of the channel, cannot escape it, and this prevents them from travelling to their expected equilibrium position. Consequently they are captured in an unexpected outlet.

The effect of  $F_D$  in wall-bounded shear flows is associated with shape distortion, e.g. it has been reported that droplets with low viscosity exhibit a larger curvature on the side near the channel wall that is accounted for the larger repulsing forces acting on the surface of the

droplet near the wall. However, as shown in **Fig. 4.12**, both soft and stiff cells flowing in the spiral channel at  $Re=237$ , exhibited an undistorted nearly spherical shape. Hur *et al.* 2011 reported that highly viscous droplets do not undergo shape alterations, but still they were pushed away from the wall in comparison to solid plastic beads of similar sizes. That suggests presence of different dynamics contributing to the deformability-based differential drift and further study is required to clarify this mechanism.

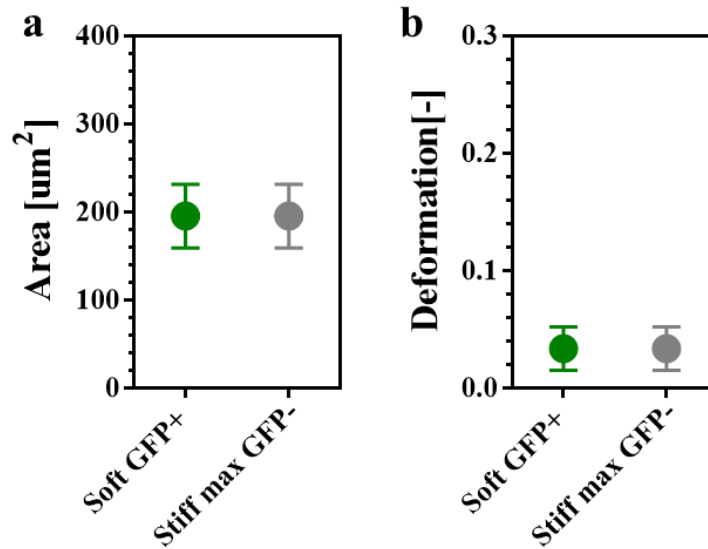


**Fig. 4.12**

*Characterisation of soft GFP+ (green) and stiff max GFP- (grey) cells passing through the design I spiral channel with  $360 \times 60 \mu\text{m}$  cross-section at flow rate corresponding to  $Re=237$ . Cells (a) area and (b) deformation were generated by analysing images captured within the channel for each population separately. The data points represent mean value measured for at least 10000 events, error bars correspond to standard deviation from the mean.*

As shown in **Fig. 4.13**, flow rates applied in design I and II are substantially higher than the majority reported in the literature for particles separation in spiral microchannels. Additionally, we apply these flow rates in devices of relatively small hydraulic diameter ( $D_h$ ), generating back pressure reaching MPa range. Our devices are made of SU8 bound PMMA (Epigem, UK), while all previously reported designs were made of PDMS bound to a substrate e.g. glass. PDMS is a widely used polymer for manufacture of microfluidic chips and a large body of work has been done towards identifying best binding techniques. Up to date, it has been reported that the strongest bonds are achieved with substrates with Si-O groups, with a maximum average bond strengths of  $\sim 0.4$  MPa, which is an order of magnitude lower than pressures applied in our systems [145]. Currently, this technical detail makes PDMS chips



unsuitable for employing the  $F_D$  effect for deformability-based separation in curvilinear microchannels.

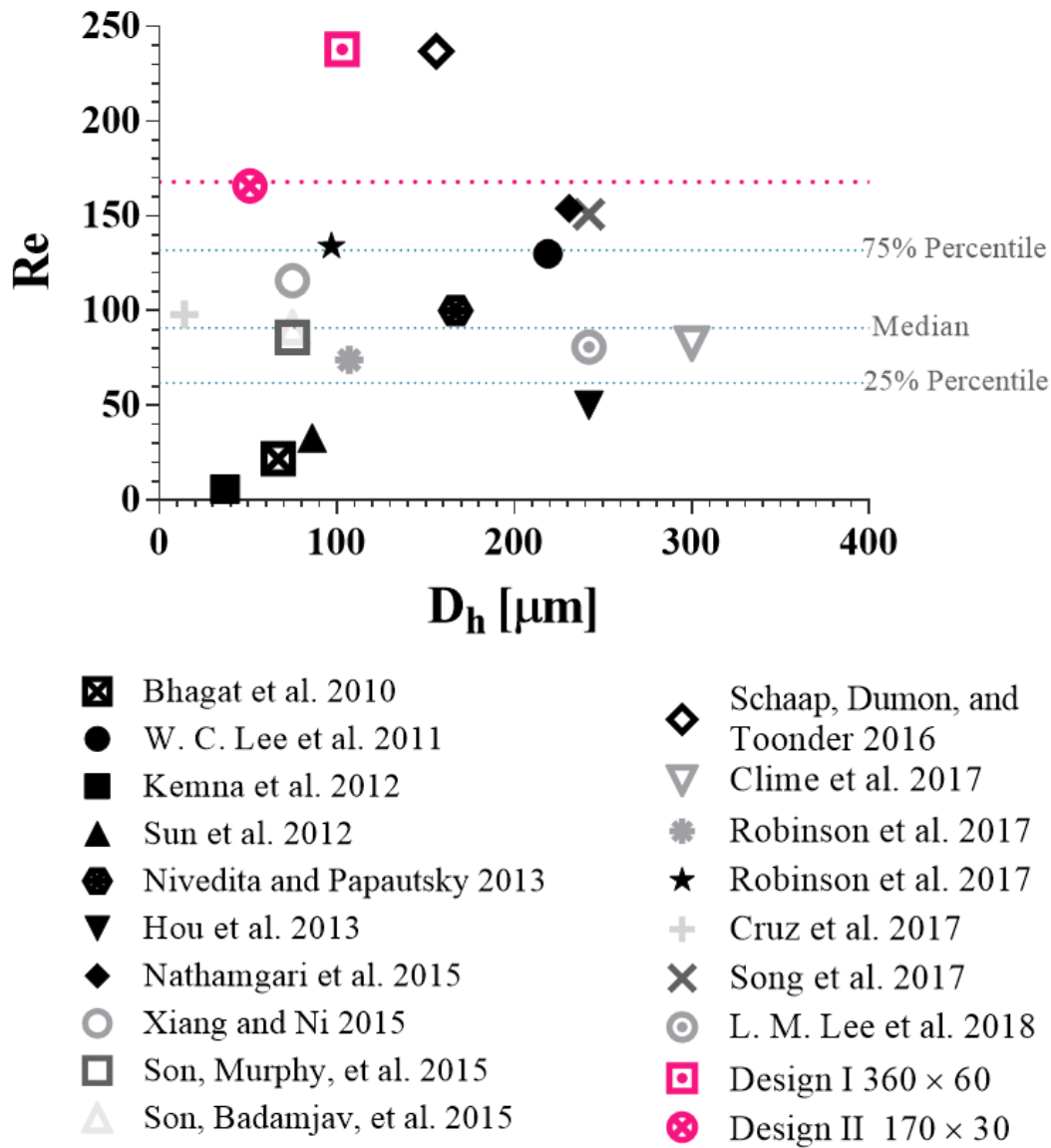


**Fig. 4.13**

*Summary of operating conditions of spiral channels reported in the literature, up to end of 2018, in comparison to design I and II (pink). The scatter plot represent applied Re numbers versus hydraulic diameter ( $D_h$ ). The grey dotted lines represent median Re number value (excluding design I and II) and lower and upper quartile as labelled on the graph. The pink dotted line represent the Re number applied in design II at which the effect of  $F_D$  was significant.*

## 4.5. Conclusion

Herein, for the first time, it has been demonstrated that at adequately high  $Re$  numbers in spiral microchannels the effect of  $F_D$  become significant in the overall process of establishing cells equilibrium positions. By studying the hydrodynamic behaviour of the five degree cellular deformability model, it has been found that cells of the same size but different deformability assemble contrary equilibrium positions within the channel cross-section. Soft cells travel close to the outer wall, while their stiff counterparts are focused close to the inner wall of the channel. This experimental observation was successfully adapted into passive label-free approach for separating cells of different deformability properties, without compromising cells quality. This hydrodynamic microfluidic phenomena appears promising and in order to fully exploit it, further theoretical investigation of the underlying physics is required. Given these results, a novel sorting approach is possible, for simultaneous sorting based on size and deformability with one system, with all the advantages offered by the spiral microchannels. This study presents a much needed label-free high-throughput (millions of cells/ min, ml of medium/ min) scalable and continuous cell sorting approach for samples of clinical importance, such as novel stem-cell derived therapeutic products.

## 4.6. Materials and methods

### 4.6.1. Deriving the cellular deformability model

Cell samples for all experiments were collected at day 2 after seeding when they were at the exponential growth phase (cell concentration never exceeded  $5 \times 10^5$  cell/ml. To derive the cellular model for deformability cells were treated with CytochalasinD and Glutaraldehyde.

Cytochlasin D (Sigma Aldrich) was added directly to cell suspension of  $1 \times 10^6$  cells/ml in whole cell culture medium and incubated for 10 min, in a humidified incubator at  $37^\circ\text{C}$  in 5%  $\text{CO}_2$ . Prior to the RT-DC measurements as well as experiments in the spiral channels and flow cytometry cells were collected by centrifugation at 300 g for 5min and re-suspended in 0.5% methylcellulose or phosphate-buffered saline without calcium and magnesium (PBS-/-, ThermoFisher Scientific), respectively. Cytochlasin D in dimethyl sulfoxide (DMSO, Sigma Aldrich) concentration was adjusted to 0.01, 0.1, 1 and 10  $\mu\text{M}$ . Final DMSO concentration in the cell sample was yielding 0.25% (v/v) for 0.01, 0.1 and 1  $\mu\text{M}$  Cytochalasin D and 2.5% (v/v) for 10 $\mu\text{M}$  Cytochalasin D. Cytochalasin D desired concentrations were always maintained in cell buffers through-out the experiments due to the reversibility of the effect.

Prior to treatment with Glutaraldehyde (Sigma Aldrich) cells were washed twice in PBS-/- to remove any residual proteins. Next cells were re-suspended at  $1 \times 10^6$  cell/ml in PBS-/- supplemented with Glutaraldehyde to the final concentrations of 0.0001, 0.001, 0.01 and 0.1% (v/v) and incubated at room temperature for 40 min. After the incubation time cells were washed once in PBS-/- and re-suspended either in 0.5% methylcellulose for RT-DC (and/or RT-FDC) measurements or PBS-/- for experiments in the spiral channels and flow cytometry.

Size of cells treated with Cytochalasin D and Glutaraldehyde were assessed by flow cytometric measurement of the forward light scatter (FSC-A) (BD LSR II, BD, Germany). Collected data was further analysed using FlowJo V10 CL. The receiver operating characteristic curves (ROC) were generated and the area under the curve (AUC) was calculated using GraphPad Prism 6.

In order to distinguish untreated soft cell from Glutaraldehyde-treated stiff cells, for the purpose of separation efficiency quantification, Jurkat cells expressing green fluorescence protein (GFP), were kindly provided by Dr Miguel Hermida (Heriot-Watt University, UK) by transduction with a second generation lentiviral system generated in house with pHR-SIN EGFP and VSV-G and delta 8.2 vectors. To ensure high GFP expression level ( $\sim 100\%$ ) within the population GFP-positive cells from the starting population were sorted by FACS (FACSAria IIu flow cytometer, Beckton Dickinson Immunocytometry Systems (BD, UK) running BD FACSDiva v6 Software) and re-cultured for further experiments. The GFP-positive cells served as control sample, which was mixed 1:1 with GFP- negative cell treated with Glutaraldehyde.

#### **4.6.2. Cell characterisation RT-FDC**

Cells deformability was assessed using real-time fluorescence and deformability cytometry (RT-FDC), in order to distinguish between GFP+ and GFP- cells, when needed. Measurements were performed as per Nat. Methods 2018 [125] and **Chapter 2**. Prior to measurements, cells were harvested by centrifugation at 300 g for 5 min and re-suspended in a 0.05% methylcellulose solution at  $1-2 \times 10^6$  cell/ml. Jurkat cells were assessed using a PDMS chip with a  $30 \times 30 \mu\text{m}$  cross-section channel. Cells were introduced into the channel at 0.16  $\mu\text{l}/\text{min}$ . Obtained data was analysed using original RT-FDC software ShapeOut 0.8.4 (available at [www.zellmechanik.com](http://www.zellmechanik.com)). Next, the data was extracted from the software and further inspected, plotted and fitted using FlowJo V10 CL and GraphPad Prism 6.

#### **4.6.3. Cells separation in spiral channels**

Cells suspension at concentration around  $1 \times 10^6$  cells/ml was processed as described in **Chapter 2**. Cell separation efficiency was quantified by flow cytometry (BD LSR II, BD, Germany in order to compare the fraction of each cell population (characterised by a unique fluorescent properties) in samples collected at each outlets. Additionally, cell yield was assessed by counting number of cells at each outlet using either a standard glass haemocytometer or MoxiZ automated cell counter (Orflo, US). Further data analysis was performed using GraphPad Prism 6 and FlowJo V10 CL.

#### **4.6.4. Viability flow cytometric assay**

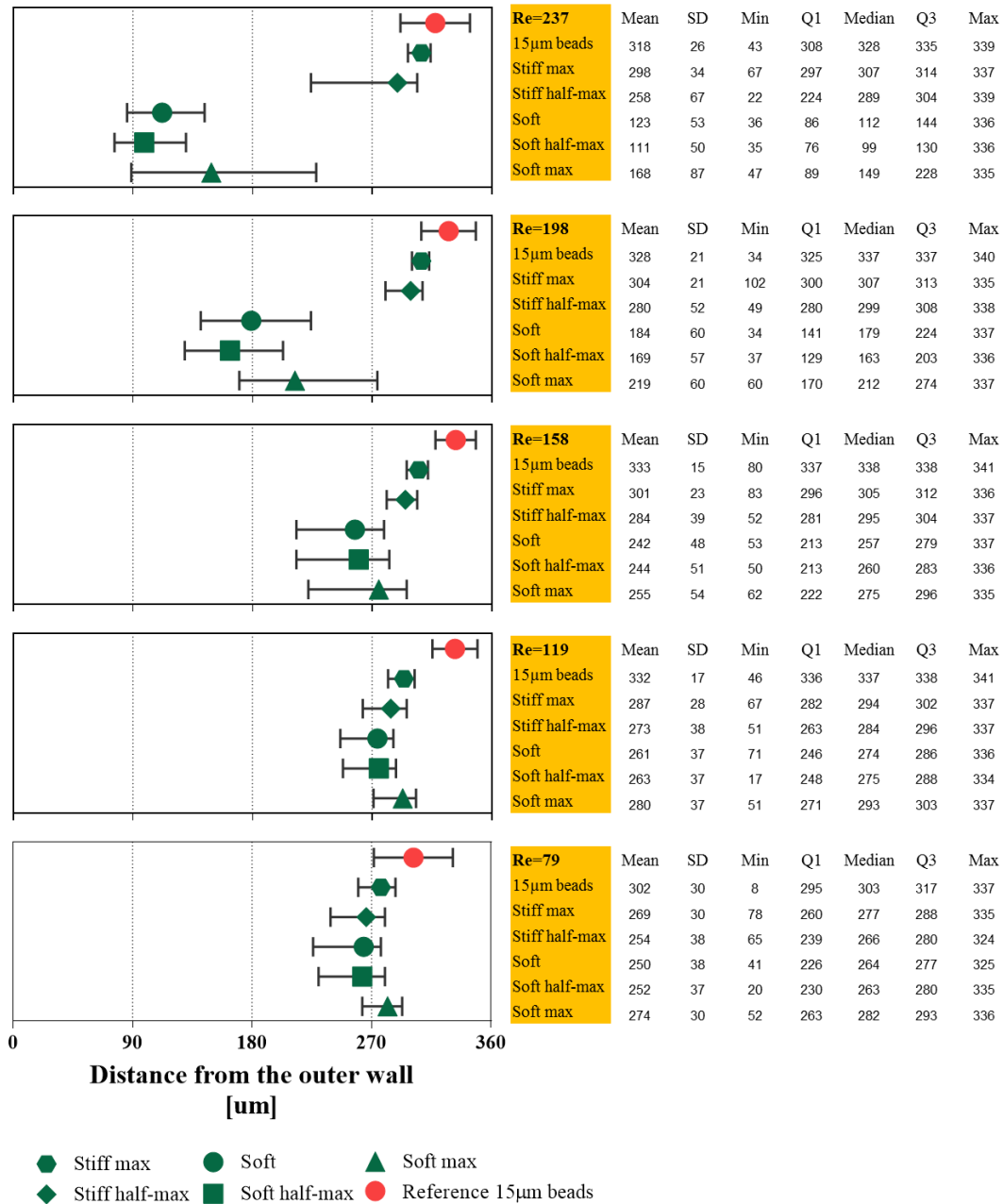
Cells viability after processing in spiral microchannels was assessed using Alexa Fluor® 488 Annexin V/Dead Cell Apoptosis Kit (ThermoFisher Scientific). Control cells as well as cells after processing were harvested by centrifugation at 200 g for 5 min and washed in cold PBS<sup>-/-</sup> and stained as per manufacturer's protocol. Briefly, after washing in PBS cells were re-suspended in annexin-binding buffer at around  $10^6$  cells/ml. 100  $\mu$ l aliquote of each sample was transferred to fresh centrifuge tube and 5  $\mu$ L Alexa Fluor® 488 annexin V and 1  $\mu$ L 100  $\mu$ g/mL PI working solution was added to each 100  $\mu$ L of cell suspensions. Cells were incubated in dark at room temperature for 15 min. After the incubation time samples were further diluted by adding 400  $\mu$ l annexin-binding buffer and analysed by flow cytometry (BD FACSCalibur), measuring the fluorescence emission at 530 nm (FL1) and  $>575$  nm (FL3).

## Appendix B

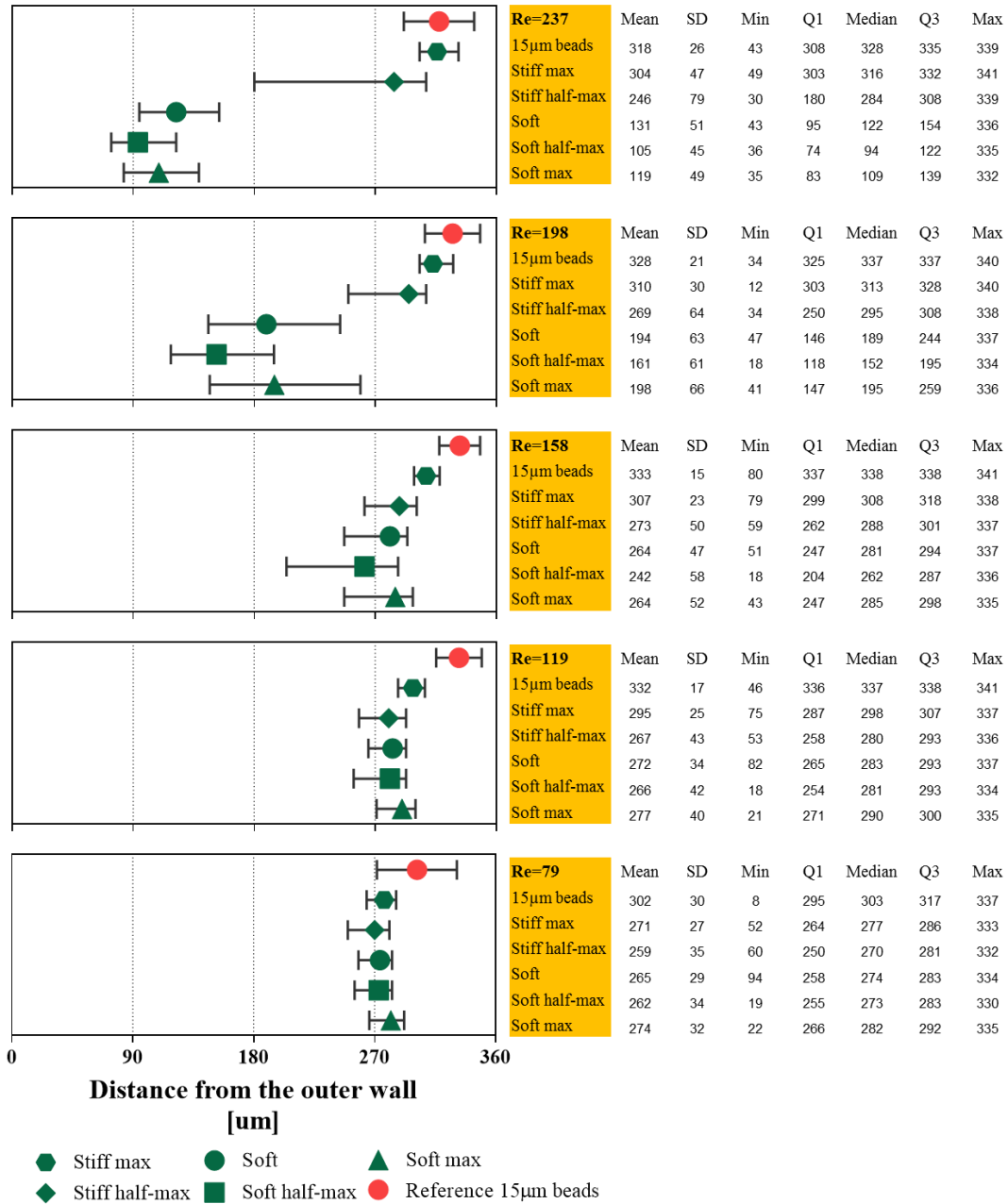
<b>Re=237</b>	Re=237	Mean	SD	Min	Q1	Median	Q3	Max
	Soft max	122	49	37	86	112	144	328
	Soft half-max	110	44	33	79	101	131	334
	Soft	132	50	38	98	124	156	335
	Stiff half-max	251	77	34	191	289	308	338
	Stiff max	305	45	33	304	316	331	341
	15 $\mu$ m beads	318	26	43	308	328	335	339
<b>Re=198</b>	Re=198	Mean	SD	Min	Q1	Median	Q3	Max
	Soft max	201	66	46	150	198	261	335
	Soft half-max	169	59	36	127	161	205	335
	Soft	203	62	46	155	201	256	337
	Stiff half-max	270	62	20	254	294	308	338
	Stiff max	310	29	63	303	313	327	339
	15 $\mu$ m beads	328	21	34	325	337	337	340
<b>Re=158</b>	Re=158	Mean	SD	Min	Q1	Median	Q3	Max
	Soft max	265	51	48	248	285	298	336
	Soft half-max	242	57	43	206	262	286	335
	Soft	265	46	47	251	282	295	337
	Stiff half-max	273	51	49	263	289	302	338
	Stiff max	306	24	61	299	308	318	338
	15 $\mu$ m beads	333	15	80	337	338	338	341
<b>Re=119</b>	Re=119	Mean	SD	Min	Q1	Median	Q3	Max
	Soft max	281	34	69	276	291	301	335
	Soft half-max	269	39	16	259	281	292	334
	Soft	273	33	40	266	283	293	335
	Stiff half-max	268	42	71	259	281	292	336
	Stiff max	294	24	67	287	297	306	337
	15 $\mu$ m beads	332	17	46	336	337	338	341
<b>Re=79</b>	Re=79	Mean	SD	Min	Q1	Median	Q3	Max
	15 $\mu$ m beads	302	30	8	295	303	317	337
	Stiff max	270	27	35	264	277	286	334
	Stiff half-max	259	36	49	249	270	281	332
	Soft	265	29	90	259	274	283	335
	Soft half-max	263	34	18	255	273	283	332
	Soft max	273	32	20	265	282	292	334

**Distance from the outer wall  
[ $\mu$ m]**

Tables showing statistical summary (mean and standard deviation from the mean (SD), median, 25<sup>th</sup> (Q<sub>i</sub>) and 75<sup>th</sup> (Q<sub>3</sub>) percentile as well as minimal (min) and maximal (max) measured value) of lateral equilibrium positions obtained for at least 10000 events for 15  $\mu$ m beads and cells from the cellular deformability model, in design I spiral channel with 360  $\times$  60  $\mu$ m cross-section, at five applied Re numbers for **replica I** out of three, expressed as distance from the outer wall [ $\mu$ m].



Hydrodynamic behaviour of cells of five different degrees of deformability (Soft max, soft half-max, soft, stiff half-max and stiff) in comparison to reference 15 μm beads, in design I spiral channel with 360 × 60 μm cross-section at five different flow rates corresponding to Re=79, 119, 158, 198 and 237 (as outlined in the tables on the right). The lateral equilibrium positions were measured as a distance from the outer wall (μm) at the end of the spiral channel and there were generated by image analysis. Here, it is reported as median (represented as the symbols) and the interquartile range (indicated by the short vertical lines). Vertical dotted lines indicate four sections of the channel corresponding to four outlets of the channel (0-90 μm-outlet A, 90-180 μm- outlet B, etc.). Events belonging to a given section have the highest probability of being captured within the corresponding outlet. Tables showing statistical summary (mean and standard deviation from the mean (SD), median, 25<sup>th</sup> (Qi) and 75<sup>th</sup> (Q3) percentile as well as minimal (min) and maximal (max) measured value) of latera equilibrium positions obtained for at least 10000 events for **replica II** out of three.



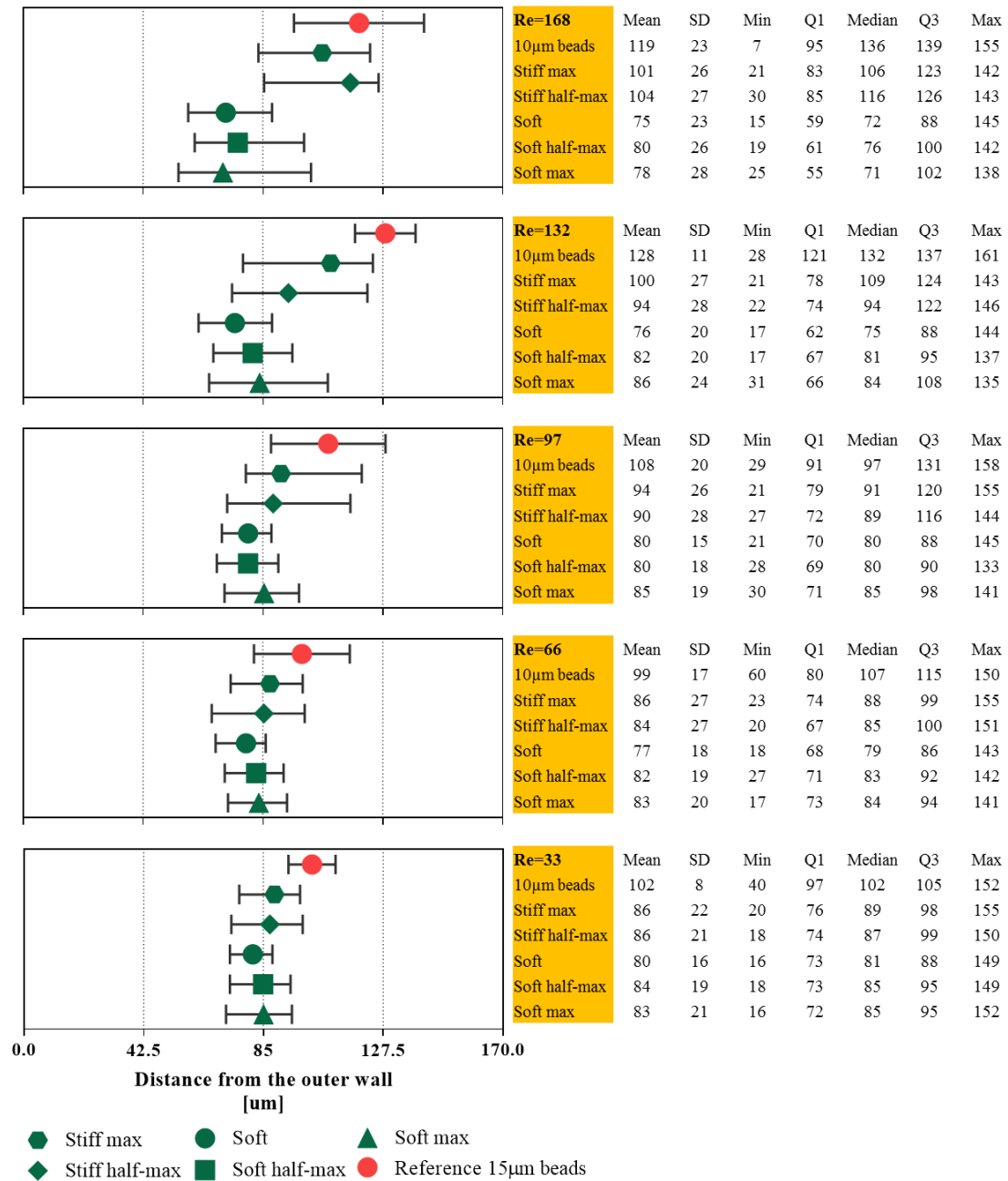
Hydrodynamic behaviour of cells of five different degrees of deformability (Soft max, soft half-max, soft, stiff half-max and stiff) in comparison to reference 15  $\mu$ m beads, in design I spiral channel with  $360 \times 60 \mu\text{m}$  cross-section at five different flow rates corresponding to  $Re=79, 119, 158, 198$  and  $237$  (as outlined in the tables on the right). The lateral equilibrium positions were measured as a distance from the outer wall ( $\mu\text{m}$ ) at the end of the spiral channel and there were generated by image analysis. Here, it is reported as median (represented as the symbols) and the interquartile range (indicated by the short vertical lines). Vertical dotted lines indicate four sections of the channel corresponding to four outlets of the channel (0-90  $\mu\text{m}$ -outlet A, 90-180  $\mu\text{m}$ - outlet B, etc.). Events belonging to a given section have the highest probability of being captured within the corresponding outlet. Tables showing statistical summary (mean and standard deviation from the mean (SD), median, 25<sup>th</sup> (Q1) and 75<sup>th</sup> (Q3) percentile as well as minimal (min) and maximal (max) measured value) of latera equilibrium positions obtained for at least 10000 events for **replica III** out of three.

## Appendix C

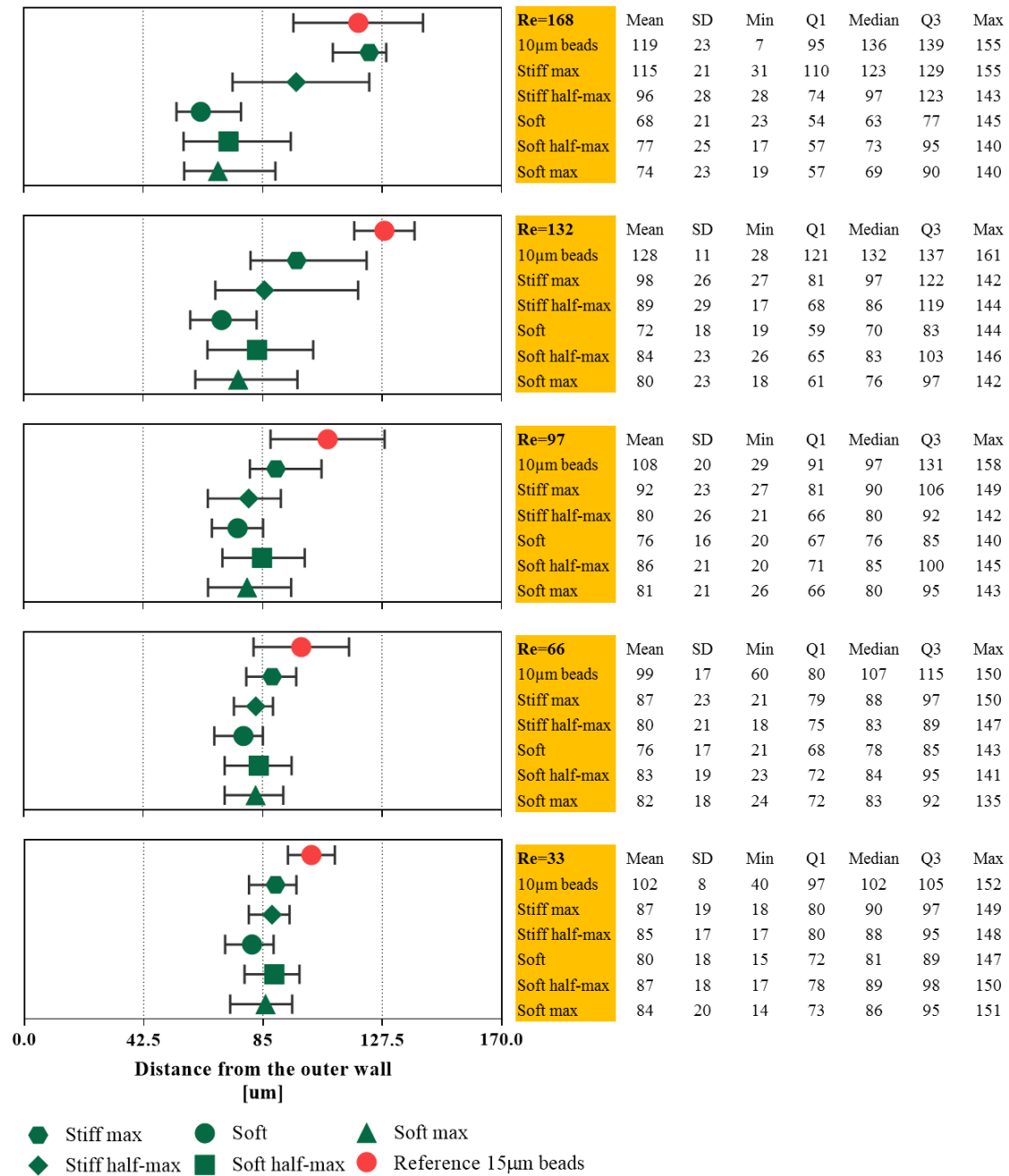
	Re	Distance from the outer wall [ $\mu\text{m}$ ]						
		Mean	SD	Min	Q1	Median	Q3	Max
<b>Re=168</b>	Re=168	Mean	SD	Min	Q1	Median	Q3	Max
	10 $\mu\text{m}$ beads	119	23	7	95	136	139	155
	Stiff max	113	21	34	102	121	128	143
	Stiff half-max	100	27	21	78	109	124	143
	Soft	68	21	20	54	62	79	161
	Soft half-max	80	26	20	59	74	96	142
	Soft max	75	24	19	57	70	92	142
<b>Re=132</b>	Re=132	Mean	SD	Min	Q1	Median	Q3	Max
	10 $\mu\text{m}$ beads	128	11	28	121	132	137	161
	Stiff max	101	25	29	84	107	123	147
	Stiff half-max	88	29	26	67	85	119	143
	Soft	75	18	23	63	74	86	141
	Soft half-max	84	23	20	66	83	102	143
	Soft max	80	23	15	62	77	97	162
<b>Re=97</b>	Re=97	Mean	SD	Min	Q1	Median	Q3	Max
	10 $\mu\text{m}$ beads	108	20	29	91	97	131	158
	Stiff max	89	25	25	76	87	107	144
	Stiff half-max	79	24	21	64	79	92	148
	Soft	85	20	24	70	85	99	141
	Soft half-max	85	20	24	70	85	99	141
	Soft max	82	21	20	66	81	97	141
<b>Re=66</b>	Re=66	Mean	SD	Min	Q1	Median	Q3	Max
	10 $\mu\text{m}$ beads	99	17	60	80	107	115	150
	Stiff max	82	26	18	70	84	94	145
	Stiff half-max	80	21	18	75	83	89	148
	Soft	78	18	21	69	80	87	149
	Soft half-max	84	18	19	74	85	96	144
	Soft max	82	18	21	71	83	93	138
<b>Re=33</b>	Re=33	Mean	SD	Min	Q1	Median	Q3	Max
	10 $\mu\text{m}$ beads	102	8	40	97	102	105	152
	Stiff max	87	19	18	80	90	97	150
	Stiff half-max	84	18	17	78	87	94	150
	Soft	82	17	19	74	83	90	149
	Soft half-max	86	19	18	77	89	98	148
	Soft max	84	20	17	73	86	96	150

Tables showing statistical summary (mean and standard deviation from the mean (SD), median, 25<sup>th</sup> (Q1) and 75<sup>th</sup> (Q3) percentile as well as minimal (min) and maximal (max) measured value) of lateral equilibrium positions obtained for at least 10000 events for 15  $\mu\text{m}$  beads and cells from the cellular deformability model, in design II spiral channel with  $170 \times 30 \mu\text{m}$  cross-section, at five applied Re numbers for **replica I** out of three, expressed as distance from the outer wall [ $\mu\text{m}$ ].





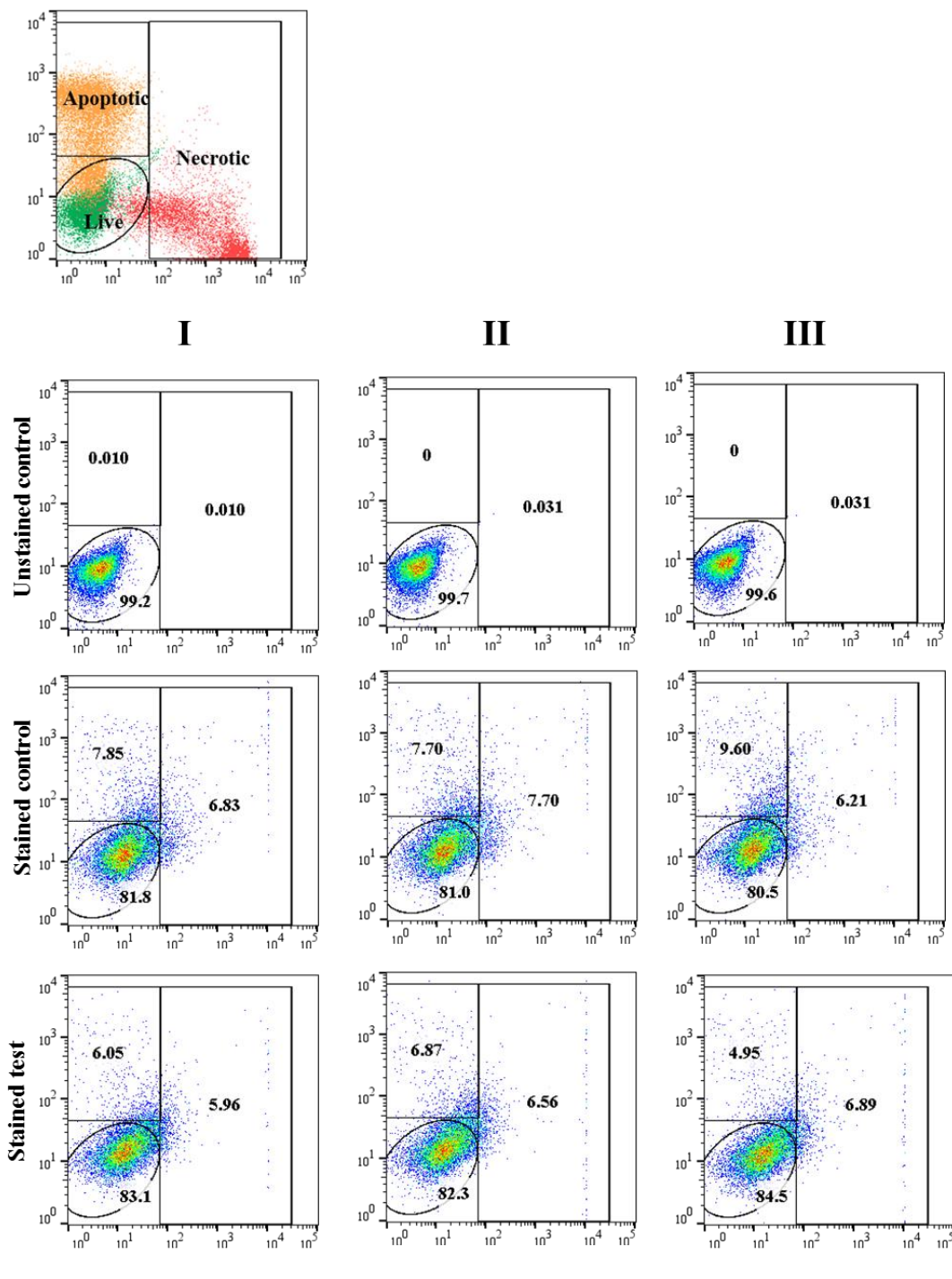
Hydrodynamic behaviour of cells of five different degrees of deformability (Soft max, soft half-max, soft, stiff half-max and stiff) in comparison to reference 15 µm beads, in design II spiral channel with  $170 \times 30$  µm cross-section at five different flow rates corresponding to  $Re=33, 66, 97, 132$  and  $168$  (as outlined in the tables on the right). The lateral equilibrium positions were measured as a distance from the outer wall (µm) at the end of the spiral channel and there were generated by image analysis. Here, it is reported as median (represented as the symbols) and the interquartile range (indicated by the short vertical lines). Vertical dotted lines indicate four sections of the channel corresponding to four outlets of the channel (0-90. µm-outlet A, 90-180 µm- outlet B, etc.). Events belonging to a given section have the highest probability of being captured within the corresponding outlet **and** tables showing statistical summary (mean and standard deviation from the mean (SD), median, 25<sup>th</sup> (Qi) and 75<sup>th</sup> (Q3) percentile as well as minimal (min) and maximal (max) measured value) of latera equilibrium positions obtained for at least 10000 events for **replica II** out of three.



Hydrodynamic behaviour of cells of five different degrees of deformability (Soft max, soft half-max, soft, stiff half-max and stiff) in comparison to reference 15 µm beads, in design II spiral channel with 170 × 30 µm cross-section at five different flow rates corresponding to Re=33, 66, 97, 132 and 168 (as outlined in the tables on the right) . The lateral equilibrium positions were measured as a distance from the outer wall (µm) at the end of the spiral channel and there were generated by image analysis. Here, it is reported as median (represented as the symbols) and the interquartile range (indicated by the short vertical lines). Vertical dotted lines indicate four sections of the channel corresponding to four outlets of the channel (0-90. µm-outlet A, 90-180 µm- outlet B, etc.). Events belonging to a given section have the highest probability of being captured within the corresponding outlet **and** tables showing statistical summary (mean and standard deviation from the mean (SD), median, 25<sup>th</sup> (Q1) and 75<sup>th</sup> (Q3) percentile as well as minimal (min) and maximal (max) measured value) of latera equilibrium positions obtained for at least 10000 events for **replica II** out of three.

## Appendix D

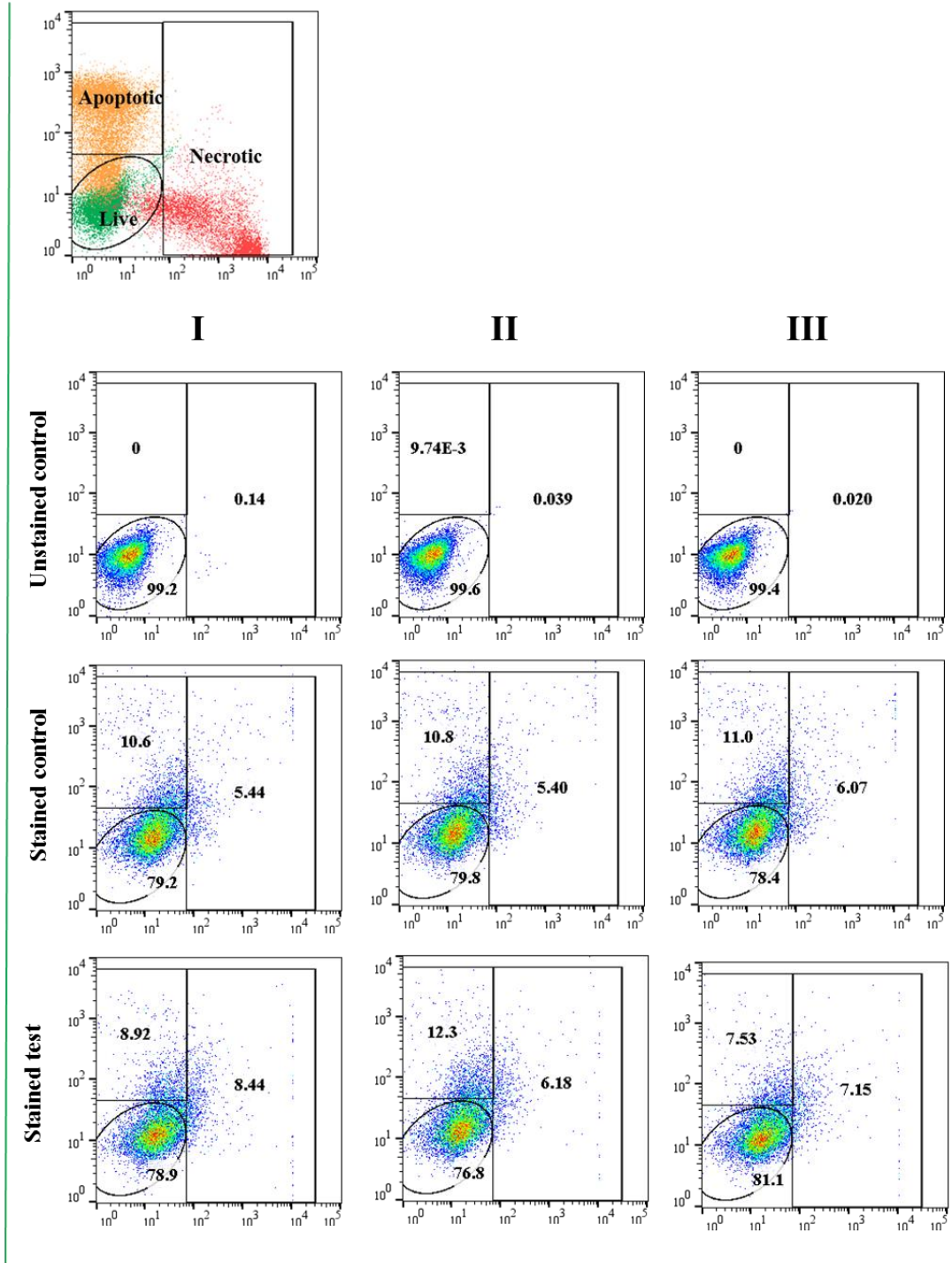
Alexa Fluor® 488 annexin V



### Propidium iodide fluorescence

Summary of flow cytometric viability assay. On the top- an exemplary scatter plot showing gating strategy for live cell (green, negative for both Alexa Fluor 488-annexin V and propidium iodide (PI) fluorescence), apoptotic cells (orange, annexin V-positive and PI-negative) and necrotic (red, annexin V-positive and PI-positive). Summary of flow cytometric assessment of the presence of live, apoptotic and necrotic Jurkat cells before (stained control and after processing (stained test) in design I spiral channel with  $360 \times 60 \mu\text{m}$  cross-section at highest applied flow rate ( $Re=237$ ) for three replicas.

**Alexa Fluor® 488 annexin V**



**Propidium iodide fluorescence**

Summary of flow cytometric viability assay. On the top- an exemplary scatter plot showing gating strategy for live cell (green, negative for both Alexa Fluor 488-annexin V and propidium iodide (PI) fluorescence), apoptotic cells (orange, annexin V-positive and PI-negative) and necrotic (red, annexin V-positive and PI-positive). Summary of flow cytometric assessment of the presence of live, apoptotic and necrotic Jurkat cells before (stained control and after processing (stained test) in design I spiral channel with  $360 \times 60 \mu\text{m}$  cross-section at highest applied flow rate ( $Re=237$ ) for three replicas.

## **Chapter 5. Purifying stem cell-derived red blood cells: Translating cell mechanical properties into complete high-throughput label-free downstream processing strategy.**

### **Highlights**

- Combining cells mechanical characteristic and the phenomenon of deformability-induced lift force ( $F_D$ ) (described in **Chapter 4**) in spiral microchannels, a complete purification strategy for label-free passive mRBC purification has been proposed, consisting of two steps: (1) processing in spiral microchannel enhanced by (2) membrane filtration, reaching 99% purity.
- End-product of CB CD34+ cells *in vitro* erythroid differentiation, derived from two additional donors have been characterised and compared to results described in **Chapter 3**- demonstrating donor-to-donor-variability

### **5.1. Introduction**

In order to address the limiting lack of suitable purification strategies of mRBCs, herein, we propose a complete customised label-free downstream processing approach, based solely on mRBC profoundly characterised mechanical properties. It is a two-step process consisting of cell processing in a spiral microchannel and membrane filtration. As discussed in the introduction, due to simplicity in operation, low manufacturing cost and proven scalability by parallelisation (allowing processing millions of cells per minute and millilitres of medium per minute) inertial focusing in spiral microchannels has been recognised as an attractive approach for high-throughput cell sorting [90] for myriad point of care and clinical diagnostics (please consult **Table 1.3 in Chapter 1**). Particles of different sizes interact to a different degree with the fluid flow pattern generated within the spiral channel and that leads to particles ordering and separation. The deformable nature of cells adds complexity to their ordering within the spiral channels and in the previous **Chapter 4** and Guzniczak et al. 2018 [118] it was reported that at sufficiently high flow rates, particles of the same size but different deformability adopt substantially different equilibrium positions within the channel cross-section.

In this study, for the first time, the previously observed contribution of the deformability-induced lift force to the differential focusing of particles of the same size but contrasting deformable properties within a spiral channel, has been translated into an effective label-free purification protocol for mRBC derived from CB CD34+ cells. This approach offers

a viable alternative to FACS and MACS for sorting mRBC at industrial scale in a label-free manner up to high purities without compromising cell quality, consequently creating a route to bring mRBC into clinical use.

## **5.2. Results and Discussion**

### **5.2.1. Sample characterisation**

As described in **Chapter 3**, CB CD34+ cells undergo *in vitro* differentiation into mRBC over the course of 21 days protocol by balancing the opposite effects of proliferation-promoting factors and differentiation-inducing factors. During this time, cells change their morphology, they decrease in size, lose some intracellular structures, start producing haemoglobin and the nucleus becomes smaller and more condensed to eventually become expelled during the enucleation event [128][129]. In *in vivo* circumstances, the expelled nuclei are removed by macrophages, while during the *in vitro* erythropoiesis they remain in the culture [146]. Although the differentiation process is strictly controlled by adjusting the cell culture conditions, some of the stem cells will not differentiate fully, meaning they will remain at earlier development stages. Consequently, the end-product of the differentiation protocol is a heterogeneous population containing enucleated mRBC, partially differentiated or undifferentiated nucleated cells as well as free-floating nuclei.

The first step to develop the label-free strategy for purifying mRBC from the contaminant nucleated cells and free-floating nuclei was to identify if there was a unique set of label-free markers (label-free marker means that no modifying agents (e.g. antibodies) have to be added in order to reveal them) such as cell size and deformability that would allow characterisation of each of the subsets within the final product. In order to identify differences in cell size and deformability, the cells were characterised using image analysis of cytopspin slides and flow cytometry (forward light scatter parameter (FSC-A) for relative size measurement) and real-time fluorescence and deformability cytometry (RT-FDC) [125], at the end of the differentiation procedure. To quantify the degree of the size and deformability overlap, receiver operating characteristic (ROC) curves were plotted and the corresponding area under the curve (AUC) was calculated.

### **5.2.2. Size measurements**

Size measurements of events belonging to one of the three subpopulations have been proven challenging due to their heterogeneous nature. RT-DC allows for size measurements and it is recommended to do so in the reservoir section of the chip- where cells do not distort from their original shape due to negligible shear. Differentiating CB CD34+ were

characterised, using RT-FDC, and they were measured in a mixed population fluorescently stained to distinguish between enucleated and nucleated cells and nuclei. Currently, it is technically impossible to monitor fluorescent signal in the reservoir section. Due to this reason, to estimate the size of each subpopulation cells were fixed onto a glass slide and stained for the nucleus (purple) and cytoplasm (pink) as shown in **Fig. 5.1 a**, which allowed to discriminate between enucleated and nucleated cells as well as free floating nuclei. Cell size was reported as area and expressed in  $\mu\text{m}^2$  (**Fig. 5.1 b**). As per this approach, nuclei are smaller ( $24.3 \pm 7.6 \mu\text{m}^2$ , mean  $\pm$  SD) than enucleated ( $75.7 \pm 22.4 \mu\text{m}^2$ ) and nucleated ( $77.3 \pm 27.5 \mu\text{m}^2$ ) cells. However, the same cell population was analysed using flow cytometry and each subset was plotted for the forward light scatter (FSC-A) parameter. **Fig. 5.1 c** (and **Appendix E** for three replicas) shows a clear overlap in size between enucleated cells (pink) and nuclei (grey), while nucleated cells (purple) remain the largest within the sample.

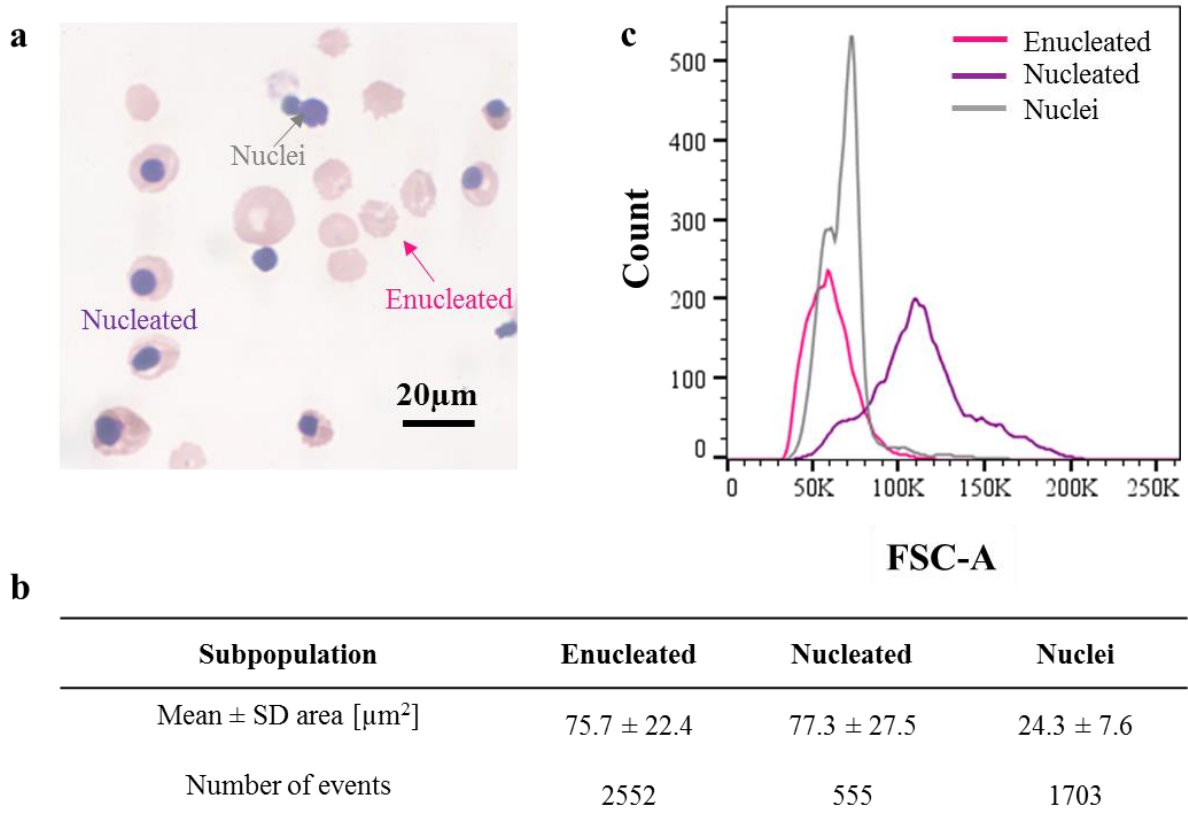


**Fig. 5.1**

*Characterisation of enucleated and nucleated cells as well as expelled nuclei present in the end-product of CB CD34+ undergoing in vitro erythropoiesis. (a) An exemplary cytospin image of the end product of the differentiation protocol of cord blood CD34+ cells into red blood cells. Cytoplasm is stained in pink and nuclei are stained in dark purple. The scale bar corresponds to 20  $\mu\text{m}$ . (b) Table summarising size measurement (expressed as cell area in  $\mu\text{m}^2$ ) obtained from cytospin image analysis for enucleated cells, nucleated cells as well as free floating nuclei (c) Histogram of FSC-A (forward light scatter) parameters measured using flow*



*cytometry, reflecting the relative size of enucleated cells (pink), nucleated cells (purple) and the free-floating nuclei (grey). For summary of triplicate results please consult **Appendix E***

The contradictory findings are most probably the consequence of the nature of sample preparation for each technique. In contrast to cytopsin, flow cytometry allows size measurement for live cells in suspension. FSC intensity produces a voltage which is proportional to the cell diameter, however, cell size is not reported in physical units. In the cytopsin technique deformable enucleated cells spread on the slide more than rigid nuclei, consequently appearing larger than they really are. Thus, if the physical value plays an important role (e.g. for fine-tuning sorting device dimensions) a supplementary approach to flow cytometry is required.

Combining information obtained from flow cytometric measurements and cytopsin image analysis, it has been concluded that the cell diameter at the end of the differentiation protocol ranges between  $5.5 \pm 0.8 \mu\text{m}$  and  $9.7 \pm 1.7 \mu\text{m}$ , within this range enucleated cells and nuclei occupied the smaller side of the spectrum with  $\sim 94\%$  size overlap (AUC=0.95, 94 and 93 for three independent measurements, **Fig. 5.2 a**). Despite the pronounced FSC-A peak resolution between enucleated and nucleated cells, 7-18 % (AUC= 68, 57 and 64, **Fig.5.2 a**) of cells remain within the same size range.



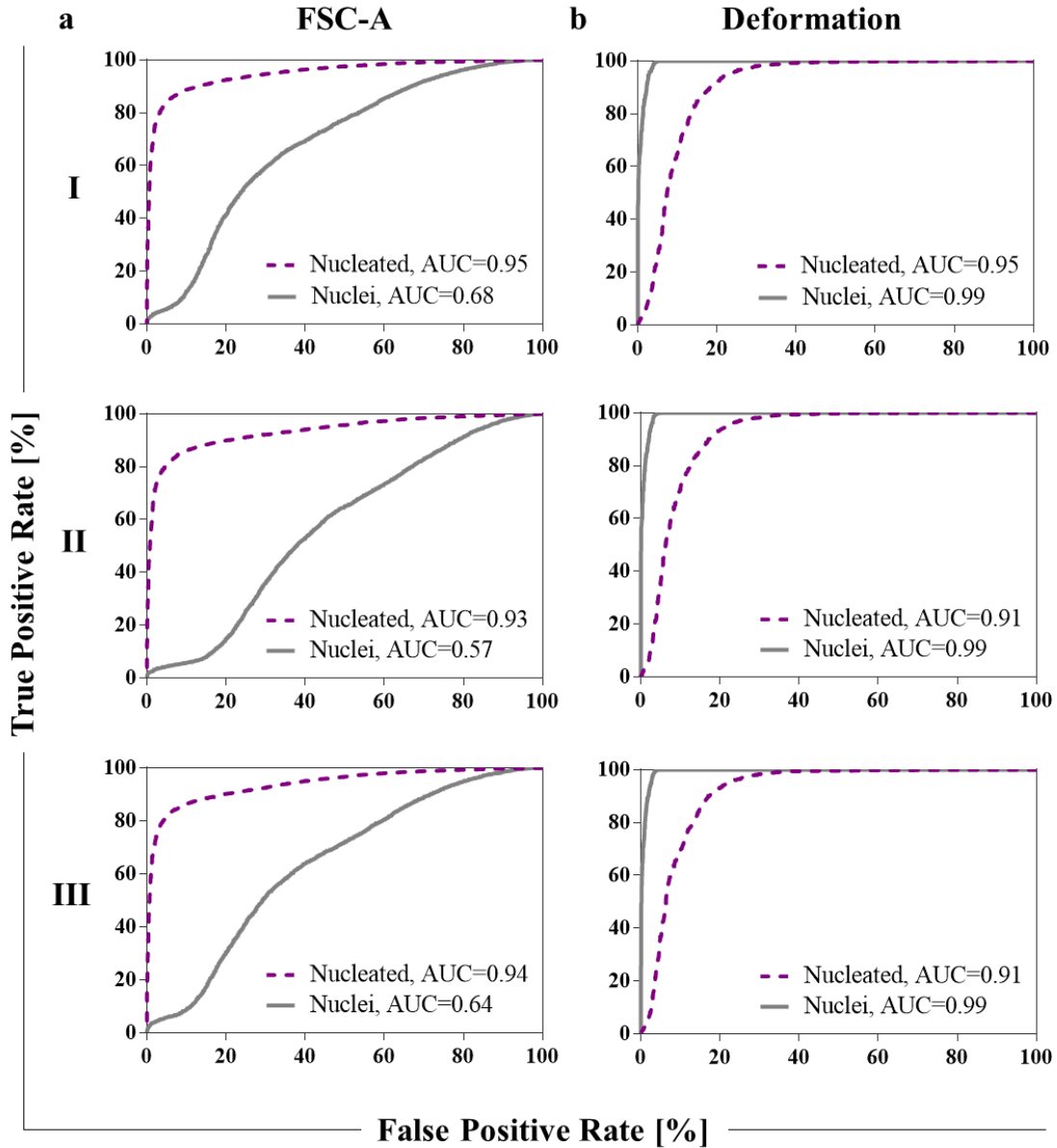


**Fig. 5.2**

Receiver Operating Characteristic (ROC) curves were plotted for (a) size (expressed as FSC-A parameter) and (b) deformability [-] for enucleated versus nucleated cells (purple-dashed) and enucleated cells versus nuclei (grey) at the end of the differentiation protocol for three replicas for donor I. The True Positive Rate is defined as the number of enucleated cells measured for a certain cut-off point (size or deformability) and divided by the total number of enucleated cells. The False Positive Rate is the corresponding number of nucleated cells (resp. nuclei) divided by the total number of enucleated cells (resp. nuclei) for the same cut-off. The Area Under the Curve (AUC) was calculated to quantify the size and deformability overlaps.

### 5.2.3. Deformability measurements

RT-FDC is a high-throughput (thousands of events per minute) microfluidic platform that enables mechanotype analysis of cells within a heterogeneous sample with no necessity of

pre-sorting into pure populations, due to the integration of fluorescent signal for confirmation of cell identity [125], as described in **Chapter 2**.

**Fig. 5.3 a & b** displays deformability measurements for enucleated and nucleated cells and nuclei. Comparison of events belonging to each subpopulation (indicated by colour-coded contour plots in **Fig. 5.3 a**) reveals that the free-floating nuclei exposed to shear stress behave like rigid spheres ( $D=0.028 \pm 0.016$ , mean  $\pm$  SD) while enucleated cells deform substantially from their original spherical shape ( $D= 0.289 \pm 0.084$ ).

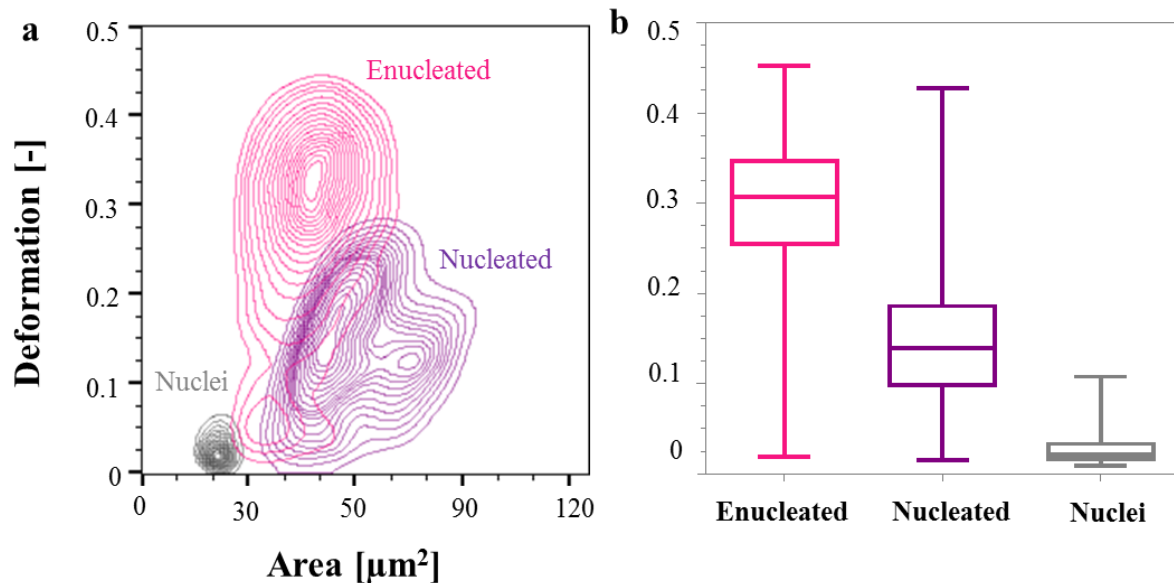


**Fig. 5.3**

*RT-FDC Characterisation of enucleated (pink) and nucleated (purple) cells as well as expelled nuclei (grey) present in the end-product of CB CD34+ undergoing in vitro erythropoiesis. (a) Equal probability contour plots (the same number of cells fall between each pair of contour lines) of deformation vs cell size (expressed as projected cell area in  $\mu\text{m}^2$ ) for enucleated and nucleated cells and nuclei generated using the RT-FDC. Measurements were performed at  $0.12 \mu\text{l}/\text{min}$  flow rate in a  $20 \mu\text{m} \times 20 \mu\text{m}$  channel ( $n=10,000$  cells) (b) Box plots summarising the deformation of enucleated/nucleated cells and nuclei, where the line in the box represents the median, the box itself represents data from lower and upper quartile and the whiskers correspond to the lowest and highest extreme values. For summary of triplicate results please consult **Appendix E***

Hence, these subpopulations are almost 100% separated ( $\text{AUC}=0.99$ , for three replicas, **Fig. 5.2 b**). Nucleated cells also deform ( $D=0.143 \pm 0.062$ ), however as reported previously, the presence of the stiff condensed nucleus limits their further deformation and that distinguishes more than 90% of them from enucleated cells ( $\text{AUC}=0.91, 0.95$  and  $0.91$ , for each of three replicas respectively, **Fig. 5.2 b**).

### 5.2.4. Sorting- principles and optimisation

Traditionally, spiral-shaped microchannels have been used for sorting cells based on size differences. Cells traveling within the channel experience inertial lift force and Dean drag, and if cells travel a distance long enough, these forces balance and situate cells at distinct lateral equilibrium positions, which depend upon particle size [147][90]. As shown in **Fig. 5.3** in the design used in this study, smaller cells are positioned closer to the inner wall, and with the increasing size, they move closer to the channel centreline. As previously reported [118], at sufficiently elevated Re numbers there is a distinct hydrodynamic behaviour of cells of the same size but different deformability. At high Re numbers, stiff cells remain focused close to the inner wall, while their softer counterparts experience additional drag (the consequence of the deformability-induced lift force[117]) and they travel across the channel to be equilibrated near the outer wall.

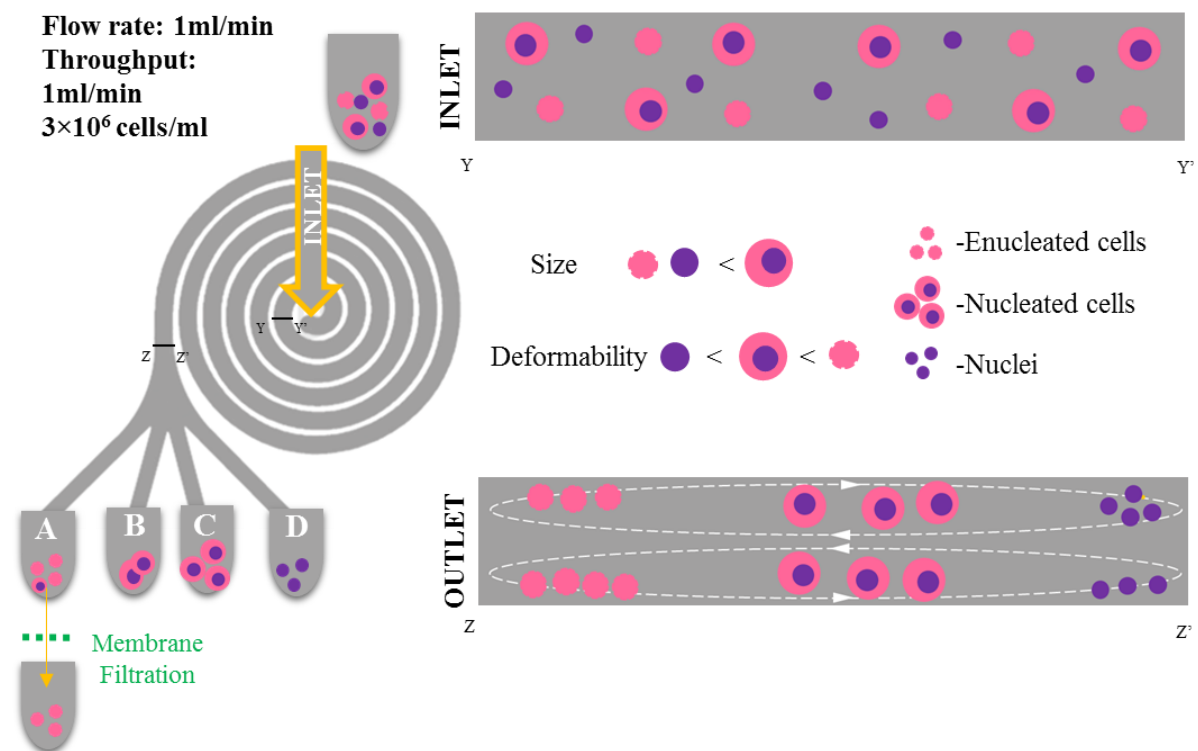


**Fig. 5.3**

*Proposed label-free strategy for sorting CB CD34<sup>+</sup>-derived RBC. The input sample contains mRBC (enucleated cells) as well as nucleated cells and expelled nuclei. Each population is characterised by a unique combination of size and deformability range used for sorting. Nuclei are small and rigid, enucleated cells are within the size range of nuclei, but are more deformable while nucleated cells are the largest of all. The sorting protocol consists of two steps: first, the sample is processed in a spiral microchannel with a rectangular cross-section*

*(170x30  $\mu\text{m}$ ), 6 loops, 1 inlet and 4 outlets (A, B, C and D). Cells align in the spiral channel at distinct lateral equilibrium positions depending on their size and deformability, facilitating their capture in one of the four outlets. The majority of the desired enucleated cells is captured in outlet D with some contaminant nucleated cells, which are further removed by membrane filtration.*

In order to identify optimal conditions to take advantage of the deformability-induced lift force for the mRBC purification, the device performance has been tested with pre-sorted by FACS pure populations of enucleated and nucleated cells and nuclei. Each of the subpopulations was run separately at gradually increasing flow rates from 0.2 to 1 ml/min at intervals of 0.2 ml/min (**Fig. 5.4 a**). The separation potential of enucleated cells from nucleated (**Fig. 5.4 b**) and nuclei (**Fig. 5.4 c**), was estimated for each tested flow rate by generating ROC curves and calculating the AUC. At lower flow rates (0.2, 0.4 and 0.6 ml/min) all three subpopulations were pushed toward the inner wall. Enucleated and nucleated cells occupy the same section of the channel (enucleated:  $100 \pm 24 \mu\text{m}$ ,  $123 \pm 22 \mu\text{m}$  and  $131 \pm 23 \mu\text{m}$ , nucleated:  $110 \pm 20 \mu\text{m}$ ,  $125 \pm 15 \mu\text{m}$  and  $134 \pm 11 \mu\text{m}$  at 0.2, 0.4 and 0.6 ml/min, respectively) with a substantial overlap in the assembled lateral equilibrium position (AUC= 0.62, 0.51 and 0.52, for 0.2, 0.4 and 0.6 ml/min, respectively) closer to the channel centreline. Increasing flow rate to 1 ml/min triggered the characteristic shift of more deformable enucleated cells toward the outer wall to the equilibrium lateral position at  $36 \pm 21 \mu\text{m}$ , while less deformable nucleated cells recapitulated the unfocused transition pattern ( $103 \pm 32 \mu\text{m}$ ) observed for enucleated cells at 0.8 ml/min ( $103 \pm 33 \mu\text{m}$ ). Except for the 0.2 ml/min flow rate, nuclei always remained focused along the inner wall in a fairly tight stream ( $151 \pm 23 \mu\text{m}$  at 0.4 ml/min,  $156 \pm 11 \mu\text{m}$  at 0.6 ml/min,  $158 \pm 11 \mu\text{m}$  at 0.8 ml/min and  $154 \pm 18 \mu\text{m}$  at 1ml/min). In conclusion, theoretically, operating at 1ml/min would allow separation of 96% of nucleated cells (AUC=0.96) and 99% of nuclei (AUC=0.99%) from the enucleated cells.

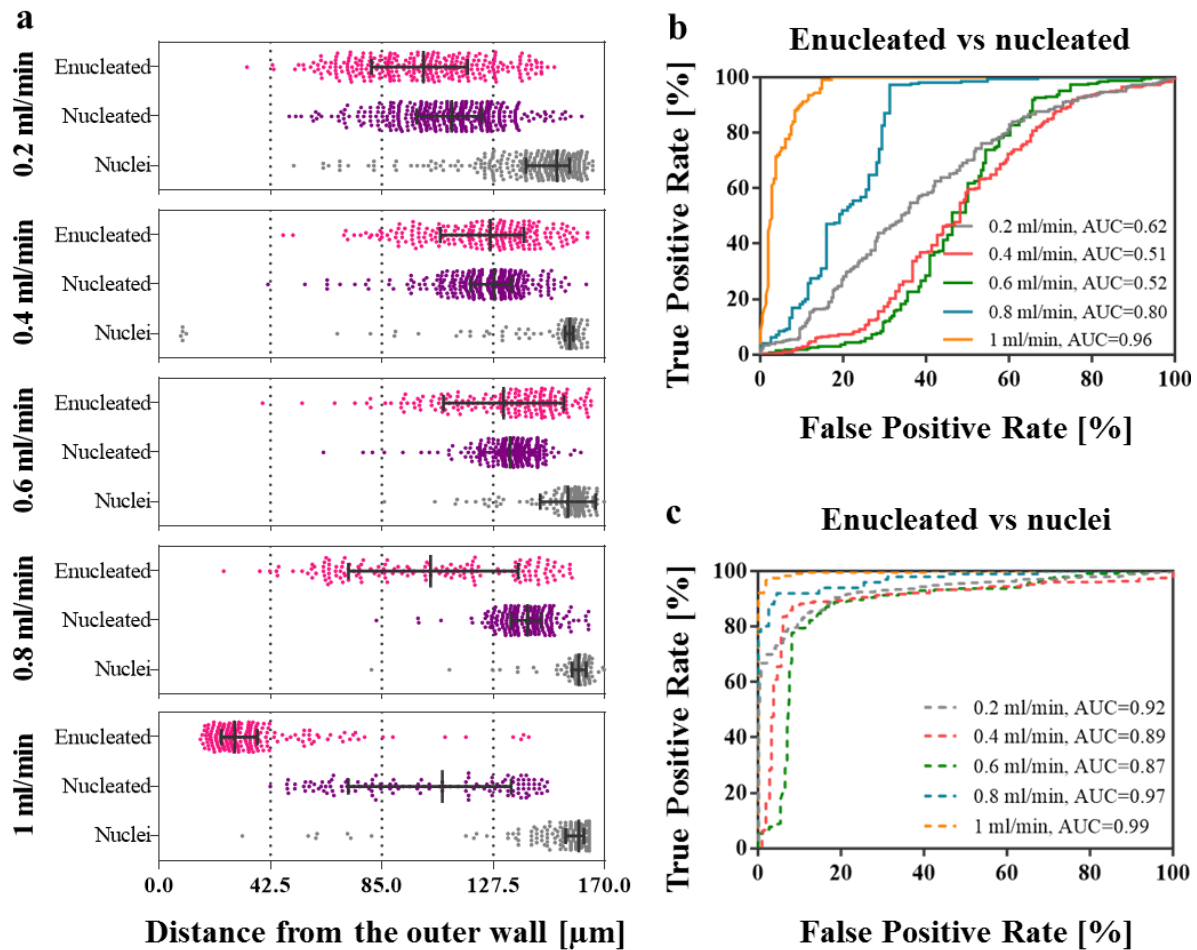


**Fig. 5.4**

Characterising the spiral channel performance with pure populations of enucleated and nucleated cells as well as expelled nuclei. (a) The hydrodynamic behaviour of enucleated (pink) and nucleated (purple) cells and free-floating nuclei (grey) is assessed in a spiral channel with a  $30 \times 170 \mu\text{m}$  cross-section at five different flow rates (0.2, 0.4, 0.6, 0.8 and 1 ml/min). Lateral equilibrium positions are measured as a distance from the outer wall ( $\mu\text{m}$ ) at the end of the spiral channel. Here, data are reported as median (represented as the longest vertical line) and the interquartile range (indicated by the short vertical lines) on top of scatter plots, where each dot represents one event. Around 200 events are shown for each subpopulation. Vertical dotted lines indicate four sections of the channel corresponding to four outlets of the channel (0-42.5  $\mu\text{m}$ - outlet A, 42.5-85  $\mu\text{m}$ - outlet B, etc.). Events belonging to a given section have the highest probability of being captured within the corresponding outlet.

Receiver Operating Characteristic (ROC) curves were plotted for lateral equilibrium position for (b) enucleated cells versus nucleated cells and (c) enucleated cells versus nuclei for each applied flowrate. The True Positive Rate is defined as the number of enucleated cells found at a given lateral position and divided by the total number of enucleated cells. The False Positive Rate is the corresponding number of nucleated cells (resp. nuclei) divided by the total number of nucleated cells (resp. nuclei) for the same cut-off. To determine which of the applied flow rate ensures the best separation efficiency the Area Under the Curve (AUC) was calculated.

### 5.2.5. mRBC purification process

Differences in hydrodynamic behaviour of enucleated and nucleated cells, as well as nuclei observed at a 1ml/min flow rate, was translated and incorporated into a label-free purification process. The heterogeneous end product of the differentiation protocol was injected into the spiral microchannel at the optimal flow rate at a concentration of around  $3 \times 10^6$  cell/ml. **Fig. 5.5a** shows an averaged fraction of each subset in the input sample as well as collected at the four outlets for three independent replicas. Enucleated cells constituted around 20-25% of the starting sample and as predicted, due to their deformable nature, the majority ( $92 \pm 0.2\%$ , mean  $\pm$  SD, recovery **Fig. 5.5 b**) of them were hydrodynamically directed to the outlet A (closest to the outer wall). The purity at each outlet was assessed using flow cytometry (for summary of scatter plots for triplicate results please consult **Appendix F**).

Enucleated cells in the best performing outlet A were enriched  $3.2 \pm 0.04$  (**Fig. 5.5 c**) reaching  $71 \pm 3\%$  purity (**Fig. 5.5 a**), where majority of the nuclei were depleted (enrichment ratio  $0.05 \pm 0.02$  (**Fig. 5.5 c**), recovery  $1.7 \pm 0.43\%$  (**Fig. 5.5 b**), purity  $1.8 \pm 0.54\%$  (**Fig. 5.5 a**)) and nucleated cells constituted the main contaminant (purity  $26.6 \pm 2.8\%$ , **Fig. 5.5 a**).

Transfusion of nucleated cells poses leucemogenic risk [3], thus this product should be further purified if intended for clinical application. That was achieved by adding a filtration step after processing in the spiral channel (**Fig. 5.3**). Cells collected at the outlets A and B were passed through  $3\mu\text{m}$  polycarbonate Isopore<sup>TM</sup> filter membrane counted and assessed by flow cytometry (**Appendix G**). This enhanced purity of enucleated cells collected at the outlet A to 99% (**Fig. 5.5 d**). The high purity, however, was a trade-off for recovery since during this process 50-70% of enucleated cells were lost (**Fig. 5.5 e**). Only 5% of enucleated cells was found in outlet B, but the recovery rate after filtration of the sample was much higher than for outlet A, reaching  $86 \pm 13\%$  (**Fig. 5.5 e**), however in return the purity was compromised ( $93.0 \pm 6.61\%$ , **Fig. 5.5 d**). For the overall performance of the purification process, I think it is sensible to sacrifice a fraction of the cell material in order to maintain highest possible purity which is one of the greatest priorities for the safety of any cell therapy products[148].

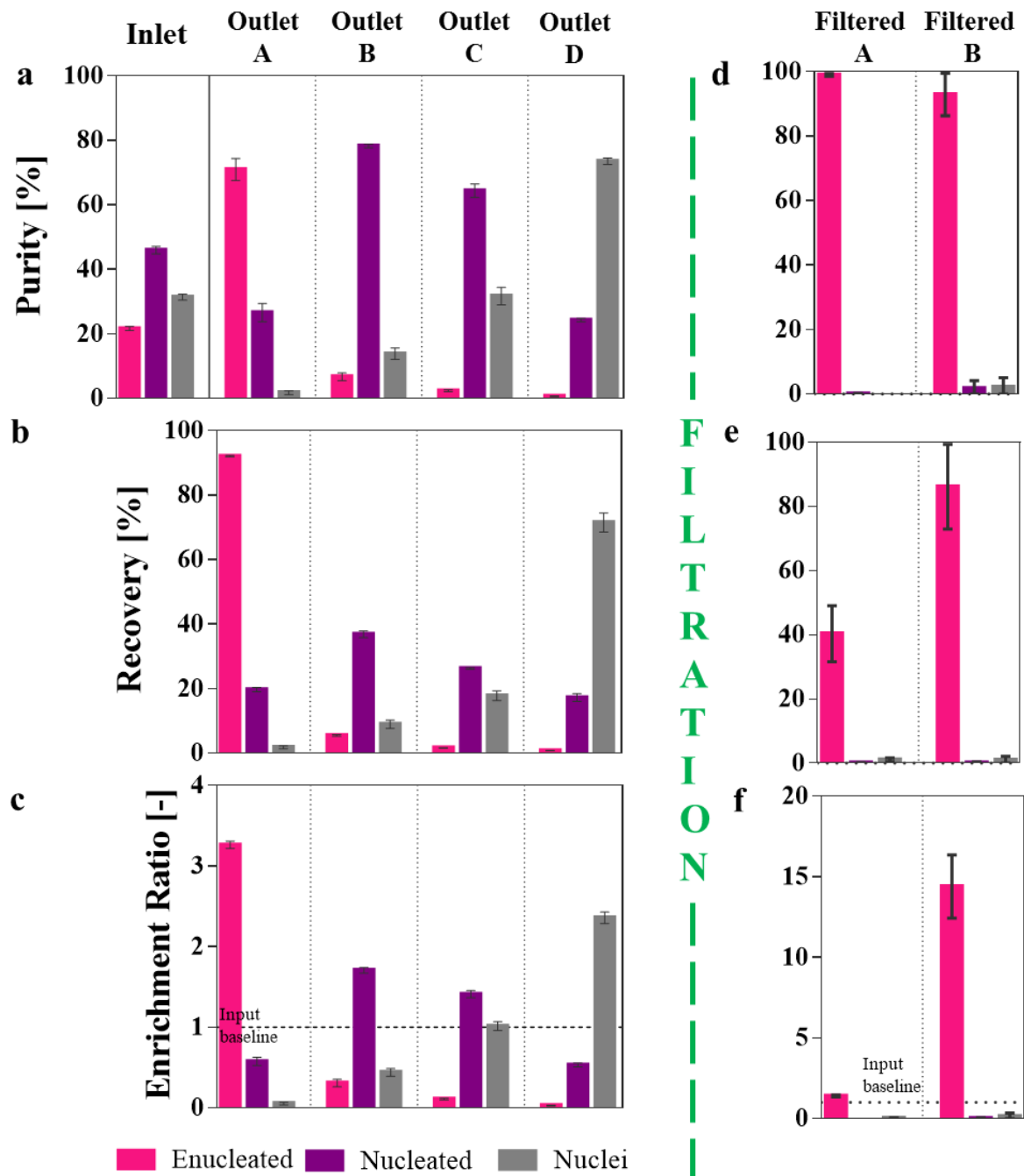


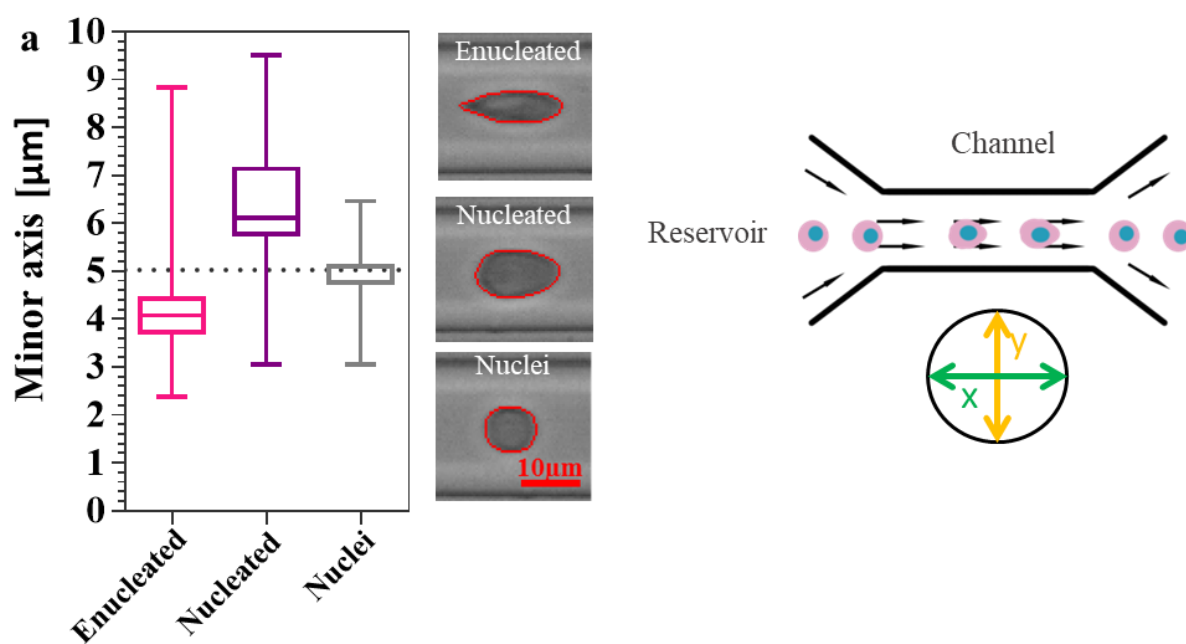
**Fig. 5.5**

Characterisation of the label-free mRBC purification process. Separation efficiency of enucleated cells (pink) from contaminant nucleated cells (purple) and nuclei (grey) after processing in a spiral channel with a  $30 \times 170 \mu\text{m}^2$  cross-section and four outlets (A -closest to the outer wall, B, C and D) at 1 ml/min flow rate (a, b & c) and enhanced by filtration (d, e & f). A filtration step was performed only on cells collected at the best performing outlets (A and B). Both approaches were characterised with three parameters: purity, recovery and enrichment ratio. The process validation was performed with three replicas, the bars representing the mean value and error bars the standard deviation of the mean. Dotted lines on the enrichment ratio diagrams represent input baseline.

### 5.2.6. Filtration justifications

Prior to identifying the next best approach to remove the contaminant residues in the collected samples after processing in the spiral channel, we had to understand their properties. Choosing membrane filtration as the purity enhancing step in the mRBC purification workflow was motivated with the observation that cell deformability under applied load is determined not only by cytoskeletal properties [52] but also the presence and properties of nucleus [41][136]. At the very last stages of the differentiation procedure, the enucleated and nucleated cells indicate similarities in their cytoskeleton. The actin cortex is downregulated [128] and in fluorescent microscopy, it is visible as little aggregates distributed on cell peripheries and that determines the soft nature of these cells [41]. The most distinct difference between enucleated and nucleated cells, however, is the presence of the nucleus. While under sufficiently high load, like during the RT-FDC experiments, the deformation of nucleated cells is limited by the presence of the nucleus [41]. As shown in **Fig. 5.6 a** when cells enter the RT-FDC measurement channel, the enucleated cells assemble the tear-like shape and their minor axis ( $4.3 \pm 0.81$ , mean  $\pm$  SD) perpendicular to the flow direction) is shorter than nuclei minor axis ( $5.0 \pm 0.38$ ), on the contrary nucleated cells assemble the bullet-like shape and their minor axis length ( $6.42 \pm 0.9$ ) remains above the nuclei. The nucleus is a rigid structure restricting the degree to which a nucleated cell deform from its original shape under applied load. Nuclei within nucleated cells as well as the free floating nuclei captured in the outlet A were sized by image analysis of cytospin slides (**Fig.5.6 b**). The nuclei within nucleated cells mean minor axis was  $4.8 \pm 0.8$   $\mu\text{m}$ , with the minimal measured value of  $2.8$   $\mu\text{m}$ . The free floating nuclei were of similar sizes (minor axis  $4.6 \pm 0.7$ , the minimal measured value was  $2.9$   $\mu\text{m}$ ).





<b>b</b>	
<b>Nucleated cells collected in outlet A</b>	
Whole cell mean $\pm$ SD area [ $\mu\text{m}^2$ ]	75.8 $\pm$ 25.2
Nucleus mean $\pm$ SD area [ $\mu\text{m}^2$ ]	26.4 $\pm$ 6.7
Nucleus/whole cell mean $\pm$ SD ratio	0.38 $\pm$ 0.12
Nucleus mean $\pm$ SD minor axis [ $\mu\text{m}$ ]	4.8 $\pm$ 0.8
Nucleus min-max minor axis [ $\mu\text{m}$ ]	2.8 - 6.2
Number of events	113
<b>c</b>	
<b>Free-floating nuclei collected in outlet A</b>	
Whole mean $\pm$ SD area [ $\mu\text{m}^2$ ]	26.1 $\pm$ 7.2
Nucleus mean $\pm$ SD minor axis [ $\mu\text{m}$ ]	4.6 $\pm$ 0.7
Nucleus min-max minor axis [ $\mu\text{m}$ ]	2.9 - 6.3
Number of events	168

**Fig. 5.6**  
 (a) Minor axis (y-axis, perpendicular to the flow direction within the RT-DC chip) of enucleated cells (pink), nucleated cells (purple) and nuclei (grey) in the input sample, measured by RT-DC in the measurement channel section. Measurements were performed at 0.12  $\mu\text{l}/\text{min}$  flow rate in a 20  $\mu\text{m} \times 20 \mu\text{m}$  channel. More than 10,000 events were acquired and split accordingly between each subset. Box plots summarising the length of minor axis [ $\mu\text{m}$ ] for enucleated and nucleated cells and nuclei, where the line in the box represents the median, the box itself represents data from lower and upper quartile and the whiskers correspond to

*the lowest and highest extreme values. The dotted line indicates mean minor axis length for nuclei. To get further insight into the properties of contaminants found in the outlet A cytospin image analysis was performed to extract useful parameters describing (b) nucleated cell and (c) nuclei.*

The sizes of the free-floating nuclei and the nuclei within nucleated cells did not allow them to pass through 3  $\mu\text{m}$  membrane pores and hence they should have been retained on the top of the filter.

This study did not aim to develop new membrane filtration methodology, thus initially we tested six commercially available membranes, three with 5  $\mu\text{m}$  pore size and three with 3  $\mu\text{m}$  pore size.

1. 5 $\mu\text{m}$  SVPP Durapore (Merck, cat. SVLP04700 )
2. 5 $\mu\text{m}$  Polyester PETE (SterliTech, cat. PET5047100)
3. 5 $\mu\text{m}$  NYLON (cat. NY5047100)
4. 3  $\mu\text{m}$  SIGMA (Sigma, cat. 23339483)
5. 3  $\mu\text{m}$  ISOPORE<sup>TM</sup> (Merc, cat. TSTP04700)
6. 3  $\mu\text{m}$  NUCLEOPRE<sup>TM</sup> (Whatman, cat. WHA110412)

All membranes were tested specifically with the end product of the CB CD34+ erythroid differentiation. A mixed population containing enucleated and nucleated cell as well as nuclei was passed through the filter membranes fitted onto syringe adapter and cell material retention on the membranes was assessed by performing a cell count (**Table 5.1**). 5 $\mu\text{m}$  NYLON and 3  $\mu\text{m}$  SIGMA were discriminated from further tests due to high retention, 99.95% and 99.75%, respectively, of input cells, did not go through the membrane. The cut-off point of the 5 $\mu\text{m}$  Polyester PETE membrane was larger than the largest cells found in the input sample and that resulted in 100% of all components of the input sample passing through the filter.

Membrane	Input [cells/ ml]	Output [cells/ ml]	Recovery of all cells [%]	Enucleated recovery [%]	Nucleated recovery [%]	Nuclei recovery [%]
5 µm SVPP Durapore	$1.28 \times 10^6$	$1.08 \times 10^5$	8.4	16.3	7.0	3.1
5 µm Polyester PETE	$1.28 \times 10^6$	$1.32 \times 10^6$	100	100	100	100
5 µm NYLON	$1.28 \times 10^6$	$3.13 \times 10^3$	0.2	0	0	0
3 µm SIGMA	$2.38 \times 10^6$	$1.03 \times 10^3$	0.0	0	0	0
3 µm ISOPORE™	$2.38 \times 10^6$	$7.83 \times 10^5$	32.9	9.1	24.9	65.1
3 µm NUCLEOPRE™	$2.38 \times 10^6$	$1.26 \times 10^6$	52.9	17.1	46.1	73.4

**Table 5.1**

*Summary of performance of the six initially tested filter membrane. Membrane type column indicates pore size and brand name of tested membranes. Input and output columns show cell concentration before and after filtration, respectively, and recovery column indicates a fraction of input sample that passed through the filter with no distinction into the three subsets.*

Next, input sample as well as samples collected after filtration through the best performing 3 µm ISOPORE™, 3 µm NUCLEOPRE™ and 5µm SVPP Durapore membranes, were characterised using standard flow cytometric assay (**Fig. 5.7**). In order to identify the most suitable membrane, sizes of enucleated and nucleated cells, as well as nuclei from samples collected after filtration, were compared with sizes of their counterpart subsets found in the outlet A, after processing in the spiral channel. Box plots of FSC-A parameter were generated separately for enucleated (**Fig. 5.7 a**) and nucleated (**Fig. 5.7 b**) cells and the free-floating nuclei (**Fig. 5.7 c**), then ROC curves were generated and AUC was calculated (**Fig. 5.7 d, e & f**).

The assumption for desired enucleated cells was that AUC for the best performing membrane should be either closest to 0.5 (meaning exactly the same size range) or 1 with the shift toward small sizes within the measured size range. In contrast, for contaminant particles, like nucleated cells and nuclei, AUC ideally should be equal to 1, with the population shift towards the larger sizes. Based on these assumptions we found that the best performing membrane was the 3 µm ISOPORE™, the size range of enucleated cells passing through the membrane was almost 100% aligned with enucleated cells found in the outlet A (AUC=0.54, **Fig. 5.7 a**), which should minimise the additional cell losses. Moreover, the 3 µm ISOPORE™ had a very sharp cut-off point for nucleated cells and nuclei, with 75% of all events remaining in the minimal side of the spectrum (shown as box plot in **Fig. 5.7 b & c**) and being

substantially smaller than that nucleated cells (AUC=93, **Fig. 5.7 e**) and nuclei (AUC=89, **Fig. 5.7 f**) found in outlet A.

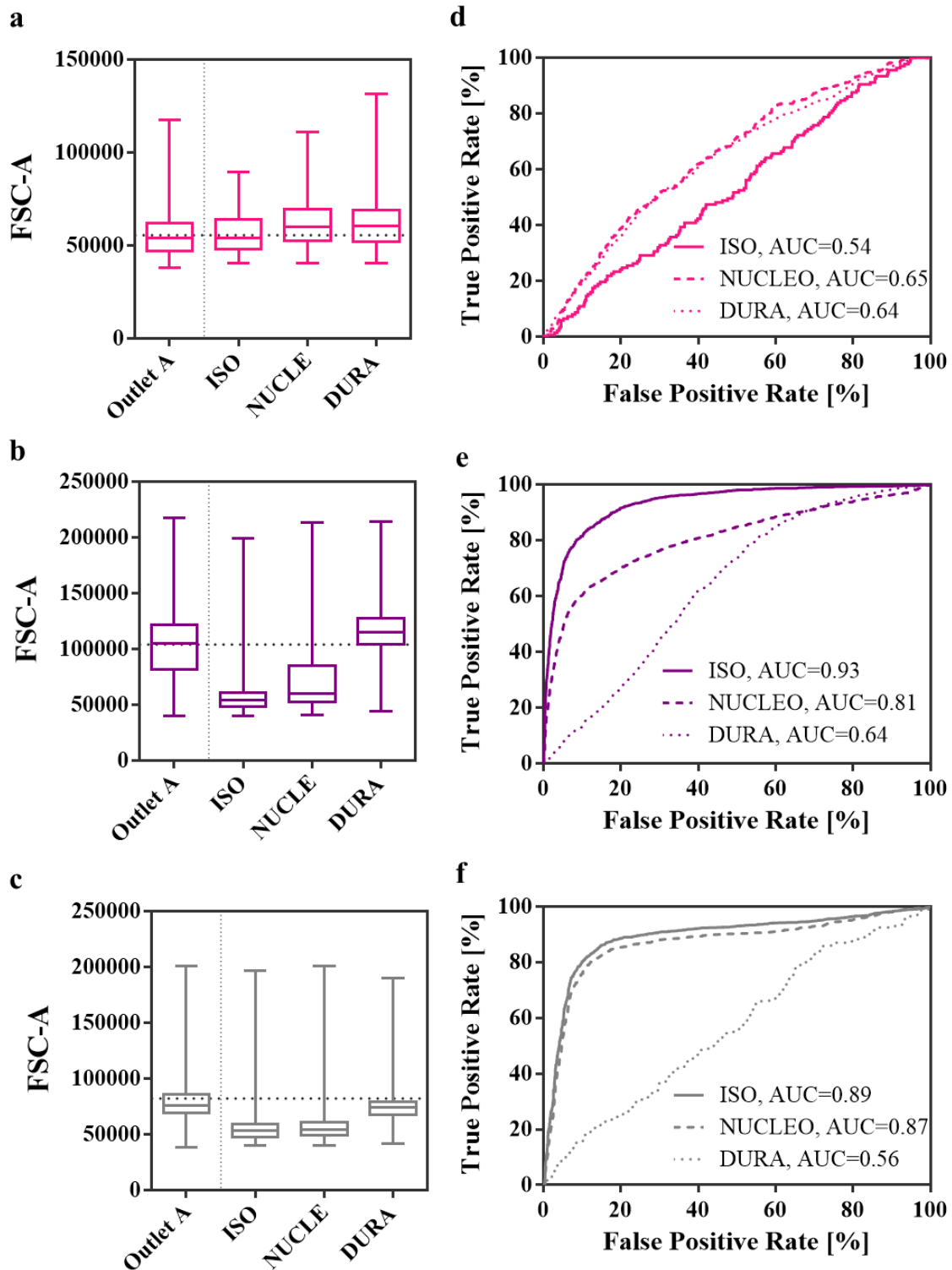


**Fig. 5.7**

Comparison of sizes of (a) enucleated cells, (b) nucleated cells and (c) free floating nuclei captured in the outlet A and after passing through 3µm ISOPORE™ (ISO), 3µm NUCLEOPRE™ (NUCLE) and 5µm SVPP Durapore (DURA). Box plots summarising the

*FSC-A parameter indicating relative sizes for enucleated and nucleated cells and nuclei, where the line in the box represents the median, the box itself represents data from lower and upper quartile and the whiskers correspond to the lowest and highest extreme values. The dotted line indicates mean FSC-A for an adequate subset found in the outlet D. Receiver Operating Characteristic (ROC) curves were plotted for the sizes expressed as FSC-A parameters comparison between (d) enucleated cells, (e) nucleated cells and (f) nuclei found in the outlet D and passed through passing through 3 $\mu$ m ISOPORE<sup>TM</sup> (solid line), 3 $\mu$ m NUCLEOPRE<sup>TM</sup> (dashed line) and 5 $\mu$ m SVPP Durapore (dotted line). The True Positive Rate is defined as the number of events (enucleated/ nucleated/ nuclei) found in the outlet D for a certain FSC-A cut-off point divided by the total number of events (enucleated/ nucleated/ nuclei, respectively). The False Positive Rate is defined as the number of events (enucleated/ nucleated/ nuclei) found in samples after filtration, divided by the total number of events (enucleated/ nucleated/ nuclei, respectively). In order to quantify size overlap, the Area Under the Curve (AUC) was calculated.*

### **5.2.7. Donor-to-donor variability and reproducibility**

The indigenous properties of cells, such as size and deformability, have been recognised as promising inexpensive label-free markers [45]. In some cases, alterations in cell mechanical properties are correlated with their molecular activity, such as cell cycle regulation [149][46] and differentiation [41][150][151]. Label-free biomarkers are cost-effective since there is no need to add costly antibodies to reveal cell identity markers and number of processing steps (staining, washing) is reduced [137], thus they are seen as a potential route to develop industrially-viable processes for large-scale high-throughput cell enrichment [152][153][154], e.g. like in this study purifying stem-cell derived RBC. This approach is not suitable in many cases due to the lack of the correlation of the desired molecular phenotype and the mechanotype, thus the first step in designing any customised label-free purification strategy is profound characterisation and understanding of properties of a given sample.

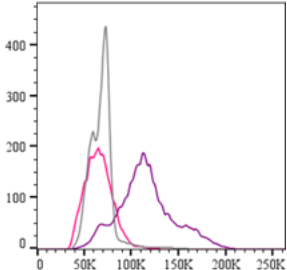
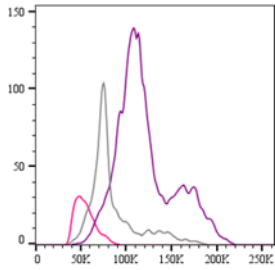
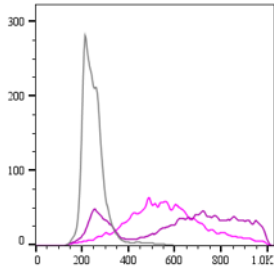
Luckily, the enucleated and nucleated cells and the free-floating nuclei found in the end-product of the CB CD34+ differentiation protocol could be distinguished based on their size and deformability. CB CD34+, among other cell types used as a starting material, offer relatively high enucleation rate and yields providing numerous units of mRBC. However, CB CD34+ expansion potential is limited, meaning that cells obtained from one donor constitute a finite source and that creates a difficulty in adapting this approach for routine standardised processing [155].

Variation in donor-dependent hematopoietic differentiation potential of CB CD34+ has not been widely addressed, hence we characterised the end product of CB CD34+ *in vitro* erythropoiesis from three donors, two described in this study (donor I- **Fig. 5.1, Fig 5.2 and Fig. 5.3** and **Appendix B**, donor II- **Appendix H** and **Appendix I**) and an additional donor

was described elsewhere [41] and **Appendix J**. Our findings show that there was some degree of intrinsic variability in size and deformability characteristics between them (**Table 5.2**- a summary table for all three donors) which influenced the label-free purification outcome (**Fig. 5.5** for donor I, **Appendix K** for donor II, **Appendix L** for donor III and **Table 5.2** for the summary).

In general, the size expressed as projected cell area [ $\mu\text{m}^2$ ] remains roughly within the same range for each donor ( $24.3 \pm 7.6 - 77.3 \pm 27.5$ ,  $26.1 \pm 7.5 - 67.8 \pm 20.7$  and  $20.9 \pm 1.5 - 63.5 \pm 6.7 \mu\text{m}^2$ , for donor I, II and III, respectively). The relative size measured by flow cytometry as FSC-A parameter, show that nucleated cells always remind the largest in the samples and that was true across all three donors. It was also true across the three researched donors that there were discrepancies in the relative size of enucleated cells and nuclei. Enucleated cells derived from donor I substantially overlapped with sizes of nuclei (AUC= $0.63 \pm 0.6$ , **Fig. 5.2**) and the little shift was towards larger side of the spectrum. For donor II enucleated cells were the smallest within the sample, while as shown in **Appendix J** the subpopulation of enucleated cells derived from donor III was larger than the subpopulation of the expelled nuclei ( AUC= $0.93 \pm 0.01$ ) with a substantial overlap in terms of size with nucleated cells (AUC= $0.59 \pm 0.03$ )

Despite the size differences, nuclei always remain the most rigid within the sample while the enucleated cells are the most deformable. However, the degree to which enucleated cells can deform vary between donors, mean deformation of enucleated cells derived from the best performing donor III was  $0.33 \pm 0.03$  [41] (**Table 5.2**), which is comparable to deformation measured for peripheral blood red cells measured in RT-DC ( $D=0.35 \pm 0.03$ , **Appendix M**). In contrast, deformation of enucleated cells derived from donor II ( $D=0.21 \pm 0.07$ ), which also had the lowest expansion (data not shown) and enucleation rate among all tested donors, was closer to the deformability of nucleated cells from donor III ( $D= 0.17 \pm 0.03$ , **Table 5.2**) than to enucleated cells from donor II and RBC (**Appendix M**). Additionally, the overall cell isolation process depends on the relative abundance of the target cells in the input sample. For all three donors the purity of enucleated cells varied (**Table 5.2**), donor I  $\sim 20\%$ , donor II  $<10\%$  and donor III  $\sim 30\%$ .

Donor	I	II	III
Where it was described	Fig.5.1, Fig.5.2, Fig.5.3, Fig.5.5, Appendix B	Appendix H & I &K	Guzniczak <i>et al.</i> 2017 and Appendix J & L
Enucleated mean $\pm$ SD area [ $\mu\text{m}^2$ ]	75.7 $\pm$ 22.4	60.6 $\pm$ 18.5	52.8 $\pm$ 5.3
Nucleated mean $\pm$ SD area [ $\mu\text{m}^2$ ]	77.3 $\pm$ 27.5	67.8 $\pm$ 20.7	63.5 $\pm$ 6.7
Nuclei mean $\pm$ SD area [ $\mu\text{m}^2$ ]	24.3 $\pm$ 7.6	26.1 $\pm$ 7.5	20.9 $\pm$ 1.5
Relative size [Count vs FSC-A]			
Enucleated mean $\pm$ SD deformation [-]	0.29 $\pm$ 0.05	0.21 $\pm$ 0.07	0.33 $\pm$ 0.03
Nucleated mean $\pm$ SD deformation [-]	0.14 $\pm$ 0.04	0.10 $\pm$ 0.04	0.17 $\pm$ 0.03
Nuclei mean $\pm$ SD deformation [-]	0.03 $\pm$ 0.01	0.03 $\pm$ 0.01	0.03 $\pm$ 0.01
Nucleated mean $\pm$ SD nucleus/cytoplasm ratio	0.4 $\pm$ 0.1	0.4 $\pm$ 0.1	0.4 $\pm$ 0.1
<b>Purification in the spiral microchannel</b>			
Input Enucleated PURITY	21.7 $\pm$ 0.7 %	8.3 $\pm$ 0.7 %	34.8 $\pm$ 4.5 %
Outlet A Enucleated PURITY	71.0 $\pm$ 3.4%	62.0 $\pm$ 3.4%	71.3 %*
Outlet A Enucleated RECOVERY	92.8 $\pm$ 0.2%	79.1 $\pm$ 8.5 %	94.4%*

## Table 5.2

*Table summarising size and deformability properties for three researched donors (donor I, donor II and donor III) as well as the performance of the purification process in the spiral microchannel. All reported values are averaged results for three replicas, except for donor III outlet A Enucleated PURITY and RECOVERY marked with "\*" - performance of the spiral channel for donor III was validated only once.*

In order to verify if these difference had and influence on the label-free purification performance (donor I- **Fig. 5.5**, donor II- **Appendix K**, donor III- **Appendix L**), mRBC derived from all three donors were processed in the spiral channel at 1ml/min and the process characterisation metrics were compared (**Table 5.2**). The generic conclusion is that the high quality end-product of differentiation constitutes good quality starting material for the label-free purification resulting in highest recovery rates (>90%) and purity (>70%). Among the researched donors, donor III could be classified as an exemplary donor due to high enucleation rate, good quality of enucleated cells comparable to PB RBC (**Appendix M**) and their clearly distinguishable mechanotype. In contrast, smaller stiffer and less abundant enucleated cells derived from donor II were more troublesome to purify. Their recovery and purity in the outlet A were ~10% lower in comparison to donor I and III (**Table 5.2**). Stiffer enucleated cells from donor II, probably, experience less of the effect of the deformability induced lift force and they assemble the lateral equilibrium position closer to the channel centreline resulting in their partial capture in the outlet B (recovery 12.3%, **Appendix K b**). Additionally, due to the prevalence of contaminant nucleated cells and nuclei, the filter membrane was more prone to fouling and that resulted in 17% lower recovery rate of enucleated cells (**Appendix K e**) in comparison to the donor I.

In conclusion, CB CD34+ derived from the same donor, behave in a uniform way during the *in vitro* differentiation into RBC- even when processed in batches. The differentiation process for each batch is recapitulated either exactly or with very close similarities in terms their expansion and enucleation rate, levels of expression of CD235a and well as characteristics of their label-free markers (size and deformability). However, not all researched donors had the same capacity to differentiate into enucleated mRBC. In this study, we showed that erythroid differentiation did not occur at the same levels for all studied donors. This means that the cells origin is probably the major determinant of variation in hematopoietic differentiation of CB CD34+ cells and that could be the limiting factors for implementing standardised label-free purification protocols.



The issue of limited proliferative capacity has been addressed by the scientific community by introducing iPSC cells [156] as well as creating immortalised adult erythroid cell line (BEL-A)[23], presenting an interesting alternative to CB and PB hematopoietic stem cells as a potentially unlimited source of erythroid progenitors. Consequently, both of the approaches create a route to manufacture standardised mRBC with highly reproducible phenotypes and genotypes. To achieve that, technical hurdles specific for each approach have to be overcome, GMP compliance has to be addressed and their safety and efficacy have to be proven [157].

### 5.2.8. Processing impact on cells

Inertial microfluidic techniques are considered as a gentle method for biological samples processing, with a vast literature evidence supporting unaffected cell quality (e.g. viability, cell membrane integrity, proliferation or altered gene expression) after processing [158]. In this study, the novel deformability-induced lift force ( $F_D$ ) was used to sort mRBC in spiral microchannel, and as described in **Chapter 4**, in order to reveal the effect of  $F_D$ , elevated flow rates are required. To investigate if the hydrodynamically-induced mechanical stress on the cells exerted any adverse effect on the mRBC phenotype, cell integrity and global gene expression profile were studied.

Populations of mRBC derived from donor I and II, at concentration of  $3-4 \times 10^6$  cell/ml were processed in the design II ( $170 \times 30 \mu\text{m}$  cross-section) spiral microchannel at 1 ml/ min flow rate, and eluents from all outlets were collected into one vial (test sample) and their quality was compared against unprocessed cells (control).

Cell integrity of the control and processed cells was investigated via trypan blue exclusion assay. Live cells are impenetrable for trypan blue, while damaged cells with impaired cell membrane integrity uptake trypan blue and they appear blue. As shown in **Fig. 5.8**, the high viability of  $>85\%$  was comparable at the inlet (control) and at the outlet after processing (test).

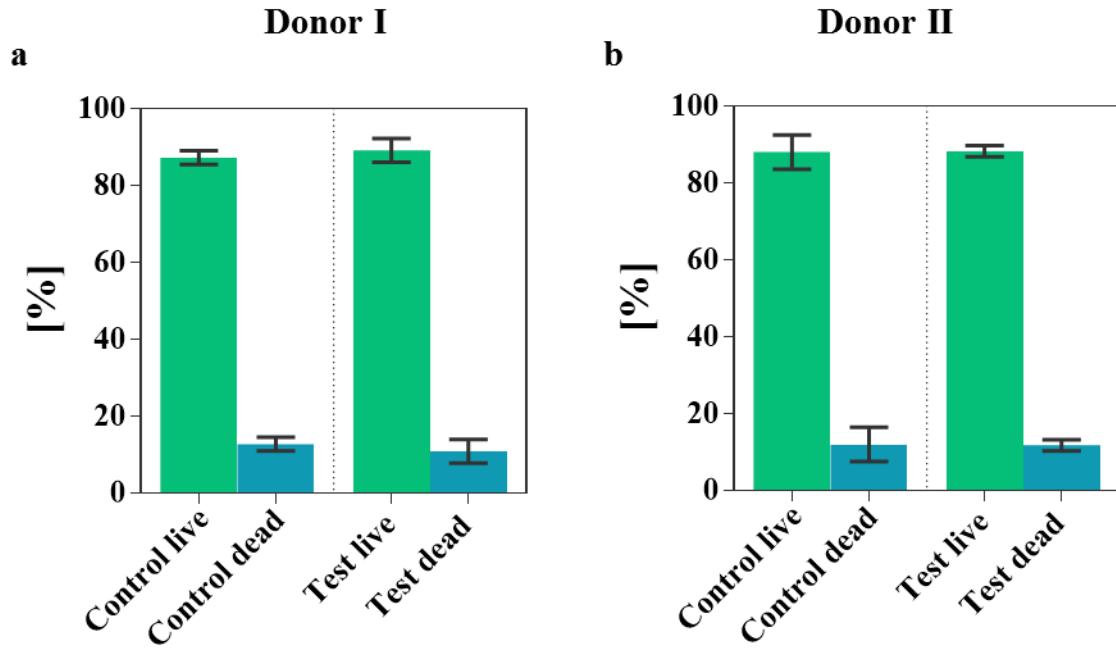


**Fig. 5.8**

*Viability of mRBC derived from (a) donor I and (b) donor II, before (control) and after (test) processing in design I ( $170 \times 30 \mu\text{m}$  cross-section) spiral microchannel at 1 ml/min flow rate, as measured by Trypan Blue exclusion assays. Bars represent mean fraction of live (green) or dead (blue) cells found in the samples, measured at three independent experimental occasion. Error bars correspond to the standard deviation of the mean.*

Next, the global gene expression patterns were investigated in control and test samples, using poly-A selection method to detect if the relatively high flow rates (in comparison to reports from literature- please consult **Fig. 4.12** for summary of Re numbers) trigger more subtle changes at molecular level.

Please note that the **bioinformatic analysis and data interpretation was performed by Neil A. Robertson (MRC DTP PhD Studentship)**. After sequencing, a standard pipeline was run that seeks to describe the variance and correlative behaviour across the data before classifying those genes that are differentially expressed in each core comparison. Sample by sample correlation analysis was performed to attempt to ascertain how strongly or weakly each sample correlates across the range of gene expression values (Spearman Correlation Clustering, hierarchically clustered). Strong tendency for samples to cluster by sample group (donor I and door II), overriding the effects of processing in the spiral microchannel (**Fig. 5.9**) was observed.

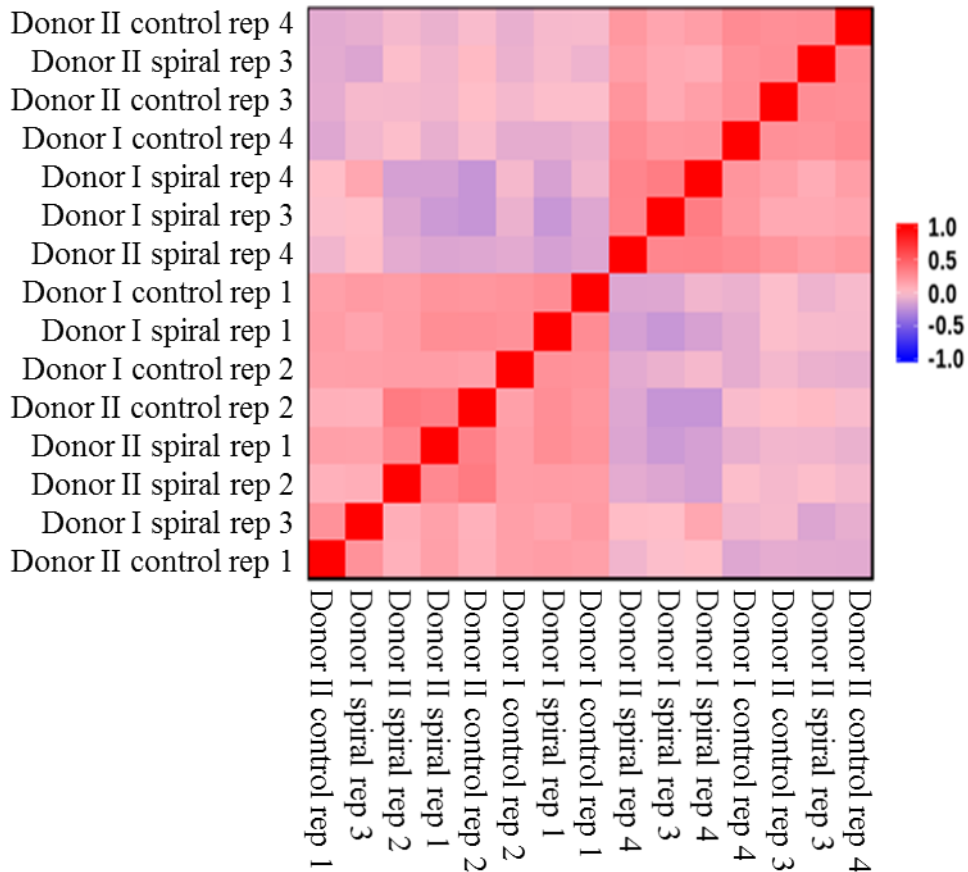


**Fig. 5.9**

*Heatmap of sample correlation. Correlations between each pairwise combination of samples is shown. The correlations were calculated using Spearman Correlation based on all gene expression values. The level of correlation (Spearman Correlation Coefficient) is represented by colour intensity, with strong positive correlation in red, no correlation in light pink and strong anti-correlation in blue. The plot has been hierarchically clustered on both axis using, Spearman distances, with UPMGA agglomeration and mean reordering.*

We then sought to describe the individual changes in gene expression using CuffDiff. Here, a small number of genes changing significantly ( $p\text{-value} < 0.05$ ) as a result of cell processing— 40 and 42 changing genes in samples from donor I and donor II, respectively, was observed. This was eclipsed by the scale of changes between sample groups with over 2400 changing (donor I vs donor II) at control and treatment stages (**Fig. 5.10**).

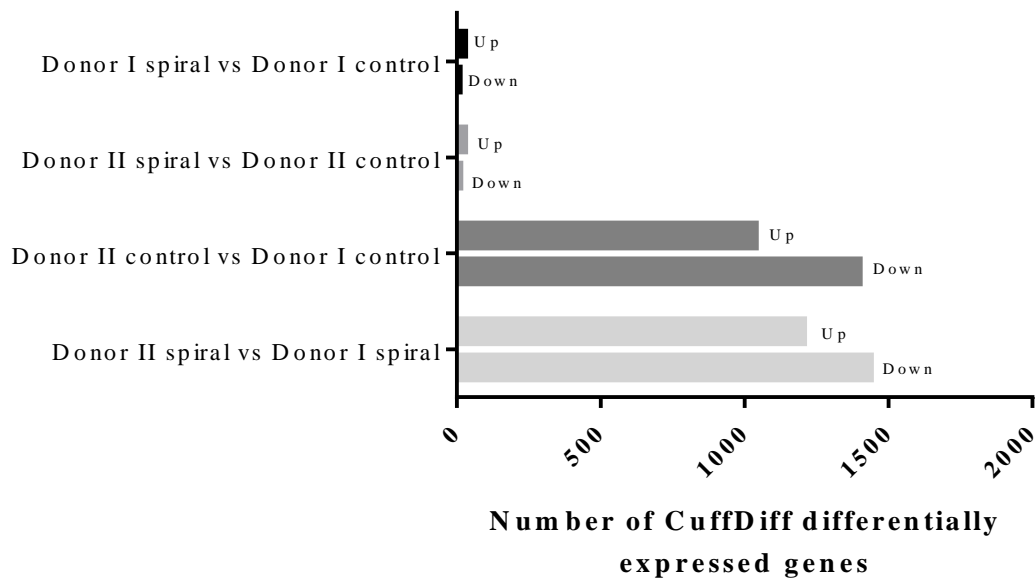


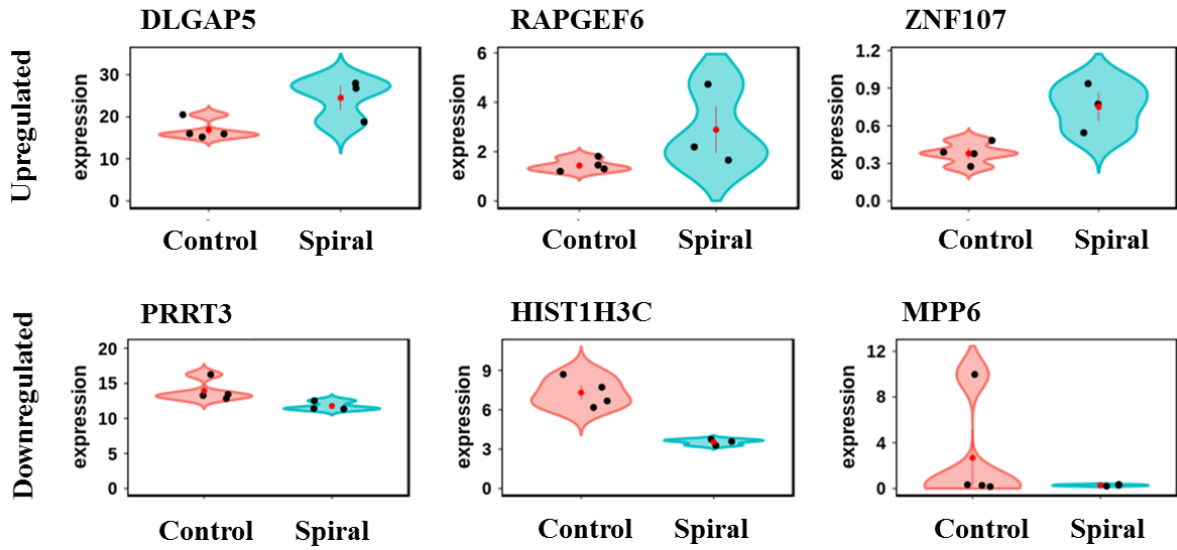
**Fig. 5.10**

*Bar chart showing the number of significantly ( $p$ -value  $< 0.05$ ) upregulated (up) and downregulated (down) genes, between donor I (and donor II respectively) cells processed in the spiral microchannel compared to control sample as well as donor II control and processed cells compared to control and processed cells derived from donor I.*

Heatmaps of significantly differentially expressed genes (please see **Appendix O**), show that although genes change in relatively robust patterns, their expression changes are rarely recapitulated within treatment groups. Additionally, as shown in the violin plots (**Fig. 5.11**) for the most up- and downregulated genes (top three each of up and down regulated selected by smallest  $p$  value), the level of changes are small when compared to the spread in the expression levels between replicates.

In summary, it has been confirmed that mRBC after processing within the spiral microchannel at sufficiently high flow rate to take advantage of the effect of  $F_D$  for cells focusing, retain high degree of viability and that there is no distinct gene expression alteration. That confirms that the proposed approach for using the spiral microchannel for mRBC sorting, is indeed a suitable and safe technique for processing these cells.

## Donor I



## Donor II

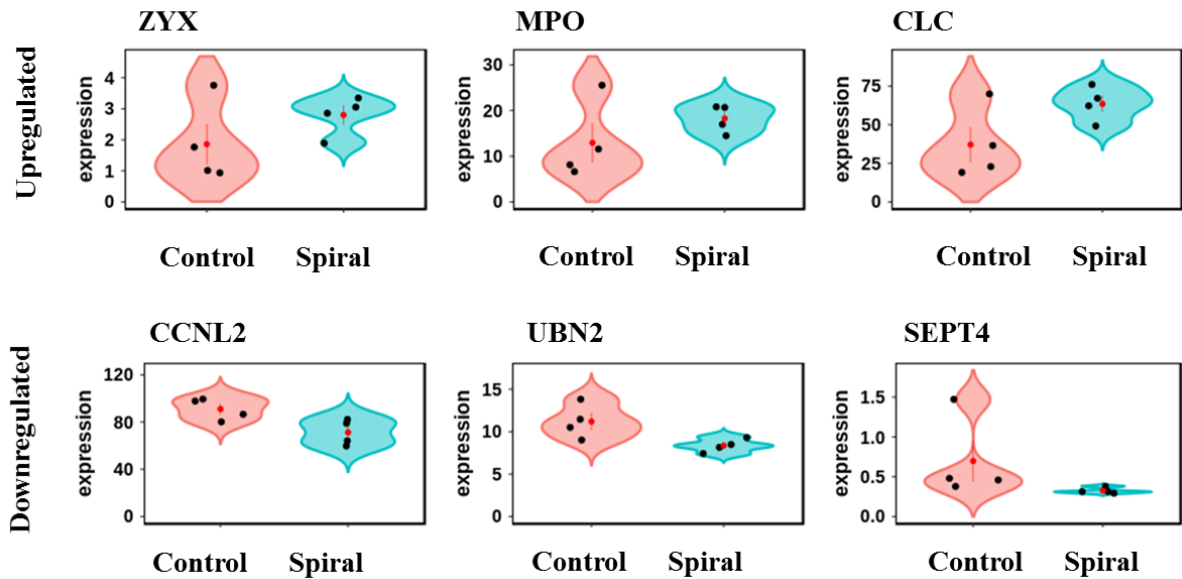


**Fig. 5.11**

Violin plots showing three most significantly (selected by the lowest  $p$ -value) upregulated and downregulated genes after processing in the design II ( $170 \times 30 \mu\text{m}$  cross-section) at 1 ml/min flow rate in comparison to control cells, for both donor I and II. Each dot is one sample, with sample groups given on the x-axis and gene expression on the y-axis. The mean and standard error for each sample group is given as a red dot and line. The spread of the samples within a sample group gives an idea of sample heterogeneity at a given gene.

### 5.3. Conclusion and future outlook

In this work, we successfully developed a passive label-free high-throughput and complete purification strategy for CB CD34<sup>+</sup>- derived red blood cells. Using advancements in the microfluidic RT-FDC approach for high-throughput cell mechnotyping the heterogeneous end-product of CB CD34<sup>+</sup> *in vitro* erythropoiesis was characterised and label-free identity markers were identified and formulated for the target enucleated cells as well as contaminant nucleated cells and expelled nuclei. Next these label-free markers were used as a motivation for developing and optimising the label-free purification strategy, which consists of two steps: (1) processing raw sample in spiral microchannel where most of the contaminant material is depleted (enrichment ratio  $\sim 0.5$  for both nucleated cells and nuclei, below the input baseline) and high recovery ( $>90\%$ ) of the target enucleated cells up to high ( $>70\%$ ) but not satisfactory purities, further enhanced by adding (2) membrane filtration step resulting in removal of  $\sim 99\%$  of the potentially harmful impurities (mainly nucleated cells since  $>98\%$  of nuclei were removed by the spiral microchannel). The membrane filtration requires further optimisation and development since in this study due to the usage of dead-end filtration which is prone to membrane fouling, led to the recovery of 30-50 % of enucleated cells.

In the demonstrated approach,  $3-4 \times 10^6$  cells/ min are processed by a single device when operating at the optimal 1ml/min flow rate. The current throughput seems reasonable for processing cells that are routinely cultured within similar concentration range in large volumes. At present, mRBC culture is routinely carried in static culture conditions, facilitating maximal cell concentration at around  $5 \times 10^6$  cells/ml [11], as Timmins *et al.* 2009 estimated, that would take 9000 T175 cm<sup>2</sup> flasks to produce a single blood unit [14]. This approach definitely is not sustainable and cost effective. To overcome the limitation mRBC cultured at minimum  $50 \times 10^6$  cell/ml should decrease required volume of medium to 40 litres and consequently the total cost to around \$8000 per blood unit [14][3][11]. The downstream processing proposed in this study has the capacity for further scale-up by two means: increasing cell sample concentration (the estimated concentration limit for this particular system is at  $20 \times 10^6$  cells/ml,  $\alpha=1$ , please see **Equation (17)**) and system parallelisation. Stacking microfluidic devices (stack of 20 devices reported [159]) is a common practice resulting in a rapid and efficient throughput improvement.

All current protocols for the manufacture of RBC from stem cells face the same technological challenge of low enucleation rate. The most efficient solution is co-culture with macrophages, which eliminate the expelled nuclei by the means of phagocytosis. This is an

organic solution but it comes with its own technological costs, such as finding ways to retrieve the macrophages from the culture and the complexity of a co-culture system with feeder layer impairs scaling-up. Hence, a significant research effort is invested into understanding the enucleation process and identifying and isolating key factors responsible for the process [25][31]. In the most optimistic scenario, even if the enucleation rate would be improved to reach the desirable 100% and nucleated cells would not be present in the end-product of the *in vitro* erythropoiesis, in the absence of macrophages the expelled nuclei will still remain within the sample. Having a robust label-free procedure for mRBC purification at high-throughput with no impact on cell quality will consequently be of significant importance for bringing mRBC a step closer to clinical use.

## **5.4. Materials and methods**

The differentiation protocol, flow cytometric staining protocol and cytopsin slides preparation were performed as per **Chapter 2**

### **5.4.1. Flow cytometry**

Fluorescently-stained cells were analysed on a flow cytometer (BD LSR II, BD, Germany). Obtained data were processed using FlowJo V10 CL. The receiver operating characteristic curves (ROC) were generated and the area under the curve (AUC) was calculated and further data analysis was performed using GraphPad Prism 6.

### **5.4.2. Real-time fluorescence and deformability cytometry (RT-FDC)**

Correlation between the molecular markers and mechnotype was assessed using real-time fluorescence and deformability cytometry (RT-FDC) [125]. Measurements were performed as per Nat. Methods 2018 [125] and as described in **Chapter 2**. Briefly, prior to measurements, CB CD34+ in the end of the differentiation protocol were harvested by centrifugation at 200 g for 5 min and re-suspended in a 0.05% methylcellulose solution (CellCarrier, Zellmechanik Dresden, Germany)  $1-2 \times 10^6$  cell/ml. Differentiated CB CD34+ cells, due to their small size, were characterised in  $20 \times 20 \mu\text{m}$  cross-section channel at 0.12  $\mu\text{l}/\text{min}$  flow rate. Due to the fragile nature of these cells, they were stained directly in CellCarrier by adding 5 mM DRAQ5<sup>TM</sup> Fluorescent Probe (BD) (to obtain a final concentration of 5  $\mu\text{M}$ ) per 100  $\mu\text{l}$  buffer volume. Cells were incubated for 2 min, in darkness at room temperature and analysed immediately after the staining. Gating strategy for the enculated and nucleated cell as well as nuclei was applied as per **Appendix N**. Obtained data was analysed using original RT-FDC software ShapeOut 0.8.4 (available at [www.zellmechanik.com](http://www.zellmechanik.com)). Next,

the data was extracted from the software and further inspected and plotted using FlowJo V10 CL and GraphPad Prism 6.

#### **5.4.3. Cytospin analysis**

Images were analysed using bespoke LabView software developed by Dr Graeme Whyte (Heriot Watt University) which detected the outline of the cells and nuclei by thresholding. The detected objects were classified into nucleated cells, enucleated cells and free floating nuclei, and the measurements of the morphological features extracted for further processing.

#### **5.4.4. Cell processing**

The current differentiation protocol involves human serum as a supplement to cell culture media. It provides high concentrations of growth factors, macromolecules, carrier proteins for lipids, trace elements, attachment and spreading factors, nutrients and hormones [160] and it plays a crucial role in the process. We found, similarly to others [161], that our devices are being clogged instantaneously when serum is presented in the processing buffer [161], thus we recommend exchanging the buffer to serum-free for the processing time. Our buffer of choice was PBS-/- supplemented with 0.1% biocompatible surfactant Pluronic F-68 [162] (TermoFisher Scientific, cat. 24040032). It was motivated with PBS-/- compatibility with technical requirements of quality control assays such as flow cytometry [163] and cell counts performed using MoxiZ automated cell counter as well as improved image quality [54]. Presence of phenol red (pH indicator in basal medium) impairs reads from both flow cytometry and automated cell count, thus cells processed in the basal medium could not be directly sampled for the quality control tests. Pluronic F-68 was added to surrogate the serum protective mechanism from mechanical damages (e.g. due to shear stress generated within the spiral microchannel) [160][164][162]. For a further application, cells can be processed in serum-free medium or any other buffer of choice, as long as the medium viscosity is not significantly different than the viscosity of water at room temperature, which is necessary to generate the large velocity gradient as a mean of manipulating particles in inertial microsystems.

Cells suspended in PBS-/- supplemented with 0.1% Pluronic F-68 at a concentration around  $3-4 \times 10^6$  cells/ml was introduced into the device with a mid-pressure syringe pump (neMESYS 1000N, Cetoni, Germany) through 1/1600 PTFE tubing of 0.5 mm internal diameter (Thames Restek, UK). Cell concentration is a critical factor influencing focusing within the spiral microchannel. If the concentration is too high, so-called steric crowding effect occurs, meaning that there is physically not enough space for particles to focus in a tight single



stream. In order to identify if the crowding effect will occur the length fraction  $\alpha$  (number of particle diameters per channel length) can be calculated.

$$\alpha = \frac{6WHV_F}{\pi a^2} \quad (16)$$

where  $V_F$  is the volume fraction of particles in the solution,  $a$  is particle diameter,  $W$  is the channel width and  $H$  is the channel height. For  $\alpha > 1$ , focusing to a single stream cannot be expected due to steric interactions between particles [91]. Assuming that all the particles in the input sample were of the size of the largest nucleated cells ( $\varnothing \sim 10 \mu\text{m}$ ), at concentrations between  $3\text{-}5 \times 10^6$  cells/ml,  $\alpha$  varies between 0.153-0.255, satisfying the condition necessary to avoid the steric crowding effect.

Hydrodynamic behaviour of cells was assessed in terms of lateral equilibrium position as described in **Chapter 2**. Lateral position within the channel was recorded for more than 10,000 events at three independent occasions, for each researched condition, using a custom-written program ShapeIn and quantified using ShapeOut version 0.8.4 (available at [www.zellmechanik.com](http://www.zellmechanik.com)). To enhance the purification efficiency cells collected at the outlet A & B were passed through  $3 \mu\text{m}$  polycarbonate Isopore<sup>TM</sup> filter membrane (Merc, UK) fitted onto plastic adapter for syringe filtration. Cell suspension was loaded into a 5 ml plastic syringe and pumped through the filter membrane at 2 ml/ min using a syringe pump (neMESYS, Cetoni, Germany). Cell separation efficiency was quantified by flow cytometry (BD LSR II, BD, Germany) in order to compare the fraction of each cell population (characterised by unique fluorescent properties- please see the ‘‘Flow cytometry’’ section) in samples collected at each outlet. Additionally, cell yield was assessed by counting a number of cells at each outlet using either a standard glass haemocytometer or MoxiZ automated cell counter (Orflo, US). In order to define mRBC sorting performance collected metrics were formulated into three parameters:

$$\text{Recovery } [C]_{\text{outlet}_i} = \frac{[C]_{\text{outlet}_i}}{\sum_{i=1}^4 [C]_{\text{outlet}_i}} \quad (17)$$

of each cell type in each outlet, where  $[C]$  is enucleated cell/ nucleated cell/ nuclei number per ml.

$$\text{Purity } [C]_{\text{outlet}_i} = \frac{[C]_{\text{outlet}_i}}{[\text{Enucleated} + \text{Nucleated} + \text{Nuclei}]_{\text{outlet}_i}} \times 100\% \quad (18)$$

indicating a fraction of each subset in a sample collected after processing and

$$Enrichment\ ratio = \frac{[C/(Enucleated + Nucleated + Nuclei)]_{outlet_i}}{[C/(Enucleated + Nucleated + Nuclei)]_{inlet}} \quad (19)$$

Data analysis and plotting were performed using GraphPad Prism 6 and FlowJo V10 CL.

#### **5.4.5. Trypan blue exclusion assay**

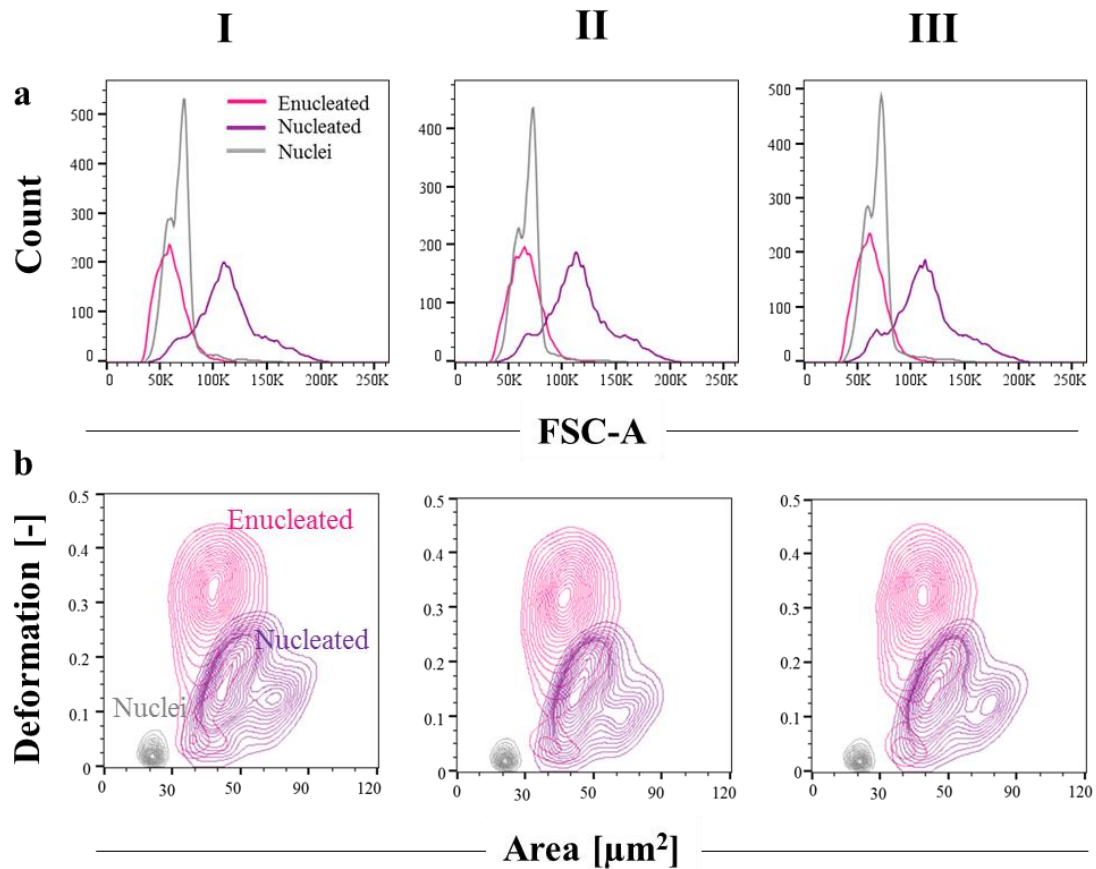
100 µl of cell suspension (control/ after processing in the spiral channel) was mixed with an equal part of 0.4% trypan blue dye (Gibco, UK), to obtain 1:2 dilution, incubated for less than three minutes at room temperature, loaded onto a glass haemocytometer and counted using a light microscope (AXIO Scope.A1 Zeiss, Germany).

#### **5.4.6. Global gene expression**

The global gene expression test by poly-A selection was outsourced to Edinburgh Clinical Research Facility (<https://www.edinburghcrf.ed.ac.uk/Genetics>) and run according to their internal SOPs.

The bioinformatic analysis (performed by Neil A. Robertson (MRC DTP PhD Studentship)) comprised of trimming N bases and the filtering of poor-quality reads (phred-score  $\leq 30$ ) with trim-galore before aligning with HISAT2 to the GRCh38 human genome (Ensembl version 94). Post alignment, reads were sorted with samtools before quantifying explicit normalised expression (FPKM) with the Cufflinks suite. Differential expression analysis was performed using CuffDiff where significance was determined at an FDR  $\leq 0.05$  cut-off.

## Appendix E

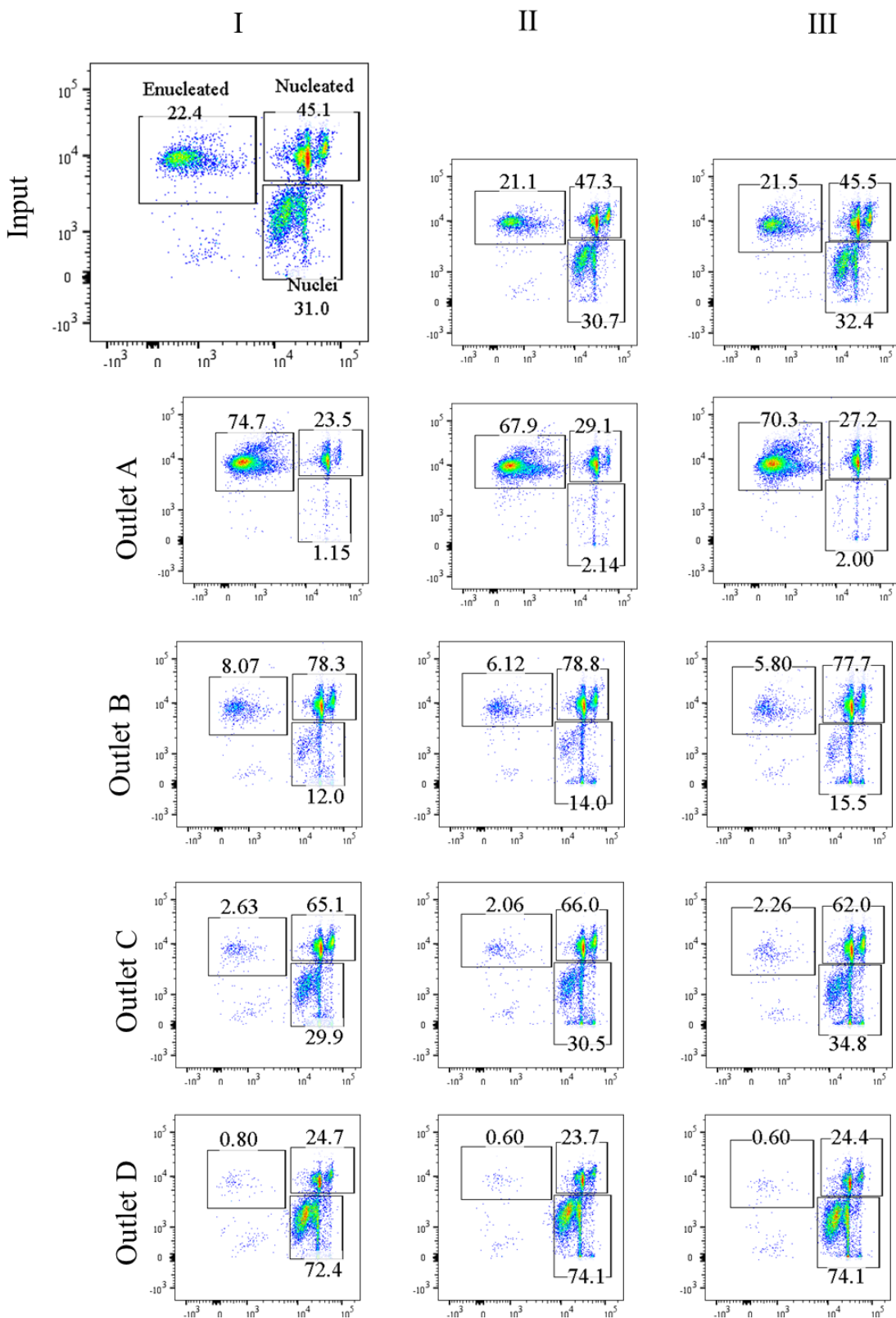


Replica	I			II			III		
	Enucleated	Nucleated	Nuclei	Enucleated	Nucleated	Nuclei	Enucleated	Nucleated	Nuclei
Number of values	3400	4169	3176	2991	4384	3415	3088	4378	3860
Mean	0.289	0.143	0.028	0.285	0.136	0.026	0.289	0.140	0.026
Std. Deviation	0.084	0.062	0.016	0.082	0.060	0.014	0.083	0.060	0.015
Std. Error of Mean	0.001	0.001	0.000	0.002	0.001	0.000	0.001	0.001	0.000
Minimum	0.019	0.015	0.009	0.019	0.016	0.009	0.016	0.016	0.009
25% Percentile	0.255	0.098	0.017	0.247	0.091	0.016	0.251	0.096	0.016
Median	0.307	0.139	0.022	0.299	0.133	0.021	0.305	0.139	0.021
75% Percentile	0.347	0.186	0.033	0.341	0.180	0.030	0.344	0.182	0.029
Maximum	0.452	0.427	0.108	0.452	0.369	0.108	0.450	0.394	0.110

Three replicas of flow cytometric and RT-FDC measurements of the end-product of CB CD34+ derived from **donor I**- *in vitro* differentiation into red blood cells. **(a)** Histograms of FSC-A parameter reflecting relative sizes of enucleated (pink) and nucleated (purple) cells as well as the free-floating nuclei (grey), measured by flow cytometry. The number of events on each diagram is around 10,000 - split accordingly between each subpopulation. **(b)** Equal probability contour plots (the same number of cells fall between each pair of contour lines) of deformation *vs* cell size (expressed as projected cell area in  $\mu\text{m}^2$ ) for each enucleated and nucleated cells and nuclei generated using RT-FDC for three replicas. **(c)** A summary table showing the statistical summary of deformation of each subset found in the end product of the differentiation protocol.

# Appendix F

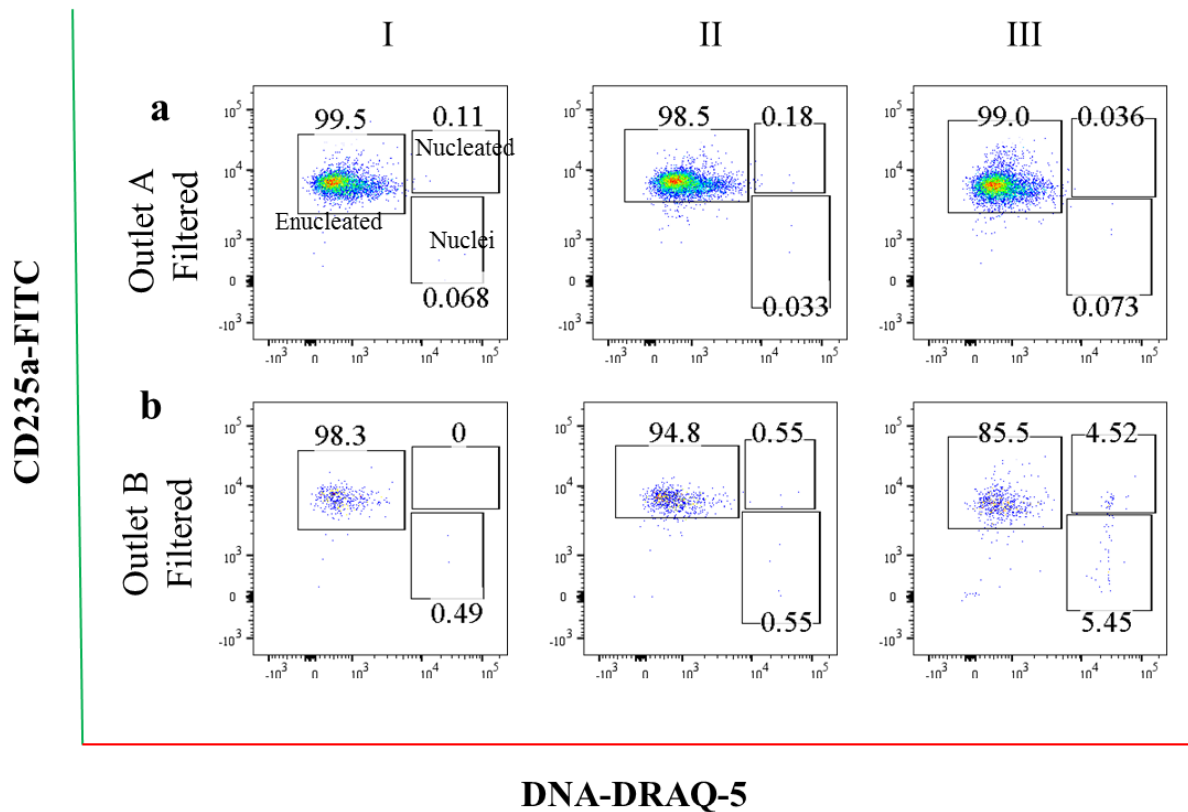
CD235a-FITC



DNA-DRAQ-5

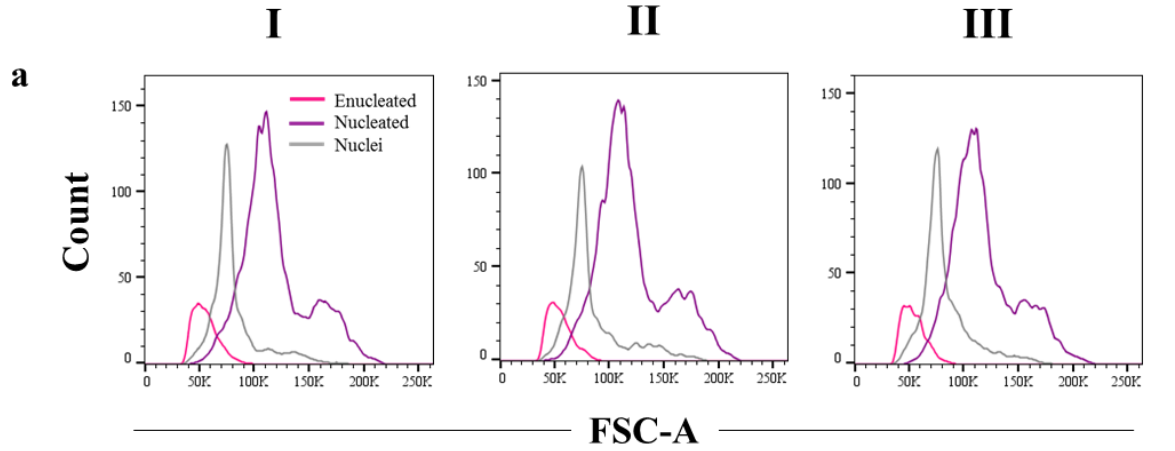
Summary of flow cytometric assessment of the presence of enucleated cells, nucleated cells and expelled nuclei in the input samples as well as samples collected at each outlet (A, B, C and D) after processing them at 1ml/min flow rate in the spiral channel, for three independent sorting occasions. Enucleated cells are DNA- and CD235a+, nucleated cells are DNA+ and CD235a+, free-floating nuclei are DNA+ and CD235+, however, they express lower levels of CD235a than nucleated cells. Each scatter plot displays around 10000 events split accordingly between each subpopulation.

## Appendix G



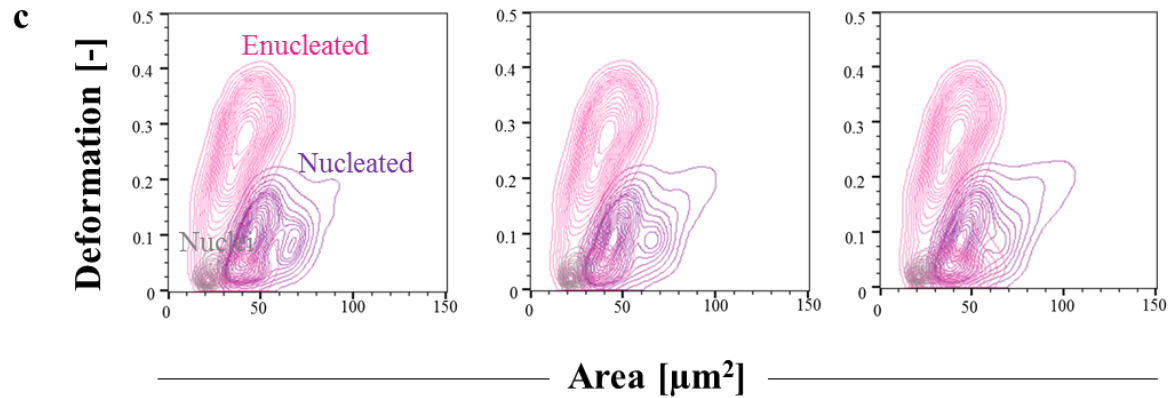
Summary of flow cytometric assessment of the presence of enucleated cells, nucleated cells and expelled nuclei in samples collected in (a) outlet C and (b) outlet D and passed through the 3 $\mu$ m ISOPORE™ for three independent replicates. Enucleated cells are DNA- and CD235a+, nucleated cells are DNA+ and CD235a+, free-floating nuclei similarly to nucleated cells are DNA+ and CD235+, however, they express lower levels of CD235a than nucleated cells. Each scatter plot for “outlet D filtered” displays around 5000 events split accordingly between each subpopulation, while events in “outlet C filtered” events were so rare that the sample size is around 2000 events, split accordingly between each subset.

## Appendix H



**b**

Subpopulation	Enucleated	Nucleated	Nuclei
Mean $\pm$ SD area [ $\mu\text{m}^2$ ]	60.6 $\pm$ 18.5	67.8 $\pm$ 20.7	26.1 $\pm$ 7.5
Number of events	2509	476	1372



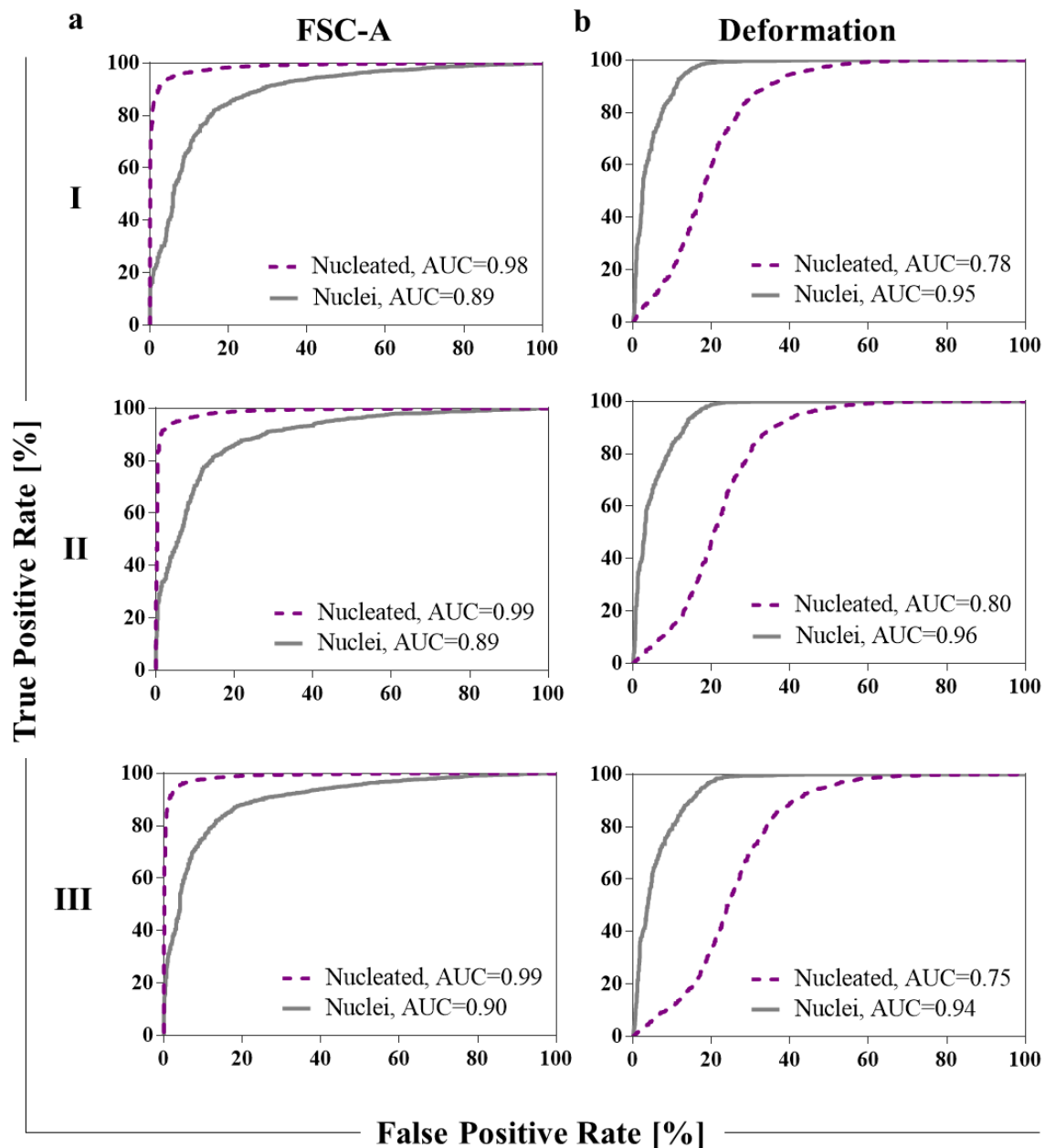
**d**

Replica	I			II			III		
	Enucleated	Nucleated	Nuclei	Enucleated	Nucleated	Nuclei	Enucleated	Nucleated	Nuclei
Deformation [-]									
Number of values	1430	9345	4095	1374	5559	2598	1528	5400	3086
Mean	0.210	0.102	0.030	0.216	0.100	0.031	0.200	0.102	0.028
Std. Deviation	0.108	0.054	0.019	0.105	0.055	0.020	0.112	0.057	0.018
Std. Error of Mean	0.003	0.001	0.000	0.003	0.001	0.000	0.003	0.001	0.000
Minimum	0.009	0.008	0.009	0.009	0.007	0.010	0.009	0.009	0.009
25% Percentile	0.123	0.060	0.018	0.134	0.058	0.019	0.098	0.057	0.018
Median	0.226	0.097	0.024	0.231	0.094	0.025	0.213	0.095	0.023
75% Percentile	0.296	0.135	0.035	0.299	0.133	0.036	0.293	0.137	0.031
Maximum	0.457	0.345	0.270	0.457	0.321	0.230	0.457	0.336	0.256

Three replicas of flow cytometric and RT-FDC measurements of the end product of CB CD34+ derived from **donor II**- *in vitro* differentiation into red blood cells. **(a)** Histograms of FSC-A parameter reflecting relative sizes of enucleated (pink) and nucleated (purple) cells as well as the free-floating nuclei, measured by flow cytometry. The number of events on each diagram is around 10000 split accordingly between each of the subpopulations. **(b)** Table summarising size measurement (expressed as cell area in  $\mu\text{m}^2$ ) obtained from cytopsin image analysis for enucleated cells, nucleated cells, as well as free floating nuclei (c) Equal probability contour plots (the same number of cells fall between each pair of contour lines) of deformation vs cell size (expressed as projected cell area in  $\mu\text{m}^2$ ) for each enucleated and nucleated cells and nuclei, generated using the RT-FDC for three replicas. **(d)** A summary table showing the statistical summary of deformation of each subset found in the end product of the differentiation protocol.

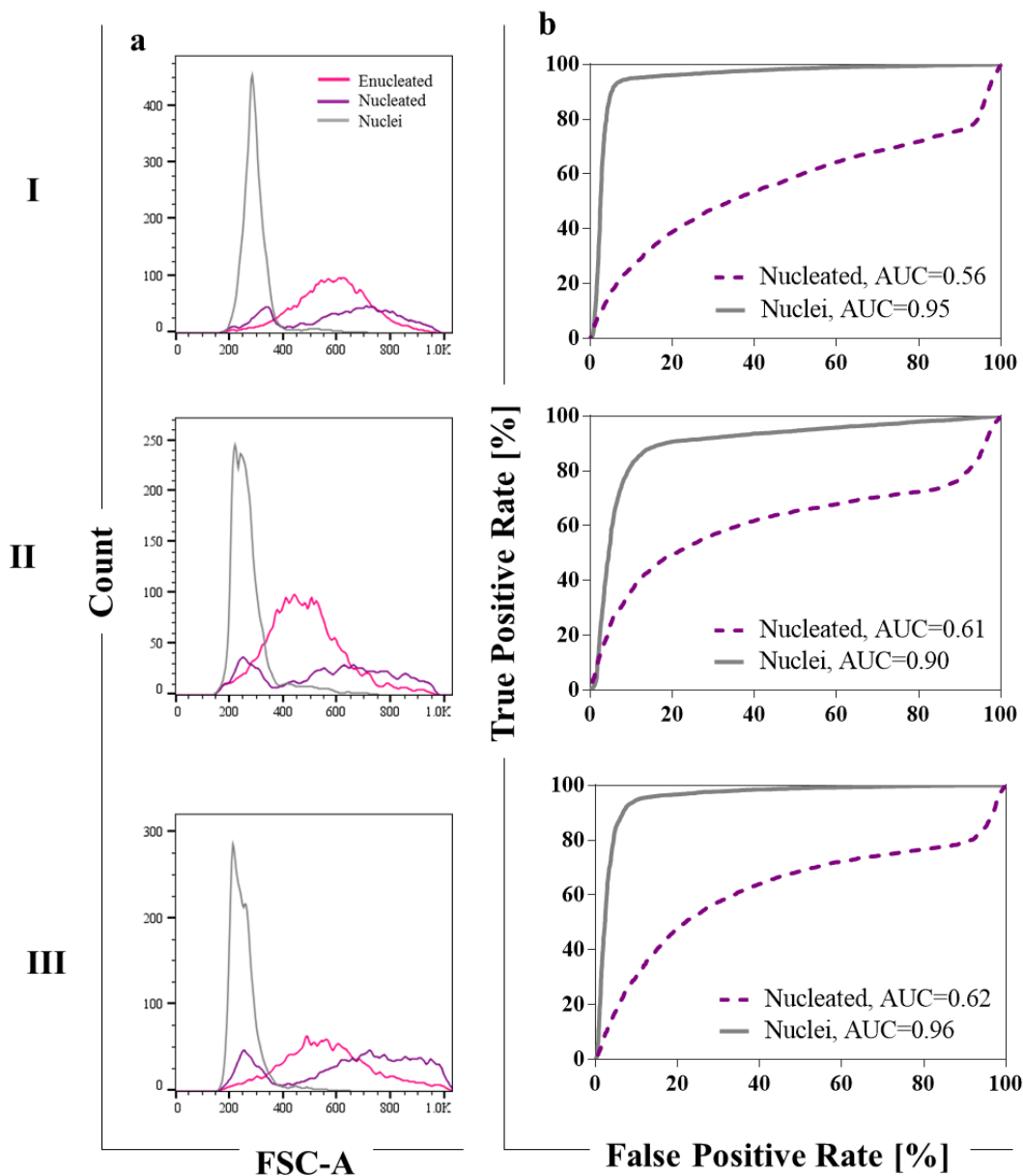


## Appendix I



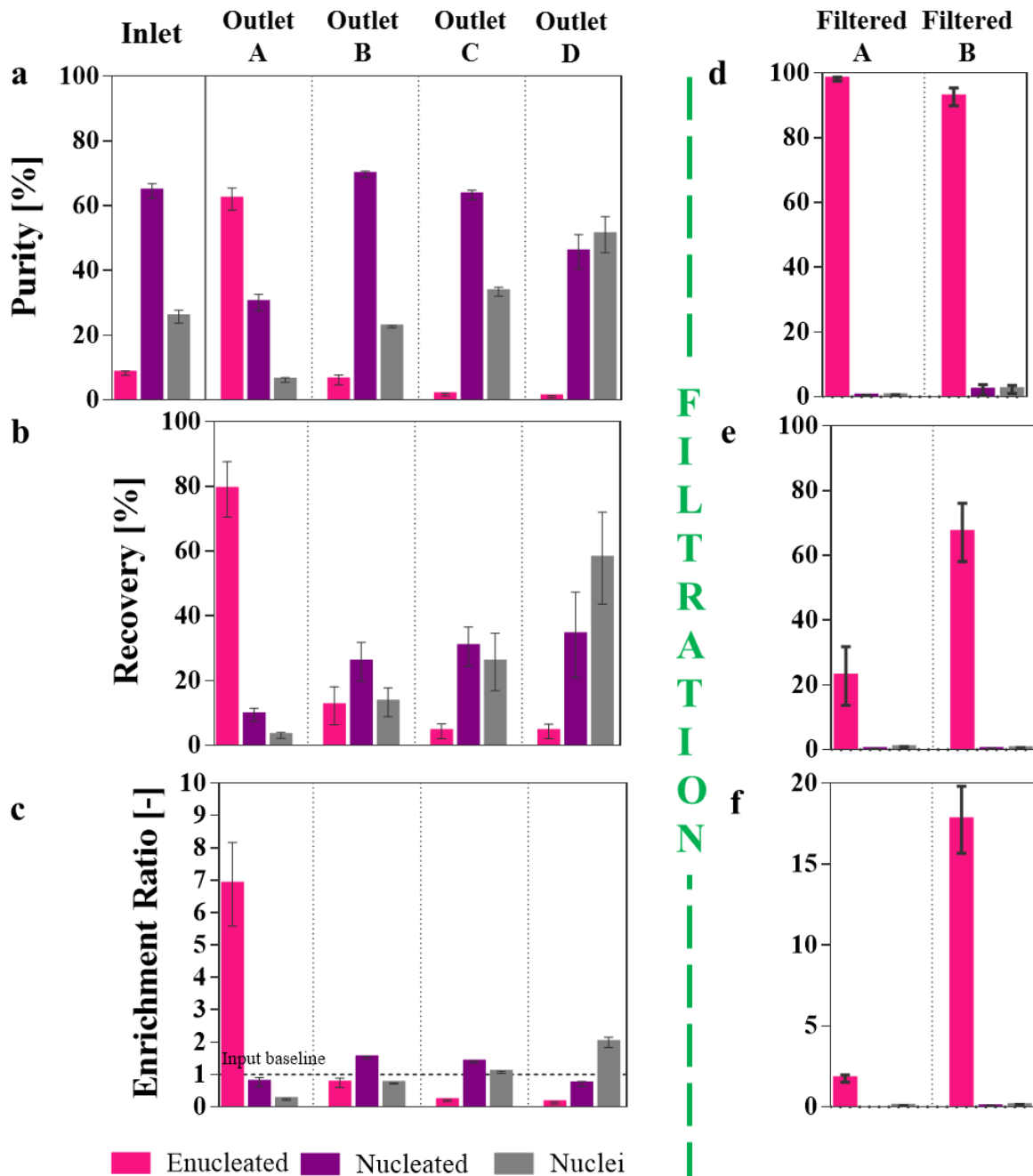
Receiver Operating Characteristic (ROC) curves were plotted for (a) size (expressed as FSC-A parameter) and (b) deformability [-] for enucleated versus nucleated cells (purple-dashed) and enucleated cells versus nuclei (grey) at the end of the differentiation protocol for three replicas for **donor II**. The True Positive Rate is defined as the number of enucleated cells measured for a certain cut-off point (size or deformability) and divided by the total number of enucleated cells. The False Positive Rate is the corresponding number of nucleated cells (resp. nuclei) divided by the total number of enucleated cells (resp. nuclei) for the same cut-off. The Area Under the Curve (AUC) was calculated to quantify the size and deformability overlaps.

## Appendix J



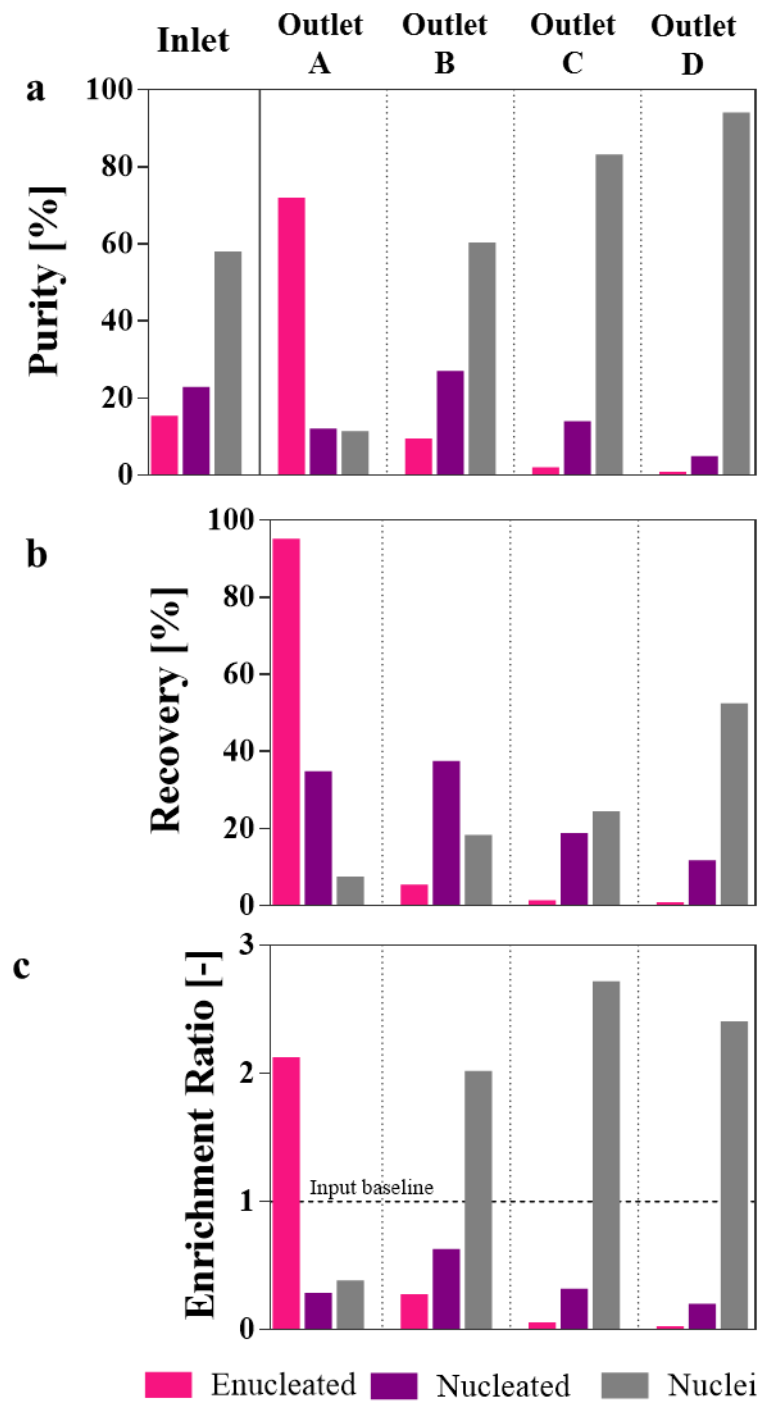
Relative size measurements by flow cytometry (FSC-A) for **donor III** (a) Histograms of FSC-A parameter reflecting relative sizes of enucleated (pink) and nucleated (purple) cells as well as the free-floating nuclei (grey). The number of events on each diagram is around 10000 split accordingly between each of the subpopulations. Receiver Operating Characteristic (ROC) curves were plotted for (b) size (expressed as FSC-A parameter) for enucleated versus nucleated cells (purple-dashed) and enucleated cells versus nuclei (grey) at the end of the differentiation protocol for three replicas for donor III. The True Positive Rate is defined as the number of enucleated cells measured for a certain cut-off point (size or deformability) and divided by the total number of enucleated cells. The False Positive Rate is the corresponding number of nucleated cells (resp. nuclei) divided by the total number of enucleated cells (resp. nuclei) for the same cut-off. The Area Under the Curve (AUC) was calculated to quantify the size and deformability overlaps.

## Appendix K



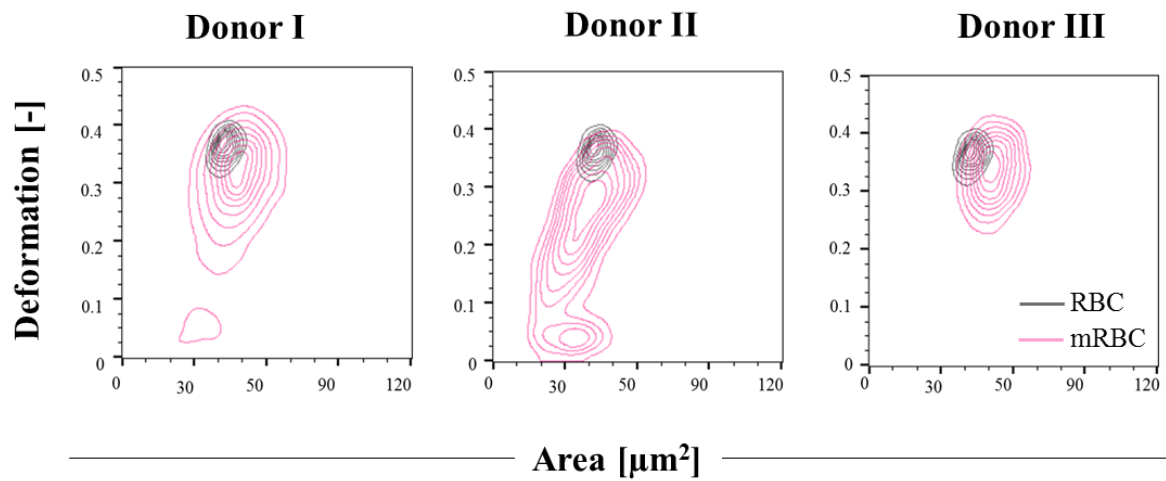
Characterisation of the label-free mRBC purification process for **donor II**. The purification efficiency of enucleated cells (pink) from the contaminant nucleated cells (purple) and nuclei (grey) after processing in the spiral channel with the  $30 \times 170 \mu\text{m}$  cross-section and four outlets (A -closest to the inner wall, B, C and D) at 1 ml/min flow rate as well as after (a, b & c) processing in the spiral channel and (d, e & f) enhanced by filtration. Filtration step was performed only on cells collected at the best performing outlets C and D. Both approaches were characterised with three parameters: purity, recovery and enrichments ratio. The process validation was performed at three independent occasions, the bars represent mean value and error bars correspond to the standard deviation of the mean. The dotted lines on the enrichment ratio diagrams represent input baseline.

## Appendix L



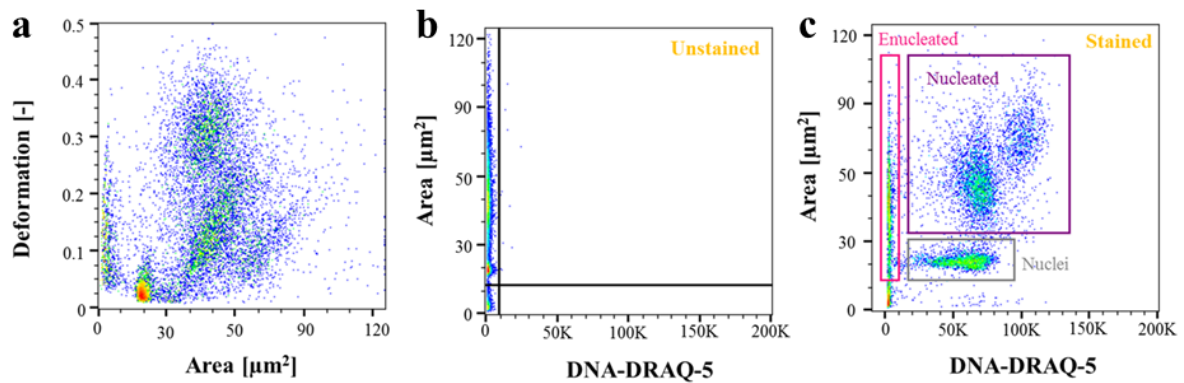
Characterisation of label-free mRBC purification process in the spiral channel for **donor III**. The purification efficiency of enucleated cells (pink) from the contaminant nucleated cells (purple) and nuclei (grey) after processing in the spiral channel with the  $30 \times 170 \mu\text{m}$  cross-section and four outlets (A -closest to the inner wall, B, C and D) at 1 ml/min flow rate.. The process was characterised three parameters (a) purity, (b) recovery and (c) enrichments ratio. The process validation was performed only once. The dotted lines on the enrichment ratio diagrams represent input baseline.

## Appendix M



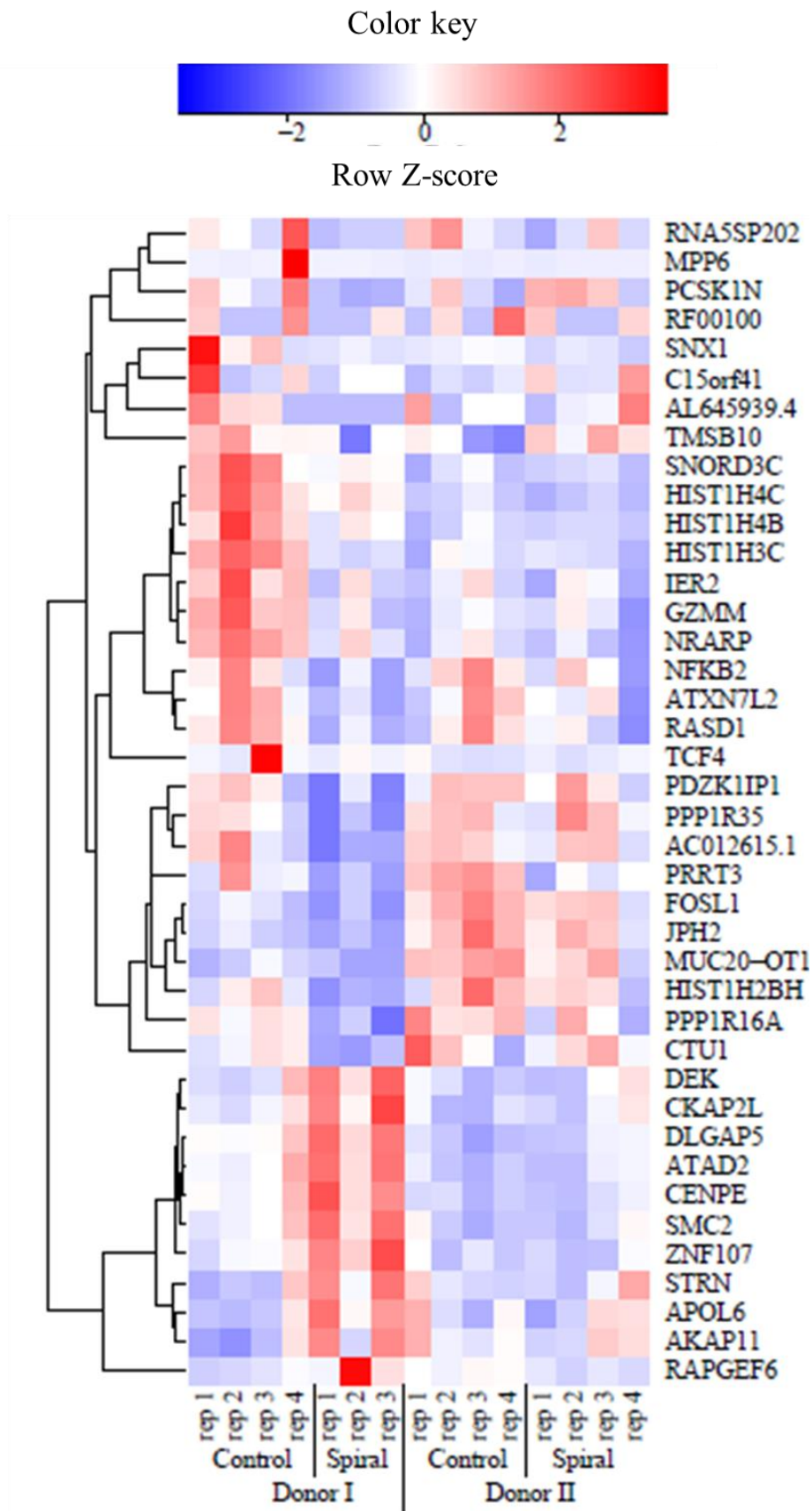
Comparison of mRBC derived from CB CD34+ from three donors (I, II and III) with RBC from peripheral blood. Equal probability contour plots (the same number of cells fall between each pair of contour lines) of deformation vs cell size (expressed as projected cell area in  $\mu\text{m}^2$ ) for enucleated cells derived from each researched donor (pink) and packed RBC purchased commercially (grey).

## Appendix N

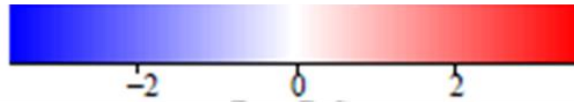


Gating strategy applied to characterise the end product of CB CD34+ *in vitro* erythropoiesis. The sample collected at the end of the differentiation protocol was stained with a nuclear stain DRAQ-5 to check for the presence of a nucleus. Each subpopulation can be characterised by a combination of size and fluorescent signal. Enucleated cells are inherently negative for DNA (DRAQ-5-DNA -), nucleated cells are larger than the free floating nuclei and both are DRAQ-5-DNA+. Events between 0-15  $\mu\text{m}^2$  were assumed to be cell debris and they were excluded from the analysis. **(a)** Scatter plot of the area [ $\mu\text{m}^2$ ] vs deformability [-] for a control unstained sample for more than 20000 acquired events. **(b)** Scatter plot of DRAQ-5-DNA vs area [ $\mu\text{m}^2$ ] for the unstained sample. The gate splits the scatter plot into DNA-negative region on the left hand side and DNA-positive region on the right hand side. **(c)** Scatter plot for the sample stained with DRAQ-5 for the presence of DNA. Gates for each subpopulations are shown as colour-coded rectangles: pink for enucleated cells, purple for nucleated cells and grey for nuclei.

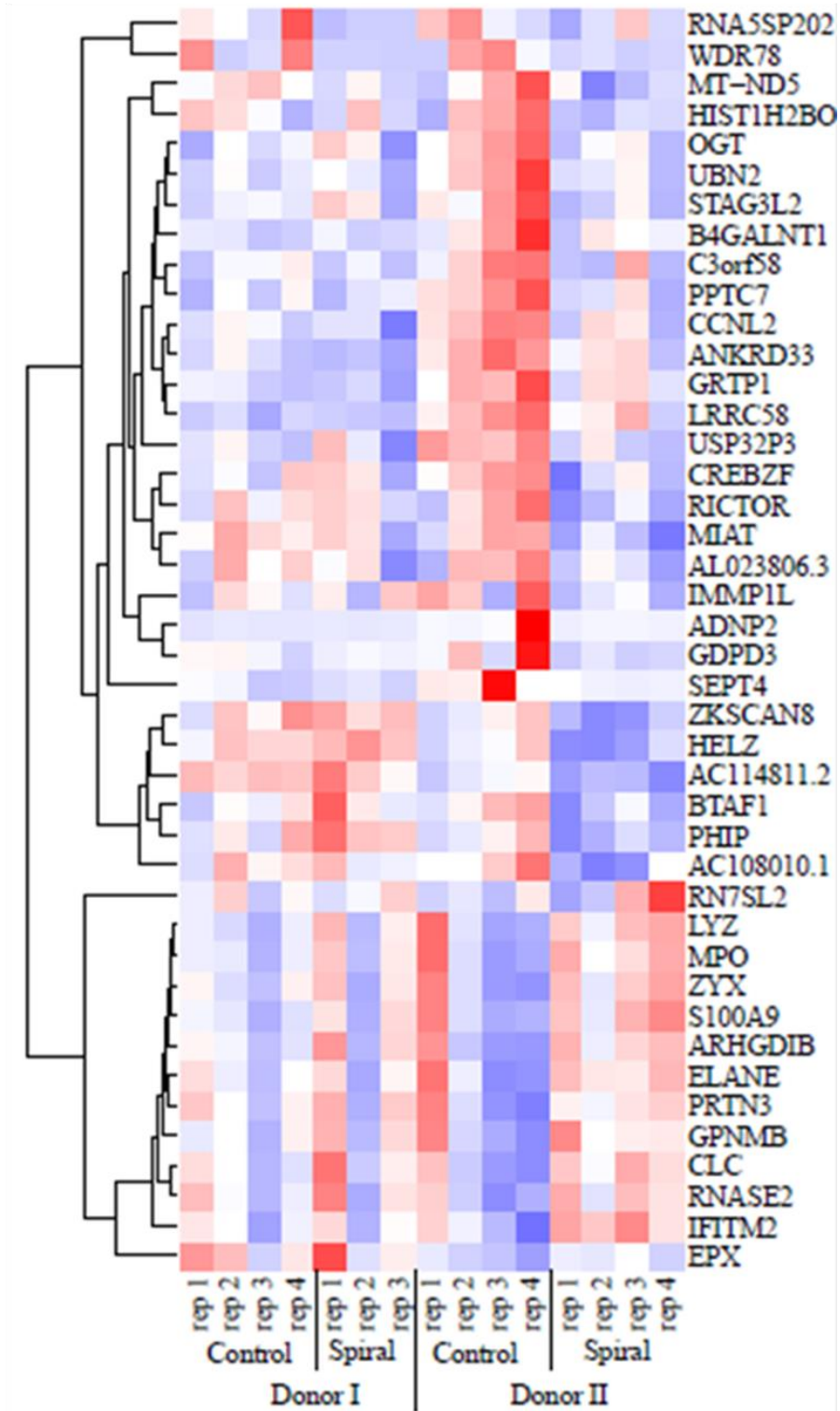
## Appendix O



Color key



Row Z-score



Donor II Significant Genes Heatmap



Hierarchically clustered heatmap of the significantly differentially expressed genes for the comparisons: donor I spiral and donor I control and donor II spiral and donor II control, for all sample in the sample groups: donor I spiral, donor I control, donor II spiral and donor II control. Samples are on the x axis and genes on the y axis. Colour intensity represents expression level, with blue representing low expression, and red representing high expression. Expression levels have been row scaled into z-scores. The y-axis (both plots) and x-axis (right plot) have been hierarchically clustered using, Spearman distances, with UPMGA agglomeration and mean reordering.

## Chapter 6. Bioprocess considerations Part I- predicted versus experimental results

### Highlights

- Heterogeneous mixtures of particles (of different sizes) behave differently within spiral microchannels than their homogeneous components tested as pure populations.
- The fluid flow pattern within spiral microchannel generated by the channel geometry is reshaped by presence of particles, which translates downstream into altered hydrodynamic behaviours.
- Large particles introduce additional vortices capturing smaller particles in “trains of particles” impacting their predicted equilibrium position, while smaller particles have no impact on the large particles.

### 6.1. Introduction

Inertial focusing in spiral microchannels has been adapted to separate various biological specimens from heterogeneous samples based upon their size, shape and deformability [90]. Particle focusing within a spiral microchannel is determined by the particles properties and their interplay with the fluid. In curved channels, the amplitude of Dean vortices is characterised by the Dean number (as defined in **Equation (8)**). In a given channel,  $De$  can be consequently changed by adjusting the Reynolds number ( $Re$ ) (see **Equation (1)**)-  $De$  increasing with increasing  $Re$  [165][166][99].

Currently, there is no robust numerical model that would allow precise prediction of equilibrium lateral positions which is crucial for identifying optimal flowrates for efficient separation and recovery. Consequently, the common practice is to quantify and describe the hydrodynamic behaviour for each subset (characterised by unique size and/or deformability) found within a heterogeneous sample, separately, as pure pre-sorted populations [83]. However, the impact of having mixed populations has not been investigated in depth in the literature.

In this study, the spiral channel ends with four balanced outlets (A, B, C and D), meaning that the channel itself could be divided into four sections along channel width (respectively, 0-42.5  $\mu\text{m}$ , 42.5-85  $\mu\text{m}$ , 85-127.5  $\mu\text{m}$  and 127.5-170  $\mu\text{m}$  measured from the outer wall), corresponding to these four outlets. Due to the laminar flow regime, particles found in each section at the end of the spiral channel, proceed, with negligible error, to the corresponding outlets. Hence, we assumed that if pure populations found in the end product of *in vitro*

erythropoiesis of CB CD34+ cells behaved in a certain way and they were found in the certain section of the spiral channel, they certainly should be captured in a corresponding outlet when tested as mixed populations. However, as shown in **Fig. 6.1**, the actual sorting performance, presented here as cell recovery [%] in each outlet, was different from predicted results. For each subpopulation, it is true that more events than anticipated (9.2% for enucleated cells, 18.9% for nucleated cells and 1.4% for nuclei) travelled to the outlet A and for nuclei and nucleated cells a shift towards the outer wall was observed, with a substantial depletion (16% for nucleated cells and 24% for nuclei) from the outlet D.

Recovery [%]	Enucleated				Nucleated				Nuclei			
	A	B	C	D	A	B	C	D	A	B	C	D
Predicted	82.9	13.4	1.9	1.9	0.8	35.7	30.2	33.3	0.4	2.5	1.6	95.5
Experimental	92.1	5.5	1.6	0.8	19.7	36.8	26.3	17.2	1.8	8.9	17.8	71.5
Difference	9.2	-7.9	-0.3	-1.1	18.9	1.1	-3.9	-16.1	1.4	6.4	16.2	-24

**Fig. 6.1**

*Table summarising predicted and experimental outcome of mRBC purification in the spiral channel at 1ml/min flow rate. Predicted recovery had been estimated by assessing hydrodynamic behaviour of pure pre-sorted populations of enucleated cells, nucleated cells and nuclei. Predicted recovery was generated by counting the number of cells/ nuclei found at lateral equilibrium positions within virtual boundaries of four section within the channel, which correspond to the four outlets.*

Particles focusing within the spiral microchannel is a complex process, where not only the distinct fluid flow pattern interacts with particles, but also the presence of particles shapes and disturbs the flow pattern and depending on particles properties, particle-particle interaction occurs [91]. The effect of particle-particle interaction is minimised by maintaining the optimal particles concentration to prevent their steric interaction (steric crowding effect), which can be estimated by calculating the number of particles diameters per channel length- the length fraction  $\alpha$  as defined in **Equation (17)**. For  $\alpha > 1$ , focusing to a single stream cannot be expected due to steric interactions between particles [91]. For more troublesome biological particle adhesion/ aggregation preventing additives like biocompatible surfactant Pluronic F-68 [162] and EDTA (ethylene diamine tetra-acetic acid) [167], are used. The cell-cell interaction in this study was minimised by working at cell concentrations ensuring  $\alpha \ll 1$  and the buffer was supplemented with 0.1% Pluronic F-68.

## 6.2. Results

Maximum separation efficiency of mRBC is achieved at 1ml/min flow rate. At this condition cells travel within the channel at  $\sim 3$  m/s velocity, making all present subpopulations indistinguishable in the imaging set-up used in this study. Hence, to further understand the differences between the predicted and experimental separation outcome, we researched if there was a difference in the hydrodynamic behaviour of pure and mixed populations using a model system consisting of cells of Jurkat cell line (round,  $\text{Ø}13 \pm 2\mu\text{m}$ , grown in suspension) and  $4\mu\text{m}$  spherical polystyrene beads. In order to reflect heterogeneous properties of events found in the end-product of the *in vitro* erythroid differentiation, mechanical properties of Jurkat cells were altered by fixing with 0.1% glutaraldehyde, known for its cross-linking property resulting in cell stiffening without altering cell size [168].

Soft (control, untreated) and stiff (fixed with glutaraldehyde) cells, as well as  $4\mu\text{m}$  beads, were passed through the spiral channel as pure populations at five previously tested flow rates (0.2, 0.4, 0.6, 0.8 and 1 ml/min), their equilibrium lateral position within the channel was assessed by image analysis (**Fig. 6.2 a**). In order to assess optimal flow rate for separating  $4\mu\text{m}$  beads from soft and stiff cells Receiver Operating Curves (ROC) curves were generated and Area under the Curve (AUC) was calculated (**Fig. 6.2 b** for separating  $4\mu\text{m}$  beads from soft cells and **Fig. 6.2 c** for separating  $4\mu\text{m}$  beads from stiff cells) and it was established that at the flow rate of 0.4 ml/min, streak of  $4\mu\text{m}$  beads would be physically 100% (AUC=1) separated from streaks of soft and stiff cells.

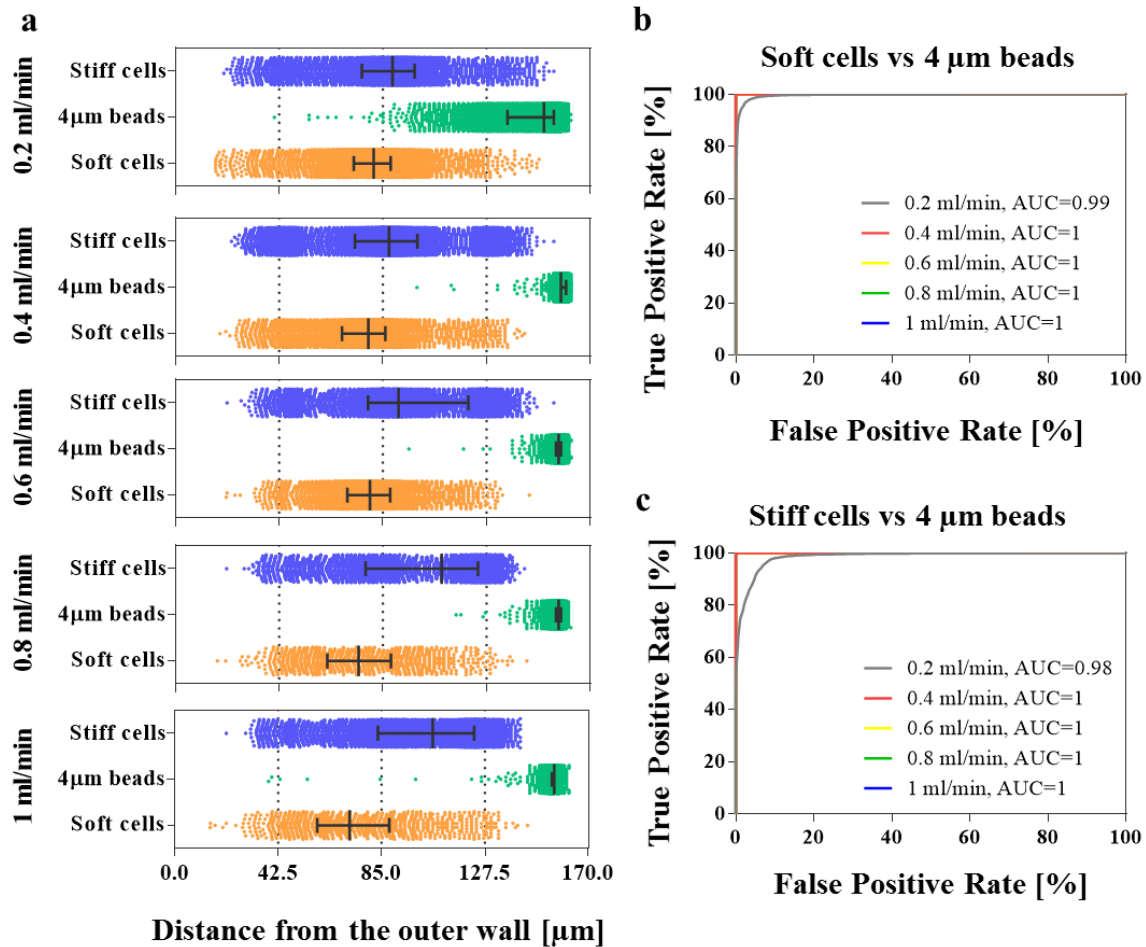


**Fig. 6.2**

Sorting optimisation with pure populations of 4µm beads (green), soft cells (orange) and stiff cells (blue). (a) Hydrodynamic behaviour of 4µm beads, soft and stiff cells assessed in the spiral channel with the  $30 \times 170 \mu\text{m}$  cross-section at five different flow rates (0.2, 0.4, 0.8 and 1 ml/min). The lateral equilibrium position was measured as a distance from the outer wall (µm) at the end of the spiral channel and it was generated by image analysis. Here, it is reported as median (represented as the longest vertical lines) and the interquartile range (indicated by the short vertical lines) on the top of scatter plots, where each dot represent one event. Receiver Operating Curves for (b) 4 µm beads versus soft cells and (c) 4 µm beads versus stiff cells, for each applied flow rate, were generated. The True Positive Rate is defined as the number of 4 µm found at a given lateral position and divided by the total number of 4 µm beads. The False Positive Rate is the corresponding number of soft cells (resp. stiff cells) divided by the total number of 4µm beads for the same cut-off. To determine which of the applied flow rates ensures the best separation efficiency the Area Under the Curve (AUC) was calculated.

To verify the predicted outcome, cells and beads collected at the outlets were quantified by flow cytometry to determine their purity and by performing cell count in order to calculate their recovery (Fig. 6.3).

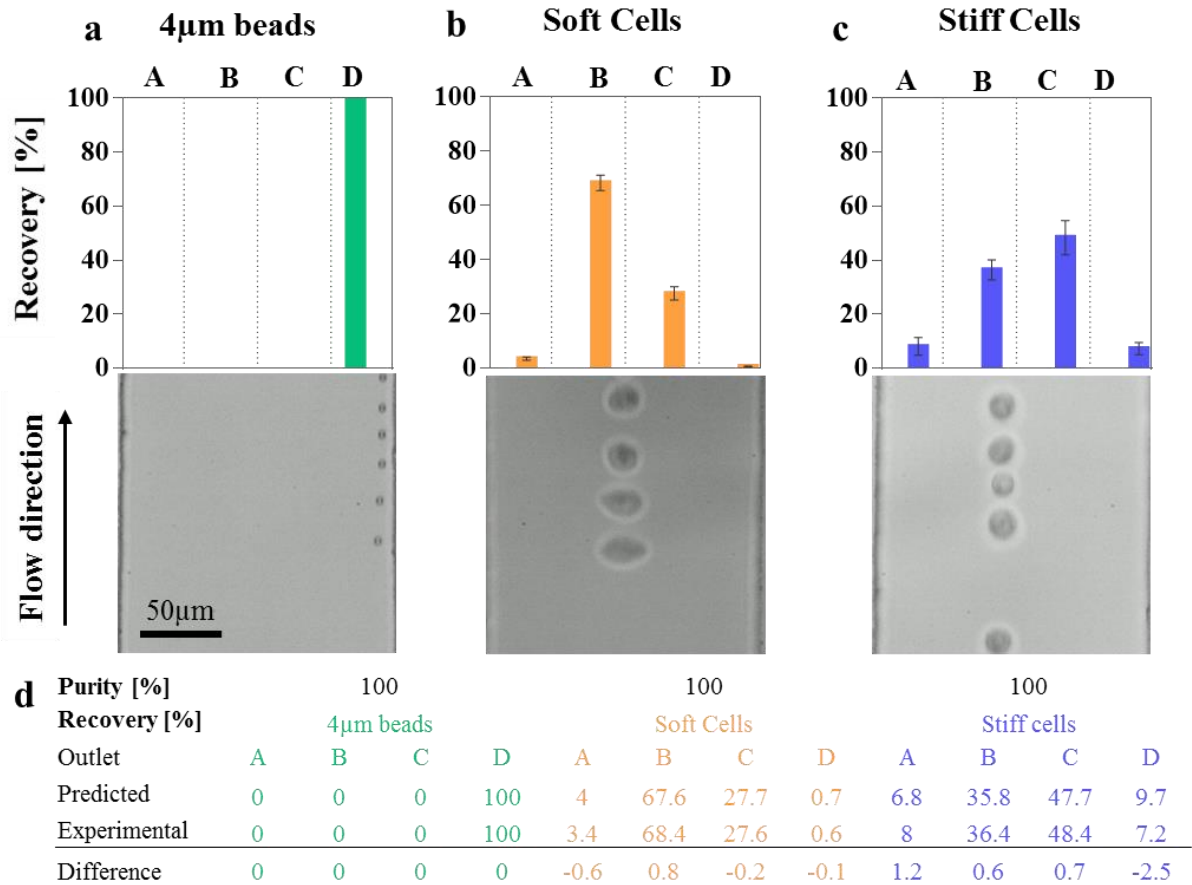


**Fig. 6.3**

Outcome of processing (a) 4 μm beads (green), (b) soft cells (orange) and (c) stiff cells (blue) in the spiral channel with the 30 × 170 μm cross-section and four outlets (A -closest to the outer wall, B, C and D) at 0.4 ml/min flow rate. Recovery of each population was assessed at three independent occasions, the bars represent mean value and error bars correspond to the standard deviation of the mean. The dotted vertical lines represent sections of the channel corresponding to outlets A/ B/ C/ D as indicated above the diagrams. Additionally, exemplary images for each population were acquired. The scale bar corresponds to 50 μm. (d) Table summarising predicted and experimental outcome of processing each population in the spiral channel. Predicted recovery was generated counting number of beads/ cells found at lateral equilibrium positions within virtual boundaries of four section within the channel, which correspond to the four outlets.

At the optimal 0.4 ml/min flow rate, 4 μm beads were focused in a tight streak at  $159 \pm 1.9 \mu\text{m}$  measured from the outer wall, and as expected 100% of beads were collected in outlet D (Fig. 6.3 a). Meanwhile soft (Fig. 6.3 b) and stiff (Fig. 6.3 c) cells were equilibrated closer to the channel centre ( $77 \pm 18.2 \mu\text{m}$  and  $86 \pm 26.8 \mu\text{m}$  for soft and stiff cells respectively).

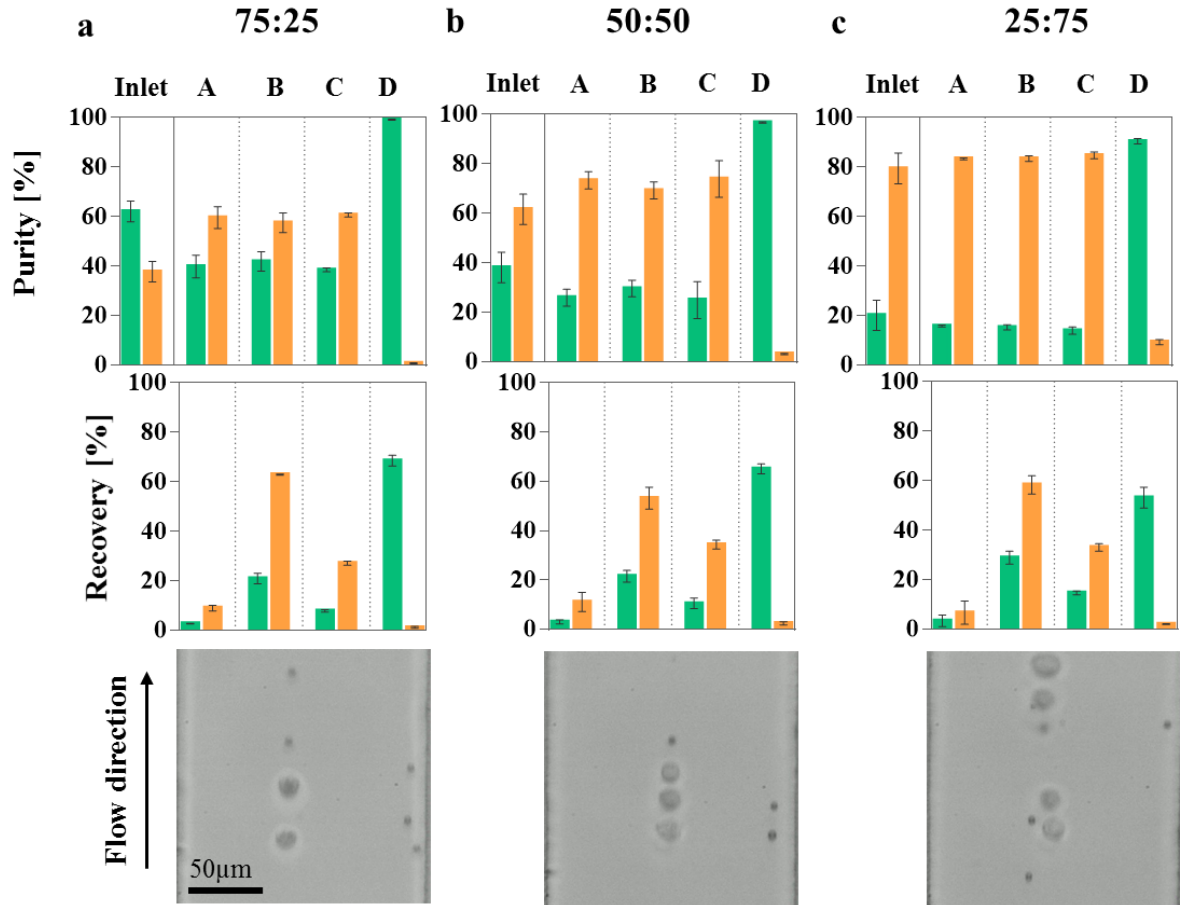
Due to their large size in comparison to the channel cross-section, cells are geometrically pushed toward the channel centreline and they occupy a relatively wide section in the middle of the channel. Consequently, they were mostly found in the middle outlets C

and B.  $63 \pm 2.9$  % soft cells and  $36 \pm 3.7$  % stiff cells travelled to outlet B and  $27 \pm 2.5$  % of soft and  $48 \pm 6.3$  % stiff cells were found in outlet C. Only a small portion of both cell types was directed to the outmost outlets A and D. These experimental results were in line with the predicted recovery of beads/ cells in each outlet, with a minimal ( $0.5 \pm 0.7\%$ ) error (**Fig. 6.3 d**). Predicted recovery was generated by counting the number of beads/ cells found at lateral equilibrium positions within virtual boundaries of the four sections within the channel which correspond to the four outlets.

Next, two types of mixtures were prepared, 4  $\mu\text{m}$  beads with soft cells (**Fig. 6.4**) and 4  $\mu\text{m}$  beads with stiff cells (**Fig. 6.5**). Beads and cells were meant to be mixed at three different beads/cells ratios: 75:25, 50:50 and 25:75, however due to an error live cells were mixed with beads at ratios closer to 40:60, 60:40 and 25:75- for the easiness of reading, the original values are used throughout the text. All six mixtures were run through the spiral channel at 0.4 ml/min and the separation efficiency was assessed by quantifying the portion of beads and cells in each outlet and calculating the recovery rate.

For both conditions, soft cells and 4  $\mu\text{m}$  bead and stiff cells and 4  $\mu\text{m}$  beads it was found that with the decreasing beads to cells ratio, the number of beads recovered in outlet D decreases, from predicted 100% for pure beads population, down to  $53 \pm 4.3$  % and  $62 \pm 1$  % when beads were mixed 25:75 with soft (**Fig. 6.4 a**) and stiff cells (**Fig. 6.5**), accompanied by a small increase (0.3-1.3%) of soft cells retrieved in outlet D, observed for all three conditions. Throughout the experiments with soft cells, the most noticeable changes was recorded in outlet B, with 4.7%, 14.5% and 9.3% depletion of cells for samples mixed at 75:25, 50:50 and 25:75 receptively, in favour of flanking outlets C and A. when cells outnumbered beads (50:50 and 25:75).

A similar pattern was observed for stiff cells (**Fig. 6.5**), for the 50:50 (**Fig. 6.5 b**) and 25:75 (**Fig. 6.5 c**) samples, where the number of stiff cells collected in the outlet D increased slightly by 2.3-6.5 %, while for the 75:25 sample (**Fig. 6.5 a**) the number dropped by 3.5%. For all three conditions stiff cells were depleted from outlets B and C in favour of the outlet A for the 75:25 sample and outlets A and D for the 50:50 and 25:75 samples.



**d**

Purity [%]	75				50				25			
Recovery [%]	4μm beads				4μm beads				4μm beads			
Outlet	A	B	C	D	A	B	C	D	A	B	C	D
Predicted	0.0	0.0	0.0	100.0	0.0	0.0	0.0	100.0	0.0	0.0	0.0	100.0
Experimental	2.7	20.9	7.8	68.6	3.0	21.5	10.5	65.0	3.3	28.9	14.6	53.1
Difference	2.7	20.9	7.8	-31.4	3.0	21.5	10.5	-34.9	3.3	28.9	14.6	-46.8

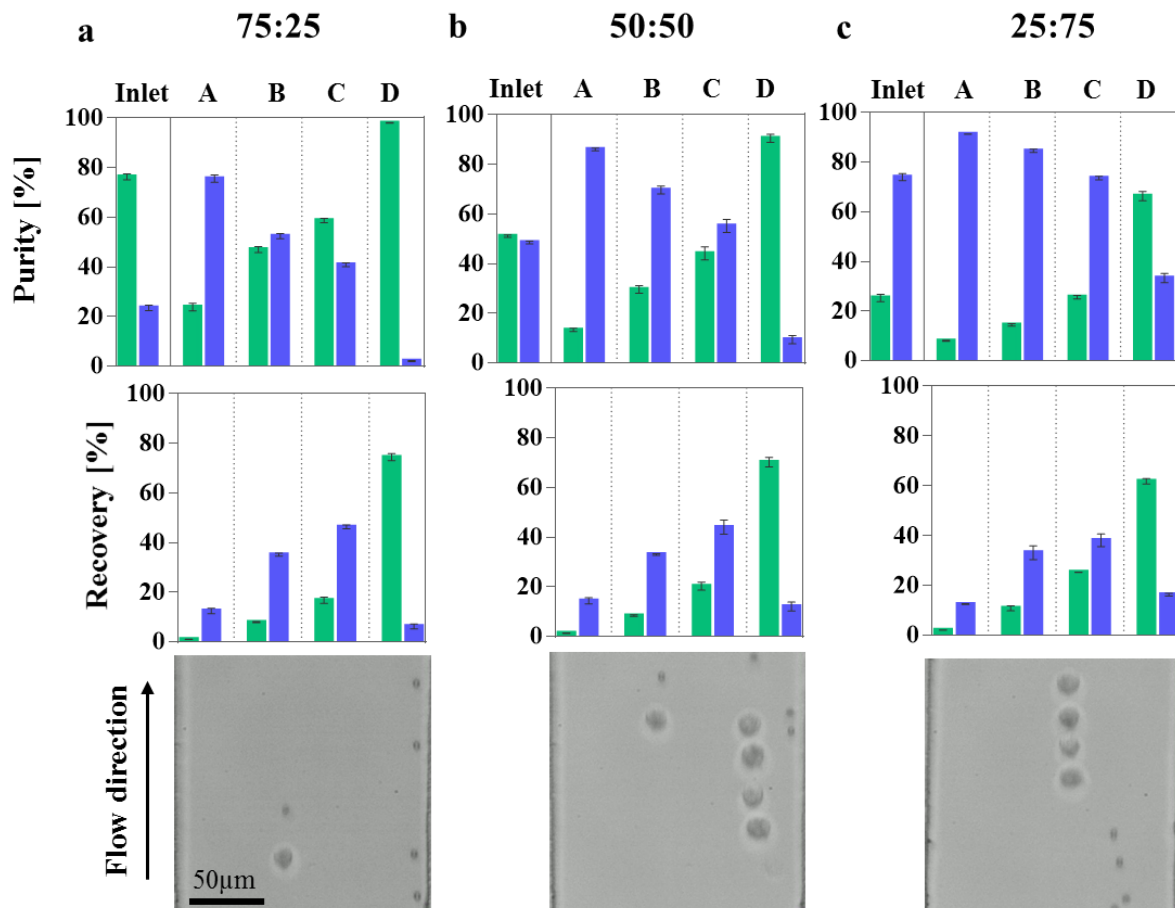
Purity [%]	25				50				75			
Recovery [%]	Soft Cells				Soft Cells				Soft Cells			
Outlet	A	B	C	D	A	B	C	D	A	B	C	D
Predicted	4.0	67.6	27.7	0.7	4.0	67.6	27.7	0.7	4.0	67.6	27.7	0.7
Experimental	8.9	62.9	27.1	1.1	11.1	53.1	34.4	2.3	6.7	58.3	33.1	2.0
Difference	4.9	-4.7	-0.7	0.4	7.1	-14.5	6.6	1.7	2.6	-9.3	5.3	1.3

**Fig. 6.4**

Characterisation of separation of 4 μm beads (green) from soft cells (orange) in the spiral channel with the  $30 \times 170 \mu\text{m}^2$  cross-section and four outlets (A -closest to the outer wall, B, C and D) at 0.4 ml/min flow rate. 4μm beads and soft cells were mixed at three different beads/cells ratios: (a) 75:25, (b) 50:50 and (c) 25:75 to the final concentration of  $1 \times 10^6$  events/ml. Please note that due to an error live cells were mixed with beads at ratios closer to 40:60, 60:40 and 25:75- for the easiness of reading, the original values are used throughout the text. Purity [%] was assessed quantifying the portion of beads and cells in the inlet sample, as well as samples collected at each outlet and recovery [%] of each population, was assessed. The process was characterised at three independent occasions, the bars represent mean value and



error bars correspond to the standard deviation of the mean. The dotted vertical lines represent sections of the channel corresponding to outlets A/B/C/D of as indicated above the diagrams. Additionally, exemplary images for each population were acquired. The scale bar corresponds to 50  $\mu\text{m}$ . (d) Table summarising predicted and experimental outcome of processing each population in the spiral channel. Predicted recovery was generated counting number of beads/cells found at lateral equilibrium positions within virtual boundaries of four section within the channel which correspond to the four outlets.



**d**

Purity [%]	75				50				25			
Recovery [%]	4 $\mu\text{m}$ beads				4 $\mu\text{m}$ beads				4 $\mu\text{m}$ beads			
Outlet	A	B	C	D	A	B	C	D	A	B	C	D
Predicted	0.0	0.0	0.0	100.0	0.0	0.0	0.0	100.0	0.0	0.0	0.0	100.0
Experimental	1.0	7.9	16.7	74.4	1.3	8.3	20.2	70.2	2.1	10.8	25.3	61.8
Difference	1.0	7.9	16.7	-25.6	1.3	8.3	20.2	-29.8	2.1	10.8	25.2	-38.1

Purity [%]	25				50				75			
Recovery [%]	Stiff cells				Stiff cells				Stiff cells			
Outlet	A	B	C	D	A	B	C	D	A	B	C	D
Predicted	6.8	35.8	47.7	9.7	6.8	35.8	47.7	9.7	6.8	35.8	47.7	9.7
Experimental	12.4	35.1	46.3	6.2	14.3	33.0	44.0	12.0	12.5	33.2	38.1	16.3
Difference	5.6	-0.7	-1.3	-3.5	7.5	-2.8	-3.7	2.3	5.6	-2.6	-9.5	6.5

**Fig. 6.5**

*Characterisation of separation of 4  $\mu\text{m}$  beads (green) from stiff cells (blue) in the spiral channel with the  $30 \times 170 \mu\text{m}$  cross-section and four outlets (A -closest to the outer wall, B, C and D) at 0.4 ml/min flow rate. 4 $\mu\text{m}$  beads and soft cells were mixed at three different beads/cells ratios: (a) 75:25, (b) 50:50 and (c) 25:75 to the final concentration of  $1 \times 10^6$  events/ml. Purity [%] was assessed quantifying the portion of beads and cells in the inlet sample, as well as samples collected at each outlet and recovery [%] of each population, was assessed. The process was characterised at three independent occasions, the bars represent mean value and error bars correspond to the standard deviation of the mean. The dotted vertical lines represent sections of the channel corresponding to outlets A/ B/ C/ D as indicated above the diagrams. Additionally, exemplary images for each population were acquired. The scale bar corresponds to 50  $\mu\text{m}$ . (d) Table summarising predicted and experimental outcome of processing each population in the spiral channel. Predicted recovery was generated counting number of beads/ cells found at lateral equilibrium positions within virtual boundaries of four section within the channel which correspond to the four outlets.*

### **6.3. Discussion**

In order to utilise the inertial effect in microchannels for particles ordering, such systems have to operate at intermediate Re [94]. In microfluidic systems operating within hydrodynamic regimes, where inertia is no longer negligible, particles constitute an active component of the system, shaping and altering fluid flow pattern [94]. As proposed by Amini *et al.* 2012 [169] for straight microchannels, with rectangular cross-section, the interplay between fluid flow and particles results from a combination of fluid inertia, fluid flow around the particle, particle rotation and particle to channel confinement ratio. Amini *et al.* 2012 verified experimentally two important hydrodynamic cases: (1) when particles dimensions are approaching those of the microchannel, they rotate in response to the flow field. Consequently, fluid streamlines approaching the rotating particle are diverted to a new cross-sectional position by so-called particle-induced convection. That causes the formation of a secondary flow, which resembles the characteristic of Dean flows found in curvilinear microchannels. (2) The cross-sectional lateral equilibrium position of particles large enough to trigger the particle-induced convection is not affected by the downstream consequences of the secondary flows. This statement is in line with the results observed in this study. Only negligible minute changes in hydrodynamic behaviour of Jurkat cells (both soft and stiff) were observed in mixed samples, while up to 50% of 4  $\mu\text{m}$  beads diverged from their primary cross-sectional lateral equilibrium position. This suggests that in a heterogeneous in size sample (e.g. mRBC), the presence of large (approaching channel dimensions) particles has a significant impact on the fluid streamline topology in the whole system and that in return modifies the predicted performance of the system. As highlighted numerous times in this study, cells intrinsic deformability adds

complexity to their hydrodynamic behaviour within inertial focusing (IF) devices. Interestingly,  $\sim 10\%$  more  $4\ \mu\text{m}$  beads were affected by the presence of soft cells, in comparison to the stiff cells. The cells deformability contribution to the overall IF is not fully-understood yet, but on multiple occasions, we appreciated its importance in harnessing the full-potential of IF.

Additionally, it is visible that cells flowing through the spiral microchannel travel in an ordered fashion, creating “trains” of cells with evenly distributed spaces between cells. This intriguing phenomena has been reported previously for inertial flows and is called interparticle spacing and to date, it is poorly understood [170]. However, W. Lee *et al.* 2010 proposed that the interparticles spacing is another consequence of particle-induced convection [171].

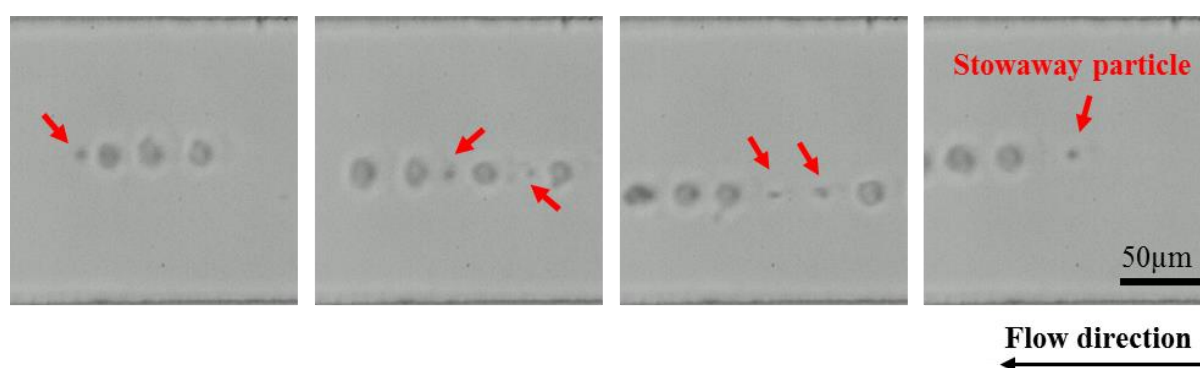


**Fig. 6.6**

*Exemplary images of soft Jurkat cells and  $4\ \mu\text{m}$  beads mixed at 50:50, flowing through the spiral microchannel at  $400\ \mu\text{l}/\text{min}$  flow rate assembled in trains.  $4\ \mu\text{m}$  beads (stowaway particles) joined the train positioned at lateral equilibrium position close to the channel centreline, typical for Jurkat cells. Images were taken at the end of the spiral channel and the scale bar represents  $50\ \mu\text{m}$ .*

Viscous disturbance flow generated by a rotating particle under confinement acts on a neighbouring approaching particle, repelling it a certain distance which is stabilised by inertial lift force (once particles assemble into the train with defined interparticles spacing this state is preserved by the action of inertial lift force). Consequently, even if there is no direct physical contact between particles (e.g. due to aggregation), hydrodynamic particle-particle interaction occurs due to the mechanism of self-assembly into either pairs or trains of particles. Hence, the pattern of particles ordering within the spiral microchannel is determined not only by inertial lift forces and secondary Dean flow (focusing position) but also it is modulated by the hydrodynamic particle-particle interaction (interparticles spacing). In all mixed systems tested in this study, we did not identify cells joining trains of  $4\ \mu\text{m}$  beads focused near the inner

wall of the channel, in contrast, “stowaway” beads were commonly found at different configurations (as shown in **Fig. 6.6**) in trains of cells positioned close to the channel centreline.

In the light of this study and literature reports discussed above, it can be hypothesised that in the mRBC sample, smaller rigid nuclei were affected by the presence of larger nucleated cells in a similar fashion as 4  $\mu\text{m}$  beads by Jurkat cells. Nuclei were substantially (24%) depleted from outlet A, on account of outlet B and C, where majority of nucleated cells were found. Additionally, the lower magnitude difference between the predicted and the experimental outcome for enucleated and nucleated cells across all outlets, could be a consequence of the, so far, uncontrollable and unpredictable train of particles formation.

## **6.4. Conclusion**

In conclusion, we experimentally investigated possible causes of differences in hydrodynamic behaviour of pure and mixed populations of particles of different sizes and deformability. In mixed samples, in the presence of particles whose diameter approaches the size of the channel, commonly negligible rotation of particles causes disturbances and modification in the focusing pattern for smaller particles, which translate into significant changes in the sorting performance. The rotation-induced secondary flows cause fluid mixing across the channel introducing aberrations into the fluid flow pattern. Additionally, the rotation-induced secondary flows promote hydrodynamic particle-particle interaction resulting in particles self-assembly in trains. These forces have been implicated as a cause of focusing alterations for smaller particles, adversely affecting particle separation in the spiral microchannel. The mixing effect is desirable for certain applications (e.g. for fluid mixing and switching in sample preparation protocols prior to flow cytometry). However, these poorly understood factors altering focusing positions of particles in inertial sorters can constitute a significant technical issue. Profound understating of these effects would aid better control over inertial devices performance and facilitate making inertial focusing a mainstream technology in the future.

## **6.5. Materials and methods**

### **6.5.1. Sample preparation**

Cells from the same batch were collected when at their exponential growth phase, split into fresh cell culture flask to maintained researched conditions. Prior to treatment with Glutaraldehyde (SigmaAldrich) cells were washed twice in PBS-/- (phosphate buffered saline without calcium and magnesium, Gibco) to remove any residual proteins. Next cells were re-

suspended at  $1 \times 10^6$  cell/ml in PBS-/- supplemented with 0.1% (v/v) Glutaraldehyde) and incubated at room temperature for 40 min. After the incubation time cells were washed once in PBS-/- and re-suspended accordingly in PBS-/- supplemented with 0.1% Pluronic F-68 (ThermoFisher Scientific) for experiments in the spiral channels

Nine types of samples were prepared at a final concentration of  $1 \times 10^6$  particles/ml in PBS-/- supplemented with 0.1% Pluronic F-68: three pure suspensions of  $4 \mu\text{m}$  beads, soft (untreated) Jurkat cells, stiff (glutaraldehyde-treated) Jurkat cells, three mixtures of  $4 \mu\text{m}$  beads and soft cells and three mixtures of  $4 \mu\text{m}$  beads (Magasphere Ltd.) and stiff cells. Mixtures of beads and cells were prepared at three different beads: cells ratio, 75:25, 50:50 and 25:75.

### 6.5.2. Hydrodynamic behaviour in spiral microchannel

Hydrodynamic behaviour of all nine samples was tested in a spiral microchannel with  $170 \times 30 \mu\text{m}$  cross-section, 6 loops, 1 inlet and four outlets as described in **Chapter 2**. As shown in **Table 6.1**,  $4 \mu\text{m}$  beads do not achieve the desirable  $Re_p > 1$  at flow rates lower than 1 ml/min, but we verified experimentally that despite the unsatisfactory  $Re_p$ , at lower flow rates they remain focused within the spiral microchannel (**Fig. 6.2**).

Flow rate [ml/min]	Velocity [m/s]	Re [-]	$Re_p$ [-] 4 $\mu\text{m}$ beads	$Re_p$ [-] Jurkat cells	De
0.2	0.65	33	0.2	2.1	5.19
0.4	1.3	66	0.4	4.3	10.38
0.6	1.9	97	0.6	6.3	15.18
0.8	2.6	132	0.8	8.6	20.77
1	3.3	168	1.0	10.9	26.36

**Table 6.1**

*Summary of useful parameters for optimising spiral microchannel performance. Re is channel Reynolds number,  $Re_p$  is particle Reynolds number, De is Dean number.*

Cell separation efficiency was quantified by flow cytometry in order to compare the fraction of each cell population (characterised by size difference measured as forward light scatter parameter FSC-A, as shown in **Fig. 6.7**) in samples collected at each outlets. Cell yield was assessed by counting a number of cells at each outlet using either a standard glass haemocytometer or MoxiZ automated cell counter (Orflo, US)

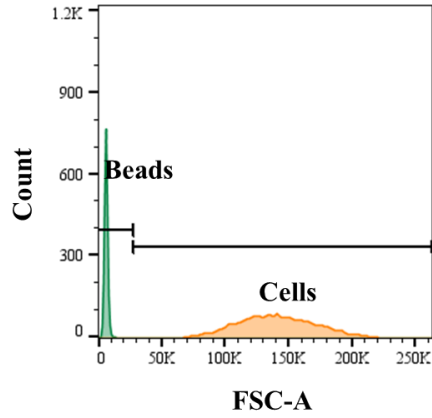


**Fig. 6.7**

An exemplary histogram of forward light scatter (FSC-A) parameter measured for 4  $\mu\text{m}$  beads (green) and soft Jurkat cells (orange), reflecting their relative sizes. Displayed gating was used to quantify purity of each subpopulation in samples collected at four outlets after processing in the spiral microchannel.

In order to define the sorting performance collected metrics were formulated into two parameters:

$$\text{Recovery } [P]_{\text{outlet}_i} = \frac{[P]_{\text{outlet}_i}}{\sum_{i=1}^4 [P]_{\text{outlet}_i}} \quad (20)$$

of each particle type  $[P]$ , and

$$\text{Purity}[P]_{\text{outlet}_i} = \frac{[P]_{\text{outlet}_i}}{[4 \mu\text{m beads} + \text{Cells}]_{\text{outlet}_i}} \times 100\% \quad (21)$$

indicating a fraction of each subset in a sample collected after processing. Data analysis and plotting were performed using GraphPad Prism 6 and FlowJo V10 CL.

# Chapter 7. Bioprocessing considerations Part II- medium choice- impact of Poloxamer 188 (Pluronic F-68) additive on cell mechanical properties

## Highlights

- Commonly used additive Pluronic F-68 can change mechanical properties of cells and consequently alter their processing.
- This effect has been quantified for cell types commonly used in the microfluidic field: red blood cells (RBC) and a lymphoblastic cell line-Jurkat and human embryonic kidney (HEK) cells.
- The RT-DC approach enabled fast processing of cells, leading to an accurate picture of the time (1-5 hours) and concentration (0.01%, 0.05% and 1%) -dependence of cell deformability in the presence of additives.

## Published work

Ewa Guzniczak, Melanie Jimenez, Matthew Irwin, Oliver Otto, Nicholas Willoughby, and Helen Bridle, **Impact of Poloxamer 188 (Pluronic F-68) Additive on Cell Mechanical Properties, Quantification by Real-Time Deformability Cytometry.** *Biomicrofluidics* 12 (4), 44118 (2018).- reproduced with the permission of AIP Publishing. for the authors contributions please consult research thesis submission form.

## 7.1. Introduction

The label-free purification strategy proposed in this study was designed specifically for stem cell- derived red blood cells (mRBC) purification. As described in **Chapters 3 & 5**, the current manufacture protocol involves human serum as a supplement to cell culture media. We found, similarly to others, that our devices tend to clog when serum is presented in the processing buffer [161], thus we recommend exchanging the buffer to serum-free for the processing time. Additionally, our devices were clogging due to channel cross-section merely larger than a couple of cell diameters. One of the most commonly accepted solutions to prevent clogging issues is the use of additives such as poloxamers, dextran or methylcellulose [172].

Our buffer of choice was PBS-/- (phosphate buffered saline without calcium and magnesium) supplemented with 0.1% biocompatible surfactant Pluronic F-68 [162] (TermoFisher Scientific, cat. 24040032). It was motivated with PBS-/- compatibility with technical requirements of quality control assays such as flow cytometry [163] and cell counts performed using MoxiZ automated cell counter as well as improved image quality [54]. Presence of phenol red (pH indicator in basal medium) impairs reads from both flow cytometry

and automated cell count, thus cells processed in the basal medium could not be directly sampled for the quality control tests. Moreover, Pluronic F-68 was added to surrogate the serum protective mechanism from mechanical damages (e.g. due to shear stress generated within the spiral microchannel)[160][164][162].

Pluronic F-68 is a biocompatible amphiphilic and nonionic compound consisting of a central polyoxypropylene (POP) block, flanked on both sides by hydrophilic chains of polyoxyethylene (POE) [173]. This surface-active macromolecule (molecular weight 8400) is used as an antifoam agent in stirred cell culture vessels and large scale bioreactors [174][175][164] among numerous other applications (*e.g.* as antithrombotic [176] or anti-inflammatory [177] agents, as an artificial blood emulsifier [178] or skin wound cleanser [179]).

Pluronic F-68 and other poloxamers have been adopted as a coating agents and additives in microfluidic systems engineered for cell analysis [180], lysis [181], separation [182] and detection [183], in microconstrictions for assessing cell mechanical properties [54] and digital microfluidics [184]. Poloxamers added to a flow buffer can coat glass [185], silicon [186], PDMS [187] and PMMA [188] - materials commonly used for microfluidic fabrication. This kind of treatment prevents clogging, reagents adsorption, protein fouling, cell-cell interaction, reduces electro-osmotic flow and can provide cell protection against a high degree of shear stress [189]. This repair and protective mechanism of Pluronic on cells is not fully-understood yet, however, some literature evidence suggests direct interaction with cell membrane causing cell stiffening [190][191].

As mentioned previously, mechanical cell properties are seen as a potential marker for label-free separation with applications in large-scale bioprocessing. However, the observation that Pluronic can stiffen cells suggests that the use of such additives could potentially impact upon the performance of mechanical based purification approaches. Thus, we investigated the effect of Pluronic F-68 on cells commonly used in microfluidic studies: Jurkat cells, red blood cells and human embryonic kidney (HEK) cells. The aim was to quantify if the addition of Pluronic F-68 significantly influenced cell mechanotype, which could have implications for mechanical phenotype based downstream cellular processing in spiral microchannels. For the first time, observed changes were quantified using real-time deformability cytometry (RT-DC) [46] to assess the short-term impact of Pluronic F-68, in comparison to controls with and without serum.



## 7.2. Results

### 7.2.1. Effect of Pluronic on Jurkat cells size and deformability- time-dependency

To understand the short-term effect of the Pluronic F-68 additive on cell mechanotype, we measured the size and deformability of Jurkat cells cultured either in cell culture medium containing serum or phosphate-buffered saline (PBS<sup>-/-</sup>) and I compared them against cells whose medium was supplemented with 1% Pluronic F-68. The choice of a serum-free experiment is motivated by experience with microfluidic systems. Most tissue culture systems contain serum, which easily clogs microfluidic chips (due to the high protein content), and therefore replacing cell culture medium with PBS<sup>-/-</sup> for the time of the experiments is a common practice [192][54][193]. The RT-DC measurements were taken each hour for 3 hours. The chosen time-scale was motivated by an average longevity of experiments in microfluidic systems used in our laboratory.

**Fig. 7.1 a & b** shows time-dependent changes in cell deformability. The effect of Pluronic F-68 was normalised to the untreated control. For both conditions addition of Pluronic F-68 causes significant changes after 3 hrs of addition. The alteration of deformability, expressed here as differential deformation (DD) (please see materials and methods for details) of cells cultured in serum (**Fig. 7.1 a**), progresses slowly but gradually for the first two hours causing initially slight (> 5%), almost negligible (p-value no significant), stiffening. Incubating cells for 3 hrs in the presence of Pluronic F-68 causes significant (p-value <0.01) decreases of cell deformability (~ 23%). Specifically, it drops within 3hrs from  $DD=0.051 \pm 0.0017$  to  $DD=0.039 \pm 0.0045$  (DD expressed as mean of three experimental replicates  $\pm$  standard error of the mean).

Interestingly, when medium containing serum is replaced with PBS<sup>-/-</sup> (control from **Fig. 7.1 b**) cell deformability drops by ~22% from the original  $DD= 0.051 \pm 0.0017$  to  $DD= 0.040 \pm 0.0015$  within less than 15 min of medium replacement and it equilibrates within an hour at  $DD=0.032 \pm 0.0016$ . During the first two hours Pluronic F-68-treated sample and PBS<sup>-/-</sup> control are indistinguishable. After 3 hrs of incubation Pluronic F-68-treated sample diverges and becomes stiffer ( $DD= 0.022 \pm 0.0023$ ) by ~ 29%.

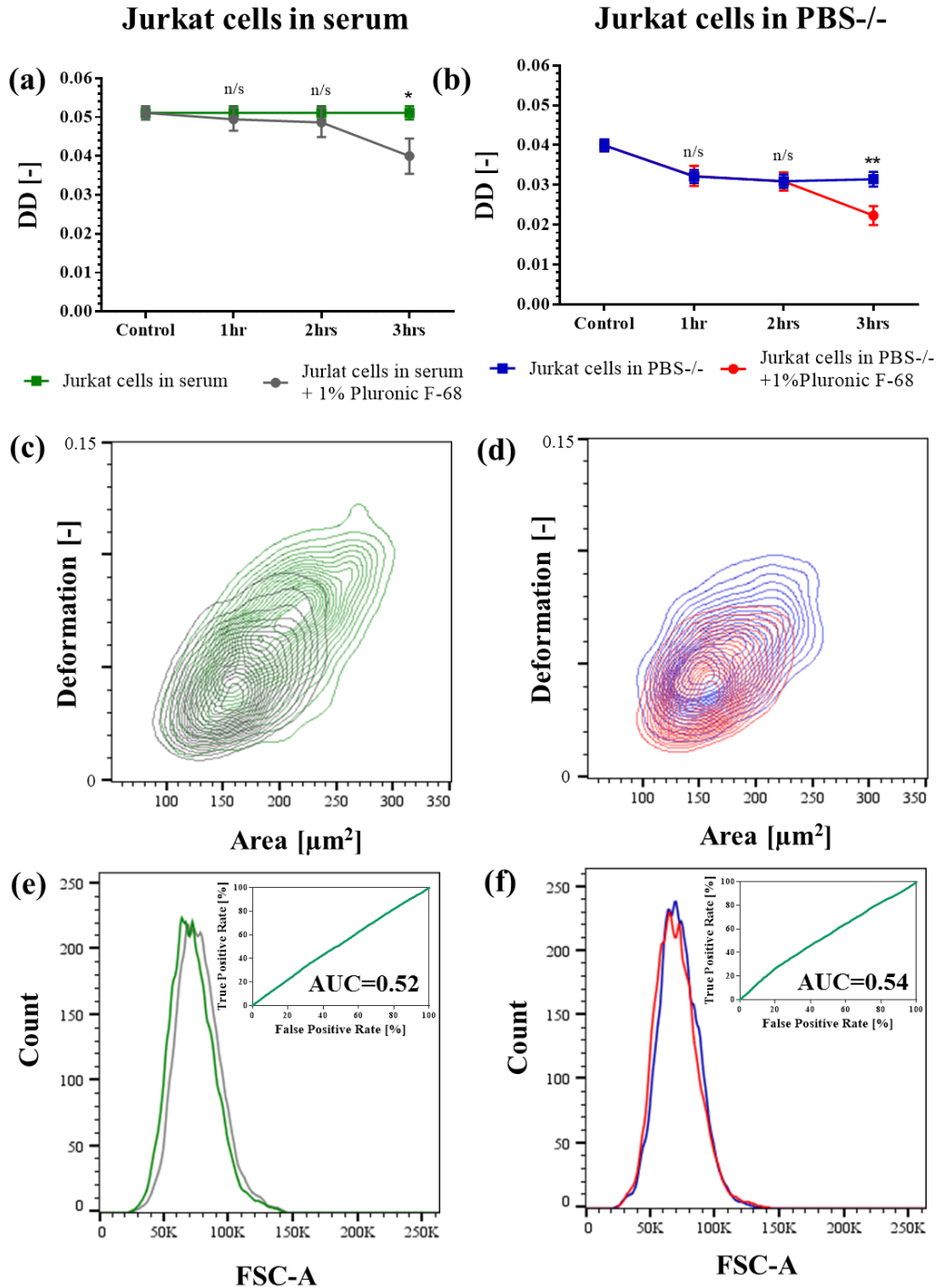


**Fig. 7.1**

Effect of Pluronic F-68 on cells of Jurkat cell line mechanical properties was quantified using real-time deformability cytometry (RT-DC) and flow cytometry. Cells from four conditions: Jurkat cells in serum (green)- extracted directly from tissue culture containing serum; Jurkat cells in serum +1% (w/v) Pluronic F-68 (gray)- cells cultured in medium containing serum supplemented with 1% Pluronic F-68; Jurkat cells in PBS -/- (blue)- cells incubated in PBS-/- without serum and Jurkat cells in PBS-/- + 1% Pluronic F-68 (red)- cells incubated in PBS-/- supplemented with 1% Pluronic F-68, without serum, were examined. Deformation was measured every hour for three hours. **(a & b)** Time-dependent response graphs show mean differential deformation (DD) values of three experimental replicates. Error bars correspond

to the standard error of the mean (SEM). P-values were calculated using the linear mixed model (\*p-value <0.01, \*\* p-value<0.001, n/s no significant). (c & d) Exemplary contour plots show outlines of assessed populations (more than 4000 events per population) for deformation versus size (expressed as projected cells area in  $\mu\text{m}^2$ ) recorded in the measurement channel section of the RT-DC chip. All samples were examined at 0.04 $\mu\text{l/s}$  flow rate in a 20x20 $\mu\text{m}^2$  cross section RT-DC channel after 3 hrs of incubation. (e & f) Cell size was assessed using forward light scatter parameter (FSC-A) measured using flow cytometer for 10000 cells. Receiver Operating Characteristic (ROC) curves were plotted for size expressed as FSC-A. The True Positive Rate is defined as the number of control cells measured for a certain size cut-off point and divided by the total number of control cells. The False Positive Rate is the corresponding number of Pluronic F-68- treated cells divided by the total number of treated cells for the same cut-off. The Area Under the Curve (AUC) was calculated to quantify the size overlap between control and treated cells after 3 hours.

The RT-DC technique is based on image analysis allowing for size measurement, which is expressed as a projected cell area reported in  $\mu\text{m}^2$  as shown in the contour plots **Fig. 7.1 c & d**. Although accurate, the technique can at times be sensitive to the changes in focus setting. Hence rather than reporting the projected cell area we used flow cytometry to quantify forward light scatter (FSC-A) - a measurement of the amount of a laser beam that passes around the cell - providing a relative cell size. **Fig. 7.1 e & f** show acquired values of FSC-A for all conditions. To quantify the degree of size overlap Receiver Operating Curves (ROC) curves were generated and the corresponding Area Under the Curve (AUC) was calculated. Supplementing medium with Pluronic F-68 has a negligible effect on cell size, and it remains unchanged for both cells in serum (AUC=0.52) and cells in PBS-/- (AUC=0.54).

### 7.2.2. Effect of Pluronic on Jurkat cell size and deformability- concentration dependency

Recommended poloxamer additive concentrations depend on the purpose and intended application. Proposed working concentrations for cell culture vary between 0.1% and 1% w/v [194][195][164]. Here we examined the effect of different Pluronic F-68 concentrations (0.1, 0.5 and 1% w/v) on Jurkat cells, incubated for 3hrs in supplemented medium with and without serum and compared to untreated controls.

**Fig. 7.2** shows the effect of different Pluronic F-68 concentrations on Jurkat cells in serum exerted in terms of cell deformability. Lower concentrations (0.1% and 0.5%) do not trigger changes in cell deformability within the first 3 hours of exposure. Cell size (expressed as FSC-A measured by flow cytometry) remains unaffected as reported in **Fig. 7.2 b** (AUC=0.53 for 1%, AUC=0.50 for 0.5% and AUC=0.54 for 0.1% Pluronic F-68).

Jurkat cells in PBS  $-/-$  (**Fig. 7.2 c**) are slightly more sensitive to the presence of Pluronic F-68 since small ( $\sim 6\%$ ) but consistent changes (standard error of the mean SEM= 0.0007 for three replicates of the experiment, p-value  $<0.01$ ) are observed after 3 hours of exposure to 0.5% Pluronic F-68. Similarly to the previous samples, cell size remains unaffected for all conditions (**Fig. 7.2 d**).

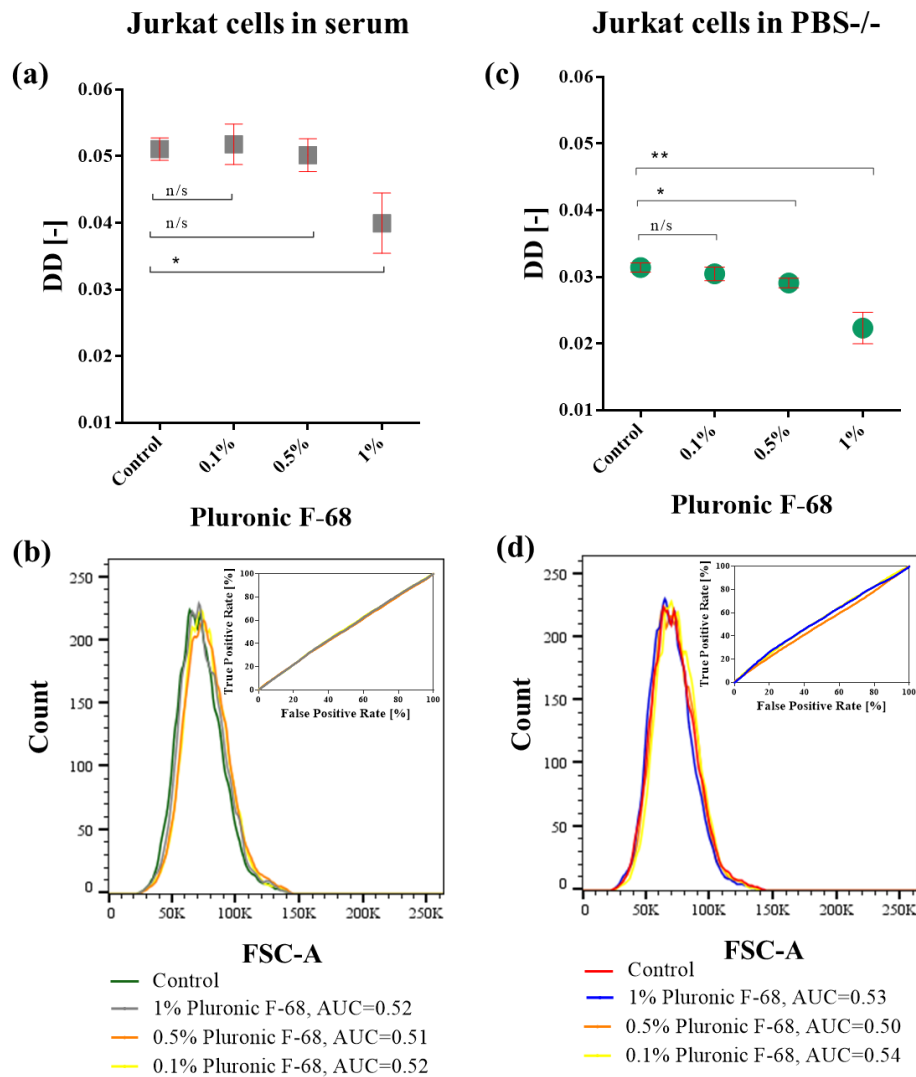


**Fig. 7.2**

Cells of Jurkat cell line were used to examine concentration-dependent deformability and size alteration caused by Pluronic F-68 additive. Cells were incubated for 3 hours in medium containing serum and PBS  $-/-$  supplemented with 0.1 (yellow), 0.5 (orange) and 1% (grey) Pluronic F-68. (**a & c**) Concentration-dependent graphs show Jurkat cells' response to increasing concentration of Pluronic F-68 in comparison to untreated control. The data points represent mean differential deformation (DD) values of Jurkat cells treated with Pluronic F-68 measured on three separate occasions. The bar graphs represent the standard error of the mean (SEM), the significance of results was calculated using the linear mixed model (\* p-value  $<0.01$ , \*\* p-value  $<0.001$ , n/s no significant). (**b & d**) To assess if treatment with Pluronic F-

68 causes changes in size, cells were characterised by flow cytometry for the forward light scatter (FSC-A) for 10000 cells from each condition. Receiver Operating Characteristic (ROC) curves were plotted for size expressed as FSC-A. The True Positive Rate is defined as the number of control cells measured for a certain size cut-off point and divided by the total number of control cells (green). The False Positive Rate is the corresponding number of Pluronic F-68- treated cells divided by the total number of treated cells for the same cut-off. The Area Under the Curve (AUC) was calculated to quantify the size overlap between control and treated cells. Data for all samples was collected at  $0.04\mu\text{l/s}$  flow rate in a  $20\times 20\mu\text{m}^2$  cross section RT-DC channel.

### 7.2.3. Effect of Pluronic F-68 on RBCs size and deformability

In previous works the effect of Pluronic F-68 on red blood cells (RBCs) was examined for diseased erythrocytes in sickle anaemia, where it was discovered that Pluronic F-68 minimises cell-cell adherence and blood viscosity [196][197]. Here we focused on the impact of pluronic on mechanical properties and we compared the deformation of packed RBCs stored in a serum-free buffer and RBCs treated with 1% Pluronic F-68 over the course of 3 hours.

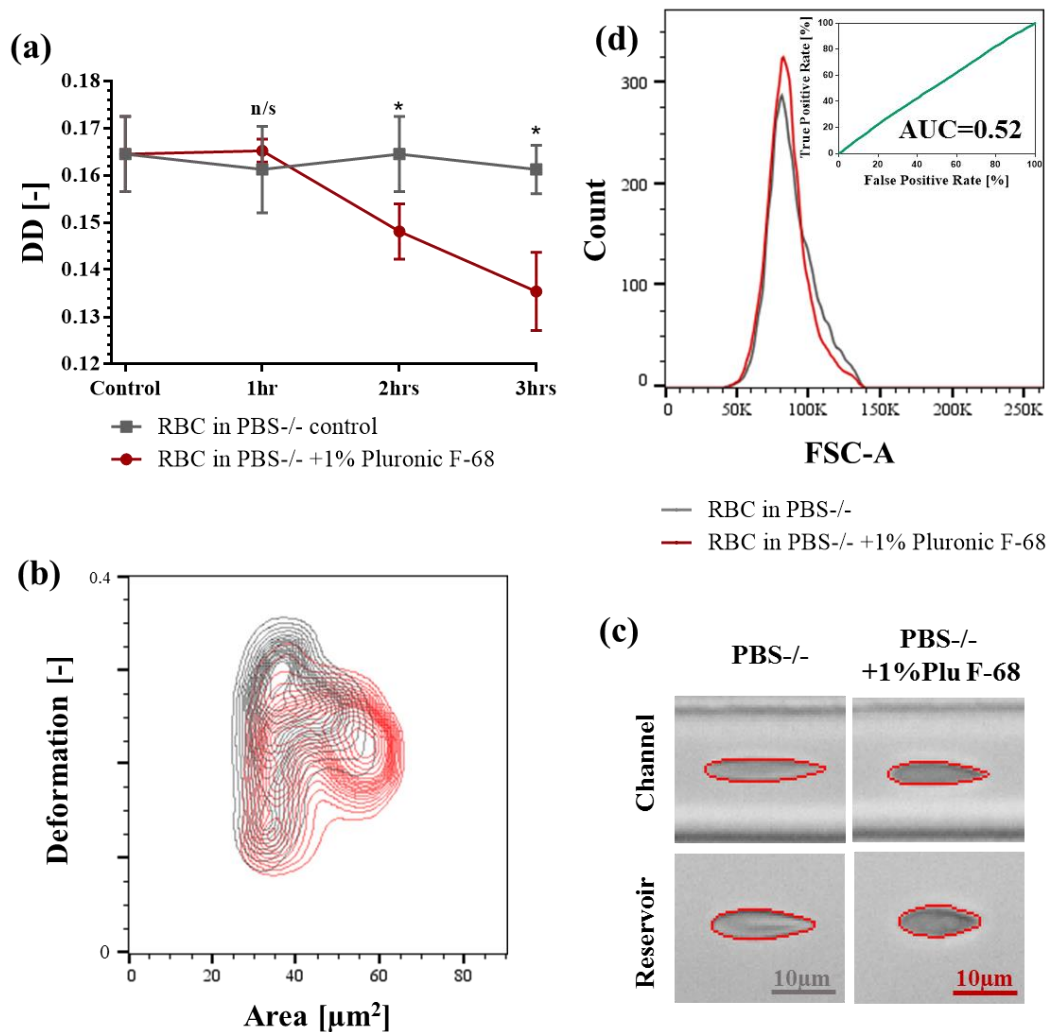


**Fig. 7.3**

*Deformability and size of isolated packed red blood cells (RBC) treated with 1% Pluronic F-68 (red) were compared to untreated control (grey). Both samples were examined at 0.12  $\mu\text{l}/\text{min}$  flow rate in  $20\times 20\mu\text{m}^2$  cross-section RT-DC channel. (a) Time-dependent alteration in deformability as a response to 1% Pluronic F-68 is presented as mean differential deformation (DD) values measured on three separate occasions. The error bars are standard error of the mean. P-values were calculated using the standardized mixed model (\*p-value <0.01, n/s no significant). (b) Contour plots (for more than 2000 cells from each population) were drawn, presenting cell deformability vs projected cell area ( $\mu\text{m}^2$ ). (c) Representative images of cells extracted from the channel and reservoir section of the RT-DC chip for cells incubated for 3 hours. (d) To assess if treatment with Pluronic F-68 causes changes in size, cells (10000 events for each condition) were characterised by flow cytometry for the forward light scatter (FSC-A). Receiver Operating Characteristic (ROC) curves were plotted for size expressed as FSC-A. The True Positive Rate is defined as the number of control cells measured for a certain size cut-off point and divided by the total number of control cells (green). The False Positive Rate is the corresponding number of Pluronic F-68- treated cells divided by the total number of treated cells for the same cut-off. The Area Under the Curve (AUC) was calculated to quantify the size overlap between control and treated cells.*

**Fig. 7.3 a & b** demonstrate that the stiffening effect observed for Jurkat cells, when incubated for a short time (up to 3 hours) in poloxamer additives, is also shown by RBCs, however to a smaller degree. Decrease in RBCs deformation from its original value  $DD=0.164 \pm 0.008$  is visible after 2 hours of incubation ( $DD=0.148 \pm 0.006$ ). Initially cell deformation drops by  $\sim 10\%$  (p-value <0.01) to reach  $\sim 16\%$  ( $DD=0.135 \pm 0.008$ , p-value <0.01) after 3 hours of exposure to Pluronic F-68. RBCs are not spherical, while in suspension they are biconcave discs and when exposed to shear in laminar flow, they streamline and assemble the tear-like shape as shown in Fig. 3 c. To assess if exposure to Pluronic F-68 causes changes to the size, RBCs from both conditions at the 3 hrs time-point were assessed by flow cytometry for the FSC-A parameter (Fig. 3 d). A ROC curve with  $AUC=0.52$  was generated to confirm that cell size is unaffected by short-term exposure to Pluronic F-68.

**7.2.4. Effect of Pluronic F-68 on adherent HEK cells**

Human embryonic kidney (HEK) cells are adherent cells commonly used in cell biology [198]. Due to the wide-spread application of HEK cells, we used this cell line to research if there is a short-term (1-3 hrs exposure) effect of Pluronic F-68 exerted on adherent cells, using the same methodology as presented above. Deformability of cells cultured in

medium with serum, incubated in PBS<sup>-/-</sup> as well as PBS<sup>-/-</sup> supplemented with 1% Pluronic F-68 was examined (Fig. 7.4 a & b). Prior to the measurement cells were harvested into suspension by enzymatic treatment with TrypLE™ (Fig. 7.4 c). The enzymatic harvest protocol requires serum removal, to prevent enzyme inhibition. The serum is removed by replacing cell culture medium with PBS<sup>-/-</sup> and washing with PBS<sup>-/-</sup> in order to remove traces of the protein-rich serum.

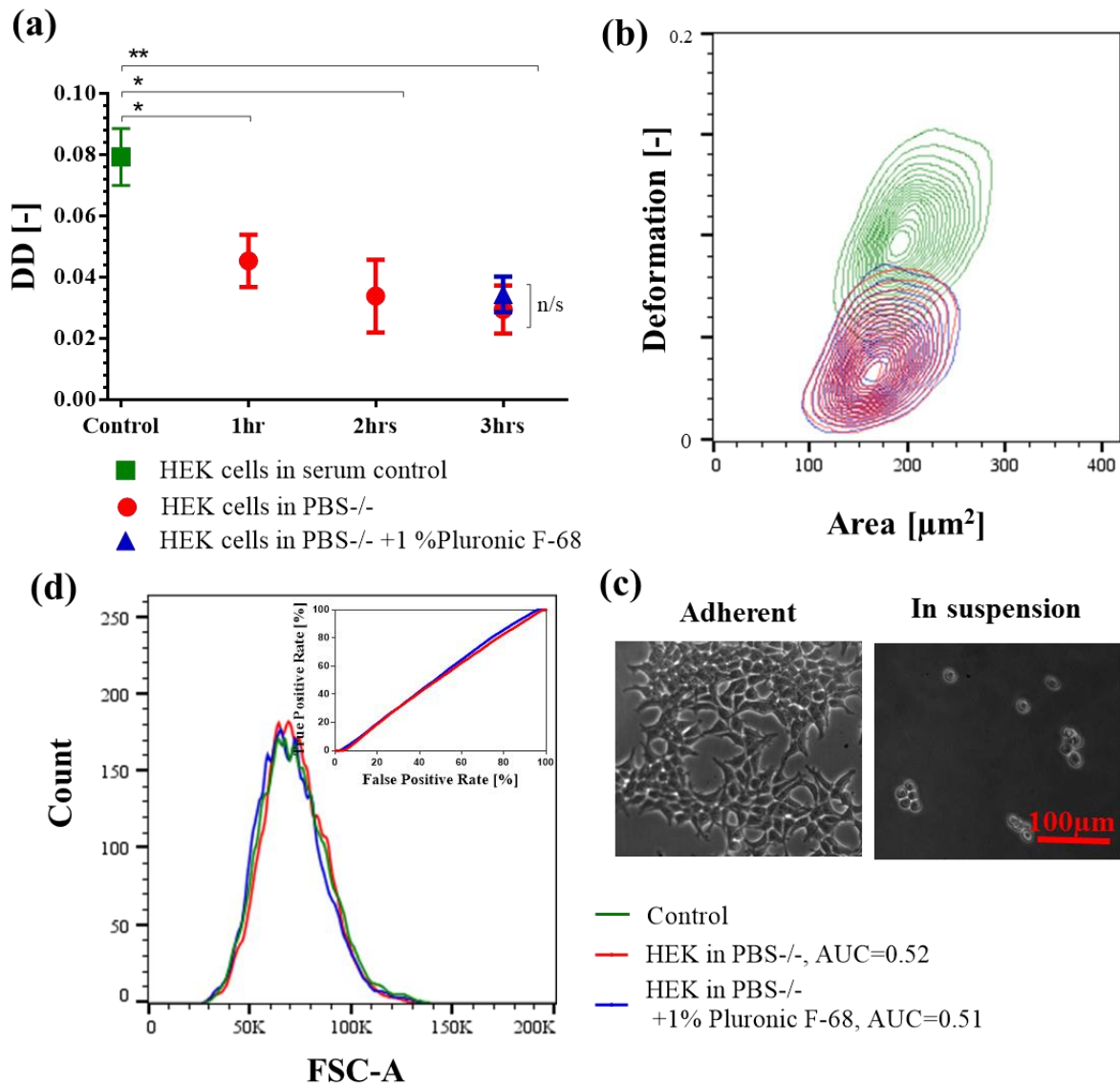


**Fig. 7.4**

*Effect of Pluronic F-68 on adherent HEK cells deformability was quantified using real-time deformability cytometry. Cells from three conditions: HEK cells in serum (green)- harvested directly from tissue culture containing serum, HEK cells in PBS<sup>-/-</sup> (red)- cells incubated in PBS<sup>-/-</sup> without serum for 1, 2 and 3 hrs and HEK cells in PBS<sup>-/-</sup> + 1% Pluronic F-68 (blue)- cells incubated in PBS<sup>-/-</sup> supplemented with 1% Pluronic F-68, without serum, were examined in 20 × 20  $\mu\text{m}^2$  cross-section RT-DC channel at 0.04  $\mu\text{l/s}$  flow rate. (a) Time-dependent response graphs show mean differential deformation (DD) values of three experimental*

replicates. Error bars correspond to the standard error of the mean (SEM). P-values were calculated using the linear mixed model (\*p-value <0.01, \*\* p-value<0.001, n/s no significant). (b) Exemplary contour plots show outlines of assessed populations for deformation vs size (expressed as projected cells area in  $\mu\text{m}^2$ ) recorded in the measurement channel section of the RT-DC chip for more than 4000 cells. (c) Prior to the measurement cells were harvested into suspension using enzymatic treatment. Representative images obtained at  $\times 20$  magnification show morphology of adherent cells and cells in suspension. (d) Cell size was assessed by flow cytometry for the forward light scatter (FSC-A) for 10000 cells from each condition. Receiver Operating Characteristic (ROC) curves were plotted for size expressed as FSC-A. The True Positive Rate is defined as the number of control cells measured for a certain size cut-off point and divided by the total number of control cells (green). The False Positive Rate is the corresponding number of treated cells (either in PBS-/- or PBS-/- +1% Pluronic F-68 respectively) divided by the total number of treated cells for the same cut-off. The Area Under the Curve (AUC) was calculated to quantify the size overlap between control and treated cells.

**Fig. 7.4 a** shows changes in deformation measured by RT-DC for HEK cells cultured in PBS-/- (red) and PBS-/- supplemented with 1% Pluronic F-68 (blue) for 3 hours and compared control cells (green) cultured in whole cell culture medium. There was no significant (p-value n/s) change observed between PBS-/- cells ( $DD=0.029 \pm 0.0078$ ) and PBS-/- + 1% Pluronic F-68 ( $DD=0.034 \pm 0.0058$ ). The most dramatic change in deformation ( $\sim 63\%$  after 3 hrs, p-value<0.001) was triggered by replacing whole medium ( $DD=0.079 \pm 0.0093$ ) with PBS-/. To assess if replacing cell culture medium with PBS-/- and PBS-/- supplemented with 1% Pluronic F-68 triggers any changes in size, cells were assessed by flow cytometry for FSC-A parameter (**Fig. 7.4 d**). Despite the dramatic change in cell deformation caused by replacing whole medium with PBS -/- there is no size alteration (AUC=0.52). Similarly, supplementing PBS-/- buffer with 1% Pluronic F-68 does not contribute to cell size alteration (AUC=0.51).

### 7.2.5. Hydrodynamic behaviour in spiral microchannel

Exposure of Jurkat cells and RBC to 1% Pluronic F-68 for 3 hours triggered statistically significant changes in their deformability. In order to understand practical significance of the induced changes we compared hydrodynamic behaviour of control and Pluronic-treated cells within microfluidic systems used in this study. As described previously, spiral microchannels are sensitive to cell deformability due to contribution of the deformability-induced lift force, which together with inertial lift force and Dean force stabilises cells at certain equilibrium positions. At elevated flow rates deformable cells experience the effect of a deformability-induced lift force, first manifested with defocusing, when cells occupy large section of the



channel, followed by assembly into a new equilibrium position on the opposite side of the channel (shift from inner wall to outer wall). Jurkat cells were tested in a design I spiral microchannel with  $360 \times 60 \mu\text{m}$  cross-section at five flow rates (1., 1.5, 2., 2.5 and 3 ml/min). RBC were tested in a design II spiral microchannel with  $170 \times 30 \mu\text{m}$  cross section at flow rates ranging between 0.2- 1 ml/min. The lateral equilibrium position was generated by image acquisition in the end of the spiral microchannels and it is expressed here as distance from the outer wall ( $\mu\text{m}$ ). To quantify differences in cells behaviour ROC curves were generated and AUC was calculated for control versus Pluronic-treated samples.

As shown in **Fig. 7.5 a**, and quantified in **Fig. 7.5 b**, the focusing pattern for control Jurkat cells cultured in serum and their counterparts treated with Pluronic F-68, is similar (AUC varies between 0.51-0.63). At lower flow rates (1, 1.5 and 2 ml/min) they remain focused closer to the inner wall (respectively,  $261 \pm 36$ ,  $277 \pm 38$  and  $264 \pm 55 \mu\text{m}$  for control cells and  $248 \pm 41$ ,  $273 \pm 41$  and  $257 \pm 59 \mu\text{m}$  for Pluronic-treated cells). At 2.5 ml/min they experience the characteristic defocusing, occupying wide section of the channel (control:  $214 \pm 68 \mu\text{m}$  and treated:  $211 \pm 71 \mu\text{m}$ ) to be shifted closer to the inner wall at 3 ml/min (control:  $143 \pm 59$  and treated:  $136 \pm 57$ ).

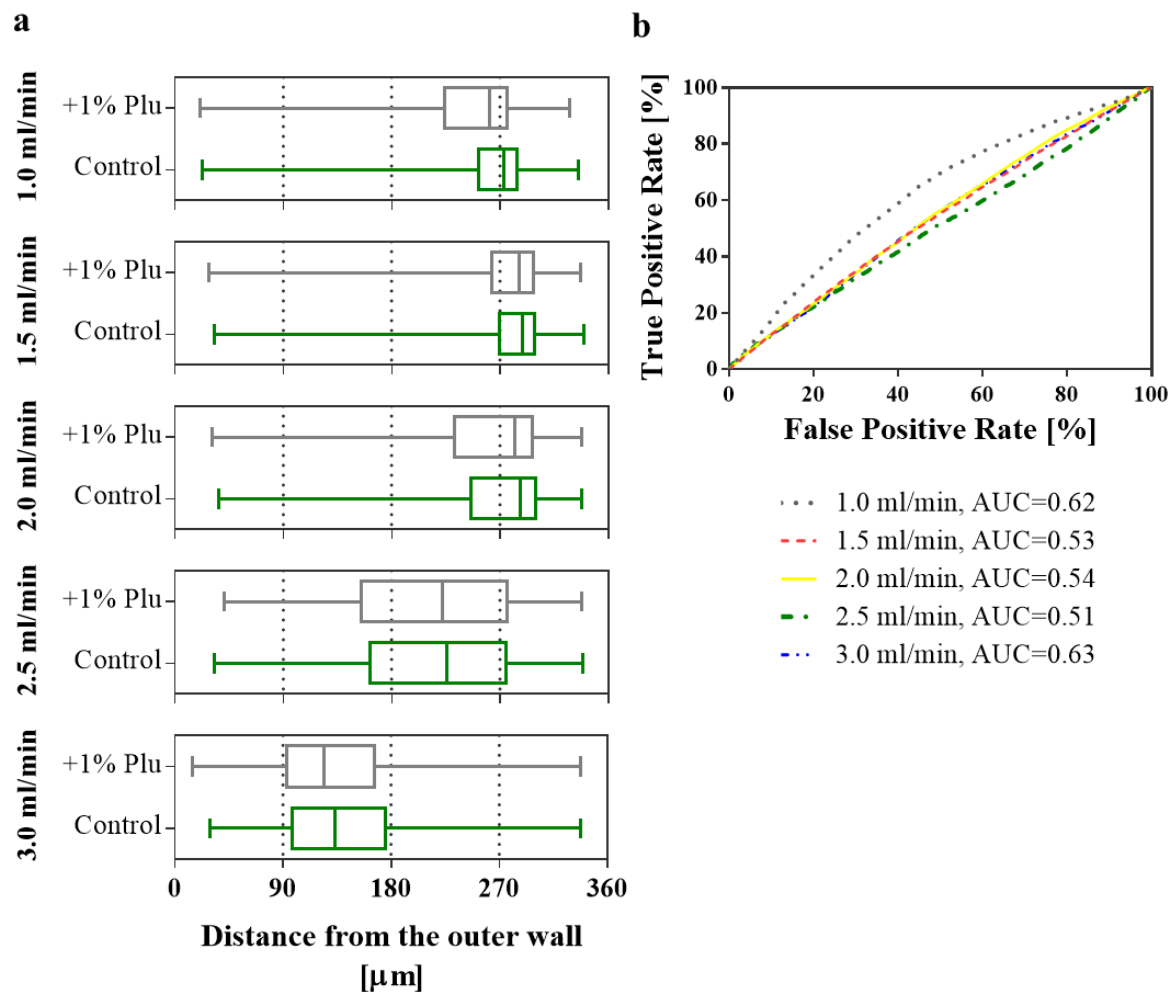


**Fig. 7.5**

(a) Hydrodynamic behaviour of control Jurkat cells cultured complete medium containing serum (green) and Jurkat cells incubated for 3 hrs in a complete medium with serum and supplemented with 1% pluronic F-68, assessed in a spiral microchannel with  $360 \times 60 \mu\text{m}$  cross-section at five different flow rates (1, 1.5, 2, 2.5 and 3 ml/min). Box plots summarising lateral equilibrium positions, measured as a distance from the outer wall ( $\mu\text{m}$ ), where the line in the box represents the median, the box represents data from lower and upper quartile and the whiskers correspond to the lowest and highest extreme values

(b) Receiver Operating Characteristic (ROC) curves were plotted for lateral equilibrium position for control versus Pluronic-treated cells, for each applied flow rate. The True Positive Rate is defined as the number of control cells found at a given lateral position and divided by the total number of control cells. The False Positive Rate is the corresponding number of Pluronic-treated cells divided by the total number of control cells for the same cut-off. To quantify differences in the assembled equilibrium positions the Area Under the Curve (AUC) was calculated. For summary of triplicate results please consult **Appendix P**

Exchanging complete medium containing serum to PBS-/- causes a 22% drop in Jurkat cells' deformability within first hour, which is comparable to the change induced by 3 hrs exposure to 1% Pluronic F-68 in presence of serum. Deformability of Jurkat cells in PBS-/-

decreases by another 29% after 3 hrs exposure to Pluronic F-68 and this change (as shown in **Fig. 7.6 a**) contributed to alteration of response to increased flow rate, which is a trigger for the characteristic defocusing before shifting sides of the channel. At lower flow rates (1, 1.5 and 2 ml/min) both control and treated cells are focused close to the inner wall (control:  $253 \pm 46$ ,  $271 \pm 52$  and  $242 \pm 73$ , treated cells:  $248 \pm 40$ ,  $275 \pm 43$  and  $255 \pm 60 \mu\text{m}$ ), with little differences in their equilibrium position (AUC= 0.56, 0.51 and 0.53 at 1, 1.5 and 2 ml/min, respectively, **Fig. 7.6 b**). At 2.5 ml/min, control cells defocus, occupying a wide section close to the channel centre ( $176 \pm 77 \mu\text{m}$ ), substantially (AUC=0.85) shifting from Pluronic-treated cells, which lagged their response to the deformability-induced lift force and remaining focused close to the inner wall ( $275 \pm 50 \mu\text{m}$ ). Finally, at 3 ml/min, both control and treated cells were found closer to the outer wall, (control:  $118 \pm 58 \mu\text{m}$ , treated:  $139 \pm 61 \mu\text{m}$ ), suggesting that Pluronic-treated cells require higher than 2.5ml/min flow rate to trigger the defocused transition state, but 3 ml/min is sufficient for the full-shift.

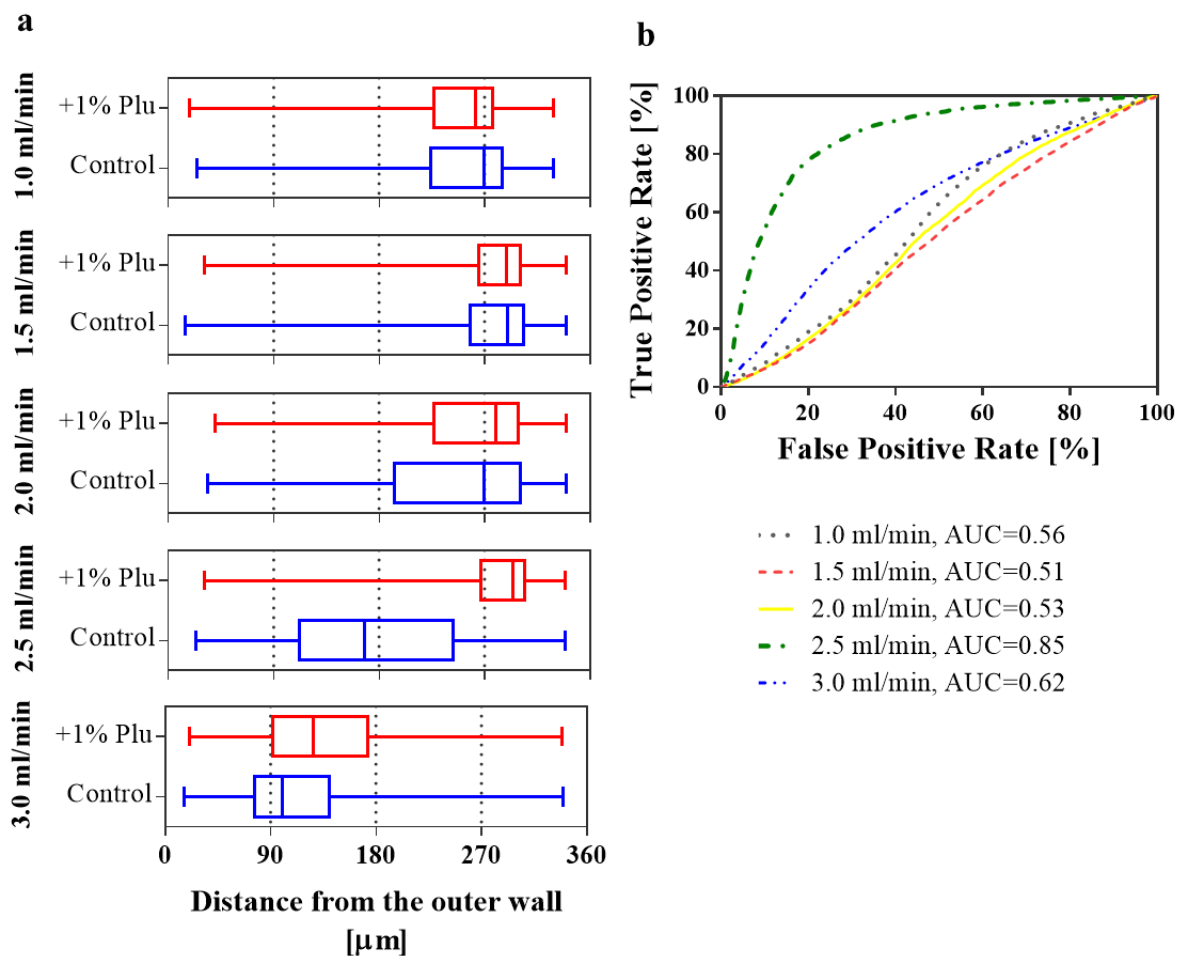


**Fig. 7.6**

(a) Hydrodynamic behaviour of control Jurkat cells incubated for 3 hrs in PBS-/- (blue) and Jurkat cells incubated for 3 hrs in PBS-/- and supplemented with 1% pluronic F-68, assessed

*in a spiral microchannel with  $360 \times 60 \mu\text{m}$  cross-section at five different flow rates (1, 1.5, 2, 2.5 and 3 ml/min). Box plots summarising lateral equilibrium positions, measured as a distance from the outer wall ( $\mu\text{m}$ ), where the line in the box represents the median, the box represents data from lower and upper quartile and the whiskers correspond to the lowest and highest extreme values (b) Receiver Operating Characteristic (ROC) curves were plotted for lateral equilibrium position for control versus Pluronic-treated cells, for each applied flow rate. The True Positive Rate is defined as the number of control cells found at a given lateral position and divided by the total number of control cells. The False Positive Rate is the corresponding number of Pluronic-treated cells divided by the total number of control cells for the same cut-off. To quantify differences in the assembled equilibrium positions the Area Under the Curve (AUC) was calculated. For summary of triplicate results please consult **Appendix R***

As shown in **Fig. 7.7**, control and Pluronic-treated RBC repeated the pattern of hydrodynamic behaviour observed for PBS-/- versus PBS-/- supplemented with 1% Pluronic F68 Jurkat cells. At lower flow rates (0.2, 0.4 and 0.6 ml/min), both control and treated RBC were focused close to the inner wall (control:  $112 \pm 20$ ,  $122 \pm 14$  and  $123 \pm 19 \mu\text{m}$ , treated:  $110 \pm 20$ ,  $122 \pm 15$  and  $125 \pm 15 \mu\text{m}$ , respectively). Increasing flow rate to 0.8 ml/min triggered the defocusing of control RBC, substantially (AUC=0.73) shifting them at  $100 \pm 30 \mu\text{m}$ , in relation to Pluronic-treated RBC, which remained focused closer to the inner wall ( $122 \pm 19 \mu\text{m}$ ). Again, at the maximal applied flow rate, control and treated cells experienced the full shift toward the outer wall of the channel, being equilibrated at almost identical (AUC=50) lateral positions (control:  $54 \pm 28 \mu\text{m}$ , treated:  $54 \pm 28 \mu\text{m}$ ).

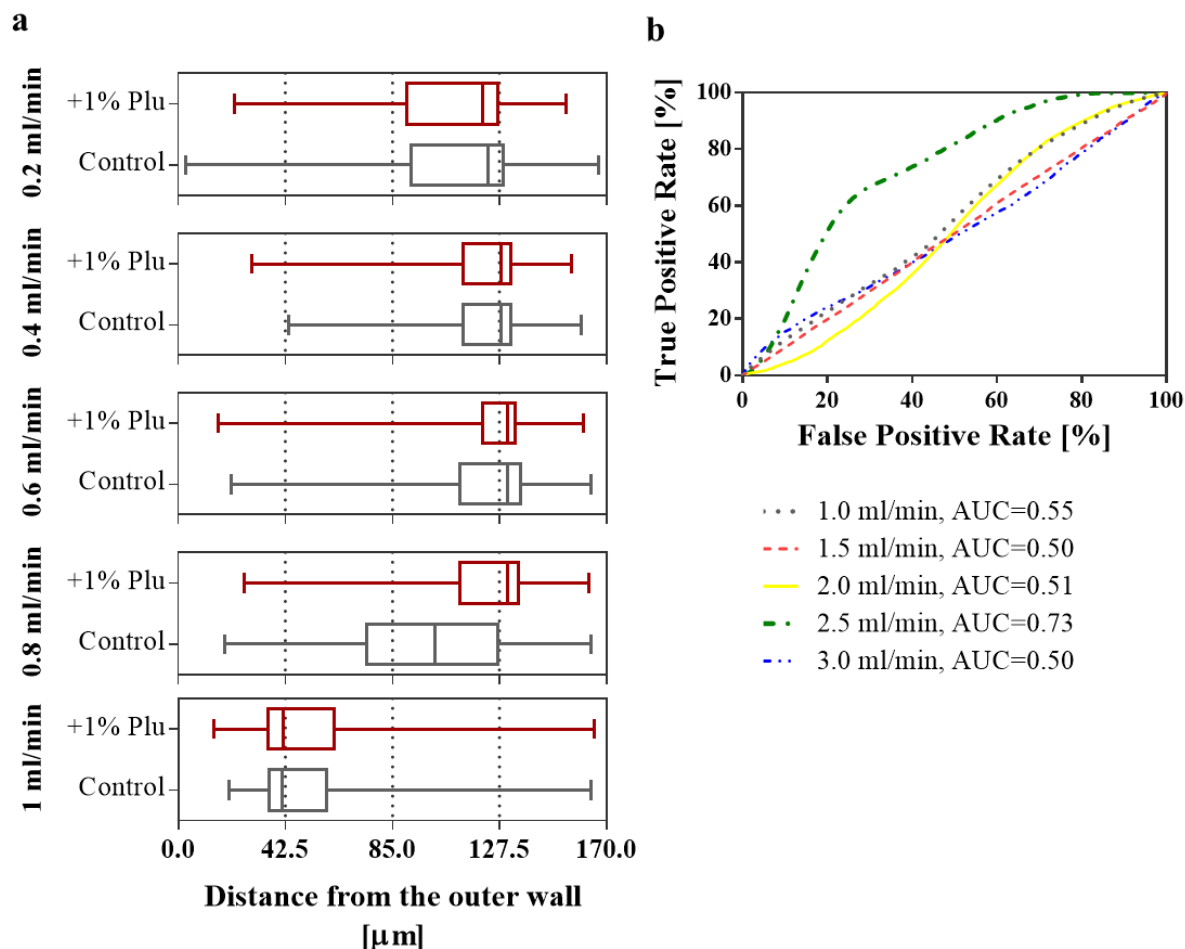


**Fig. 7.7**

**(a)** Hydrodynamic behaviour of control RBC (grey) and RBC incubated for 3 hrs in PBS/- and supplemented with 1% pluronic F-68, assessed in a spiral microchannel with  $170 \times 30 \mu\text{m}$  cross-section at five different flow rates (0.2, 0.4, 0.6, 0.8 and 1 ml/min). Box plots summarising lateral equilibrium positions, measured as a distance from the outer wall ( $\mu\text{m}$ ), where the line in the box represents the median, the box represents data from lower and upper quartile and the whiskers correspond to the lowest and highest extreme values. **(b)** Receiver Operating Characteristic (ROC) curves were plotted for lateral equilibrium position for control versus Pluronic-treated cells, for each applied flow rate. The True Positive Rate is defined as the number of control cells found at a given lateral position and divided by the total number of control cells. The False Positive Rate is the corresponding number of Pluronic-treated cells divided by the total number of control cells for the same cut-off. To quantify differences in the assembled equilibrium positions the Area Under the Curve (AUC) was calculated. For summary of triplicate results please consult **Appendix S**

### 7.3. Discussion and conclusion

In this study it was demonstrated that Pluronic F-68 alters cell mechanical properties, causing cell stiffening with no impact on cell size. The short-time (1-3 hours) effect was examined for cells of Jurkat (suspension) cell line, red blood cells and adherent HEK cells. It was established that cell deformability undergoes significant alteration within the first hours of

exposure to Pluronic F-68, even at concentrations as low as 0.5% w/v for cells in suspension without serum. Adherent HEK cells do not show the stiffening trend as observed for Jurkat cells and RBCs.

We speculate that results could be explained with the cell preparation protocol, since prior to RT-DC measurements (similarly to other common microfluidic applications) HEK cells have to be harvested into suspension. We believe that the harvesting procedure exerts a more dramatic effect than the Pluronic treatment itself. By imaging HEK cells we observed that cell detachment is followed by changes in cytoskeleton (**Fig. 7.8**), known to substantially contribute to cell mechanical properties [199].

More specifically, when cells adhere to a surface the F-actin (in green in **Fig. 7.8**) spreads creating angular shapes surrounding the cell nucleus (in blue in **Fig. 7.8**). When cells are harvested into suspension F-actin rearranges to maintain a spherical shape, the characteristic sharp-corners being replaced with some irregular round local accumulations of F-actin and smooth appearance.

The cell mechanical response to treatment with Pluronic F-68 are relatively small and due to the biocompatible nature of Pluronic they are physiologically negligible (with no effect on cell size and viability). However, it must be considered that cell deformability can be significantly affected by the poloxamer additive as well as serum removal from the experimental system and it can introduce implications to performance of a deformability-sensitive microfluidic system, like the spiral microchannels used throughout this study. Jurkat cells and RBC incubated for 3 hrs in PBS-/- supplemented with 1% Pluronic F-68 experienced less of the effect of deformability-induced lift force at elevated flow rates in comparison to their controls, causing a delay in entering the defocused transition state.

The exact mechanism of altering cell deformability is not fully understood yet, however it has been shown that Pluronic F-68 decreases plasma membrane fluidity [200], probably due to its surfactant properties, enabling pluronic to integrate into the lipid bilayer of the cell [190]. Additionally, Gigout *et al.* tracked Pluronic F-68 uptake within Jurkat cells discovering that fluorescently-tagged Pluronic F-68 is continually transferred into the cell, enclosed in endosomes, and transported alongside the endocytotic pathway. Based on these results they suggested that the stiffening effect could be explained partially by the alteration of the cell membrane and cytoplasm properties, as a consequence of high pluronic content accumulated in intracellular vesicles localised across cytoplasm and just beneath the plasma membrane.

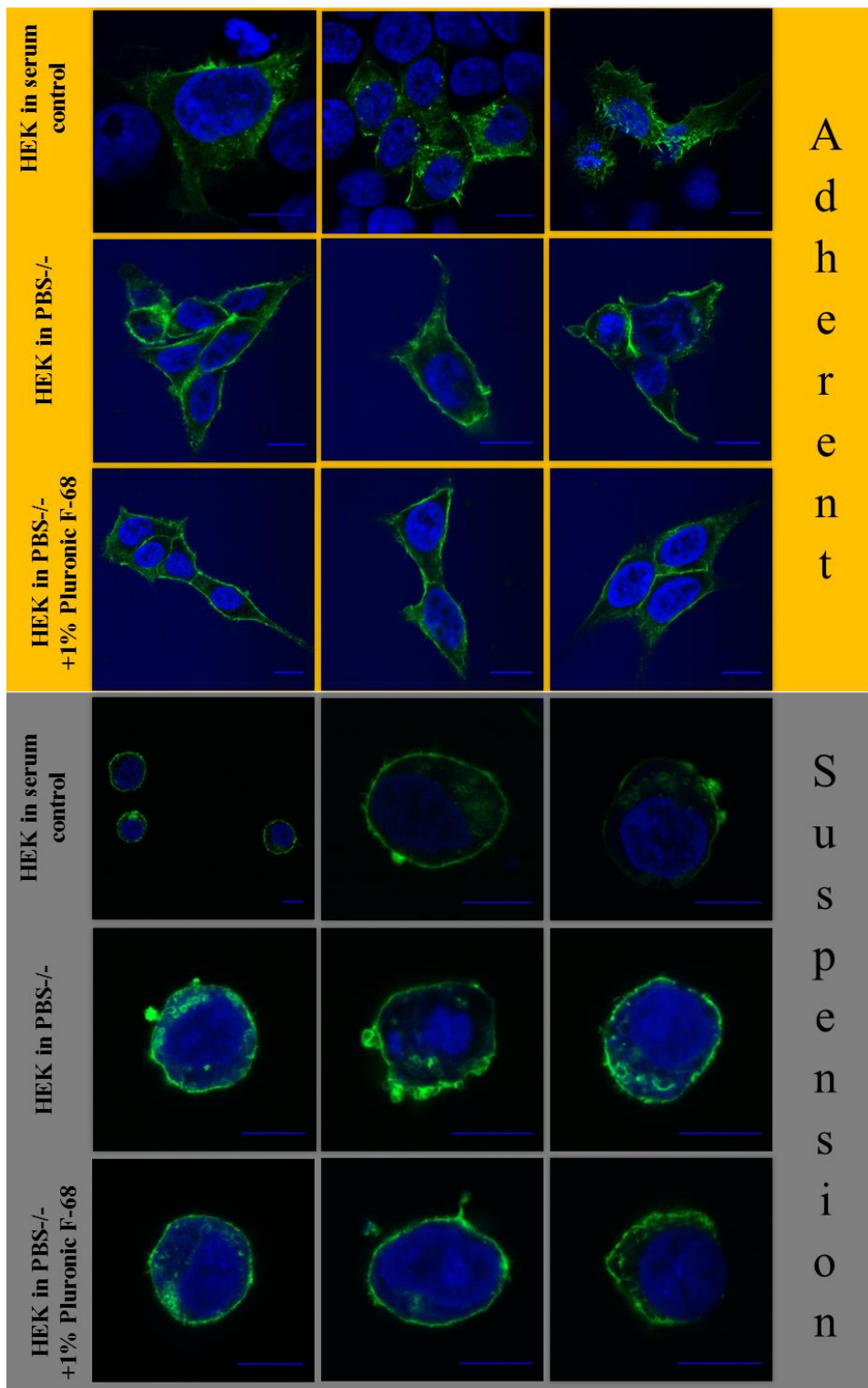


**Fig. 7.8**

To visualise changes in HEK cells cytoskeleton in the transition from the adherent to the suspended state during cell harvest required for RT-DC measurements, cytoskeletal protein F-actin (green) and nuclei (blue) were stained with fluorophores and visualised using confocal microscopy. Scale bars correspond to 10  $\mu\text{m}$ .

Cell deformability is gaining recognition as a novel cell state marker. Reduced cell deformability is commonly associated with a pathological phenotype, *e.g.* in malaria [50][201], sickle-cell disease [202] and thalassemia [203]. Additionally, deformability is seen as a valuable label-free marker associated with various cell activities, such as cell cycle regulation [149], differentiation [150], metastasis [204] and leukocyte activation [205]. As discussed in **Chapter 1**, many available technologies for deformability analysis (Atomic Force Microscopy, microconstrictions, optical stretchers, micropipette aspiration, magnetic bead twisting) require prolonged operational time to gain a reasonable number of measurements. Our findings highlight the importance of seeking high-throughput technologies, as well as careful consideration of experimental conditions to measure deformability changes and analyse mechanical phenotype.

## **7.4. Materials and methods**

### **7.4.1. Real-time deformability cytometry**

Cell mechanical properties were assessed using a Real-Time Deformability Cytometer (RT-DC) as described in previous works [206][46][79] and **Chapter 2**. Cells were pumped into the channel at two different flow rates: 0.04 (Jurkat and HEK) and 0.12 (red blood cells)  $\mu\text{l/s}$ , generating a shear stress (corresponding to approximately 1.2 and 4 kPa, respectively) resulting in cell deformation. RT-DC data were analysed using the ShapeOut 0.8.4 software (available at [www.zellmechanic.com](http://www.zellmechanic.com)). Further analysis were performed using MatLab R2016b and GraphPad Prism 7. P-values were calculated using the linear mixed model.

### **7.4.2. Viability study**

Jurkat cells viability was assessed using the Live/Dead Viability/Cytotoxicity kit for mammalian cells (Life Technologies Ltd.) as per the manufacturer's manual. The flow cytometric analysis was performed with excitation at 488 nm. Live cells stained with calcein emit green fluorescence (530/30 bandpass) while dead cells appear red (610/20 bandpass) due to staining with ethidium homodimer. Cells were analysed on a FACSCalibur machine (BD Bioscience) immediately after staining and obtained raw data was analysed using FlowJo V10 CL software.

### **7.4.3. Sample preparation- Jurkat cells**

Impact of Pluronic F-68 was examined for four different conditions: a control incubated in medium with serum, a sample from complete medium supplemented with Pluronic F-68,



cells incubated in PBS-/- (phosphate buffered saline without calcium and magnesium, Gibco, cat. 10010023) and PBS-/- containing Pluronic F-68 and incubated for a desired time (1, 2 and 3 hrs) in a humidified incubator at 37°C in 5% CO<sub>2</sub>. The chosen time scale is motivated by an approximate time required to perform experiments using microfluidic systems and ensuring unaffected cell viability for unbiased results (**Fig. 7.9**).

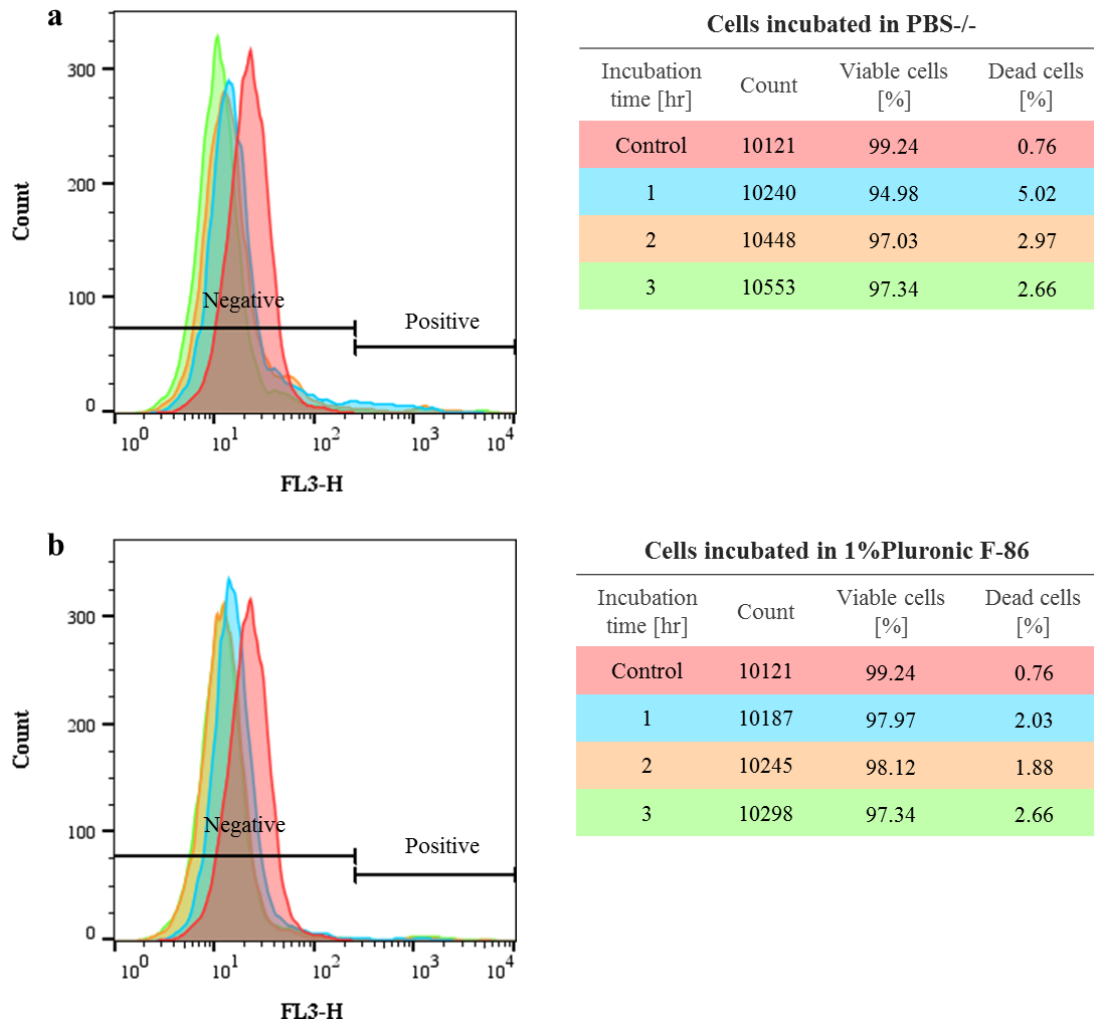


**Fig. 7.9**

Cells of Jurkat cell line were used to assess if there is an adverse effect of chosen incubation conditions that could compromise cell viability. Cells were incubated for 3 hrs in PBS-/- (a) and a 1% solution of Pluronic F-68 (b). Ratio of live/ dead cells were assessed by flow cytometric assay, performed each hour on a portion of cells extracted from incubated flasks and compared with a control (cells extracted directly from a cell culture cultivated in a presence of serum). Dead cells emit red fluorescence (610/20 bandpass) detected in FL-3 channel, due to staining with ethidium homodimer.

#### **7.4.4. Sample preparation- red blood cells**

Packed purified red blood cells (RBCs) from healthy donors stored in a serum-free buffer were purchased from Cambridge Bioscience Ltd. Cells were stored at 4°C and cells from three batches were used for experimental work within a week of collection. Cells for experiments were counted on a haemocytometer and cell density was adjusted to  $10 \times 10^6$  cells/ml by addition of an adequate PBS-/- volume (experimental control) or PBS-/- supplemented with Pluronic F-68 to a 1% (w/v) final concentration. Prepared cells were incubated at 4°C prior to measurements on RT-DC then collected by centrifugation at  $500 \times g$  for 5 min and re-suspended in 0.5% methylcellulose.

#### **7.4.5. Sample preparation- HEK cells**

Impact of Pluronic F-68 was examined for three different conditions: a control incubated in medium with serum, a sample, cells incubated in PBS-/- and cells incubated in PBS-/- supplemented with 1% Pluronic F-68. HEK cells from the same batch were collected for RT-DC measurements by harvesting them into suspension using TrypLE™ (ThermoFisher Scientific). Prior to the TrypLE™ treatment cells were washed twice in PBS-/- and an appropriate volume (5ml for 75 cm<sup>2</sup> flask) of TrypLE™ was added. Cells were incubated in a humidified incubator at 37°C in 5% CO<sub>2</sub> for 5 min. After the monolayer dissociation complete medium containing serum was added to inactivate the TrypLE™ and wash cells of the surface of the flask. Next, cells were transferred into 15ml centrifuge tube and they were collected by centrifugation at  $300 \times g$  for 5 min, the supernatant was discarded and cells were re-suspended in 0.5% solution of methylcellulose at  $1 \times 10^6$  cell/ml. A control containing serum was collected straight from the cell culture flask. The remaining two samples were cultured for 1, 2 and 3 hrs in either (PBS-/-) (serum-free experiment) or PBS -/- supplemented with 1% (w/v) cell culture grade Pluronic F-68 (ThermoFisher Scientific) (treated sample) and incubated for a desired time in a humidified incubator at 37°C in 5% CO<sub>2</sub> and harvested prior to measurements as described above. All obtained data results from three independent replicates, from cells of the same cell line coming from different batches.

#### **7.4.6. Microscopy**

HEK cells were also examined for cytoskeletal re-arrangements in their adherent and suspended state by examining F-actin. Cells (adherent and harvested in suspension HEK in serum control, HEK incubated for 3 hrs in PBS and PBS supplemented with 1% Pluronic F-68) were stained for 30 min at room temperature against F-actin with Actin Green 488 Ready Probes reagents (Life Technologies, cat. R37110). 10 minutes before the end of the incubation

time, Hoechst 33342 (Sigma Aldrich, cat. 14533) was added to a final 10ng/ml concentration to visualise cell nucleus. To avoid additional cytoskeletal re-arrangements due to cell preparation for microscopy, cells after treatment were fixed in 4% paraformaldehyde (PFA) (ThermoFisher Scientific, cat. 28906). Acquisition was performed on a Leica SP5 SMD (Single Molecule Detection) confocal laser-scanning microscope using a 63 × 1.4NA HCX PL Apo oil immersion objective lens. The Actin Creen 488 was excited using a tuneable white light laser operating at 488 nm and 80 MHz pulse rate. Hoechst 33342 was excited with a pulsed 405 nm laser at 40 MHz pulse rate. Emission was detected with a photon multiplier tube (PMT).

#### **7.4.7. Assessing hydrodynamic behaviour of Pluronic-treated Jurkat cells and RBC in spiral microchannel**

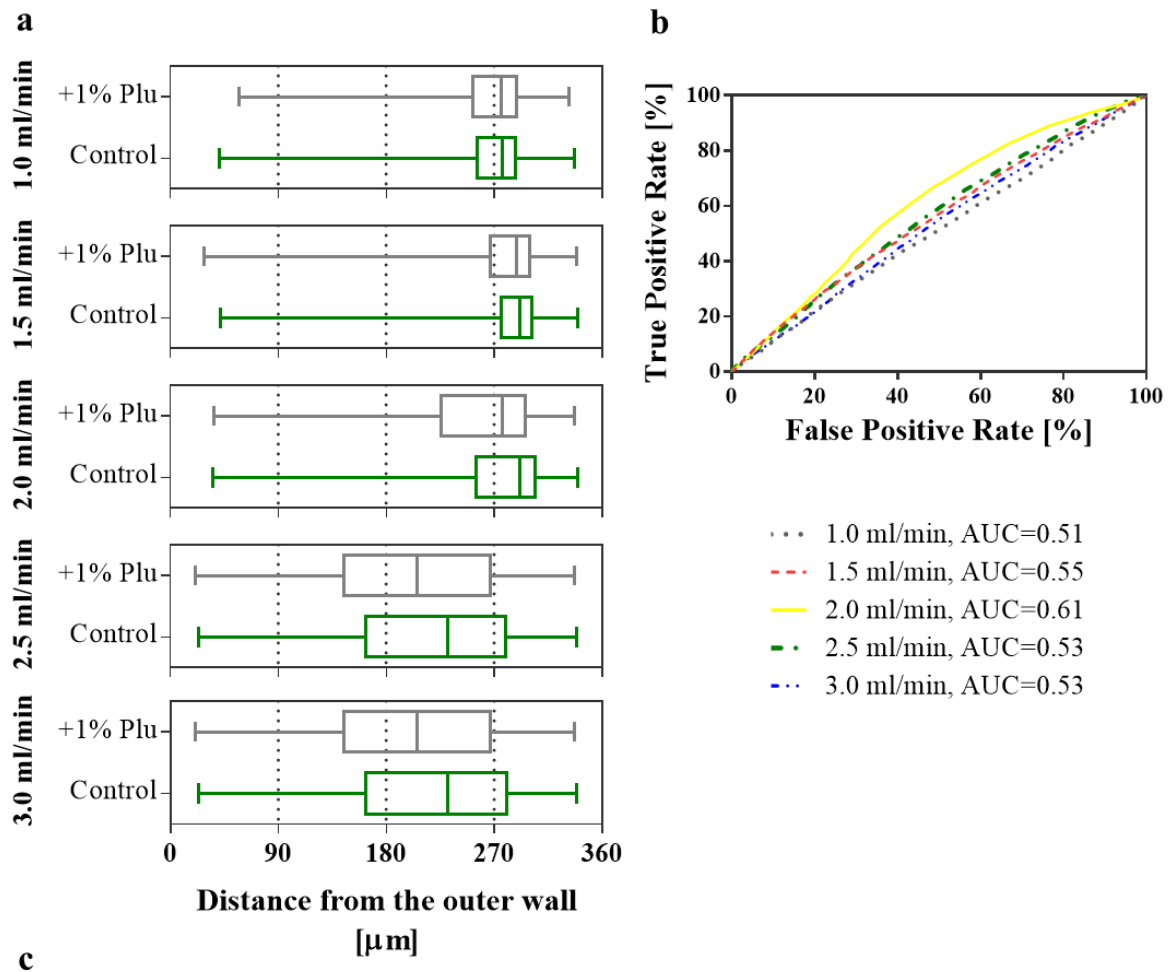
To research if changes in cells deformability caused by Pluronic F-68 treatment could influence their focusing positions with spiral channel we assessed hydrodynamic behaviour of Jurkat cells in serum, Jurkat cells in serum + 1% Pluronic incubated for 3 hrs, Jurkat cells in PBS-/- incubated for 3 hours and Jurkat cells in PBS-/- supplemented with 1% pluronic F-68, incubated for 3 hrs, RBC in PBS-/- and RBC in PBS-/- supplemented with 1% Pluronic F-68. Jurkat cells were incubated in a humidified incubator at 37°C in 5% CO<sub>2</sub>, while RBC were incubated at 4°C. Jurkat cells were tested in a spiral channel with 360 × 60 μm cross-section (design A) at flow rates ranging between 1 -3 ml/min. RBC were tested in a device with 170 × 30 μm cross-section (design B) at flow rates ranging between 0.2 – 1 ml/min.

Both Jurkat cells and RBC suspensions at concentration around  $1 \times 10^6$  cells/ml were introduced into the device as described in **Chapter 2**. Cell separation efficiency was quantified by flow cytometry in order to compare the fraction of each cell population (characterised by a unique fluorescent properties) in samples collected at each outlets. Further data analysis was performed using GraphPad Prism 6.

## Appendix P

Replica I	Flow rate [ml/min]	Mean	SD	Min	Q1	Median	Q3	Max
Jurkat cells in serum	1	262	36	23	252	273	284	335
	1.5	277	38	33	270	289	299	340
	2	264	55	37	246	287	300	338
	2.5	215	68	33	162	226	275	339
	3	143	59	29	98	133	175	338
Jurkat cells in serum +1% Pluronic F-68	1	248	41	21	224	261	276	328
	1.5	273	41	28	263	286	298	337
	2	257	59	31	232	282	297	338
	2.5	211	71	41	155	222	276	338
	3	136	57	15	94	124	166	338

Tables showing statistical summary (mean and standard deviation from the mean (SD), median, 25<sup>th</sup> (Q1) and 75<sup>th</sup> (Q3) percentile as well as minimal (min) and maximal (max) measured value) of lateral equilibrium positions obtained for at least 10000 events for Jurkat cells in serum and Jurkat cells in serum +1% Pluronic F-68, in design II spiral channel with 360 × 60 μm cross-section, at five applied flow rates for **replica I** out of three, expressed as distance from the outer wall [μm].

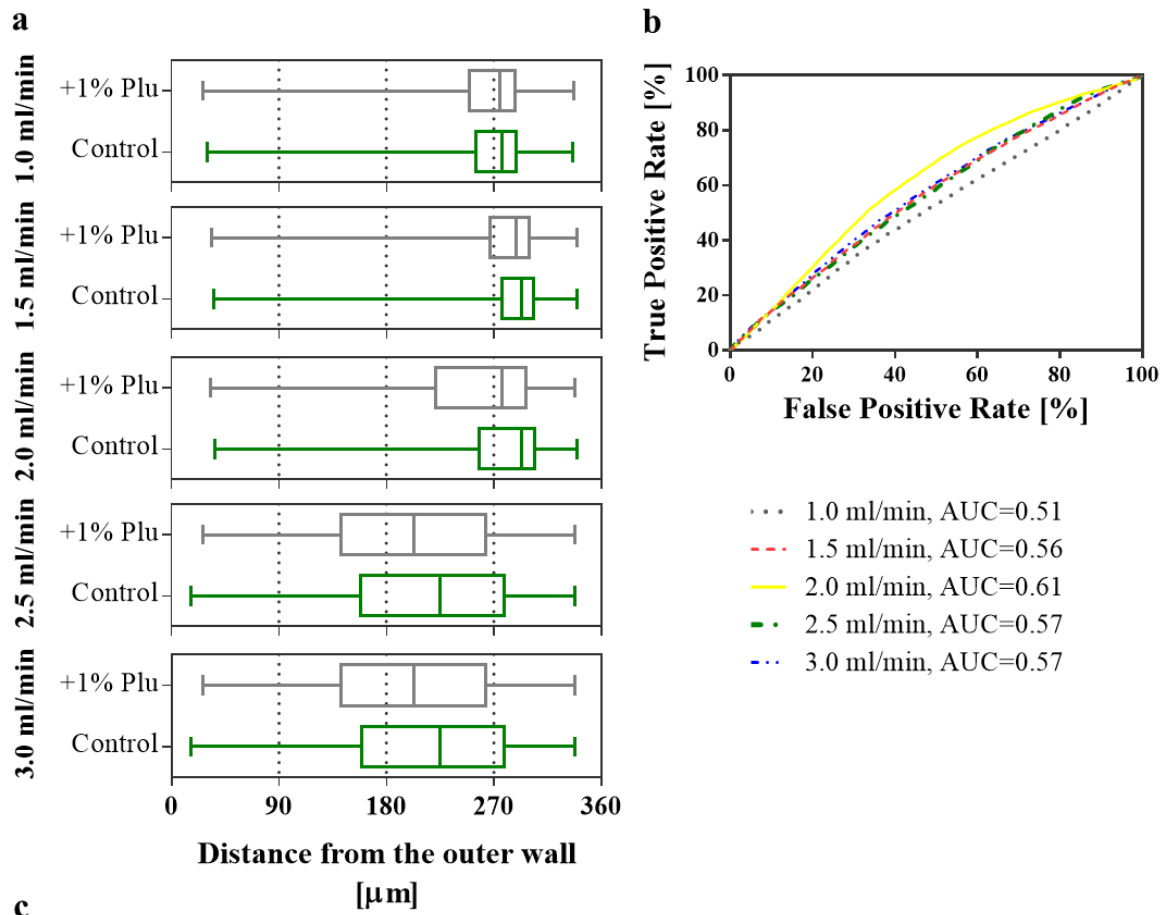


**c**

Replica II	Flow rate [ml/min]	Mean	SD	Min	Q1	Median	Q3	Max
Jurkat cells in serum	1	267	35	41	256	277	288	337
	1.5	282	38	42	276	292	302	340
	2	269	55	36	255	292	304	340
	2.5	217	71	24	163	231	280	339
	3	140	58	29	96	130	171	339
Jurkat cells in serum +1% Pluronic F-68	1	265	36	57	252	276	289	333
	1.5	275	42	28	267	289	300	339
	2	254	59	36	226	277	296	337
	2.5	202	71	21	145	206	267	337
	3	135	56	24	93	123	163	339

**Replica II (a)** Hydrodynamic behaviour of control Jurkat cells cultured complete medium containing serum (green) and Jurkat cells incubated for 3 hrs in a complete medium with serum and supplemented with 1% pluronic F-68, assessed in a spiral microchannel with  $360 \times 60 \mu\text{m}$  cross-section at five different flow rates (1, 1.5, 2, 2.5 and 3 ml/min). Box plots summarising lateral equilibrium positions, measured as a distance from the outer wall ( $\mu\text{m}$ ), where the line in the box represents the median, the box represents data from lower and upper quartile and the whiskers correspond to the lowest and highest extreme values **(b)** Receiver Operating Characteristic (ROC) curves were plotted for lateral equilibrium position for control versus

Pluronic-treated cells, for each applied flow rate. The True Positive Rate is defined as the number of control cells found at a given lateral position and divided by the total number of control cells. The False Positive Rate is the corresponding number of Pluronic-treated cells divided by the total number of control cells for the same cut-off. To quantify differences in the assembled equilibrium positions the Area Under the Curve (AUC) was calculated. (c) Tables showing statistical summary (mean and standard deviation from the mean (SD), median, 25<sup>th</sup> (Q1) and 75<sup>th</sup> (Q3) percentile as well as minimal (min) and maximal (max) measured value) of latera equilibrium positions obtained for at least 10000 events for Jurkat cells in serum and Jurkat cells in serum +1% Pluronic F-68 at five applied flow rates for **replica II** out of three, expressed as distance from the outer wall [ $\mu\text{m}$ ].



**Replica III (a)** Hydrodynamic behaviour of control Jurkat cells cultured complete medium containing serum (green) and Jurkat cells incubated for 3 hrs in a complete medium with serum and supplemented with 1% pluronic F-68 (grey), assessed in a spiral microchannel with  $360 \times 60 \mu\text{m}$  cross-section at five different flow rates (1, 1.5, 2, 2.5 and 3 ml/min). Box plots summarising lateral equilibrium positions, measured as a distance from the outer wall ( $\mu\text{m}$ ), where the line in the box represents the median, the box represents data from lower and upper quartile and the whiskers correspond to the lowest and highest extreme values **(b)** Receiver Operating Characteristic (ROC) curves were plotted for lateral equilibrium position for control versus Pluronic-treated cells, for each applied flow rate. The True Positive Rate is defined as the number of control cells found at a given lateral position and divided by the total number of

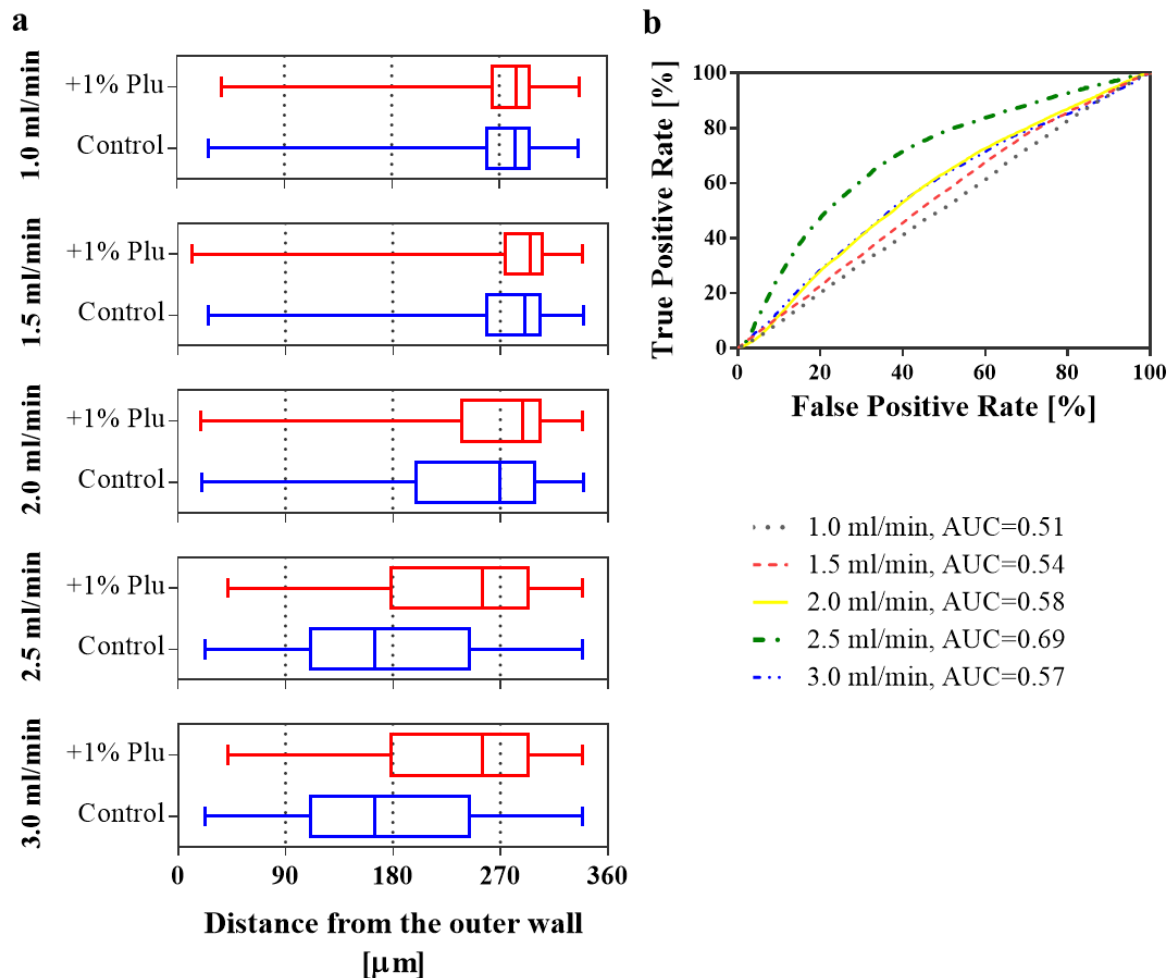
control cells. The False Positive Rate is the corresponding number of Pluronic-treated cells divided by the total number of control cells for the same cut-off. To quantify differences in the assembled equilibrium positions the Area Under the Curve (AUC) was calculated. (c) Tables showing statistical summary (mean and standard deviation from the mean (SD), median, 25<sup>th</sup> (Q1) and 75<sup>th</sup> (Q3) percentile as well as minimal (min) and maximal (max) measured value) of lateral equilibrium positions obtained for at least 10000 events for Jurkat cells in serum and Jurkat cells in serum +1% Pluronic F-68, at five applied flow rates for **replica III** out of three, expressed as distance from the outer wall [ $\mu\text{m}$ ].



## Appendix R

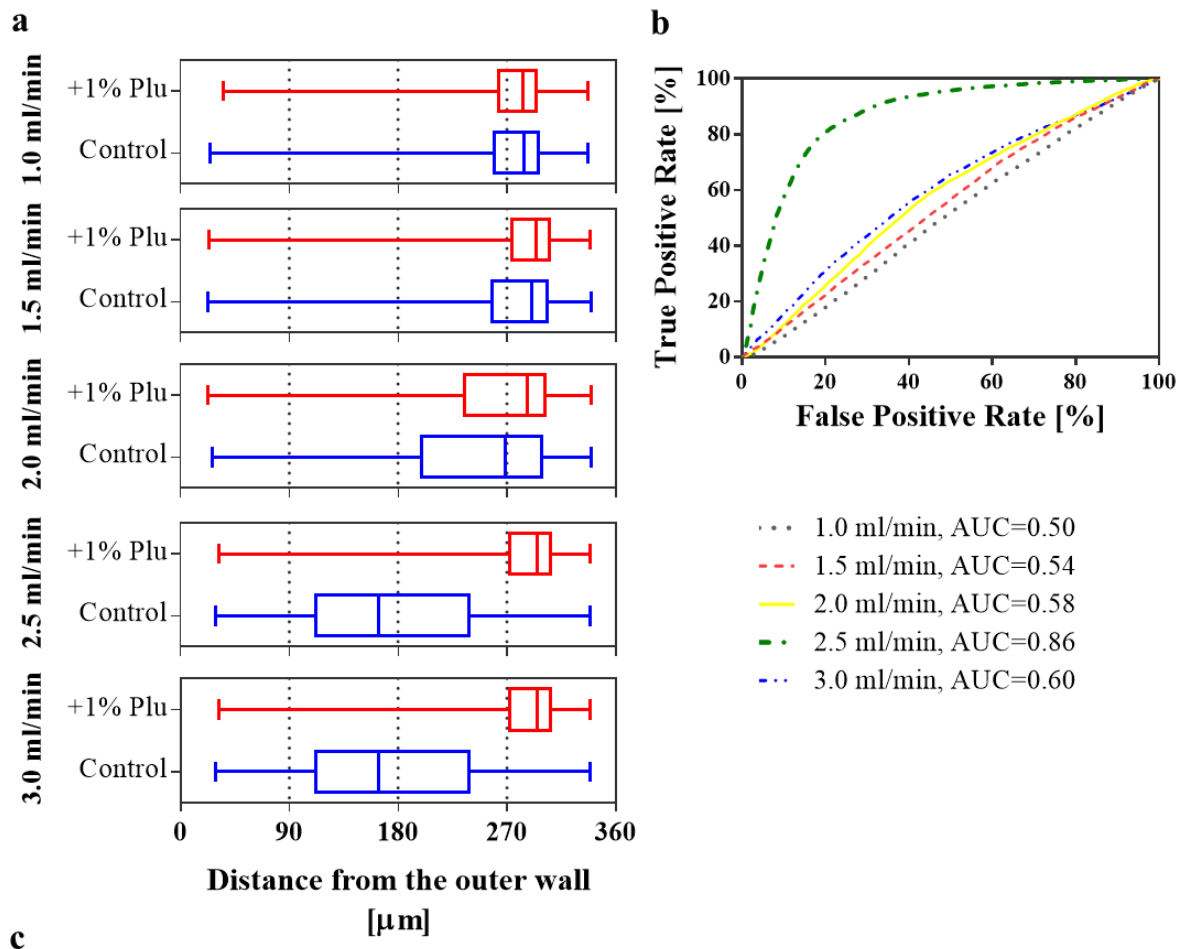
Replica I	Flow rate [ml/min]	Mean	SD	Min	Q1	Median	Q3	Max
Jurkat cells in PBS-/-	1	253	46	24	224	270	285	329
	1.5	271	52	15	258	290	303	340
	2	242	73	34	193	270	301	340
	2.5	177	77	24	112	168	243	339
	3	118	58	16	76	100	140	340
Jurkat cells in PBS-/- +1% Pluronic F-68	1	249	40	18	227	262	277	329
	1.5	275	43	30	265	289	301	340
	2	255	61	40	227	280	299	340
	2.5	275	50	31	267	294	304	339
	3	140	61	21	92	127	173	339

Tables showing statistical summary (mean and standard deviation from the mean (SD), median, 25<sup>th</sup> (Q1) and 75<sup>th</sup> (Q3) percentile as well as minimal (min) and maximal (max) measured value) of latera equilibrium positions obtained for at least 10000 events for Jurkat cells in PBS-/- and Jurkat cells in PBS-/- +1% Pluronic F-68, in design I spiral channel with  $360 \times 60 \mu\text{m}$  cross-section, at five applied flow rates for **replica I** out of three, expressed as distance from the outer wall [ $\mu\text{m}$ ].



**Replica II (a)** Hydrodynamic behaviour of control Jurkat cells incubated for 3 hrs in PBS-/- (blue) and Jurkat cells incubated for 3 hrs in PBS-/- and supplemented with 1% pluronic F-68 (red), assessed in a spiral microchannel with  $360 \times 60 \mu\text{m}$  cross-section at five different flow rates (1, 1.5, 2, 2.5 and 3 ml/min). Box plots summarising lateral equilibrium positions, measured as a distance from the outer wall ( $\mu\text{m}$ ), where the line in the box represents the median, the box represents data from lower and upper quartile and the whiskers correspond to the lowest and highest extreme values **(b)** Receiver Operating Characteristic (ROC) curves were plotted for lateral equilibrium position for control versus Pluronic-treated cells, for each

applied flow rate. The True Positive Rate is defined as the number of control cells found at a given lateral position and divided by the total number of control cells. The False Positive Rate is the corresponding number of Pluronic-treated cells divided by the total number of control cells for the same cut-off. To quantify differences in the assembled equilibrium positions the Area Under the Curve (AUC) was calculated. **(c)** Tables showing statistical summary (mean and standard deviation from the mean (SD), median, 25<sup>th</sup> (Q1) and 75<sup>th</sup> (Q3) percentile as well as minimal (min) and maximal (max) measured value) of lateral equilibrium positions obtained for at least 10000 events for Jurkat cells in PBS-/- and Jurkat cells in PBS-/- +1% Pluronic F-68 at five applied flow rates for **replica II** out of three, expressed as distance from the outer wall [ $\mu\text{m}$ ].



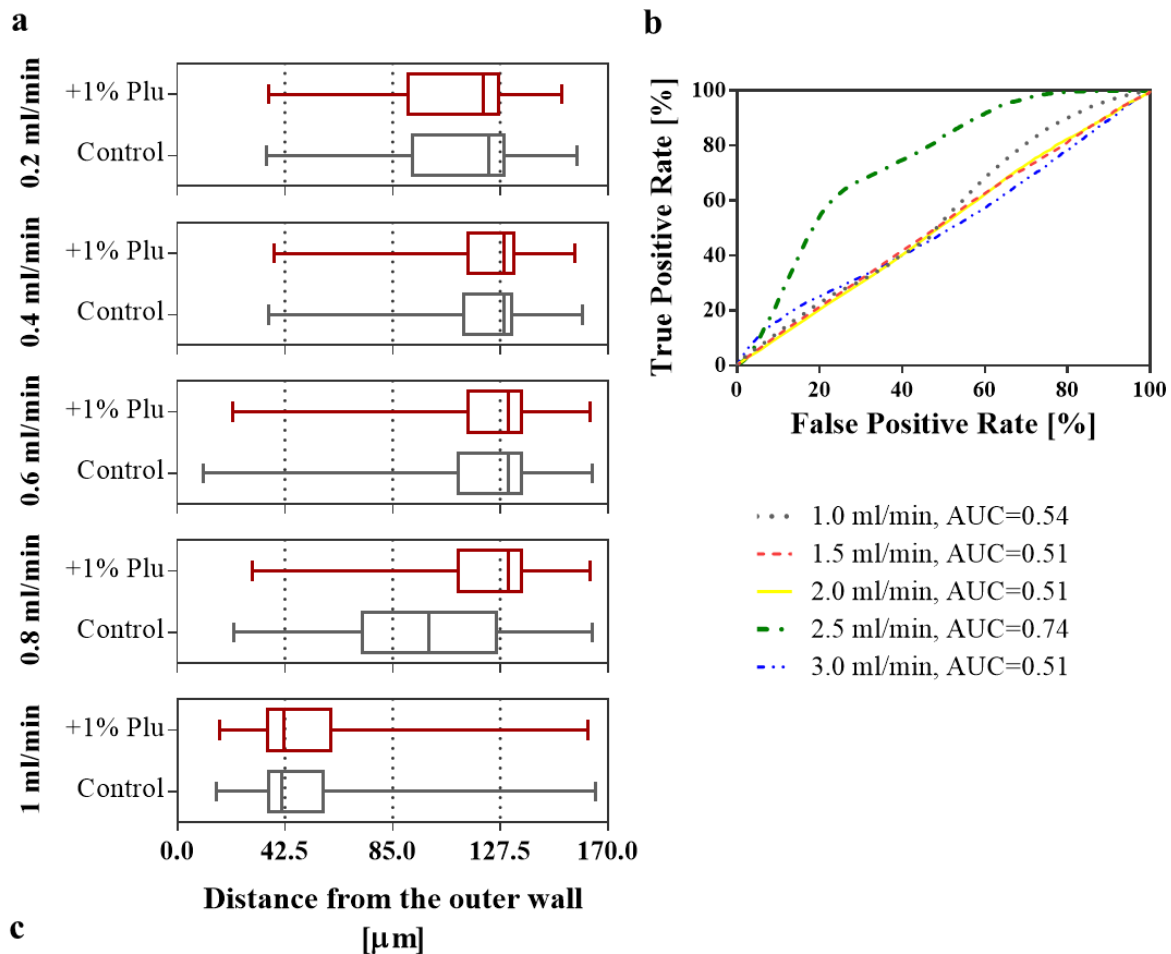
**Replica III (a)** Hydrodynamic behaviour of control Jurkat cells incubated for 3 hrs in PBS-/- (blue) and Jurkat cells incubated for 3 hrs in PBS-/- and supplemented with 1% pluronic F-68 (red), assessed in a spiral microchannel with  $360 \times 60 \mu\text{m}$  cross-section at five different flow rates (1, 1.5, 2, 2.5 and 3 ml/min). Box plots summarising lateral equilibrium positions, measured as a distance from the outer wall ( $\mu\text{m}$ ), where the line in the box represents the median, the box represents data from lower and upper quartile and the whiskers correspond to the lowest and highest extreme values **(b)** Receiver Operating Characteristic (ROC) curves were plotted for lateral equilibrium position for control versus Pluronic-treated cells, for each applied flow rate. The True Positive Rate is defined as the number of control cells found at a

given lateral position and divided by the total number of control cells. The False Positive Rate is the corresponding number of Pluronic-treated cells divided by the total number of control cells for the same cut-off. To quantify differences in the assembled equilibrium positions the Area Under the Curve (AUC) was calculated. (c) Tables showing statistical summary (mean and standard deviation from the mean (SD), median, 25<sup>th</sup> (Q1) and 75<sup>th</sup> (Q3) percentile as well as minimal (min) and maximal (max) measured value) of latera equilibrium positions obtained for at least 10000 events for Jurkat cells in PBS-/- and Jurkat cells in PBS-/- +1% Pluronic F-68 at five applied flow rates for **replica III** out of three, expressed as distance from the outer wall [ $\mu\text{m}$ ].

## Appendix S

Replica I	Flow rate [ml/min]	Mean	SD	Min	Q1	Median	Q3	Max
RBC in PBS-/-	0.2	112	20	3	92	123	129	167
	0.4	122	14	44	113	128	132	160
	0.6	123	19	21	112	131	136	164
	0.8	100	30	19	75	102	127	164
	1	54	28	20	36	41	59	164
RBC in PBS-/- +1% Pluronic F-68	0.2	110	20	22	91	121	127	154
	0.4	122	15	29	113	128	132	156
	0.6	125	15	16	121	131	134	161
	0.8	122	19	26	112	131	135	163
	1	55	28	14	36	42	62	165

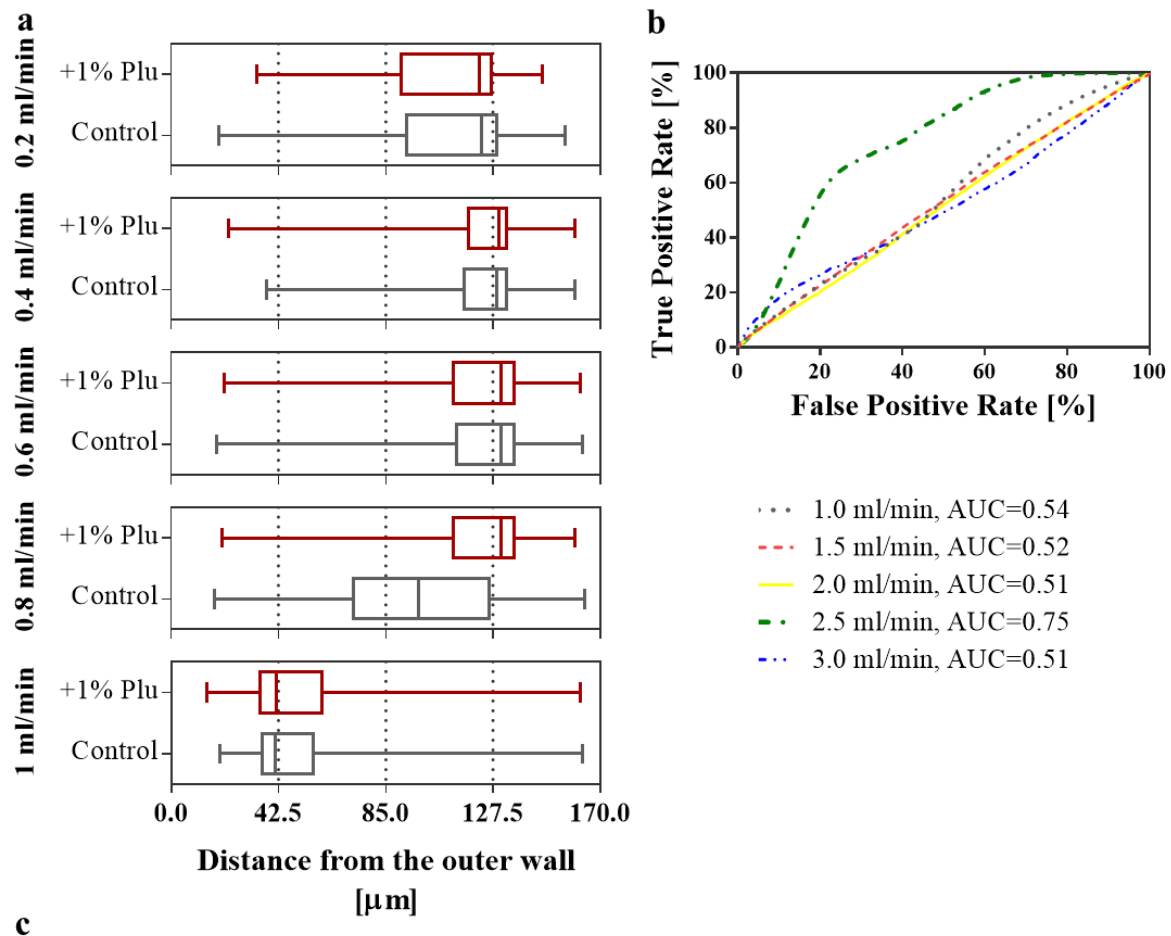
Tables showing statistical summary (mean and standard deviation from the mean (SD), median, 25<sup>th</sup> (Q1) and 75<sup>th</sup> (Q3) percentile as well as minimal (min) and maximal (max) measured value) of latera equilibrium positions obtained for at least 10000 events for RBC in PBS-/- and RBC in PBS-/- +1% Pluronic F-68, in design II spiral channel with  $170 \times 30 \mu\text{m}$  cross-section, at five applied flow rates for **replica I** out of three, expressed as distance from the outer wall [ $\mu\text{m}$ ].



**Replica II (a)** Hydrodynamic behaviour of control RBC (grey) and RBC incubated for 3 hrs in PBS-/- and supplemented with 1% pluronic F-68 (red), assessed in a spiral microchannel with  $170 \times 30 \mu\text{m}$  cross-section at five different flow rates (0.2, 0.4, 0.6, 0.8 and 1 ml/min). Box plots summarising lateral equilibrium positions, measured as a distance from the outer wall ( $\mu\text{m}$ ), where the line in the box represents the median, the box represents data from lower and upper quartile and the whiskers correspond to the lowest and highest extreme values. **(b)** Receiver Operating Characteristic (ROC) curves were plotted for lateral equilibrium position

for control versus Pluronic-treated cells, for each applied flow rate. The True Positive Rate is defined as the number of control cells found at a given lateral position and divided by the total number of control cells. The False Positive Rate is the corresponding number of Pluronic-treated cells divided by the total number of control cells for the same cut-off. To quantify differences in the assembled equilibrium positions the Area Under the Curve (AUC) was calculated. (c) Tables showing statistical summary (mean and standard deviation from the mean (SD), median, 25<sup>th</sup> (Q1) and 75<sup>th</sup> (Q3) percentile as well as minimal (min) and maximal (max) measured value) of latera equilibrium positions obtained for at least 10000 events for RBC in PBS<sup>-/-</sup> and RBC in PBS<sup>-/-</sup> +1% Pluronic F-68, at five applied flow rates for **replica II** out of three, expressed as distance from the outer wall [ $\mu\text{m}$ ].





Replica III	Flow rate [ml/min]	Mean	SD	Min	Q1	Median	Q3	Max
RBCs in PBS-/-	0.2	113	20	19	93	123	129	156
	0.4	123	14	38	116	129	133	160
	0.6	123	18	18	113	131	136	163
	0.8	98	30	17	72	98	126	164
	1	53	26	19	36	41	57	163
RBC in PBS-/- +1% Pluronic F-68	0.2	111	20	34	91	122	127	147
	0.4	124	14	23	118	130	133	160
	0.6	123	19	21	112	131	136	162
	0.8	123	19	20	112	131	136	160
	1	53	27	14	35	42	60	162

**Replica III (a)** Hydrodynamic behaviour of control RBC (grey) and RBC incubated for 3 hrs in PBS-/- and supplemented with 1% pluronic F-68 (red), assessed in a spiral microchannel with  $170 \times 30 \mu\text{m}$  cross-section at five different flow rates (0.2, 0.4, 0.6, 0.8 and 1 ml/min). Box plots summarising lateral equilibrium positions, measured as a distance from the outer wall ( $\mu\text{m}$ ), where the line in the box represents the median, the box represents data from lower and upper quartile and the whiskers correspond to the lowest and highest extreme values. **(b)** Receiver Operating Characteristic (ROC) curves were plotted for lateral equilibrium position for control versus Pluronic-treated cells, for each applied flow rate. The True Positive Rate is defined as the number of control cells found at a given lateral position and divided by the total

number of control cells. The False Positive Rate is the corresponding number of Pluronic-treated cells divided by the total number of control cells for the same cut-off. To quantify differences in the assembled equilibrium positions the Area Under the Curve (AUC) was calculated. (c) Tables showing statistical summary (mean and standard deviation from the mean (SD), median, 25<sup>th</sup> (Qi) and 75<sup>th</sup> (Q3) percentile as well as minimal (min) and maximal (max) measured value) of latera equilibrium positions obtained for at least 10000 events for RBC in PBS-/- and RBC in PBS-/- +1% Pluronic F-68, at five applied flow rates for **replica III** out of three, expressed as distance from the outer wall [ $\mu\text{m}$ ].

## Chapter 8. Summary and future outlook

The overarching goal of this project was to develop a novel purification method to isolate mRBC from the contaminant by-products of the differentiation protocol, while maintaining their integrity and quality, in a timely (processing millions of cells/min and mls of medium/min) label-free (no modifying agents added) and continuous manner. To meet these requirements, I investigated label-free separation in spiral microchannels based on cells' endogenous properties such as size and deformability. The main achievements of my work included:

1. First study to track cell mechanotype changes during mRBC production with a high-throughput approach, utilising data from over 10000 cells, to determine that size and deformability could be exploited as label-free markers for mRBC purification.
2. Demonstrating, for the first time, applicability of spiral microchannels for deformability-based separation.
3. Translating the mechanical properties identified in point 1 and findings from point 2 into a complete bespoke label-free downstream process for isolation of enucleated mRBC, up to high purities (99%).
4. Identifying and researching factors influencing performance of the process and impact of the processing conditions on cell quality.

To assess the changing mechanotype of CD34+ undergoing differentiation into mRBC, I used cutting-edge technology- RT-DC- for contactless assessment of cells deformation in a high-throughput fashion. I observed that cells undergoing the 21 day differentiation protocol, become progressively softer due to re-arrangements in cytoskeleton and decreasing nucleus to cytoplasm ratio. At the end of the protocol, subpopulations found in the heterogenous mixture, enucleated mRBC and nucleated cells together with free-floating nuclei, can be characterised and classified based on the unique combination of size and deformability. These results confirmed that mRBC could be purified from the nucleated cells and nuclei populations, based strictly on their label-free makers. These findings are detailed in Guzniczak. *et al.* 2017 [41]

Since size and deformability were confirmed to be suitable label-free markers, spiral channels were investigated as a means of size-based separations. Successful size based separations have been previously demonstrated in a range of applications and it has been noted that deformability of cells influences performance. However, in this study, for the first time, I

demonstrated the deformability-induced lift force ( $F_D$ ) can be utilised for cellular separation. I developed a unique cellular model to demonstrate that cells of identical size could be separated purely based on deformability. I identified that in order to take advantage of the effect of  $F_D$  for particles focusing and ordering in the spiral geometry, sufficiently high flow rates are required (3ml/min in design I and 1 ml/min in design II). Cells are dynamic structures responding to mechanical stresses such as hydrodynamic compressibility by rearranging their cytoskeletal structures to offset the stresses. This causes generation of  $F_D$ , which, in combination with inertial lift forces and Dean drag, pushes cells of the same size but different deformability properties, to contrary lateral equilibrium positions within the channel cross-section. This principle has been successfully adapted to enhance and conduct label-free and continuous cell separation in spiral microchannels.

A bespoke spiral channel (design II, with  $170 \mu\text{m} \times 30 \mu\text{m}$  rectangular cross-section, 6 loops and one inlet) has been used for the purification of mRBC by means of utilising the impact of  $F_D$ . By using the differences in dynamic equilibrium positions it was possible to enrich the enucleated mRBC up to 70 % purity, recovering >90% of the input cells. These results varied from predicted (>95% purity) performance of the device, initially validated using pure populations of pre-sorted enucleated and nucleated cells and nuclei, due to particle interactions. In order to improve the purity, a membrane filtration step has been added to the process. This inclusion was motivated by the fact that the degree of deformation could be measured by looking at changes in the minor axis. Under conditions where there are no applied deforming forces the minor axis of enucleated and nucleated cells are comparable. Because deformability and size are coupled, when a deforming force is exerted, the enucleated cells minor axis shortens more than for nucleated cells and a 2-3  $\mu\text{m}$  difference is revealed. The size difference revealed by applied stress constituted the basis for cell separation using a porous physical barrier (ISOPORE™ membrane) with a cut-off size of 3 $\mu\text{m}$ . This approach improved cell purity to 99%, but at a cost of losing 70% of input cells which were retained at the membrane.

In the proposed approach,  $3\text{-}4 \times 10^6$  cells/ min are processed by a single device when operating at the optimal 1ml/min flow rate. The current throughput seems reasonable for processing cells that are routinely cultured within similar concentration range in large volumes. Up to date, mRBC culture is routinely carried in static culture conditions, facilitating maximal cell concentration at around  $5 \times 10^6$  cells/ml [11]. As Timmins *et al.* 2009 estimated, this would require 9,000 T175  $\text{cm}^2$  flasks to produce a single blood unit [14]. To overcome this limitation, mRBC cultured at  $50 \times 10^6$  cell/ml should decrease the required volume of medium to 40 litres

and consequently the total cost to around \$8000 per blood unit [14][3][11]. The downstream processing proposed in this study has the capacity for further scale-up to process such volumes by two means: increasing cell sample concentration (the estimated concentration limit for this particular system is at  $20 \times 10^6$  cells/ml,  $\alpha=1$ ) and system parallelisation. Stacking microfluidic devices (stack of 20 devices reported [159]) is a common practice resulting in a rapid and efficient throughput improvement.

Spiral microchannels have been positively validated as a practical solution for mRBC purification. However, one of the remaining bottlenecks with such microsystems is their tendency to clog due to a channel cross-section that is merely larger than a couple of cell diameters. One of the most commonly accepted solutions to prevent clogging issues is the use of additives such as Pluronic F-68. I investigated the effect of this biocompatible surfactant on cells commonly used in microfluidic studies, like Jurkat and HEK cells and red blood cells. This published research [162] provides a substantial explanation of the additive impact on cell mechanotype, which should be considered prior to experiments and measurements performed using the microfluidics technologies.

By taking advantage of thoroughly characterised mechanical properties, a label-free passive platform for cost-effective mRBC downstream processing has been successfully developed. This study provided robust proof of principle and the next logical step would involve translation into industrial scale processing. Prior to the successful transition, a profound understanding of the basis of inertial focusing in spiral microchannels is required, including the hydrodynamic particle-particle interactions, particle-medium interactions and the mechanism of the  $F_D$  action. That requires development of computational methods, which would allow to precisely model and optimise process performance. Bringing mRBC into clinics requires reproducible unit operations. CB CD34+ cells are a limited source of mRBC and as verified in this study, starting cell material derived from different donors give a final product characterised by different pheno- and mechanotypes, thus implementation of universal downstream protocols is currently challenging. The field of stem cell-derived therapeutic products is maturing and with introduction of iPSC and immortalised erythroid cell lines, it should be possible to produce large quantities of standardised mRBC and integrate technology proposed here into the formulation step of the cellular product derivation process.

## Bibliography

- [1] Daley, G.Q. (2012) The promise and perils of stem cell therapeutics. *Cell Stem Cell*, **10**, 740–9. <https://doi.org/10.1016/j.stem.2012.05.010>
- [2] World Health Organisation, Blood safety and availability, <http://www.who.int/en/> (2017).
- [3] Zeuner, A., Martelli, F., Vaglio, S., Federici, G., Whitsett, C. and Migliaccio, A.R. (2012) Concise review: stem cell-derived erythrocytes as upcoming players in blood transfusion. *Stem Cells (Dayton, Ohio)*, United States. **30**, 1587–96. <https://doi.org/10.1002/stem.1136>
- [4] Douay, L. and Andreu, G. (2007) Ex vivo production of human red blood cells from hematopoietic stem cells: what is the future in transfusion? *Transfusion Medicine Reviews*, United States. **21**, 91–100. <https://doi.org/10.1016/j.tmr.2006.11.004>
- [5] Peyrard, T., Bardiaux, L., Krause, C., Kobari, L., Lapillonne, H., Andreu, G. et al. (2011) Banking of pluripotent adult stem cells as an unlimited source for red blood cell production: potential applications for alloimmunized patients and rare blood challenges. *Transfusion Medicine Reviews*, United States. **25**, 206–16. <https://doi.org/10.1016/j.tmr.2011.01.002>
- [6] Cabrita, G.J.M., Ferreira, B.S., da Silva, C.L., Goncalves, R., Almeida-Porada, G. and Cabral, J.M.S. (2003) Hematopoietic stem cells: from the bone to the bioreactor. *Trends in Biotechnology*, England. **21**, 233–40. [https://doi.org/10.1016/S0167-7799\(03\)00076-3](https://doi.org/10.1016/S0167-7799(03)00076-3)
- [7] Shah, S., Huang, X. and Cheng, L. (2014) Concise review: stem cell-based approaches to red blood cell production for transfusion. *Stem Cells Translational Medicine*, United States. **3**, 346–55. <https://doi.org/10.5966/sctm.2013-0054>
- [8] Li, X., Wu, Z., Fu, X. and Han, W. (2013) How Far Are Stem-Cell-Derived Erythrocytes from the Clinical Arena? *BioScience*, **63**, 632–43. <https://doi.org/10.1525/bio.2013.63.8.6>
- [9] Migliaccio, A.R., Whitsett, C., Papayannopoulou, T. and Sadelain, M. (2012) The potential of stem cells as an in vitro source of red blood cells for transfusion. *Cell Stem Cell*, **10**, 115–9. <https://doi.org/10.1016/j.stem.2012.01.001>
- [10] Bayley, R., Ahmed, F., Glen, K., McCall, M., Stacey, A. and Thomas, R. (2018) The productivity limit of manufacturing blood cell therapy in scalable stirred bioreactors. *Journal of Tissue Engineering and Regenerative Medicine*, England. **12**, e368–78.

<https://doi.org/10.1002/term.2337>

- [11] Rousseau, G.F., Giarratana, M.-C. and Douay, L. (2014) Large-scale production of red blood cells from stem cells: what are the technical challenges ahead? *Biotechnology Journal*, Germany. **9**, 28–38. <https://doi.org/10.1002/biot.201200368>
- [12] Glen, K.E., Cheeseman, E.A., Stacey, A.J. and Thomas, R.J. (2018) A mechanistic model of erythroblast growth inhibition providing a framework for optimisation of cell therapy manufacturing. *Biochemical Engineering Journal*, **133**, 28–38. <https://doi.org/https://doi.org/10.1016/j.bej.2018.01.033>
- [13] McGowan, N.W.A., Campbell, J.D.M. and Mountford, J.C. (2018) Good Manufacturing Practice (GMP) Translation of Advanced Cellular Therapeutics: Lessons for the Manufacture of Erythrocytes as Medicinal Products. *Methods in Molecular Biology (Clifton, NJ)*, United States. **1698**, 285–92. [https://doi.org/10.1007/978-1-4939-7428-3\\_18](https://doi.org/10.1007/978-1-4939-7428-3_18)
- [14] Timmins, N.E. and Nielsen, L.K. (2009) Blood cell manufacture: current methods and future challenges. *Trends in Biotechnology*, England. **27**, 415–22. <https://doi.org/10.1016/j.tibtech.2009.03.008>
- [15] Migliaccio, G., Di Pietro, R., di Giacomo, V., Di Baldassarre, A., Migliaccio, A.R., Maccioni, L. et al. (2002) In vitro mass production of human erythroid cells from the blood of normal donors and of thalassemic patients. *Blood Cells, Molecules & Diseases*, United States. **28**, 169–80.
- [16] Baek, E.J., Kim, H.-S., Kim, S., Jin, H., Choi, T.-Y. and Kim, H.O. (2008) In vitro clinical-grade generation of red blood cells from human umbilical cord blood CD34+ cells. *Transfusion*, United States. **48**, 2235–45. <https://doi.org/10.1111/j.1537-2995.2008.01828.x>
- [17] Fujimi, A., Matsunaga, T., Kobune, M., Kawano, Y., Nagaya, T., Tanaka, I. et al. (2008) Ex vivo large-scale generation of human red blood cells from cord blood CD34+ cells by co-culturing with macrophages. *International Journal of Hematology*, Japan. **87**, 339–50. <https://doi.org/10.1007/s12185-008-0062-y>
- [18] Neildez-Nguyen, T.M.A., Wajcman, H., Marden, M.C., Bensidhoum, M., Moncollin, V., Giarratana, M.-C. et al. (2002) Human erythroid cells produced ex vivo at large scale differentiate into red blood cells in vivo. *Nature Biotechnology*, United States. **20**, 467–72. <https://doi.org/10.1038/nbt0502-467>
- [19] Akker, E. Van Den, Satchwell, T.J., Pellegrin, S., Daniels, G. and Toye, A.M. (2010) The majority of the in vitro erythroid expansion potential resides in CD34 – cells ,

- outweighing the contribution of CD34 + cells and significantly increasing the erythroblast yield from peripheral blood samples. *Haematologica*, **95**, 1594–8. <https://doi.org/10.3324/haematol.2009.019828>
- [20] Ma, F., Ebihara, Y., Umeda, K., Sakai, H., Hanada, S., Zhang, H. et al. (2008) Generation of functional erythrocytes from human embryonic stem cell-derived definitive hematopoiesis. *Proceedings of the National Academy of Sciences of the United States of America*, United States. **105**, 13087–92. <https://doi.org/10.1073/pnas.0802220105>
- [21] Lu, S.-J., Feng, Q., Park, J.S., Vida, L., Lee, B.-S., Strausbauch, M. et al. (2008) Biologic properties and enucleation of red blood cells from human embryonic stem cells. *Blood*, American Society of Hematology. **112**, 4475–84. <https://doi.org/10.1182/blood-2008-05-157198>
- [22] Lapillonne, H., Kobari, L., Mazurier, C., Tropel, P., Giarratana, M.-C., Zanella-Cleon, I. et al. (2010) Red blood cell generation from human induced pluripotent stem cells: perspectives for transfusion medicine. *Haematologica*, 2010/05/21. Ferrata Storti Foundation. **95**, 1651–9. <https://doi.org/10.3324/haematol.2010.023556>
- [23] Trakarnsanga, K., Griffiths, R.E., Wilson, M.C., Blair, A., Satchwell, T.J., Meinders, M. et al. (2017) An immortalized adult human erythroid line facilitates sustainable and scalable generation of functional red cells. *Nature Communications*, The Author(s). **8**, 14750.
- [24] Migliaccio, A.R., Masselli, E., Varricchio, L. and Whitsett, C. (2012) Ex-vivo expansion of red blood cells: how real for transfusion in humans? *Blood Reviews*, England. **26**, 81–95. <https://doi.org/10.1016/j.blre.2011.11.002>
- [25] Miharada, K., Hiroyama, T., Sudo, K., Nagasawa, T. and Nakamura, Y. (2006) Efficient enucleation of erythroblasts differentiated in vitro from hematopoietic stem and progenitor cells. *Nature Biotechnology*, **24**, 1255–7. <https://doi.org/10.1038/nbt1245>
- [26] Timmins, N.E., Athanasas, S., Gunther, M., Buntine, P. and Nielsen, L.K. (2011) Ultra-high-yield manufacture of red blood cells from hematopoietic stem cells. *Tissue Engineering Part C, Methods*, United States. **17**, 1131–7. <https://doi.org/10.1089/ten.TEC.2011.0207>
- [27] Migliaccio, G., Sanchez, M., Masiello, F., Tirelli, V., Varricchio, L., Whitsett, C. et al. (2010) Humanized culture medium for clinical expansion of human erythroblasts. *Cell Transplantation*, United States. **19**, 453–69.



<https://doi.org/10.3727/096368909X485049>

- [28] Grillberger, L., Kreil, T.R., Nasr, S. and Reiter, M. (2009) Emerging trends in plasma-free manufacturing of recombinant protein therapeutics expressed in mammalian cells. *Biotechnology Journal*, Germany. **4**, 186–201. <https://doi.org/10.1002/biot.200800241>
- [29] Giarratana, M.-C., Rouard, H., Dumont, A., Kiger, L., Safeukui, I., Le Penec, P.-Y. et al. (2011) Proof of principle for transfusion of in vitro-generated red blood cells. *Blood*, American Society of Hematology, Washington, DC. **118**, 5071–9. <https://doi.org/10.1182/blood-2011-06-362038>
- [30] [Http://www.clinicaltrials.gov](http://www.clinicaltrials.gov). (2009) Cultured Red Blood Cells : Life Span in Vivo Study (GRc2008).
- [31] Keerthivasan, G., Wickrema, A. and Crispino, J.D. (2011) Erythroblast enucleation. *Stem Cells International*, 2011/10/05. SAGE-Hindawi Access to Research. **2011**, 139851. <https://doi.org/10.4061/2011/139851>
- [32] Goers, L., Freemont, P. and Polizzi, K.M. (2014) Co-culture systems and technologies: taking synthetic biology to the next level. *Journal of the Royal Society, Interface*, The Royal Society. **11**, 20140065. <https://doi.org/10.1098/rsif.2014.0065>
- [33] Baek, E.J., Kim, H., Kim, S., Jin, H., Choi, T. and Kim, H.O. (2008) In vitro clinical-grade generation of red blood cells from human umbilical cord blood CD34+ cells. *Transfusion*, **48**, 2235–45. <https://doi.org/10.1111/j.1537-2995.2008.01828.x>
- [34] Griffiths, R.E., Kupzig, S., Cogan, N., Mankelow, T.J., Betin, V.M.S., Trakarnsanga, K. et al. (2012) Maturing reticulocytes internalize plasma membrane in glycophorin A-containing vesicles that fuse with autophagosomes before exocytosis. *Blood*, United States. **119**, 6296–306. <https://doi.org/10.1182/blood-2011-09-376475>
- [35] Kupzig, S., Parsons, S.F., Curnow, E., Anstee, D.J. and Blair, A. (2017) Superior survival of ex vivo cultured human reticulocytes following transfusion into mice. *Haematologica*, Italy. **102**, 476–83. <https://doi.org/10.3324/haematol.2016.154443>
- [36] Qiu, C., Olivier, E.N., Velho, M. and Bouhassira, E.E. (2008) Globin switches in yolk sac-like primitive and fetal-like definitive red blood cells produced from human embryonic stem cells. *Blood*, American Society of Hematology. **111**, 2400–8. <https://doi.org/10.1182/blood-2007-07-102087>
- [37] Dias, J., Gumenyuk, M., Kang, H., Vodyanik, M., Yu, J., Thomson, J.A. et al. (2011) Generation of red blood cells from human induced pluripotent stem cells. *Stem Cells and Development*, United States. **20**, 1639–47. <https://doi.org/10.1089/scd.2011.0078>
- [38] Kobari, L., Yates, F., Oudrhiri, N., Francina, A., Kiger, L., Mazurier, C. et al. (2012)

- Human induced pluripotent stem cells can reach complete terminal maturation: in vivo and in vitro evidence in the erythropoietic differentiation model. *Haematologica*, Ferrata Storti Foundation. **97**, 1795–803.  
<https://doi.org/10.3324/haematol.2011.055566>
- [39] Timmins, N.E. and Nielsen, L.K. (2011) Manufactured RBC--rivers of blood, or an oasis in the desert? *Biotechnology Advances*, England. **29**, 661–6.  
<https://doi.org/10.1016/j.biotechadv.2011.05.002>
- [40] Bouhassira, E.E. (2008) Toward the manufacture of red blood cells? *Blood*, United States. **112**, 4362–3. <https://doi.org/10.1182/blood-2008-09-177212>
- [41] Guzniczak, E., Mohammad Zadeh, M., Dempsey, F., Jimenez, M., Bock, H., Whyte, G. et al. (2017) High-throughput assessment of mechanical properties of stem cell derived red blood cells, toward cellular downstream processing. *Scientific Reports*, **7**, 14457. <https://doi.org/10.1038/s41598-017-14958-w>
- [42] Blum, B. and Benvenisty, N. (2008) The tumorigenicity of human embryonic stem cells. *Advances in Cancer Research*, United States. **100**, 133–58.  
[https://doi.org/10.1016/S0065-230X\(08\)00005-5](https://doi.org/10.1016/S0065-230X(08)00005-5)
- [43] (2019) RESTORE: Recovery and Survival of Stem Cell Originated Red Cells. Identifier: NCT01609374. <https://doi.org/ClinicalTrials.gov>
- [44] Ratcliffe, E., Thomas, R.J. and Williams, D.J. (2011) Current understanding and challenges in bioprocessing of stem cell-based therapies for regenerative medicine. *British Medical Bulletin*, England. **100**, 137–55. <https://doi.org/10.1093/bmb/ldr037>
- [45] Di Carlo, D. (2012) A mechanical biomarker of cell state in medicine. *Journal of Laboratory Automation*, **17**, 32–42. <https://doi.org/10.1177/2211068211431630>
- [46] Otto, O., Rosendahl, P., Mietke, A., Golfier, S., Herold, C., Klaue, D. et al. (2015) Real-time deformability cytometry: on-the-fly cell mechanical phenotyping. *Nat Meth*, Nature Publishing Group, a division of Macmillan Publishers Limited. All Rights Reserved. **12**, 199–202.
- [47] Rossy, J., Laufer, J.M. and Legler, D.F. (2018) Role of Mechanotransduction and Tension in T Cell Function . *Front. Immunol.* . p. 2638.
- [48] Guck, J., Schinkinger, S., Lincoln, B., Wottawah, F., Ebert, S., Romeyke, M. et al. (2005) Optical deformability as an inherent cell marker for testing malignant transformation and metastatic competence. *Biophysical Journal*, **88**, 3689–98.  
<https://doi.org/10.1529/biophysj.104.045476>
- [49] Darling, E.M., Zauscher, S. and Guilak, F. (2006) Viscoelastic properties of zonal

- articular chondrocytes measured by atomic force microscopy. *Osteoarthritis and Cartilage*, England. **14**, 571–9. <https://doi.org/10.1016/j.joca.2005.12.003>
- [50] Hosseini, S.M. and Feng, J.J. (2012) How malaria parasites reduce the deformability of infected red blood cells. *Biophysical Journal*, Biophysical Society. **103**, 1–10. <https://doi.org/10.1016/j.bpj.2012.05.026>
- [51] Gossett, D.R., Weaver, W.M., Mach, A.J., Hur, S.C., Tse, H.T.K., Lee, W. et al. (2010) Label-free cell separation and sorting in microfluidic systems. *Analytical and Bioanalytical Chemistry*, **397**, 3249–67. <https://doi.org/10.1007/s00216-010-3721-9>
- [52] Fletcher, D.A. and Mullins, R.D. (2010) Cell mechanics and the cytoskeleton. *Nature*, Nature Publishing Group. **463**, 485.
- [53] (2014) Microtubules and Filaments. Scitable by Nat. Educ.
- [54] Lange, J.R., Metzner, C., Richter, S., Schneider, W., Spermann, M., Kolb, T. et al. (2017) Unbiased High-Precision Cell Mechanical Measurements with Microconstrictions. *Biophysical Journal*, Biophysical Society. **112**, 1472–80. <https://doi.org/10.1016/j.bpj.2017.02.018>
- [55] li, Q., Lee, G.Y.H., Ong, C.N. and Lim, C.T. (2008) AFM indentation study of breast cancer cells. *Biochem. Biophys. Res. Commun.* <https://doi.org/10.1016/j.bbrc.2008.07.078>
- [56] Ribeiro, A.S. and Dahl, K.N. (2010) The nucleus as a central structure in defining the mechanical properties of stem cells. *Conference Proceedings : . Annual International Conference of the IEEE Engineering in Medicine and Biology Society IEEE Engineering in Medicine and Biology Society Annual Conference*, United States. **2010**, 831–4. <https://doi.org/10.1109/IEMBS.2010.5626785>
- [57] Isermann, P. and Lammerding, J. (2013) Nuclear mechanics and mechanotransduction in health and disease. *Current Biology : CB*, **23**, R1113–21. <https://doi.org/10.1016/j.cub.2013.11.009>
- [58] Crisp, M., Liu, Q., Roux, K., Rattner, J.B., Shanahan, C., Burke, B. et al. (2006) Coupling of the nucleus and cytoplasm: role of the LINC complex. *The Journal of Cell Biology*, The Rockefeller University Press. **172**, 41–53. <https://doi.org/10.1083/jcb.200509124>
- [59] Swift, J., Ivanovska, I.L., Buxboim, A., Harada, T., Dingal, P.C.D.P., Pinter, J. et al. (2013) Nuclear lamin-A scales with tissue stiffness and enhances matrix-directed differentiation. *Science (New York, NY)*, **341**, 1240104. <https://doi.org/10.1126/science.1240104>

- [60] Darling, E.M., Zauscher, S., Block, J.A. and Guilak, F. (2007) A thin-layer model for viscoelastic, stress-relaxation testing of cells using atomic force microscopy: do cell properties reflect metastatic potential? *Biophysical Journal*, United States. **92**, 1784–91. <https://doi.org/10.1529/biophysj.106.083097>
- [61] Darling, E.M., Topel, M., Zauscher, S., Vail, T.P. and Guilak, F. (2008) Viscoelastic properties of human mesenchymally-derived stem cells and primary osteoblasts, chondrocytes, and adipocytes. *Journal of Biomechanics*, United States. **41**, 454–64. <https://doi.org/10.1016/j.jbiomech.2007.06.019>
- [62] Gonzalez-Cruz, R.D., Fonseca, V.C. and Darling, E.M. (2012) Cellular mechanical properties reflect the differentiation potential of adipose-derived mesenchymal stem cells. *Proceedings of the National Academy of Sciences of the United States of America*, United States. **109**, E1523-9. <https://doi.org/10.1073/pnas.1120349109>
- [63] Shin, D. and Athanasiou, K. (1999) Cytoindentation for obtaining cell biomechanical properties. *Journal of Orthopaedic Research : Official Publication of the Orthopaedic Research Society*, United States. **17**, 880–90. <https://doi.org/10.1002/jor.1100170613>
- [64] Darling, E.M., Pritchett, P.E., Evans, B.A., Superfine, R., Zauscher, S. and Guilak, F. (2009) Mechanical properties and gene expression of chondrocytes on micropatterned substrates following dedifferentiation in monolayer. *Cellular and Molecular Bioengineering*, United States. **2**, 395–404.
- [65] Gonzalez-Cruz, R.D. and Darling, E.M. (2013) Adipose-derived stem cell fate is predicted by cellular mechanical properties. *Adipocyte*, United States. **2**, 87–91. <https://doi.org/10.4161/adip.23015>
- [66] Jaasma, M.J., Jackson, W.M. and Keaveny, T.M. (2006) Measurement and characterization of whole-cell mechanical behavior. *Annals of Biomedical Engineering*, United States. **34**, 748–58. <https://doi.org/10.1007/s10439-006-9081-0>
- [67] Zhang, H. and Liu, K.-K. (2008) Optical tweezers for single cells. *Journal of the Royal Society, Interface*, England. **5**, 671–90. <https://doi.org/10.1098/rsif.2008.0052>
- [68] Guck, J., Ananthakrishnan, R., Mahmood, H., Moon, T.J., Cunningham, C.C. and Kas, J. (2001) The optical stretcher: a novel laser tool to micromanipulate cells. *Biophysical Journal*, United States. **81**, 767–84. [https://doi.org/10.1016/S0006-3495\(01\)75740-2](https://doi.org/10.1016/S0006-3495(01)75740-2)
- [69] Wang, N., Butler, J.P. and Ingber, D.E. (1993) Mechanotransduction across the cell surface and through the cytoskeleton. *Science (New York, NY)*, United States. **260**, 1124–7.
- [70] Crick, F.H.C. and Hughes, A.F.W. (1950) The physical properties of cytoplasm: A

- study by means of the magnetic particle method Part I. Experimental. *Experimental Cell Research*, **1**, 37–80. [https://doi.org/https://doi.org/10.1016/0014-4827\(50\)90048-6](https://doi.org/https://doi.org/10.1016/0014-4827(50)90048-6)
- [71] Valberg, P.A. (1984) Magnetometry of ingested particles in pulmonary macrophages. *Science (New York, NY)*, United States. **224**, 513–6.
- [72] RAND, R.P. and BURTON, A.C. (1964) Mechanical Properties of the Red Cell Membrane. *Biophysical Journal*, United States. **4**, 115–35.
- [73] Lee, L.M. and Liu, A.P. (2014) The Application of Micropipette Aspiration in Molecular Mechanics of Single Cells. *Journal of Nanotechnology in Engineering and Medicine*, American Society of Mechanical Engineers. **5**, 408011–6. <https://doi.org/10.1115/1.4029936>
- [74] Lee, L.M., Lee, J.W., Chase, D., Gebrezgiabhier, D. and Liu, A.P. (2016) Development of an advanced microfluidic micropipette aspiration device for single cell mechanics studies. *Biomicrofluidics*, United States. **10**, 54105. <https://doi.org/10.1063/1.4962968>
- [75] Adamo, A., Sharei, A., Adamo, L., Lee, B., Mao, S. and Jensen, K.F. (2012) Microfluidics-based assessment of cell deformability. *Analytical Chemistry*, United States. **84**, 6438–43. <https://doi.org/10.1021/ac300264v>
- [76] Byun, S., Son, S., Amodei, D., Cermak, N., Shaw, J., Kang, J.H. et al. (2013) Characterizing deformability and surface friction of cancer cells. *Proceedings of the National Academy of Sciences of the United States of America*, United States. **110**, 7580–5. <https://doi.org/10.1073/pnas.1218806110>
- [77] Chen, J., Zheng, Y., Tan, Q., Shojaei-Baghini, E., Zhang, Y.L., Li, J. et al. (2011) Classification of cell types using a microfluidic device for mechanical and electrical measurement on single cells. *Lab on a Chip*, England. **11**, 3174–81. <https://doi.org/10.1039/c1lc20473d>
- [78] Gossett, D.R., Tse, H.T.K., Lee, S.A., Ying, Y., Lindgren, A.G., Yang, O.O. et al. (2012) Hydrodynamic stretching of single cells for large population mechanical phenotyping. *Proceedings of the National Academy of Sciences of the United States of America*, National Academy of Sciences. **109**, 7630–5. <https://doi.org/10.1073/pnas.1200107109>
- [79] Xavier, M., Rosendahl, P., Herbig, M., Krater, M., Spencer, D., Bornhauser, M. et al. (2016) Mechanical phenotyping of primary human skeletal stem cells in heterogeneous populations by real-time deformability cytometry. *Integrative Biology : Quantitative Biosciences from Nano to Macro*, England. **8**, 616–23.

<https://doi.org/10.1039/c5ib00304k>

- [80] Koch, M., Wright, K.E., Otto, O., Herbig, M., Salinas, N.D., Tolia, N.H. et al. (2017) *Plasmodium falciparum* erythrocyte-binding antigen 175 triggers a biophysical change in the red blood cell that facilitates invasion. *Proceedings of the National Academy of Sciences*, **114**, 4225–30. <https://doi.org/10.1073/pnas.1620843114>
- [81] Kräter, M., Jacobi, A., Otto, O., Tietze, S., Müller, K., Poitz, D.M. et al. (2017) Bone marrow niche-mimetics modulate HSPC function via integrin signaling. *Scientific Reports*, **7**, 2549. <https://doi.org/10.1038/s41598-017-02352-5>
- [82] Schriebl, K., Lim, S., Choo, A., Tscheliessnig, A. and Jungbauer, A. (2010) Stem cell separation: A bottleneck in stem cell therapy. *Biotechnology Journal*, John Wiley & Sons, Ltd. **5**, 50–61. <https://doi.org/10.1002/biot.200900115>
- [83] Lee, L.M., Rosano, J.M., Wang, Y., Klarmann, G.J., Garson, C.J., Prabhakarpanian, B. et al. (2018) Label-free mesenchymal stem cell enrichment from bone marrow samples by inertial microfluidics. *Analytical Methods*, Royal Society of Chemistry. **10**, 713–21. <https://doi.org/10.1039/c7ay02500a>
- [84] A Mcintyre, C., T Flyg, B. and Fong, T. (2010) Fluorescence-Activated Cell Sorting for CGMP Processing of Therapeutic Cells. *Bioprocess Int.*
- [85] Willoughby, N.A., Bock, H., Hoeve, M.A., Pells, S., Williams, C., McPhee, G. et al. (2016) A scalable label-free approach to separate human pluripotent cells from differentiated derivatives. *Biomicrofluidics*, United States. **10**, 14107. <https://doi.org/10.1063/1.4939946>
- [86] Hoeve, M.A., De Sousa, P.A. and Willoughby, N.A. (2017) Challenges of Scale-up of Cell Separation and Purification Techniques. *Bioprocess. Cell Based Ther.* <https://doi.org/doi:10.1002/9781118743362.ch5>
- [87] Tien, C. (2012) 9. In: Tien CBT-P of F, editor. Elsevier, Amsterdam. p. 1–6. <https://doi.org/https://doi.org/10.1016/B978-0-444-56366-8.00001-3>
- [88] Stamatakis, K. and Tien, C. (1991) Cake formation and growth in cake filtration. *Chemical Engineering Science*, **46**, 1917–33. [https://doi.org/https://doi.org/10.1016/0009-2509\(91\)80153-P](https://doi.org/https://doi.org/10.1016/0009-2509(91)80153-P)
- [89] Shields 4th, C.W., Reyes, C.D. and López, G.P. (2015) Microfluidic cell sorting: a review of the advances in the separation of cells from debulking to rare cell isolation. *Lab on a Chip*, **15**, 1230–49. <https://doi.org/10.1039/c4lc01246a>
- [90] Gou, Y., Jia, Y., Wang, P. and Sun, C. (2018) Progress of Inertial Microfluidics in Principle and Application. *Sensors (Basel, Switzerland)*, MDPI. **18**, 1762.

- <https://doi.org/10.3390/s18061762>
- [91] Di Carlo, D. (2009) Inertial microfluidics. *Lab on a Chip*, England. **9**, 3038–46. <https://doi.org/10.1039/b912547g>
- [92] SEGRÉ, G. and SILBERBERG, A. (1961) Radial Particle Displacements in Poiseuille Flow of Suspensions. *Nature*, **189**, 209–10. <https://doi.org/10.1038/189209a0>
- [93] M. Squires, T. and R. Quake, S. (2005) Microfluidics: Fluid physics at the nanoliter scale. *Rev. Mod. Phys.* <https://doi.org/10.1103/RevModPhys.77.977>
- [94] Di Carlo, D., Irimia, D., Tompkins, R.G. and Toner, M. (2007) Continuous inertial focusing, ordering, and separation of particles in microchannels. *Proceedings of the National Academy of Sciences*, **104**, 18892–7. <https://doi.org/10.1073/pnas.0704958104>
- [95] Amini, H., Lee, W. and Di Carlo, D. (2014) Inertial microfluidic physics. *Lab Chip*. <https://doi.org/10.1039/c4lc00128a>
- [96] Zhou, J. and Papautsky, I. (2013) Fundamentals of inertial focusing in microchannels. *Lab on a Chip*, England. **13**, 1121–32. <https://doi.org/10.1039/c2lc41248a>
- [97] ASMOLOV, E.S. (1999) The inertial lift on a spherical particle in a plane Poiseuille flow at large channel Reynolds number. *Journal of Fluid Mechanics*, 1999/02/25. Cambridge University Press. **381**, 63–87. <https://doi.org/DOI:10.1017/S0022112098003474>
- [98] Gossett, D.R. and Di Carlo, D. (2009) Particle focusing mechanisms in curving confined flows. *Analytical Chemistry*, United States. **81**, 8459–65. <https://doi.org/10.1021/ac901306y>
- [99] Bhagat, A.A.S., Kuntaegowdanahalli, S.S. and Papautsky, I. (2008) Continuous particle separation in spiral microchannels using Dean flows and differential migration. *Lab on a Chip*, England. **8**, 1906–14. <https://doi.org/10.1039/b807107a>
- [100] Russom, A., Gupta, A.K., Nagrath, S., Di Carlo, D., Edd, J.F. and Toner, M. (2009) Differential inertial focusing of particles in curved low-aspect-ratio microchannels. *New Journal of Physics*, **11**, 75025. <https://doi.org/10.1088/1367-2630/11/7/075025>
- [101] Kuntaegowdanahalli, S.S., Bhagat, A.A.S., Kumar, G. and Papautsky, I. (2009) Inertial microfluidics for continuous particle separation in spiral microchannels. *Lab on a Chip*, England. **9**, 2973–80. <https://doi.org/10.1039/b908271a>
- [102] Yoon, D.H., Ha, J.B., Bahk, Y.K., Arakawa, T., Shoji, S. and Go, J.S. (2009) Size-selective separation of micro beads by utilizing secondary flow in a curved rectangular microchannel. *Lab on a Chip*, England. **9**, 87–90.

<https://doi.org/10.1039/b809123d>

- [103] Martel, J.M. and Toner, M. (2013) Particle Focusing in Curved Microfluidic Channels. *The Author(s)*. **3**, 3340.
- [104] Lee, W.C., Bhagat, A.A.S., Huang, S., Van Vliet, K.J., Han, J. and Lim, C.T. (2011) High-throughput cell cycle synchronization using inertial forces in spiral microchannels. *Lab on a Chip*, **11**, 1359–67. <https://doi.org/10.1039/c0lc00579g>
- [105] Kemna, E.W.M., Schoeman, R.M., Wolbers, F., Vermes, I., Weitz, D.A. and Van Den Berg, A. (2012) High-yield cell ordering and deterministic cell-in-droplet encapsulation using Dean flow in a curved microchannel. *Lab on a Chip*, **12**, 2881–7. <https://doi.org/10.1039/c2lc00013j>
- [106] Sun, J., Li, M., Liu, C., Zhang, Y., Liu, D., Liu, W. et al. (2012) Double spiral microchannel for label-free tumor cell separation and enrichment. *Lab on a Chip*, **12**, 3952–60. <https://doi.org/10.1039/c2lc40679a>
- [107] Hou, H.W., Warkiani, M.E., Khoo, B.L., Li, Z.R., Soo, R.A., Tan, D.S.W. et al. (2013) Isolation and retrieval of circulating tumor cells using centrifugal forces. *Scientific Reports*, **3**, 1–8. <https://doi.org/10.1038/srep01259>
- [108] Nathangari, S.S.P., Dong, B., Zhou, F., Kang, W., Giraldo-Vela, J.P., McGuire, T. et al. (2015) Isolating single cells in a neurosphere assay using inertial microfluidics. *Lab on a Chip*, Royal Society of Chemistry. **15**, 4591–7. <https://doi.org/10.1039/c5lc00805k>
- [109] Xiang, N. and Ni, Z. (2015) High-throughput blood cell focusing and plasma isolation using spiral inertial microfluidic devices. *Biomedical Microdevices*, **17**, 1–11. <https://doi.org/10.1007/s10544-015-0018-y>
- [110] Son, J., Murphy, K., Samuel, R., Gale, B.K., Carrell, D.T. and Hotaling, J.M. (2015) Non-motile sperm cell separation using a spiral channel. *Analytical Methods*, Royal Society of Chemistry. **7**, 8041–7. <https://doi.org/10.1039/c5ay02205c>
- [111] Son, J., Badamjav, O., Jenkins, T., Gale, B., Hotaling, J. and Carrell, D. (2015) Active Higher Quality Sperm Separation Using a Spiral Channel. *19th International Conference on Miniaturized Systems for Chemistry and Life Science*, Gyeongju. p. 376–8.
- [112] Clime, L., Li, K., Geissler, M., Hoa, X.D., Robideau, G.P., Bilodeau, G.J. et al. (2017) Separation and concentration of *Phytophthora ramorum* sporangia by inertial focusing in curving microfluidic flows. *Microfluidics and Nanofluidics*, Springer Berlin Heidelberg. **21**, 1–13. <https://doi.org/10.1007/s10404-016-1844-9>



- [113] Schaap, A., Dumon, J. and Toonder, J. den. (2016) Sorting algal cells by morphology in spiral microchannels using inertial microfluidics. *Microfluidics and Nanofluidics*, Springer Berlin Heidelberg. **20**, 1–11. <https://doi.org/10.1007/s10404-016-1787-1>
- [114] Robinson, M., Marks, H., Hinsdale, T., Maitland, K. and Coté, G. (2017) Rapid isolation of blood plasma using a cascaded inertial microfluidic device. *Biomicrofluidics*, **11**. <https://doi.org/10.1063/1.4979198>
- [115] Cruz, J., Hooshmand Zadeh, S., Graells, T., Andersson, M., Malmström, J., Wu, Z.G. et al. (2017) High pressure inertial focusing for separating and concentrating bacteria at high throughput. *Journal of Micromechanics and Microengineering*, **27**. <https://doi.org/10.1088/1361-6439/aa6b14>
- [116] Song, H., Rosano, J.M., Wang, Y., Garson, C.J., Prabhakarandian, B., Pant, K. et al. (2017) Spiral-shaped inertial stem cell device for high-throughput enrichment of iPSC-derived neural stem cells. *Microfluidics and Nanofluidics*, Springer Berlin Heidelberg. **21**, 1–9. <https://doi.org/10.1007/s10404-017-1896-5>
- [117] Hur, S.C., Henderson-MacLennan, N.K., McCabe, E.R.B. and Di Carlo, D. (2011) Deformability-based cell classification and enrichment using inertial microfluidics. *Lab on a Chip*, England. **11**, 912–20. <https://doi.org/10.1039/c0lc00595a>
- [118] Guzniczak, E., Jimenez, M., Otto, O., Willoughby, N. and Bridle, H. (2018) Deformability-induced lift force in curvilinear microchannels for stem cell-derived product purification. *22nd International Conference on Miniaturized Systems for Chemistry and Life Sciences*, Kaohsiung, Taiwan. p. 2049–52.
- [119] Gregoratto, I., McNeil, C.J. and Reeks, M.W. (2007) Micro-devices for rapid continuous separation of suspensions for use in micro-total-analysis-systems ( $\mu$ TAS). *ProcSPIE*,.
- [120] Seo, J., Lean, M.H. and Kole, A. (2007) Membraneless microseparation by asymmetry in curvilinear laminar flows. *Journal of Chromatography A*, Netherlands. **1162**, 126–31. <https://doi.org/10.1016/j.chroma.2007.05.110>
- [121] Vahabi, S., Nazemi Salman, B. and Javanmard, A. (2013) Atomic force microscopy application in biological research: a review study. *Iranian Journal of Medical Sciences*, Iran. **38**, 76–83.
- [122] Musielak, M. (2009) Red blood cell-deformability measurement: review of techniques. *Clinical Hemorheology and Microcirculation*, Netherlands. **42**, 47–64. <https://doi.org/10.3233/CH-2009-1187>
- [123] Herbig, M., Mietke, A., Müller, P. and Otto, O. (2018) Statistics for real-time

- deformability cytometry : clustering , dimensionality reduction and significance testing. *Biomicrofluidics*, **042214**, 1–37. <https://doi.org/10.1063/1.5027197>
- [124] Golfier, S., Rosendahl, P., Mietke, A., Herbig, M., Guck, J. and Otto, O. (2017) High-throughput cell mechanical phenotyping for label-free titration assays of cytoskeletal modifications. *Cytoskeleton*, **74**, 283–96. <https://doi.org/10.1002/cm.21369>
- [125] Rosendahl, P., Plak, K., Jacobi, A., Kraeter, M., Toepfner, N., Otto, O. et al. (2018) Real-time fluorescence and deformability cytometry. *Nature Methods*, **15**, 355–8. <https://doi.org/10.1038/nmeth.4639>
- [126] Hajian-Tilaki, K. (2013) Receiver Operating Characteristic (ROC) Curve Analysis for Medical Diagnostic Test Evaluation. *Caspian Journal of Internal Medicine*, Babol University of Medical Sciences. **4**, 627–35.
- [127] Darling, E.M. and Di Carlo, D. (2015) High-Throughput Assessment of Cellular Mechanical Properties. *Annual Review of Biomedical Engineering*, United States. **17**, 35–62. <https://doi.org/10.1146/annurev-bioeng-071114-040545>
- [128] Hu, J., Liu, J., Xue, F., Halverson, G., Reid, M., Guo, A. et al. (2013) Isolation and functional characterization of human erythroblasts at distinct stages: implications for understanding of normal and disordered erythropoiesis in vivo. *Blood*, United States. **121**, 3246–53. <https://doi.org/10.1182/blood-2013-01-476390>
- [129] Chen, K., Liu, J., Heck, S., Chasis, J.A., An, X. and Mohandas, N. (2009) Resolving the distinct stages in erythroid differentiation based on dynamic changes in membrane protein expression during erythropoiesis. *Proceedings of the National Academy of Sciences of the United States of America*, United States. **106**, 17413–8. <https://doi.org/10.1073/pnas.0909296106>
- [130] Huang, X., Shah, S., Wang, J., Ye, Z., Dowey, S.N., Tsang, K.M. et al. (2014) Extensive ex vivo expansion of functional human erythroid precursors established from umbilical cord blood cells by defined factors. *Molecular Therapy : The Journal of the American Society of Gene Therapy*, United States. **22**, 451–63. <https://doi.org/10.1038/mt.2013.201>
- [131] Chasis, J.A. and Mohandas, N. (2008) Erythroblastic islands: niches for erythropoiesis. *Blood*, United States. **112**, 470–8. <https://doi.org/10.1182/blood-2008-03-077883>
- [132] Shin, T.H., Lee, S., Choi, K.R., Lee, D.Y., Kim, Y., Paik, M.J. et al. (2017) Quality and freshness of human bone marrow-derived mesenchymal stem cells decrease over time after trypsinization and storage in phosphate-buffered saline. *Scientific Reports*, England. **7**, 1106. <https://doi.org/10.1038/s41598-017-01315-0>

- [133] Gratzner, W.B. (1981) The red cell membrane and its cytoskeleton. *The Biochemical Journal*, England. **198**, 1–8.
- [134] Hebiguchi, M., Hirokawa, M., Guo, Y.-M., Saito, K., Wakui, H., Komatsuda, A. et al. (2008) Dynamics of human erythroblast enucleation. *International Journal of Hematology*, Japan. **88**, 498–507. <https://doi.org/10.1007/s12185-008-0200-6>
- [135] Konstantinidis, D.G., Pushkaran, S., Johnson, J.F., Cancelas, J.A., Manganaris, S., Harris, C.E. et al. (2012) Signaling and cytoskeletal requirements in erythroblast enucleation. *Blood*, United States. **119**, 6118–27. <https://doi.org/10.1182/blood-2011-09-379263>
- [136] Rosenbluth, M.J., Lam, W.A. and Fletcher, D.A. (2006) Force microscopy of nonadherent cells: a comparison of leukemia cell deformability. *Biophysical Journal*, United States. **90**, 2994–3003. <https://doi.org/10.1529/biophysj.105.067496>
- [137] Diogo, M.M., da Silva, C.L. and Cabral, J.M.S. (2014) Separation Technologies for Stem Cell Bioprocessing BT - Stem Cells and Cell Therapy. In: Al-Rubeai M, and Naciri M, editors. Springer Netherlands, Dordrecht. p. 157–81. [https://doi.org/10.1007/978-94-007-7196-3\\_7](https://doi.org/10.1007/978-94-007-7196-3_7)
- [138] Zhang, J., Yan, S., Yuan, D., Alici, G., Nguyen, N.-T., Ebrahimi Warkiani, M. et al. (2016) Fundamentals and applications of inertial microfluidics: a review. *Lab on a Chip*, The Royal Society of Chemistry. **16**, 10–34. <https://doi.org/10.1039/C5LC01159K>
- [139] Uijttewaal, W.S.J., Nijhof, E. and Heethaar, R.M. (1993) Droplet migration, deformation, and orientation in the presence of a plane wall: A numerical study compared with analytical theories. *Physics of Fluids A: Fluid Dynamics*, American Institute of Physics. **5**, 819–25. <https://doi.org/10.1063/1.858629>
- [140] Coupier, G., Kaoui, B., Podgorski, T. and Misbah, C. (2008) Noninertial lateral migration of vesicles in bounded Poiseuille flow. *Physics of Fluids*, American Institute of Physics. **20**, 111702. <https://doi.org/10.1063/1.3023159>
- [141] Abkarian, M. and Viallat, A. (2008) Vesicles and red blood cells in shear flow. *Soft Matter*, The Royal Society of Chemistry. **4**, 653–7. <https://doi.org/10.1039/B716612E>
- [142] Seifert, U., Berndl, K. and Lipowsky, R. (1991) Shape transformations of vesicles: Phase diagram for spontaneous- curvature and bilayer-coupling models. *Physical Review A*, American Physical Society. **44**, 1182–202. <https://doi.org/10.1103/PhysRevA.44.1182>
- [143] Karimi, A., Yazdi, S. and Ardekani, A.M. (2013) Hydrodynamic mechanisms of cell

- and particle trapping in microfluidics. *Biomicrofluidics*, American Institute of Physics. **7**, 21501. <https://doi.org/10.1063/1.4799787>
- [144] Zeng, F., Yang, W., Huang, J., Chen, Y. and Chen, Y. (2013) Determination of the lowest concentrations of aldehyde fixatives for completely fixing various cellular structures by real-time imaging and quantification. *Histochemistry and Cell Biology*, **139**, 735–49. <https://doi.org/10.1007/s00418-012-1058-5>
- [145] Gajasinghe, R.W.R.L., Senveli, S.U., Rawal, S., Williams, A., Zheng, A., Datar, R.H. et al. (2014) Experimental study of PDMS bonding to various substrates for monolithic microfluidic applications. *Journal of Micromechanics and Microengineering*, IOP Publishing. **24**, 75010. <https://doi.org/10.1088/0960-1317/24/7/075010>
- [146] de Back, D.Z., Kostova, E.B., van Kraaij, M., van den Berg, T.K. and van Bruggen, R. (2014) Of macrophages and red blood cells; a complex love story. *Frontiers in Physiology*, Frontiers Media S.A. **5**, 9. <https://doi.org/10.3389/fphys.2014.00009>
- [147] Xiang, N., Zhang, X., Dai, Q., Cheng, J., Chen, K. and Ni, Z. (2016) Fundamentals of elasto-inertial particle focusing in curved microfluidic channels. *Lab on a Chip*, Royal Society of Chemistry. **16**, 2626–35. <https://doi.org/10.1039/c6lc00376a>
- [148] Carmen, J., Burger, S.R., McCaman, M. and Rowley, J.A. (2012) Developing assays to address identity, potency, purity and safety: cell characterization in cell therapy process development. *Regenerative Medicine*, England. **7**, 85–100. <https://doi.org/10.2217/rme.11.105>
- [149] Tsai, M.A., Waugh, R.E. and Keng, P.C. (1996) Cell cycle-dependence of HL-60 cell deformability. *Biophysical Journal*, Elsevier. **70**, 2023–9. [https://doi.org/10.1016/S0006-3495\(96\)79768-0](https://doi.org/10.1016/S0006-3495(96)79768-0)
- [150] Lin, J., Kim, D., Tse, H.T., Tseng, P., Peng, L., Dhar, M. et al. (2017) High-throughput physical phenotyping of cell differentiation. *Microsystems & Nanoengineering*, **3**, 17013. <https://doi.org/10.1038/micronano.2017.13>
- [151] Ekpenyong, A.E., Whyte, G., Chalut, K., Pagliara, S., Lautenschläger, F., Fiddler, C. et al. (2012) Viscoelastic Properties of Differentiating Blood Cells Are Fate- and Function-Dependent. *PLoS ONE*, **7**. <https://doi.org/10.1371/journal.pone.0045237>
- [152] Tadimety, A., Closson, A., Li, C., Yi, S., Shen, T. and Zhang, J.X.J. (2018) Advances in liquid biopsy on-chip for cancer management: Technologies, biomarkers, and clinical analysis. *Critical Reviews in Clinical Laboratory Sciences*, Taylor & Francis. **55**, 140–62. <https://doi.org/10.1080/10408363.2018.1425976>
- [153] Park, E.S., Duffy, S.P. and Ma, H. (2017) Microfluidic Separation of Circulating

- Tumor Cells Based on Size and Deformability. *Methods in Molecular Biology (Clifton, NJ)*, United States. **1634**, 21–32. [https://doi.org/10.1007/978-1-4939-7144-2\\_2](https://doi.org/10.1007/978-1-4939-7144-2_2)
- [154] Beili, Z.S. and Murthy. (2012) Stem Cell Separation Technologies. *Current Opinion Chem Eng*, **2**, 3–7. <https://doi.org/10.1016/j.coche.2012.11.002>
- [155] Esposito, M.T. (2018) Blood factory: which stem cells? *BMC Hematology*, England. **18**, 10. <https://doi.org/10.1186/s12878-018-0105-4>
- [156] Takahashi, K. and Yamanaka, S. (2006) Induction of pluripotent stem cells from mouse embryonic and adult fibroblast cultures by defined factors. *Cell*, United States. **126**, 663–76. <https://doi.org/10.1016/j.cell.2006.07.024>
- [157] Severn, C. and Toye, A. (2017) The challenge of growing enough reticulocytes for transfusion. *ISBT Sci. Ser.* <https://doi.org/10.1111/voxs.12374>
- [158] Kim, G.-Y., Han, J.-I. and Park, J.-K. (2018) Inertial Microfluidics-Based Cell Sorting. *BioChip Journal*, **12**, 257–67. <https://doi.org/10.1007/s13206-018-2401-2>
- [159] Miller, B., Jimenez, M. and Bridle, H. (2016) Cascading and Parallelising Curvilinear Inertial Focusing Systems for High Volume, Wide Size Distribution, Separation and Concentration of Particles. *The Author(s)*. **6**, 36386.
- [160] Heger, J.I., Froehlich, K., Pastuschek, J., Schmidt, A., Baer, C., Mrowka, R. et al. (2018) Human serum alters cell culture behavior and improves spheroid formation in comparison to fetal bovine serum. *Experimental Cell Research*, United States. **365**, 57–65. <https://doi.org/10.1016/j.yexcr.2018.02.017>
- [161] Henderson, C., Yacopucci, M., Chun, C., Lenghaus, K., Sommerhage, F. and J. Hickman, J. (2010) Investigation of the behavior of serum and plasma in a microfluidics system. *J. Vac. Sci. Technol. B Microelectron. Nanom. Struct.* <https://doi.org/10.1116/1.3475531>
- [162] Guzniczak, E., Jimenez, M., Irwin, M., Otto, O., Willoughby, N. and Bridle, H. (2018) Impact of poloxamer 188 (Pluronic F-68) additive on cell mechanical properties, quantification by real-time deformability cytometry. *Biomicrofluidics*, **12**, 044118. <https://doi.org/10.1063/1.5040316>
- [163] Biosciences, B. (2004) BD FACService™ TECHNOTES. *Solutions, Customer Focused*, **9**.
- [164] Tharmalingam, T., Ghebeh, H., Wuerz, T. and Butler, M. (2008) Pluronic Enhances the Robustness and Reduces the Cell Attachment of Mammalian Cells. *Molecular Biotechnology*, **39**, 167–77. <https://doi.org/10.1007/s12033-008-9045-8>
- [165] R., D.W. and Sydney, C. (1928) Fluid motion in a curved channel. *Proceedings of the*

- Royal Society of London Series A, Containing Papers of a Mathematical and Physical Character*, Royal Society. **121**, 402–20. <https://doi.org/10.1098/rspa.1928.0205>
- [166] Berger, S.A., Talbot, L. and Yao, L.S. (1983) Flow in Curved Pipes. *Annual Review of Fluid Mechanics*, Annual Reviews. **15**, 461–512.  
<https://doi.org/10.1146/annurev.fl.15.010183.002333>
- [167] Parzel, C.A., Pepper, M.E., Burg, T., Groff, R.E. and Burg, K.J.L. (2009) EDTA enhances high-throughput two-dimensional bioprinting by inhibiting salt scaling and cell aggregation at the nozzle surface. *Journal of Tissue Engineering and Regenerative Medicine*, England. **3**, 260–8. <https://doi.org/10.1002/term.162>
- [168] Holmes, D., Whyte, G., Bailey, J., Vergara-irigaray, N., Ekpenyong, A., Guck, J. et al. (2014) Separation of blood cells with differing deformability using deterministic lateral displacement Separation of blood cells with differing deformability using deterministic lateral. *Interface Focus*, **4**.
- [169] Amini, H., Sollier, E., Weaver, W.M. and Di Carlo, D. (2012) Intrinsic particle-induced lateral transport in microchannels. *Proceedings of the National Academy of Sciences of the United States of America*, United States. **109**, 11593–8.  
<https://doi.org/10.1073/pnas.1207550109>
- [170] Matas, J.-P., Glezer, V., Guazzelli, É. and Morris, J.F. (2004) Trains of particles in finite-Reynolds-number pipe flow. *Physics of Fluids*, American Institute of Physics. **16**, 4192–5. <https://doi.org/10.1063/1.1791460>
- [171] Lee, W., Amini, H., Stone, H.A. and Di Carlo, D. (2010) Dynamic self-assembly and control of microfluidic particle crystals. *Proceedings of the National Academy of Sciences of the United States of America*, 2010/12/13. National Academy of Sciences. **107**, 22413–8. <https://doi.org/10.1073/pnas.1010297107>
- [172] Chisti, Y. (2000) Animal-cell damage in sparged bioreactors. *Trends in Biotechnology*, **18**, 420–32. [https://doi.org/https://doi.org/10.1016/S0167-7799\(00\)01474-8](https://doi.org/https://doi.org/10.1016/S0167-7799(00)01474-8)
- [173] Alexandridis, P. and Alan Hatton, T. (1995) Poly(ethylene oxide)□poly(propylene oxide)□poly(ethylene oxide) block copolymer surfactants in aqueous solutions and at interfaces: thermodynamics, structure, dynamics, and modeling. *Colloids and Surfaces A: Physicochemical and Engineering Aspects*, **96**, 1–46.  
[https://doi.org/https://doi.org/10.1016/0927-7757\(94\)03028-X](https://doi.org/https://doi.org/10.1016/0927-7757(94)03028-X)
- [174] Goldblum, S., Bae, Y.-K., Hink, W.F. and Chalmers, J. (1990) Protective Effect of Methylcellulose and Other Polymers on Insect Cells Subjected to Laminar Shear Stress. *Biotechnology Progress*, American Chemical Society (ACS). **6**, 383–90.

- <https://doi.org/10.1021/bp00005a011>
- [175] Karleta, V., Andrlík, I., Braumüller, S., Franke, T., Wirth, M. and Gabor, F. (2010) Poloxamer 188 supplemented culture medium increases the vitality of Caco-2 cells after subcultivation and freeze/thaw cycles. *ALTEX*, Germany. **27**, 191–7.
- [176] O’Keefe, J.H., Grines, C.L., DeWood, M.A., Schaer, G.L., Browne, K., Magorien, R.D. et al. (1996) Poloxamer-188 as an adjunct to primary percutaneous transluminal coronary angioplasty for acute myocardial infarction. *The American Journal of Cardiology*, **78**, 747–50. [https://doi.org/10.1016/S0002-9149\(96\)00414-6](https://doi.org/10.1016/S0002-9149(96)00414-6)
- [177] Harting, M.T., Jimenez, F., Kozar, R.A., Moore, F.A., Mercer, D.W., Hunter, R.L. et al. (2008) Effects of poloxamer 188 on human PMN cells. *Surgery*, **144**, 198–203. <https://doi.org/10.1016/j.surg.2008.05.001>
- [178] R Schmolka, I. (1975) Artificial blood emulsifiers. *Fed. Proc.*
- [179] Rodeheaver, G.T., Kurtz, L., Kircher, B.J. and Edlich, R.F. (1980) Pluronic F-68: A promising new skin wound cleanser. *Annals of Emergency Medicine*, **9**, 572–6. [https://doi.org/10.1016/S0196-0644\(80\)80228-9](https://doi.org/10.1016/S0196-0644(80)80228-9)
- [180] McClain, M.A., Culbertson, C.T., Jacobson, S.C., Allbritton, N.L., Sims, C.E. and Ramsey, J.M. (2003) Microfluidic Devices for the High-Throughput Chemical Analysis of Cells. *Analytical Chemistry*, American Chemical Society. **75**, 5646–55. <https://doi.org/10.1021/ac0346510>
- [181] Hargis, A.D., Alarie, J.P. and Ramsey, J.M. (2011) Characterization of cell lysis events on a microfluidic device for high-throughput single cell analysis. *ELECTROPHORESIS*, John Wiley & Sons, Ltd. **32**, 3172–9. <https://doi.org/10.1002/elps.201100229>
- [182] Tan, S.J., Kee, M.Z.L., Mathuru, A.S., Burkholder, W.F. and Jesuthasan, S.J. (2013) A Microfluidic Device to Sort Cells Based on Dynamic Response to a Stimulus. *PLOS ONE*, Public Library of Science. **8**, e78261.
- [183] Brouzes, E., Medkova, M., Savenelli, N., Marran, D., Twardowski, M., Hutchison, J.B. et al. (2009) Droplet microfluidic technology for single-cell high-throughput screening. *Proceedings of the National Academy of Sciences*, **106**, 14195 LP – 14200. <https://doi.org/10.1073/pnas.0903542106>
- [184] Luk, V.N., Mo, G.C. and Wheeler, A.R. (2008) Pluronic additives: a solution to sticky problems in digital microfluidics. *Langmuir : The ACS Journal of Surfaces and Colloids*, United States. **24**, 6382–9. <https://doi.org/10.1021/la7039509>

- [185] Tan, J.L., Liu, W., Nelson, C.M., Raghavan, S. and Chen, C.S. (2004) Simple Approach to Micropattern Cells on Common Culture Substrates by Tuning Substrate Wettability. *Tissue Engineering*, Mary Ann Liebert, Inc., publishers. **10**, 865–72. <https://doi.org/10.1089/1076327041348365>
- [186] Sundblom, A., Palmqvist, A.E.C. and Holmberg, K. (2010) Study of the Pluronic–Silica Interaction in Synthesis of Mesoporous Silica under Mild Acidic Conditions. *Langmuir*, American Chemical Society. **26**, 1983–90. <https://doi.org/10.1021/la902144h>
- [187] Wong, I. and Ho, C.-M. (2009) Surface molecular property modifications for poly(dimethylsiloxane) (PDMS) based microfluidic devices. *Microfluidics and Nanofluidics*, **7**, 291. <https://doi.org/10.1007/s10404-009-0443-4>
- [188] Son, H.Y., Lee, D.J., Lee, J.B., Park, C.H., Seo, M., Jang, J. et al. (2014) In situ functionalization of highly porous polymer microspheres with silver nanoparticles via bio-inspired chemistry. *RSC Advances*, The Royal Society of Chemistry. **4**, 55604–9. <https://doi.org/10.1039/C4RA08685F>
- [189] Au, S.H., Kumar, P. and Wheeler, A.R. (2011) A new angle on Pluronic additives: Advancing droplets and understanding in digital microfluidics. *Langmuir*, **27**, 8586–94. <https://doi.org/10.1021/la201185c>
- [190] Maskarinec, S.A., Hannig, J., Lee, R.C. and Lee, K.Y.C. (2002) Direct Observation of Poloxamer 188 Insertion into Lipid Monolayers. *Biophysical Journal*, **82**, 1453–9. [https://doi.org/https://doi.org/10.1016/S0006-3495\(02\)75499-4](https://doi.org/https://doi.org/10.1016/S0006-3495(02)75499-4)
- [191] Wu, G., Majewski, J., Ege, C., Kjaer, K., Weygand, M.J. and Lee, K.Y.C. (2004) Lipid Corraling and Poloxamer Squeeze-Out in Membranes. *Physical Review Letters*, American Physical Society. **93**, 28101. <https://doi.org/10.1103/PhysRevLett.93.028101>
- [192] McGrath, J., Jimenez, M. and Bridle, H. (2014) Deterministic lateral displacement for particle separation: A review. *Lab on a Chip*, Royal Society of Chemistry. **14**, 4139–58. <https://doi.org/10.1039/c4lc00939h>
- [193] Abd Rahman, N., Ibrahim, F. and Yafouz, B. (2017) Dielectrophoresis for Biomedical Sciences Applications: A Review. *Sensors (Basel, Switzerland)*, **17**, 1–27. <https://doi.org/10.3390/s17030449>
- [194] Gigout, A., Buschmann, M.D. and Jolicœur, M. (2008) The fate of Pluronic F-68 in chondrocytes and CHO cells. *Biotechnology and Bioengineering*, John Wiley & Sons, Ltd. **100**, 975–87. <https://doi.org/10.1002/bit.21840>



- [195] Guo, Q., Duffy, S.P., Matthews, K., Santoso, A.T., Scott, M.D. and Ma, H. (2014) Microfluidic analysis of red blood cell deformability. *Journal of Biomechanics*, **47**, 1767–76. <https://doi.org/10.1016/j.jbiomech.2014.03.038>
- [196] Smith, C.M. 2nd, Hebbel, R.P., Tukey, D.P., Clawson, C.C., White, J.G. and Vercellotti, G.M. (1987) Pluronic F-68 reduces the endothelial adherence and improves the rheology of liganded sickle erythrocytes. *Blood*, United States. **69**, 1631–6.
- [197] Sandor, B., Marin, M., Lapoumeroulie, C., Rabai, M., Lefevre, S.D., Lemonne, N. et al. (2016) Effects of Poloxamer 188 on red blood cell membrane properties in sickle cell anaemia. *British Journal of Haematology*, John Wiley & Sons, Ltd (10.1111). **173**, 145–9. <https://doi.org/10.1111/bjh.13937>
- [198] Stepanenko, A.A. and Dmitrenko, V. V. (2015) HEK293 in cell biology and cancer research: phenotype, karyotype, tumorigenicity, and stress-induced genome-phenotype evolution. *Gene*, **569**, 182–90. <https://doi.org/10.1016/j.gene.2015.05.065>
- [199] Walther, C.G., Whitfield, R. and James, D.C. (2016) Importance of Interaction between Integrin and Actin Cytoskeleton in Suspension Adaptation of CHO cells. *Applied Biochemistry and Biotechnology*, Applied Biochemistry and Biotechnology. **178**, 1286–302. <https://doi.org/10.1007/s12010-015-1945-z>
- [200] Ramírez, O.T. and Mutharasan, R. (1990) The role of the plasma membrane fluidity on the shear sensitivity of hybridomas grown under hydrodynamic stress. *Biotechnology and Bioengineering*, John Wiley & Sons, Ltd. **36**, 911–20. <https://doi.org/10.1002/bit.260360906>
- [201] Toepfner, N., Herold, C., Otto, O., Rosendahl, P., Jacobi, A., Krater, M. et al. (2018) Detection of human disease conditions by single-cell morpho-rheological phenotyping of blood. *ELife*, England. **7**. <https://doi.org/10.7554/eLife.29213>
- [202] Xu, Z., Zheng, Y., Wang, X., Shehata, N., Wang, C., Xie, S. et al. (2016) Stiffening of sickle cell trait red blood cells under simulated strenuous exercise conditions. *Microsystems & Nanoengineering*, The Author(s). **2**, 16061.
- [203] Athanasiou, G., Zoubos, N. and Missirlis, Y. (1991) Erythrocyte membrane deformability in patients with thalassemia syndromes. *Nouvelle Revue Francaise d'hematologie*, Germany. **33**, 15–20.
- [204] Ochalek, T., Nordt, F.J., Tullberg, K. and Burger, M.M. (1988) Correlation between Cell Deformability and Metastatic Potential in B16-F1 Melanoma Cell Variants.

- Cancer Research*, **48**, 5124 LP – 5128.
- [205] Khismatullin, D.B.B.T.-C.T. in M. (2009) Chapter 3 The Cytoskeleton and Deformability of White Blood Cells. *Current Topics in Membranes*, Academic Press. p. 47–111. [https://doi.org/https://doi.org/10.1016/S1063-5823\(09\)64003-5](https://doi.org/https://doi.org/10.1016/S1063-5823(09)64003-5)
- [206] Mietke, A., Otto, O., Girardo, S., Rosendahl, P., Taubenberger, A., Golfier, S. et al. (2015) Extracting Cell Stiffness from Real-Time Deformability Cytometry: Theory and Experiment. *Biophysical Journal*, The Authors. **109**, 2023–36. <https://doi.org/10.1016/j.bpj.2015.09.006>